Title
Equatorial Magnetic Waves in the Stratified Ocean of Earth's Core

Author
Knezek, Nicholas R

Publication Date
2019

Peer reviewed|Thesis/dissertation

Equatorial Magnetic Waves in the Stratified Ocean of Earth's Core

By

Nicholas R. Knezek

A dissertation submitted in partial satisfaction of the

requirements for the degree of

Doctor of Philosophy

in

Earth and Planetary Science

in the

Graduate Division

of the

University of California, Berkeley

Committee in charge:

Professor Bruce Buffett, Chair
Professor Raymond Jeanloz
Professor Michael Manga
Professor Stuart Bale

Fall 2019

Abstract

Equatorial Magnetic Waves
in the Stratified Ocean of Earth's Core

by

Nicholas R. Knezek

Doctor of Philosophy in Earth and Planetary Science

University of California, Berkeley

Professor Bruce Buffett, Chair

Earth's global magnetic field envelops us all, protecting us from cosmic rays, aiding our navigation, and shielding our oxygen-rich atmosphere. Yet details about its origin, operation, and future remain unknown. Recent space-based magnetic observatories let us observe the field more precisely than ever before, and we can use these measurements to study the deep interior of the Earth and illuminate a region of our planet previously observed mainly by listening to the echoes of earthquakes. In this thesis, I use observations of changes in Earth's magnetic field to study the structure and processes occurring near the top of Earth's core. In particular, I examine the long-debated question of whether a stratified layer of fluid, termed by some as the stratified ocean of the core or SOC (Braginsky, 1998), lies at the top of Earth's outer core. I first implement a model to simulate fluid motions in the SOC, which I describe in chapter two. Then, I derive the properties of a class of eastward-propagating equatorially trapped magnetic waves I term eMAC waves in chapter three and develop a statistical threshold to detect these waves in chapter four. In chapter five, I apply my statistical test to observations of Earth's geomagnetic field and find evidence for these waves in Earth's core. Finally, in chapter six, I propose a 20-40 km thick SOC with buoyancy strength of $N \geq 10\ \Omega$ to support the observed eMAC wave modes. I then discuss the implications of this layer, propose a double-layer SOC as a way to reconcile eMAC signals with previous observations, and enumerate possible future avenues of investigation.

Contents

List of Figures

List of Tables

Acknowledgments

I wish to thank my partner Laura; my advisor Bruce; my parents Lois and Gerald; my siblings Gabe and Sarah; my committee; and many other friends and colleagues too numerous to count for their encouragement and support through the process of writing this dissertation.

Chapter 1

Background

Earth has a global geomagnetic field generated by a dynamo in its liquid iron outer core. Experimental and observational constraints from materials science, seismology, fluid dynamics, and many other fields have allowed us to produce a rough sketch of the properties and dynamics of this region of the Earth, and large-scale computer simulations reproduce the behavior of Earth's geodynamo with remarkable fidelity (Glatzmaier and Roberts, 1995; Schaeffer et al., 2017). However, many open questions about the geodynamo and deep interior of the Earth remain unanswered. In particular, one long-debated question is whether a stratified layer of fluid, termed by some as the stratified ocean of the core or SOC (Braginsky, 1998), lies at the top of Earth's outer core. While the bulk of Earth's outer core must convect to power the geodynamo, it is possible that a thin region of fluid near Earth's core-mantle boundary (CMB) is buoyantly trapped near the mantle and does not convect. The existence of the SOC has implications across many domains of Earth science and could impact our understanding of the operation of the geodynamo, core dynamics, core-mantle interactions, and geomagnetic signals from the core.

1.1 The Stratified Ocean of the Core (SOC)

The bulk of Earth's outer core must convect to power the geodynamo observed at Earth's surface. However, it is possible that some regions in the outer core do not convect with the bulk outer core due to density stratification. Stratified layers have been proposed to exist at various depths in the

outer core from the inner core boundary (Wong et al., 2018), to the CMB (Whaler, 1980) and even at intermediate depths (Gomi et al., 2013). However, here we discuss only a possible low-density, buoyantly stratified layer near the CMB, which has been termed the stratified ocean of the core (SOC) by Braginsky (1998). The existence of the SOC, if confirmed, would impact our understanding of a wide variety of open geophysical questions.

1.1.1 Implications

Most models of Earth assume that the liquid iron-alloy outer core is convecting and well-mixed throughout (e.g. Olson, 2015). The SOC breaks this assumption and so segregates the outer core into at least two regions with potentially different chemical compositions and dynamics. This segregation impacts many processes in the outer core, including the operation of Earth's geodynamo, propagation of geomagnetic signals and seismic waves, core-mantle interactions, and even Earth's history and future. Such a stratified layer in Earth's core could even be interpreted as an additional layer of the Earth, a fundamental discovery in and of itself.

1.1.1.1 Fluid Flows

The bulk of the outer core fluid consists of a rapidly rotating (2π/day) spherical shell dominated by magnetic and Coriolis forces, with buoyancy driving vigorous convection that likely keeps the fluid physically and chemically well-mixed (e.g. Jones, 2015). Rapid rotation means that the dynamics of the bulk outer core are dominated by columnar or quasi-geostrophic (QG) flows (Busse, 1970; Pais and Jault, 2008). In a quasi-geostrophic system, fluid columns aligned with Earth's rotation axis largely move coherently and cannot alter their height, meaning that the geometry of the inner core and CMB influence dynamics throughout the bulk core fluid.

The SOC, by contrast, is buoyantly stratified and therefore does not participate in the same dynamics as the rest of the outer core. Buoyancy breaks the QG constraint and suppresses convective motions, potentially preventing fluid motions in the bulk core from penetrating into the SOC. However, the SOC fluid is far from stagnant, as it supports an array of fluid dynamics from thermal winds to global wave motions across a wide range of spatial and time scales (e.g. Braginsky, 1999; Christensen and Wicht, 2008; Helffrich and Kaneshima, 2013).

As a layer of conductive fluid, the SOC would act to shield magnetic signals from deeper in the outer core and attenuate their propagation to Earth's surface. Thus, it acts as a filter for small-scale, high-frequency geomagnetic signals occurring in the bulk, convective outer core. This impacts the observed structure of the geomagnetic field, in particular by enhancing the relative strength of the dipole to higher-order components of the geodynamo (Christensen, 2006; Nakagawa, 2011; Sreenivasan and Gubbins, 2008; Yan and Stanley, 2018). Numerical simulations have also found that the SOC would influence the equatorial symmetry of the observed geomagnetic field and the distribution between zonal and non-zonal field components (Christensen et al., 2010), and may cause intense patches of magnetic flux in the polar regions of the CMB (Olson et al., 2017).

The SOC would also influence the motion of fluids in the bulk outer core. In particular, the density perturbation of the SOC modifies the frequency of both the Chandler wobble (Braginsky, 2000) and inertio-gravity modes (Seyed-Mahmoud et al., 2015) in the outer core. Vidal and Schaeffer (2015) find that while the frequencies of QG waves in the bulk core are unaffected by the SOC, the waves couple with internal wave modes in the SOC, changing the spatial expression of the waves at the CMB. On the other hand, Takehiro and Sasaki (2018) find that steady fluid motions in the bulk outer core such as zonal winds penetrate the SOC easily and are mostly unaffected by its existence, especially in the presence of large background magnetic fields.

The influence of the SOC on core flows is of particular importance when using observed geomagnetic secular variation (SV) to study the fluid dynamics of the outer core. Observations of SV do not fully constrain the fluid motions of the core (Backus and Bullard, 1968) and authors must make assumptions about the forces that dominate the dynamics of the fluid near the CMB to obtain meaningful results for core flows (e.g. Holme, 2015). Many authors apply the quasi-geostrophic constraint to inversions of SV for core flows, essentially assuming that the fluid near the CMB is subject to the same constraints as the bulk outer core fluid (Pais and Jault, 2008). Indeed, some authors explicitly downward-continue flows derived from observed SV to model the dynamics of core fluid throughout the bulk core (Pais and Jault, 2008; Schaeffer et al., 2017). However, if the SOC exists, the QG assumption may be inappropriate for inverting flows from SV, and core flows obtained using this method may be inaccurate. Instead, the buoyancy of the SOC would suppress radial fluid motions, potentially making flow constraints such as toroidal flow more appropriate for deriving accurate descriptions of

core fluid dynamics from SV (Amit, 2014; Bloxham, 1990, 1992; Lesur et al., 2015; Voorhies, 1984; Whaler, 1986). In addition, inversions for core flow explicitly damp small-scale and short-timescale fluid motions, assuming that they produce only a relatively small portion of observed SV. However, small-scale fluid motions could influence the observed SV significantly (Gillet et al., 2009). In particular, the SOC could support coherent small-scale and short-period fluid motions such as waves which produce large-scale, long-period coherent signals in observed SV.

If an SOC exists, it would also impact many of the conclusions drawn from studies of observed SV. For example, many authors have observed a large-scale westward drift of magnetic flux patches in Earth's magnetic field, and attributed this to fluid motions arising from geodynamo operation in the bulk outer core (Bullard et al., 1950). However, the westward drift could instead arise from processes within the SOC such as waves or thermal winds (Bloxham and Jackson, 1990; Whaler, 1980; Yukutake, 1981).

Geomagnetic jerks are another process observed in SV that is commonly theorized to originate in the bulk outer core. Jerks are rapid changes in SV theorized to originate due to hydromagnetic waves such as torsional oscillations in the bulk other core (Aubert and Finlay, 2019; Bloxham et al., 2002; Braginsky, 1984; Malin and Hodder, 1982). However, the SOC could impact our understanding of jerks in two ways. First, the SOC supports a wealth of additional wave modes, allowing many other possible origins for geomagnetic jerks. Second, the SOC could modify torsional oscillations by magnetically shielding their signals or preventing the propagation of their fluid motions to the CMB.

In fact, torsional oscillations (TO) are important independent of their relation to geomagnetic jerks, as they have been observed directly in Earth's core (Gillet et al., 2010). These waves propagate in the bulk outer core through an interaction between the QG constraint and the core's internal toroidal magnetic field (Braginskiy, 1970; Cox, 2015; Zatman and Bloxham, 1997), and recent studies observe their propagation in the Earth with periods less than 10 years (Gillet et al., 2010, 2015b). Magnetic signals of this frequency would be heavily attenuated by the conductive fluid of the SOC, meaning that to be detected at Earth's surface, the torsional oscillations must propagate through the SOC as physical motions of the SOC fluid. Indeed, studies have found that columnar flows like those involved in torsional oscillations can penetrate the SOC, especially at high latitudes, making detection of torsional oscillations possible even with a SOC (Christensen and

Wicht, 2008; Nakagawa, 2011; Vidal and Schaeffer, 2015). However, there are indications that the structure of the TO at the CMB may be modified by the presence of the SOC (Vidal and Schaeffer, 2015).

1.1.1.2 Interaction with the Mantle

The SOC will also impact how Earth's core and mantle interact, as the layer sits at the core-mantle boundary. Many authors have posited that spatially heterogeneous mantle heat flow influences the dynamics of the bulk outer core. In particular, Glatzmaier et al. (1999) hypothesizes that heterogeneous heat flow at the CMB can influence the reversal rate of the geodynamo, and Kutzner and Christensen (2004) find evidence that the pattern of heat flow can influence the path the virtual dipole follows during reversals. Olson et al. (2010) on the other hand, finds that the reversal frequency is insensitive to the spatial structure of heat flow at the CMB, and instead depends upon the total heat flow. However, all of these conclusions may be impacted by the presence of the SOC. First, lateral flows within the SOC would likely arise to respond to any CMB heat flow heterogeneity, possibly compensating for heat flow heterogeneity and shielding the bulk outer core from its effects (Christensen, 2018; Sumita and Olson, 1999). In addition, a thermally stratified layer can grow or shrink to respond to changes in the total mantle heat flow, reducing the influence of changes in total CMB heat flow on the dynamo operating in the bulk outer core (e.g. Buffett, 2015).

Earth's core and mantle also interact by exchanging momentum between the core fluid and the solid mantle. This momentum exchange is commonly used to explain observed changes in Earth's length of day over decadal timescales (e.g. Gross, 2015). There are several possible mechanisms proposed by which momentum could be exchanged, including topographic (Hide, 1969; Moffatt, 1977), electromagnetic (Bullard et al., 1950; Rochester, 1962), and gravitational (Buffett, 1996; Jault et al., 1988) coupling. The SOC potentially impacts the effectiveness of these mechanisms of momentum exchange, and also enables an additional hybrid mechanism whereby conductive, buoyant fluid is physically trapped by CMB topography and acts to enhance electromagnetic coupling between core fluid motions and the solid mantle (Buffett, 2010; Glane and Buffett, 2018).

The SOC may also influence chemical interactions between the core and mantle. The simplest model of Earth's core formation and evolution assumes that the core has been chemically isolated from the mantle since formation

(e.g. Rubie et al., 2015). However, this assumption may not be valid and chemical interactions between the core and mantle could continue to the present day (Jeanloz, 1990; Knittle and Jeanloz, 1989, 1991). Indeed, recent studies indicate that mass exchange between the core and mantle has occurred (Brandon and Walker, 2005; O'Rourke et al., 2016; Ozawa et al., 2009; Walker, 2005) and that the bulk outer core may be under-saturated in mantle minerals (e.g. Asahara et al., 2007; Ozawa et al., 2008, 2009). The SOC would influence these interactions by acting as a distinct chemical reservoir from the rest of the bulk outer core. Because it is buoyant, it resists mixing with the rest of the outer core, allowing compositional differences between the bulk core and SOC to arise over time and possibly providing an explanation for the bulk core's proposed under-saturation of light elements. That is, it is possible that the mantle and SOC are in equilibrium, but that light elements in the SOC do not mix into the bulk core, thus leaving the majority of the outer core under-saturated (Buffett and Seagle, 2010). Knowledge of the precise structure and properties of the SOC could thus inform our understanding of the chemical exchange between the core and mantle, with potentially large implications for other questions such as chemical energy sources for the geodynamo (e.g. Badro et al., 2016; Hirose et al., 2017) and the origin of mantle features such as ULVZs (Knittle and Jeanloz, 1991; Otsuka and Karato, 2012).

Finally, the SOC would also provide information about the thermal state of Earth's core and mantle. If the SOC is observed with properties suggesting thermal stratification (see section 1.1.2.1), this would indicate that the mantle heat flow is less than the core adiabatic gradient at the CMB. This gives information about the slope of the adiabatic gradient and thus the physical properties of the core fluid; the style of convection in the outer core; the rate of mantle convection now and in periods of recent Earth history; and potentially many other geophysical questions (Buffett, 2015; Lister and Buffett, 1998; Zhang and Zhong, 2011).

1.1.2 Origin

The SOC has a number of plausible origins. In general, buoyancy in the outer core fluid arises due to a density deficit caused by either an excess of light elements such as oxygen or sulfur, or thermal expansion from excess local heat. Both of these sources of buoyancy drive convection in the outer core, and they could contribute to the formation of the SOC individually or

in combination (e.g. Lister and Buffett, 1998). In general, compositional enrichment is more efficient at producing buoyancy, and the majority of the core convection at the present day is thought to arise due to compositional buoyancy originating from the growth of the inner-core (Labrosse, 2015; Nimmo, 2015). However, there are good reasons to think that thermal buoyancy may also contribute to the formation of the SOC (e.g. Buffett, 2014).

Whatever the source of buoyancy, the SOC must resist erosion and mixing from the convective fluid motions in the bulk outer core. Parcels of fluid rising through the bulk core could conceivably penetrate into a thin or weakly stratified SOC, mixing the fluid and eroding the layer away. This process of erosion is most effective when the layer is thin, so acts mainly as a constraint on layer formation (e.g. Buffett and Seagle, 2010). However, inertia is thought to be relatively weak compared to the other dynamic forces in Earth's core (Buffett and Knezek, 2018), so the details and effectiveness of SOC erosion in the outer core is an open question (e.g. Lister and Buffett, 1998; Gubbins and Davies, 2013). If the SOC is able to maintain its structure against erosion, thermal and compositional buoyancy can lead to very different layer properties.

1.1.2.1 Thermal Stratification

Thermal stratification arises from hot core fluid accumulating at the CMB and building up heat at a rate greater than mantle convection can transport away. In the bulk convecting core, the temperature profile is maintained very close to the the adiabatic gradient due to high flow velocities and turbulent mixing. In this region, heat is both conducted along the adiabatic gradient and transported by convective fluid motions. If the rate of local heat transfer falls below the rate at which heat can be conducted down the adiabatic gradient, all of the heat will be transferred through conduction and convection will cease in the region. In the outer core, the adiabatic gradient is steepest at the CMB due to the compressibility of liquid iron. This means that the radial heat flow required to maintain convection is highest near the CMB. Thus, if the mantle is unable to transfer heat from the core fast enough, a thermal SOC will form as hot fluid pools under the CMB and the local thermal gradient adjusts to be shallower than required to maintain convection (e.g. Lister and Buffett, 1998).

The structure of thermal SOCs depend only on the physical properties of the core fluid and the past and present CMB heat flow. Therefore, their

buoyancy and thickness can be predicted with a high degree of accuracy. Thermally stratified layers tend to form thick layers with weak buoyancy, as the temperature perturbation above the adiabat is likely to be only a few degrees (Lister and Buffett, 1998). It is possible for a thin, strongly buoyant SOC to form in response to dramatic shifts in mantle heat flow (e.g. Buffett, 2015), but, in general, thermally stratified layers are predicted to be greater than $\sim$ 100 km thick and have buoyancy frequencies on the order of N $\sim$ 1 /day or less (Buffett, 2014; Lister and Buffett, 1998). Here, N represents the Brunt–Väisälä frequency (see section A.3).

Thermal evolution models of the Earth have long proposed that at least some portions of the outer core are thermally stratified (Gubbins et al., 2004). Recent studies indicate that the thermal conductivity of the outer core fluid could be much higher than previously thought (de Koker et al., 2012; Gomi et al., 2013; Ohta et al., 2016; Pozzo et al., 2012a, 2014) which would substantially increase the likelihood that the outer core is thermally stratified (Labrosse, 2015). However, it must be noted that these thermal conductivity measurements are a source of active debate (Konôpková et al., 2016).

1.1.2.2 Compositional Stratification

The second method by which the SOC could form is through a local enrichment of light elements (e.g. Lay and Young, 1990). Unlike thermal SOCs, compositional SOCs have many possible origin mechanisms, compositions, and resulting physical properties. A compositional SOC could arise due to local enrichment of any siderophile (iron-loving) element that is less dense than iron. Commonly proposed elements include oxygen, silicon, sulfur, carbon, helium, and hydrogen. In addition, there are several mechanisms through which the enrichment could arise.

One mechanism by which a compositional SOC could form is through barodiffusion of light elements along the pressure gradient of the core (Braginsky, 2006, 2007). Barodiffusion is the tendency of light elements to migrate down a pressure gradient due to molecular motion and interactions. Because the lowest pressure in the outer core lies at the CMB, light elements would tend to migrate and accumulate in the region under the CMB, forming the SOC. This mechanism could occur with any of the light elements in the core, but authors have proposed O, S, and Si in particular as candidates to form the SOC (Gubbins and Davies, 2013). One study proposes that a SOC formed through barodiffusion could have a thickness on the order of 100 km with N

$\sim$ 20 /day (Gubbins and Davies, 2013).

A second mechanism by which compositional stratification in the core can arise is by exchange of material with the mantle. Evidence supporting this mechanism is given by several studies showing that the bulk outer core is under-saturated in oxygen and silicon at the present day (Asahara et al., 2007; Ozawa et al., 2009). If true, these elements would diffuse from the mantle into the core, enriching the local fluid with light elements and possibly forming the SOC. Because the elements forming the SOC with this mechanism originate in the mantle, the most buoyant regions at the CMB are continuously enhanced, leading to thinner and more strongly buoyant layers than those produced by other origin mechanisms (Lister and Buffett, 1998). In particular, Buffett and Seagle (2010) estimates the SOCs arising from this mechanisms to have a thickness of 70 km, with N $>$ 55 /day.

Finally, there are a two less commonly proposed SOC formation mechanisms. The SOC could have primordial origins, either through layering of successive impactor core material during Earth's formation (Helffrich and Kaneshima, 2013; Helffrich, 2014) or due to iron diapirs sinking through the primordial mantle shortly after formation and forming a buoyant layer atop the ancient core (Wood et al., 2006). However, the dominant theory of the formation of the moon from a giant impactor raises questions for these theories (Canup, 2004). Such an impact is likely to mix the core, so there must be some mechanism to maintain the layering through this extremely energetic event. Then, these primordial layers must persist to the present day despite temperature changes, inner-core growth, outer core compositional changes, and other factors over the 4.5 billion years of Earth history.

Other authors propose that a stratified layer could arise due to immiscibility between regions with different iron alloy compositions in the core (Arveson et al., 2019; Helffrich and Kaneshima, 2004). This theory posits that the temperature and pressure gradients within the core lead to regions with specific fluid compositions, which then have distinctive buoyancies and do not mix. This theory has spurred many authors to study the stability and miscibility of iron alloys with various light element compositions at core temperature and pressure ranges, but so far results are inconclusive with respect to Earth's core due to the difficulty of conducting these experiments and the unknown composition of the outer core (Corgne et al., 2008; Tsuno et al., 2007).

1.1.3 Structure

Many properties of the SOC are predicted to be the same regardless of its origin. It is typically proposed to be between 10 and 300 km thick (Eaton and Kendall, 2006; Kaneshima and Helffrich, 2013), with a buoyancy strength measured using the Brunt–Väisälä frequency (N) varying from weak stratification of $N < 1$ /day to strong stratification of $N > 55$ /day (Braginsky, 1993; Buffett and Seagle, 2011). The simplest model for a SOC is a global layer consisting of a single density jump with a constant background magnetic field. This model has been used by several authors to study the wave modes that could propagate in such a system, to great success (Bergman, 1993; Braginsky, 1993). This model could be a fairly accurate representation for the case where immiscibility of two fluid compositions causes a single density jump (see section 1.1.2.2). However, it is likely that the structure of the SOC is more complicated than this simple picture.

Most plausible origin mechanisms of the SOC would lead to a continuously varying density perturbation from the adiabat rather than a single jump. Authors have modeled this density deficit as a linear function (Knezek and Buffett, 2015) which leads to a constant N through the layer; or a linearly varying N that corresponds to an exponentially varying density deficit with radius (Buffett, 2014). These approximations are likely more realistic. However, they probably still fail to capture the full complexity of the buoyancy structure, which most likely does not have a simple constant or linear relationship with radius (see e.g. Buffett and Seagle, 2010, fig. 6).

Simple models of the SOC have invariant buoyancy and thickness across latitude and longitude. However, this has long been recognized as a potentially invalid assumption, with Shearer and H. Roberts (1998) noting that the SOC thickness could even vary over short periods of time due to influence from dynamics in the bulk outer core. In addition, there may be reasons to think that the equatorial, polar, and tangent cylinder regions of the CMB are governed by different dynamics, and so may have different SOC properties. In addition, lateral flows due to mantle heat-flow heterogeneity have been proposed by many authors, (e.g. Amit, 2014; Huguet et al., 2018), and these flows may also cause large-scale lateral heterogeneity in the structure of the SOC, especially if they interact with topography on the CMB (e.g. Glane and Buffett, 2018).

1.2 Evidence for the SOC

Evidence for the SOC has been proposed from a variety of sources, including theoretical models, seismic observations, and geomagnetic evidence. It has long been recognized that mantle heat flow may be lower than required to maintain convection at the top of the outer core (Higgins and Kennedy, 1971; Gubbins et al., 2004). In addition, recent studies suggest that the electrical and thermal conductivity of the core may be much higher than previously assumed (de Koker et al., 2012; Gomi et al., 2013; Pozzo et al., 2012b, 2014). High conductivity would means that a larger amount of heat could be transported by conduction rather than convection, and therefore common estimates of mantle heat flow are much more likely to lead to the formation of a thermal SOC (Labrosse, 2015). While this line of reasoning provides strong evidence for the existence of the SOC, it is still possible that mantle heat flow is large enough that a SOC does not form. However, several other lines of evidence also support the existence of the SOC.

1.2.1 Seismic Evidence

Seismologists have long detected anomalous seismic wave speeds near the top of Earth's core and attributed the results to stable stratification (e.g. Garnero et al., 1993; Helffrich and Kaneshima, 2010; Kaneshima and Matsuzawa, 2015; Kaneshima and Helffrich, 2013; Lay and Young, 1990; Tanaka and Hamaguchi, 1993; Tanaka, 2004, 2007). Estimates for the thickness of the region in which these seismic anomalies are detected range from 12 km (Eaton and Kendall, 2006) to 450 km (Kaneshima, 2018), with many intermediate estimates. Although these values vary wildly, the observations are not necessarily inconsistent, as all results have margins of error and different seismic studies are sensitive to different regions of the core. In addition, the results of these studies could be influenced by seismic wave interactions with the largely unconstrained structure of the lowermost D" mantle layer (e.g. Souriau and Calvet, 2015).

One interesting point is that several authors detect a region between 50 km thick and 450 km thick with low seismic wave speeds (Garnero et al., 1993; Kaneshima, 2018; Lay and Young, 1990; Tanaka, 2004), while other authors detect a thin $\sim$ 12 km thick region near the CMB with a high seismic wavespeed (Eaton and Kendall, 2006). These results could hint at the existence of a SOC with a layered buoyancy structure, perhaps a thick thermally stratified

layer combined with a thin compositionally stratified layer embedded within.

Conversely, several studies argue that seismic evidence does not support the existence of the SOC (Alexandrakis and Eaton, 2010; Helffrich and Kaneshima, 2004). In addition, there are two large open questions about the seismic results. First, the anomalous wave speeds detected by most authors are thought to be too large to arise from a purely thermal origin (Kaneshima and Matsuzawa, 2015), but a compositional SOC several hundred kilometers thick may have strong buoyancy that is difficult to reconcile with geomagnetic observations (e.g. Huguet et al., 2018). However, the seismic wave speeds, geomagnetic observations, and materials science calculations are all uncertain, so none of the results are necessarily incompatible.

The second main open question about seismic evidence for the SOC arises from the direction of the seismic wave speed anomaly observed. Theoretical calculations indicate that compositional enrichment of light elements would produce high wave speed anomalies (Braginsky, 2000; Buffett and Seagle, 2010), but most seismic studies detect low wave speed anomalies near the top of the outer core. Helffrich (2012) proposes that non-ideal mixing could allow a compositional SOC to produce low seismic wave speeds, potentially resolving this second question. However, there are still many open questions about the strength and meaning of seismic evidence for a SOC.

1.2.2 Geomagnetic Evidence

Geomagnetic observations provide another source of evidence for the SOC. Yan and Stanley (2018) use dynamo models to suggest that the high dipole-octupole ratio observed for Earth's geodynamo can be explained by an SOC between 60 and 130 km thick. They argue that the observed ratio cannot be explained without an SOC and also rule out a SOC with a thickness > 350 km. Olson et al. (2018) uses numerical dynamo simulations with a SOC to argue that high magnetic field intensity regions and reversed magnetic flux spots observed in Earth's geomagnetic field suggest up to 400 km of permeable, laterally heterogeneous thermal stratification below the core-mantle boundary. These result are roughly consistent with several other numerical dynamo studies which constrain the thickness of a SOC to < 400 km thick (Christensen, 2018; Gubbins, 2007; Olson et al., 2017). The general interaction between dynamo operation and a SOC observed in these studies is also replicated across many other studies (see 6.2), lending strength to these conclusions.

Modern satellite observations have increased the spatial and temporal resolution of geomagnetic observations by an enormous amount, greatly increasing the amount of information about Earth's core able to be obtained from observations of SV. Baerenzung et al. (2016) used Bayesian techniques to invert recent SV observations for core flows and found that they are incompatible with a purely geostrophic state as might be expected if bulk core dynamics are visible at the CMB due to a lack of the SOC. Bloxham (1990) found that observed SV is incompatible with a strongly stratified SOC if Lorentz forces are ignored, but incorporation of some Lorentz forces resolves the incompatibility. Similarly, several authors find that SV is incompatible with purely toroidal (horizontal) flow, but introducing small amounts of radial fluid motion produce flows consistent with observed SV (Amit, 2014; Huguet et al., 2018; Lesur et al., 2015). Small amounts of radial motions are consistent with the existence of the SOC, and may even be expected due to heterogeneous mantle heat flow or wave motions.

1.2.3 Geomagnetic Waves

A final source of evidence comes from searching for signals of geomagnetic waves that can only exist in the SOC. The SOC supports wave modes not present in the bulk outer core due to buoyancy acting as a strong radial restoring force in the region. Detection of these waves thus provides strong evidence for the existence of the SOC and could even allow for precise determination of its strength of buoyancy or thickness as well as the strength and structure of the background magnetic field at the CMB. Braginsky (1993) derived equations for zonal MAC waves in the SOC and argued that their effects could be seen in variations of Earth's length of day (LOD) on decadal timescales. He finds that a SOC with a thickness of 80 km and $N \sim 2$ / day can roughly explain observations. Buffett (2014) extended the study of these zonal MAC waves by using their flows to simultaneously explain decadal variations in both Earth's dipole strength and LOD. Buffett finds that a layer 140 km thick with a buoyancy of $N \sim 1$ / day can explain these observations, very similar to Braginsky's previous results.

Waves in the SOC have also been proposed to explain rapidly-varying SV observed in the equatorial region of many core-surface magnetic field models (e.g. Finlay et al., 2016; Kloss and Finlay, 2019). These sub-decadal equatorial signals are of particular interest as evidence for a SOC. In a fully mixed outer core with no SOC, two types of waves are thought to occur on sub-

decadal timescales: torsional oscillations and magneto-Coriolis waves (Finlay et al., 2010). However, torsional oscillations are incompatible with the second time derivative of the geomagnetic field, termed secular acceleration (SA) (Chulliat and Maus, 2014), and sub-decadal magneto-Coriolis waves with the appropriate wave numbers would require a magnetic field strength of about 1 T within the core (Finlay et al., 2010). This field strength is several orders of magnitude larger than estimates derived from geodynamo simulations (Christensen, 2011) and analysis of 6 year torsional oscillations (Gillet et al., 2010), making both these wave modes unlikely candidates to explain the rapid equatorial variations in SA.

Chulliat et al. (2015) examines these equatorial SA variations and finds signals consistent with waves traveling both east and west with periods between six and ten years. He appeals to equatorial magnetic-Rossby waves propagating in a SOC to explain these observations, citing wave descriptions derived by Bergman (1993). He argues that a SOC with thickness 140 km and buoyancy N $\sim$ 1 /day could support these wave motions, but admits that these results are not well constrained.

1.3 Modeling Waves in the SOC

Sub-decadal oscillations observed in the geomagnetic field are of particular interest as they may be evidence for waves in the SOC. However, to fully understand these geomagnetic signals, we must first understand how sub-decadal waves propagate within the SOC. In particular, we must understand the wave dependence on the thickness, buoyancy structure, and background magnetic field of the SOC. Authors use two main methods to study wave behavior. First, analytical models can be used to derive wave equations and dispersion relations. Analytical solutions are powerful, as closed-form solutions can fully describe the wave behavior in a range of situations and illustrate the relationship between parameters and wave properties. However, this approach often requires extensive simplifying assumptions to obtain solutions. Therefore, numerical methods can also be used to study waves in the SOC with more realistic properties and magnetic field structures. These solutions can give more accurate results, but are often computationally expensive to run. In practice, both approaches have strengths and weaknesses and are often combined to study particular classes of waves.

1.3.1 Analytical Methods

Analytical models of waves in the SOC combine decades of research on hydrodynamic and magnetohydrodynamic waves. Because the SOC is a buoyantly stratified thin layer on a rotating sphere, it is subject to many of the same dynamic constraints as Earth's oceans and atmospheres. In fact, this is the reason that it is termed the "Stratified Ocean of the Core." It has long been known that global waves such as Kelvin, Rossby, and inertio-gravity waves propagate in Earth's oceans and atmospheres, and detailed analytical solutions and wave dispersion relations for these waves have been derived (see e.g. Gill, 1982; Longuet-Higgins, 1965; Pedlosky, 1987; Platzman et al., 1968). These analytical solutions typically use shallow-water approximations of hydrodynamic equations to account for the layer thickness and Boussinesq approximations to incorporate buoyancy into the equations. Local wave solutions can be computed by ignoring the spherical geometry and using a Cartesian plane. For waves where rotation plays a role, the Coriolis force can be incorporated using a beta-plane approximation. Finally, for truly global waves the full spherical geometry can be incorporated by using spherical harmonics to decompose the wave mode solutions.

The addition of a magnetic field and a fluid conductivity adds additional complexity, but many authors have successfully utilized analytical methods to derive solutions for magnetohydrodynamic waves. Alfvén (1943) first united hydrodynamics and electromagnetism, describing waves that propagate using magnetic tension as their restoring force. Lehnert (1954) then found waves that propagate under the influence of both magnetic and Coriolis forces (MC waves). A decade later, (Braginsky, 1964) described waves that propagate under magnetic, Coriolis, and buoyancy forces, now known as MAC waves (with A for Archimedean buoyancy). Hide (1966) then used the beta-plane approximation to find magnetic wave solutions propagating in a spherical shell which he termed MC-Rossby waves. Further advances in magnetohydrodynamics were achieved by Roberts and Stewartson (1974) examining excitation mechanisms and Soward (1979) and Fearn and Proctor (1983) deriving waves in realistic geometries for Earth's bulk outer core. For a more detailed summary and brief sketch of the derivation of these waves, see section A.6.

Analytic solutions for magnetohydrodynamic waves in the SOC are derived by combining the approximations used for waves in Earth's oceans and atmospheres and those used to study magnetohydrodynamic waves. How-

ever, significant simplifying assumptions often need to be made to make analytical derivations of thin-layer MHD waves tractable. Braginsky derives solutions for waves the SOC, but states "Very strong simplifications are made in order to obtain simple analytical solutions that shed some light on the overall picture". In particular, his SOC boundary conditions assume no magnetic or fluid interactions with the bulk outer core, and he prescribes the structure and many properties of the wave modes a-priori (Braginsky, 1993, 1998). Similarly, Bergman (1993) employs a thin-layer beta-plane approximation to derive solutions for equatorial magnetic-Rossby waves in the SOC, but treats the magnetic interactions in such a way that the resulting solutions for MHD waves are purely dispersive.

Analytical solutions of magnetohydrodynamic waves in a thin stratified layer have also been studied with application towards the solar tachycline. (Gilman, 2000) derived magnetohydrodynamic shallow-water equations with a free-surface approximation appropriate for use in the solar tachycline. These solutions were then used by many other authors to study various wave modes (Schecter et al., 2001; Zaqarashvili et al., 2007, 2009). However, the solar tachycline is dominated by a toroidal background magnetic field, unlike the SOC, for which the radial magnetic field likely acts as the largest magnetic restoring force. As the toroidal magnetic field is purely horizontal, it is assumed not to interact with adjacent layers and therefore avoids complications of boundary conditions with conductive regions. In addition, radial and toroidal magnetic fields act as a restoring force on different components of wave motion, potentially leading to very different wave structures and properties. Because of these fundamental differences, the applicability of these MHD equations for the solar tachycline to the SOC in the Earth is unclear.

More recently, Buffett and Matsui (2019) use an extended beta-plane method which includes higher-order terms to derive an analytical solution and dispersion relation for MAC waves in a SOC. Their method also includes a magnetic field that varies with latitude, again incorporated into the model with a beta-plane like method. They find that these higher-order terms influence the waves to become trapped near the equator, producing the eMAC waves first described in this thesis using numerical methods.

1.3.2 Numerical Methods

While analytical solutions are useful, they often require extensive simplifying assumptions or a priori knowledge of the wave structures or properties to obtain solutions. Numerical methods can be used to overcome these limitations, as they often require fewer simplifying assumptions and can be used to search for wave modes without a priori knowledge of the wave structures or properties.

Numerical methods are often employed in conjunction with analytical methods when studying waves in the SOC. Often, analytical methods are used to derive a system of differential equations that govern a particular magnetic wave mode of interest. These systems of equations are sometimes too complex to solve in closed-form, so a numerical solver can be applied to obtain solutions. This approach is used by Bergman (1993), Hori et al. (2015), and Márquez-Artavia et al. (2017) to obtain solutions for magnetic-Rossby waves and several other magnetic wave modes in stratified layers.

Another approach is to simulate the full magnetohydrodynamic system with a numerical MHD code. This approach is commonly employed to simulate the dynamics of the bulk core and geodynamo (e.g. Hollerbach, 1996; Roberts, 2007) to great success. These codes often employ vector spherical harmonics to model variations in latitude and longitude and either finite-difference, spectral, or finite-element techniques to capture variations in radius. These models are easily adapted to study the dynamics of the SOC, with only small changes required. Because dynamos are turbulent systems that evolve in time with no natural periodicity, dynamo-simulation codes typically employ time-stepping techniques to track the state of a system as it evolves forward in time. While time-stepping codes are sometimes employed to study wave motions among the turbulent background dynamo flow (e.g. Schaeffer et al., 2017), it is computationally inefficient for detailed study of the wave modes. Instead, the time-stepping portion of these codes is typically translated into an eigenvalue problem. Eigenvalue methods do not directly simulate the system's evolution in time, and instead only examine flow components that are periodic in time. This is a particularly powerful technique to study wave motions, and if dissipation is included in the model it can describe the wave damping timescale in addition to the wave frequency.

Adapting geodynamo codes to study waves in the SOC has the advantage of being able to relatively efficiently simulate the entire core, and so can study waves that propagate both in the bulk core and the SOC (e.g. Vidal

and Schaeffer, 2015). However, adapted geodynamo codes have also been used to study waves that propagate entirely in the SOC (Buffett, 2014).

A different approach employed in this thesis uses a finite-volume method in latitude and radius with Fourier decomposition in longitude to simulate wave modes in the SOC (Knezek and Buffett, 2018). This approach has several advantages over spherical-harmonic methods, including greater flexibility in the background magnetic field and layer structures while maintaining efficient numerical computation times due to the sparse structure of the simulation matrices. This method is described in detail in chapter 2.

1.4 Wave Modes in the SOC

Studies employing analytical and numerical methods have described a number of wave modes that could propagate in the SOC across a range of timescales. There are also a number of wave modes that propagate in the bulk core that have been shown to at least partially penetrate and propagate within the SOC as well (see section 1.1.1.1). However, in this thesis we are interested in waves that propagate mainly in the SOC and either cannot exist without stable stratification or are heavily modified by the existence of the SOC. We focus on these wave modes, as if detected and described, they provide strong evidence for the existence of the SOC and potentially constrain its properties.

1.4.1 MAC Waves

The first wave mode discovered to propagate in the SOC is termed the MAC wave, named for the three forces that govern its propagation: Magnetic forces, Archimedean buoyancy, and Coriolis forces. Braginsky (1993) derived solutions for global zonal MAC waves in a SOC in Earth's core and showed that a weakly buoyant layer with a thickness near 80 km would produce zonal MAC waves with a fundamental period of approximately 65 years and a first harmonic period of ~ 30 years. These waves arise due to an interaction between pressure gradients, the Coriolis force, and Lorentz forces from a radial background magnetic field. Pressure gradients between the equator and pole drive meridional flows, which are then converted into zonal longitudinal flows by the Coriolis force. Both of these flows are then opposed by the radial magnetic field, which provides the restoring force to these waves.

Buffett (2014) extended the study of these waves to show that different background magnetic field structures can change their flow structures and in turn affect the geomagnetic dipole strength over time by concentrating magnetic field near the poles through advection.

Zonal MAC wave solutions exist with higher wavenumbers in radius and latitude. Zonal MAC waves with higher order in radius are rapidly damped due to the relative thinness of the SOC. However, it is possible that several MAC waves with higher latitudinal wave numbers could propagate within the SOC. There are also non-zonal MAC waves with nonzero longitudinal wavenumbers. Moving from a longitudinal wavenumber of zero to any nonzero value changes the behavior of MAC waves, as they now propagate around the sphere with a particular phase speed. In this thesis, we find solutions for non-zonal MAC waves that propagate both eastward and westward and have substantially different properties from zonal MAC waves (see chapter 3). The westward solutions in general propagate at mid- to high-latitudes, while eastward propagating waves span from the equatorial region to mid-latitudes. Both waves have periods ranging from years to centuries, depending on the particular wave mode and SOC or background magnetic field properties. Of note for this thesis, CMB magnetic field morphology can trap the eastward propagating non-zonal MAC waves near the equator, effectively turning them into narrow equatorial waves, which we refer to as eMAC waves.

1.4.2 Equatorial Waves

Equatorial magnetic waves in Earth's core are of particular interest for a variety of reasons. First, rapidly-varying geomagnetic signals have been observed in the equatorial region of the Earth (e.g. Finlay et al., 2016) with timescales too short to be produced by steady flow advecting magnetic fluxes. Thus, equatorial wave motions could be one possible origin (Chulliat et al., 2015).

Second, many propagating waves are observed in the equatorial region of Earth's atmosphere due to the Coriolis force acting as a waveguide (e.g. Longuet-Higgins, 1965; Platzman et al., 1968). Because similar forces govern the SOC, there may be a range of propagating equatorial MHD waves in Earth's core as well.

Finally, the equatorial region of the core near the CMB is governed by different forces and has a different magnetic field morphology than the rest of the core, so this is a region of particular interest. The bulk of the outer

core fluid is quasi-geostrophic such that the fluid moves in columns. Thus, the majority of the fluid near the CMB or beneath the SOC is connected to the bulk outer core through these axially-aligned fluid columns. However, this is not true in the equatorial region, as the fluid columns are parallel to the SOC or CMB surface. In addition, the equatorial region is where the dominantly negative radial magnetic flux in the northern hemisphere meets dominantly positive radial magnetic flux in the southern hemisphere. This indicates that the CMB radial magnetic field in equatorial region is likely a complex mixture of positive and negative patches of magnetic flux. This conclusion is supported by the latest dynamo models (Schaeffer et al., 2017), but the exact structure of the magnetic field in this region is still unknown. All of these facts indicate that the equatorial region near the CMB has largely unknown and possibly quite complex dynamics.

The first solutions derived for magnetic equatorial waves in the SOC extended the analytical methods used for equatorial hydrodynamic waves. They found that magnetic fields modify Rossby waves into magnetic-Rossby waves and can potentially break their equatorial trapping (Bergman, 1993). However, approximations Bergman uses in his derivation of analytical solutions lead to purely damped perturbations (see eq. 3.16 in that study), so these solutions may not propagate as waves in the SOC. Braginsky (1998) on the other hand derives mid-latitude magnetic-Rossby waves also using a beta-plane approximation and finds two solutions. The first is strongly damped, which he terms the magnetic diffusion mode, and the second are magnetic-Rossby waves that propagate to the west with a period of ~ 30 yrs for the fundamental and first harmonic longitudinal mode. These waves are analogous to mid-latitude hydrodynamic Rossby waves. Thus, although they do not propagate at the equator, they suggest that magnetic equatorial Rossby waves might exist in a similar analogy with equatorial hydrodynamic Rossby waves.

Magnetohydrodynamic waves have also been found to propagate in the solar tachycline. This layer is a thin, conductive layer governed by similar forces to the SOC, with the notable exception that the magnetic field is thought to be dominantly toroidal rather than radial. Zaqarashvili et al. (2007) show that Rossby waves split into two westward propagating modes in the solar tachycline, a “fast” mode which is largely similar to the non-magnetic form, and a ”slow” mode which is heavily influenced by the presence of the magnetic field, but has frequencies significantly smaller than those of either pure Rossby or Alfvén waves. Márquez-Artavia et al. (2017) then

derived dispersion relationships for several types of waves in a shallow magnetohydrodynamic spherical layer with toroidal background magnetic field. These included magneto-inertial gravity waves propagating to the east and west, magneto-Kelvin waves propagating to the east with a weak field, and a magneto-Kelvin wave propagating to the west with a strong background field. In addition, they study the behavior of magnetic-Rossby waves extensively, finding that the fast magnetic-Rossby waves propagate to the west similar to their non-magnetic counterparts, while slow magnetic-Rossby waves generally propagate to the east except for some m=1 modes at high field strengths. Finally, they find that as the field strength increases, the magnetic-Rossby waves move away from the equator and become trapped near the poles. Some of these conclusions likely also apply to waves in the SOC, for example, that strong magnetic fields can break equatorial trapping (see e.g. Bergman, 1993). However, as noted in section 1.3.1, the solar tachycline is governed by very different dynamics than the SOC, so it is unclear which of these wave modes have analogues in the SOC.

Another wave mode that may propagate strongly in the equatorial region of the SOC is described by Vidal and Schaeffer (2015). They find that quasi-geostrophic modes propagating in the bulk of Earth's core with periods of 1-2 months can penetrate into the SOC and concentrate its wave motions in the equatorial region, potentially producing observable signals in SV. These waves propagate in the bulk core as well as the SOC, and if observed, could potentially provide information on the structure or other properties of the SOC. However, their periods are too short to be relevant for the decadal oscillations observed in SA and examined in this thesis.

In this thesis, we find solutions for eastward propagating non-zonal MAC waves near the equator, which we term eMAC waves. The wave periods and propagation strength can vary enormously depending on the properties of the SOC and background magnetic field, but can potentially explain the decadal oscillations in SA observed in geomagnetic models. Because the period and structure of these waves vary so widely, they can potentially provide detailed information about the structure of both the SOC and Earth's unobserved CMB geomagnetic field. Examining these eMAC waves and their relationships to SOC layer properties and background magnetic fields is the key focus of chapter 3 of this thesis.

1.5 Detecting Waves in Geomagnetic Observations

Many authors have attempted to detect waves in observations of Earth's geomagnetic field for many decades (Whaler, 1980). We have records of Earth's magnetic field going back to Earth's early history from paleomagnetic records (Constable and Korte, 2015; Tarduno et al., 2015), and are able to reconstruct the structure of Earth's global field going back several centuries from direct measurements (Jackson et al., 2000). However, data before the advent of continuous high-resolution satellite missions were insufficiently detailed to observe the sub-decadal equatorial oscillations of interest in this thesis. In the past two decades, satellite missions have improved the fidelity of observations enormously such that small-scale, rapidly-varying signals in the core field are able to be measured that hint at previously unobservable phenomena (e.g. Finlay et al., 2016). With these data, direct observation of wave modes such as eMAC waves are possible for the first time.

1.5.1 Modern Geomagnetic Observation

It has long been recognized that satellites offer unique advantages to observe Earth's magnetic field. In fact, the very first satellite the United States launched, Explorer 1, included an instrument designed to measure regions of Earth's magnetosphere in 1958. Soon after, in 1964, Cosmos 49 was launched by the USSR and was the first satellite to return data relevant for studying geomagnetic secular variation (Jackson and Finlay, 2015). However, it was not until the launch of the Ørsted mission in 1999 that continuous high-resolution observations became available to model the evolution of Earth's core field (Olsen et al., 2000). Several other satellite missions have been launched since then, including the CHAMP mission, SAC-C/Ørsted-2 mission, and Swarm mission (Friis-Christensen et al., 2006; Maus, 2007; Sabaka et al., 2015). Together, these missions provide near-continuous high-resolution magnetic field observations from 1999 through the present day (Hulot et al., 2015). These satellites provide a wealth of data, which must then be filtered and synthesized into global field models (see e.g. Finlay et al., 2016). This thesis is interested only in the internal geomagnetic field that originates from the core. However, satellite missions record magnetic signals that originate from many other sources, including the lithosphere, ionosphere,

magnetosphere, and solar winds. Authors employ various methods to separate signals arising from each of these sources from the internal field (see e.g. Kono, 2015). Global magnetic field models generally report a separate model for each source, with the internal core field often reported as a set of spherical harmonic coefficients, potentially varying over time using B-Spline functions (see appendix A for details).

Several global magnetic field models have been produced utilizing the high-resolution satellite magnetic field data. The Ørsted Initial Field Model (OIFM) was one of the first global magnetic field models to be published and gave a field description up to degree 19 (Olsen et al., 2000). However, the model only reported the constant geomagnetic field and core secular variation at snapshots in time. Several other authors soon improved upon this work both by incorporating more observations as they were recorded and through improved data assimilation and modeling techniques. Resulting models included the MEME08 model which was one of the first to report the full time-evolution of Earth's field (Thomson et al., 2010); the POMME model series which introduced advanced methods of filtering magnetospheric and lithospheric contributions (Maus et al., 2005, 2010); and the CM series of field models which involve simultaneous fitting of many additional sources of noise such as the ionospheric currents (Sabaka et al., 2004, 2015).

Three other models deserve special attention. The GRIMM model series is of interest to this work, as it attempts to model core flows as part of the inversion process directly from magnetic observations (Lesur et al., 2008, 2010, 2015). However, the modeled flows are constrained to be slow-moving so are inappropriate for searching for waves. Second, the IGRF series of models are notable for their widespread use and application. However, they represent an ensemble estimate of Earth's global field which averages out many of the small-scale details necessary to observe eMAC waves (Macmillan and Finlay, 2011).

Finally, the CHAOS series of models provide some of the highest-resolution models spanning the longest time periods, and are the most appropriate for searching for signals of eMAC waves. The CHAOS-6 model represents the latest release of this model, and is continuously updated as new satellite observations are recorded. The CHAOS-6 field model incorporates both ground station data and satellite data to create a continuous model of Earth's main core field up to degree 14 from 1997 through 2019 as of this writing. It utilizes the B-splines to capture field variations in time, producing smoothly-varying records of both the first time derivative (secular variation or SV) and second

time derivative (secular acceleration or SA) of the field. Because it is easier to distinguish variations in the core field from the constant lithospheric field, SV is reliable to degree 16 and SA up to degree 9. Good fidelity in observations of SA is especially important for this work, as wave motions should produce relatively large amounts of SA when compared to steady flows (see chapter 4).

1.5.2 Wave Detection Methods

Each of the geomagnetic models described above separates the signal of Earth's core field from the noise of all other observational sources to produce a geomagnetic model of Earth's internal core field over time. However, we must then distinguish the signal of eMAC waves from the noise of all other core dynamics and processes that contribute to the observed internal geomagnetic field. Previous authors have used many different approaches to search for wave signals from noisy observations, and a few common approaches are described below.

First, there is a long history of attempting to observe wave motions simply by visually inspecting signals on a chart. For global waves, this typically takes the form of time-longitude plots, where the intensity of a particular observation is recorded as color or darkness, with time and longitude (or another distance metric) as the two axes. On these plots, wave motions show up as diagonal lines, and the wave propagation speed can be recovered from the line slope. This technique has been used extensively to examine oceanic and atmospheric waves (e.g. Platzman et al., 1968), and is also commonly used to study waves in geomagnetic fields (e.g. Cox, 2015). However, this method offers no objective metric to distinguish signals of waves from background noise, and detection must be judged "by eye". In addition, this method can typically only be used to examine aggregate group velocities, as it does not separate individual wave phase components.

Another method of detecting global waves and examining their properties utilizes the fast Fourier transformation (FFT). The 2D FFT can be used to transform recordings across space and time to obtain information about both the temporal and spatial patterns of individual wave phases. This technique is commonly used to study global waves by taking observations at multiple longitudinal locations over time. Then, a 2D FFT is used to transform the data to obtain the intensity of oscillation across a range of longitudinal wavenumbers and oscillation frequencies (e.g. Chulliat et al., 2015; Cox, 2015;

Gillet et al., 2010; Platzman et al., 1968). The 2D FFT has the advantage of being able to separate multiple wave modes for individual examination and recover the properties quite precisely, including information about the longitudinal wave numbers, frequencies, amplitudes, and phases.

However, FFT methods suffer from three large limitations. First, there is no standard threshold for detecting wave motions above ambient noise, so the existence of waves are typically judged "by eye", similar to time-longitude plots. Second, FFT-based methods work by computing correlations against sinusoidal signals in both time and space. Thus, they are less effective at resolving waves with more complicated spatial structures. There is a related method termed empirical orthogonal functions (EOF) that overcomes this sinusoidal limitation by allowing oscillations to have any spatial structure. It has been applied to study geomagnetic phenomena (Shore et al., 2016, 2018), but suffers from the same third flaw as FFT based methods which severely limits its usefulness in applications to Earth's core.

This third and fatal flaw is that all FFT-based and related methods have a fundamental trade-off between the timescale of data available and the resolution of the results. Typically, FFT methods are used to study oscillations with very short periods compared to the duration of the dataset, and cannot reliably be used to examine waves with periods on the order of the timescale of observations. This is a problem for the eMAC waves we hope to examine in this thesis. These waves have periods between a few years and a decade, yet there exist only around two decades of satellite observations with the required resolution to detect them (Finlay et al., 2016). The relatively short duration of geomagnetic observations available with which study wave motions (e.g. Jackson et al., 2000) is a barrier encountered by many authors (e.g. Buffett, 2014) and has led many authors to seek other methods to confirm the existence of waves in Earth's core.

One common method to improve the confidence in detection of waves is to find independent evidence of the waves in other datasets. Several authors have attempted to use variations in Earth's length of day in addition to geomagnetic observations to support the existence of waves such as torsional oscillations (Gillet et al., 2010; Pais and Hulot, 2000) and MAC waves (Braginsky, 1999; Buffett, 2014; Buffett et al., 2016) in Earth's core. Other authors have used multiple global geomagnetic field models obtained by different authors using different data, assimilation methods, and assumptions, and searched for waves that are common across several of these models (e.g. Chulliat et al., 2015).

The methods described above are difficult to apply to the study of eMAC waves in Earth's core. Because eMAC waves only extend over a small portion of Earth's core and are relatively short-period, they are unlikely to cause detectable signals in Earth's length of day or other examined datasets beyond geomagnetic observations. In addition, they are proposed to have periods of around 5 to 10 years, which is on the order of the duration of the geomagnetic observations available with required resolution, so FFT-based methods are of limited use to detect and study these waves.

Finally, there is another large complication for detecting eMAC waves in Earth's core. As the wave motions propagate, they produce geomagnetic signals by advecting the complex background magnetic field. Observations and numerical dynamo simulations indicate that the equatorial region of Earth's core likely has an extremely complex structure of positive and negative magnetic flux patches (Finlay et al., 2016; Schaeffer et al., 2017). Even if the equatorial waves in Earth's core have a relatively simple structure, they likely produce spatially-complex signals with a large amount of short-wavelength power by interacting with the background magnetic field. Indeed, this advection of background magnetic field even mixes the signals of equatorial waves which are symmetric and asymmetric across the equator. In fact, we show in chapter 4 that symmetric and asymmetric equatorial waves produce geomagnetic signals that are indistinguishable with simple examination techniques. This presents an enormous hurdle to the use of FFT-based methods to study these waves, as the inversions will not reliably recover wave properties. Instead, the frequencies and wavenumbers recovered by an FFT analysis will largely reflect the structure of the background magnetic field in the equatorial region of the CMB.

To overcome the limitations of the duration of our dataset and the complexity introduced by the advection of background magnetic field, we use a method similar to seismic waveform modeling to model and detect eMAC waves (e.g. Tromp, 2015; Woodhouse and Dziewonski, 1984). To do this, we simulate synthetic eMAC waves with various properties, then allow them to advect the observed magnetic field in the core and record the SV and SA signals produced. By computing the correlation of these synthetic SV and SA signals to observed SV and SA, we are able to determine which waves are likely to have produced the observations. With this method, we can then infer properties of the eMAC waves that exist in Earth's core, and thus recover information about the SOC.

To determine an objective threshold for detecting waves in SV using this

method, we derive a noise model for geomagnetic observations and compare the strength of correlation with only noise to those obtained from real observations. In addition, we provide an additional constraint by examining wave correlations in both SA and SV and verify that the observations are best explained by waves of similar phase in both datasets. For a full description of these methods, see chapter 4.

1.6 Thesis Layout

This thesis is laid out in six chapters. Chapter 2 summarizes the numerical modeling framework used to simulate waves in the SOC and study eMAC waves. Chapter 3 provides a full description of eMAC wave properties across a wide variety of SOC, core fluid, and background magnetic field parameters. Then, Chapter 4 describes the correlation methods and noise model used to detect eMAC waves in geomagnetic observations, and determines their sensitivity using synthetic waves. Finally, Chapters 5 and 6 apply these methods to observations of Earth's geomagnetic field and discuss the implications.

Chapter 2

Numerical Modeling

In order to understand the influence of background magnetic field configuration and layer buoyancy on waves in stratified layers, we develop a flexible numerical model that utilizes a hybrid finite-volume and Fourier method. A finite-volume formulation allows us to efficiently study wave dynamics with complex background magnetic fields while using only sparse matrices. Finite volume methods also avoid numerical singularities at the north and south poles that arise with finite difference methods and may also simplify coupling the spherical shell layer presented in this work to the non-spherical structure of geostrophic motion in the bulk core in future work. We choose not to adopt a finite-element approach because our domain is regular and so we can avoid the extra numerical overhead required to track connectivity of elements. A linearized description of the waves allows for Fourier decomposition of the problem into individual azimuthal wave modes, as modes do not couple to each other when the background magnetic field and layer buoyancy are axially-symmetric. We combine these ingredients to formulate an eigenvalue problem for the wave motion and obtain solutions for the wave structures, periods, and quality factors.

2.1 Model Formulation

We compute the velocity ($\vec{V}$), magnetic field ($\vec{B}$), pressure (P), and radial displacement (U_r) for waves within a stratified layer in Earth's core. The evolution of these variables is determined by a set of governing equations derived from the Navier-Stokes equations for velocity, the induction equation

for the magnetic field, and mass continuity equations for pressure and radial displacement. These equations are discretized using a hybrid finite volume and Fourier (FVF) method. Finally, the equations are linearized and wave solutions are obtained by using a sparse-matrix eigenvalue solver.

2.1.1 Governing Equations

We adopt the Boussinesq approximation to describe the motion of a viscous and incompressible fluid (see e.g. Jones, 2011). Gravity $\vec{g}$ and the initial density stratification $\rho_0(r)$ of the core fluid are both radial, so the buoyancy force has only a radial component $-(\rho g\hat{r})$, where ρ is the fluid density at any subsequent time (see eq. 2.6). The centrifugal force that arises in the rotating frame is incorporated in the pressure term ∇P, but the magnetic force is expressed in terms of the Maxwell magnetic stress tensor T without absorbing the magnetic pressure into P:

$$T_{ij} = \left(B_i B_j - \frac{1}{2} B^2 \delta_{ij} \right). \tag{2.1}$$

With these simplifications, the momentum equation becomes

$$\rho \frac{D\vec{V}}{Dt} = -\nabla P + \frac{1}{\mu_0} \nabla \cdot T + \rho \nu \nabla^2 \vec{V} - 2\rho\Omega \times \vec{V} - \rho g \hat{r}. \tag{2.2}$$

As we retain pressure as a variable, we must explicitly enforce the continuity equation

$$\nabla \cdot \vec{V} = 0. \tag{2.3}$$

We use the magnetohydrodynamic approximation (e.g. Roberts and King, 2013) to describe the evolution of the magnetic field

$$\frac{\partial \vec{B}}{\partial t} = \nabla \times (\vec{V} \times \vec{B}) + \eta \nabla^2 \vec{B} \tag{2.4}$$

where $\eta = 1/(\sigma\mu_0)$ is the magnetic diffusivity and σ is the electrical conductivity. The magnetic field is also subject to the condition

$$\nabla \cdot \vec{B} = 0\,. \tag{2.5}$$

Table 2.1: Physical constants used for model

Symbol	Constant	Value
Ω	Rotation Rate of Earth	7.3×10^{-5} /s
R_c	Radius of Outer Core	3480 km
ν	Momentum Diffusivity	10^{-2} m^2/s
η	Magnetic Diffusivity	0.8 m^2/s
ρ_0	Density	10^4 kg/m^3
μ_0	Vacuum Permeability	1.26×10^{-6} m kg/s^{2}A^2
N	Brunt-V$\grave{}$aisäl$\acute{}$a Frequency	$O(1\Omega)$

2.1.2 Thin-Layer Approximation

The governing equations are linearized by assuming that the waves are small perturbations of a background state

$$\vec{V} = \vec{V}_0 + \vec{v}, \qquad U_r = U_{r0} + u_r, \qquad \vec{B} = \vec{B}_0 + \vec{b}, \qquad P = P_0 + p, \qquad \rho = \rho_0 + \Delta\rho \tag{2.6}$$

In a thin layer, radial velocities are relatively small, so the radial force balance is nearly hydrostatic. We also adopt a hydrostatic background state

$$\vec{V}_0 = 0, \qquad U_{r0} = 0 \tag{2.7}$$

where P_0 and ρ_0 are the hydrostatic pressure and initial density profile.

For the radial buoyancy force, the local density of the fluid ρ is disturbed by radial motion through the (radial) background density gradient $\partial\rho_0/\partial r$. Assuming the displacement of the parcel (u_r) is small, the density perturbation can be written as $\Delta\rho = -u_r \partial\rho_0/\partial r$. The buoyancy force can therefore be written

$$-\rho g\,\hat{r} = -(\rho_0 g - \rho_0 \frac{g}{\rho_0}\frac{\partial \rho_0}{\partial r} u_r)\,\hat{r} = -(\rho_0 g + \rho_0 N^2 u_r)\,\hat{r} \tag{2.8}$$

where

$$N = \sqrt{-\frac{g}{\rho_0}\frac{\partial \rho_0}{\partial r}} \tag{2.9}$$

is the Brunt-Va$\grave{}$isa$\acute{}$illa frequency, which defines the strength of stratification (see section A.3). In this model, we allow both N and B_0 to vary with radius r and colatitude θ through the layer

$$N = N(r,\theta), \qquad \vec{B_0} = \vec{B_0}(r,\theta)$$

The radial component of the momentum equation (2.2) is nearly hydrostatic, so the radial gradient in the pressure perturbation balances the buoyancy force

$$0 = -(\nabla p)_r - N^2 u_r \tag{2.10}$$

where the subscript r is used to denote the radial component of a vector quantity.

Pressure perturbations induced by radial motion drive a horizontal flow. We make the usual assumption of retaining only the radial component of the rotation vector in the governing equations (i.e. $\Omega_r = \Omega \cos\theta$) because the horizontal component contributes to the Coriolis force only through the (small) radial velocity. Therefore, subtracting the hydrostatic state (2.7) and eliminating small terms, the horizontal momentum equations (2.2) become

$$\frac{\partial \vec{v}_{\theta,\phi}}{\partial t} = -\tfrac{1}{\rho_0}(\nabla p)_{\theta,\phi} + \frac{1}{\rho_0 \mu_0}(\nabla \cdot T_l)_{\theta,\phi} + \nu(\nabla^2 \vec{v})_{\theta,\phi} - 2(\Omega cos\theta\, \hat{r}) \times \vec{v} \tag{2.11}$$

where T_l is a linearized version of the Maxwell stress tensor T retaining only terms involving interactions between B_0 and b. Note that we retain the viscous force to promote numerical stability, although this term is typically quite small.

Small radial velocities relative to horizontal velocities ($v_r << v_{\theta,\phi}$) are expected when the characteristic radial length scale is small compared with the horizontal length scale. The corresponding radial magnetic perturbations are also very small ($b_r << b_{\theta,\phi}$) as they are related through the induction equation (2.4). Consequently, we solve for the horizontal perturbations in the magnetic field using the induction equation

$$\frac{\partial b_{\theta,\phi}}{\partial t} = (\nabla \times \vec{v} \times \vec{B_0})_{\theta,\phi} + (\eta \nabla^2 \vec{b})_{\theta,\phi} \tag{2.12}$$

and evaluate the radial component (if needed) using the solenoidal condition $\nabla \cdot \vec{b} = 0$.

2.1.3 Non-Dimensional Equations

The equations are cast into a non-dimensional form using the core radius R_c as the characteristic length scale and the reciprocal rotation rate of the Earth $1/\Omega$ for the characteristic time scale (see Table 1). This results in two dimensionless constants – the Ekman number E and the magnetic Prandtl

Table 2.2: Non-dimensional parameters with representative values

Parameter	Definition	Value in Core	Value in Model
E	$\frac{\nu}{R_c^2\Omega}$	10^{-15} – 10^{-14}	10^{-11}
P_m	$\frac{\nu}{\eta}$	10^{-6} – 10^{-5}	10^{-2}
N_Ω	$\frac{1}{\Omega}\sqrt{\frac{-g}{\rho_0}\frac{\partial\rho_0}{\partial r}}$	$0 - 10^1$	$0 - 10^1$
B_r	$\vec{B}_0 \cdot \hat{r}/\sqrt{\rho\eta\mu_0\Omega}$	0.1 – 1.0	0.0 – 1.0

number P_m – and two dimensionless parameters that can vary through the layer – buoyancy frequency N_Ω and a dimensionless radial magnetic field B_r (see table 2.2). Here, the characteristic magnetic field $B' = \sqrt{\rho\eta\mu_0\Omega}$ is 0.86 mT for $\eta = 0.8$ m^2/s, but can vary with different choices for core conductivities. Collecting terms, the governing equations (2.11) and (2.12) become

$$\frac{\partial v_{\theta,\phi}}{\partial t} = -\nabla p + \frac{E}{P_m}(\nabla \cdot T_l)_{\theta,\phi} + E\nabla^2\vec{v} - 2(\cos\theta\hat{r}) \times \vec{v} - N_\Omega^2 u_r\,\hat{r} \qquad (2.13)$$

and

$$\frac{\partial b_{\theta,\phi}}{\partial t} = (\nabla \times \vec{v} \times B_r)_{\theta,\phi} + \frac{E}{P_m}(\nabla^2\vec{b})_{\theta,\phi}. \qquad (2.14)$$

where variables now represent their non-dimensional forms. The equations are supplemented by the incompressibility condition

$$\nabla \cdot \vec{v} = 0 \qquad (2.15)$$

and a linearized relationship between u_r and v_r

$$\frac{\partial u_r}{\partial t} = v_r\,. \qquad (2.16)$$

2.1.4 Hybrid Finite Volume - Fourier Method

The governing equations are discretized using a combination of finite volume (e.g. Ferziger and Peric, 2002) and Fourier methods, jointly abbreviated as FVF. The domain is split into cells with a regular spacing in radius and colatitude. Each term in the governing equations is integrated over the cell volume then converted into a surface integral using Gauss' theorem. We then

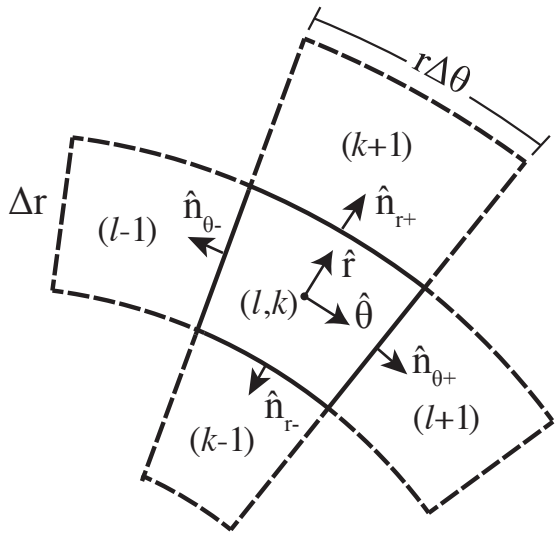

Figure 2.1: Finite-volume cell geometry. Dimensions exaggerated for illustration purposes.

divide this quantity by the cell volume to obtain operators that look similar to those used in finite difference methods. Each cell is indexed by the letter k in the radial direction and l in the latitudinal direction, while the letter m denotes the longitudinal wave number of the Fourier mode. Radial positions r, r_+, and r_-, respectively, denote the location of the center, top, and bottom faces of the cell in question, and Δr denotes the radial thickness of the cell. An analogous notation is used for the meridional position (i.e. $\theta, \theta_+, \theta_-$). An example of a cell is shown in Figure 2.1. We demonstrate the approach by deriving the (discrete) operator for the radial pressure gradient.

For the radial pressure gradient,

$$(\nabla p)_r = \left(\frac{1}{\Delta V} \int_S p \, d\vec{S} \right) \cdot \hat{r} \tag{2.17}$$

where $\Delta V = r^2 \sin\theta \Delta r \Delta\theta \Delta\phi$ represents the volume of the cell and the integral is taken over the total surface S (e.g. Aris, 1962). The surface integral is subdivided into individual faces, where A_{r_+} and A_{r_-} denote the area of the top and bottom radial faces and $\hat{n}_{r_+}$ and $\hat{n}_{r_-}$ represent the vectors normal to those faces (see figure 2.1). A similar notation is used for the other faces.

Summing the contributions from all six faces gives

$$\begin{aligned}(\nabla p)_r = \frac{1}{\Delta V}\big\{&p_{r_+}A_{r_+}(\hat{r}\cdot\hat{n}_{r_+}) + p_{r_-}A_{r_-}(\hat{r}\cdot\hat{n}_{r_-}) \\ &+p_{\theta_+}A_{\theta_+}(\hat{r}\cdot\hat{n}_{\theta_+}) + p_{\theta_-}A_{\theta_-}(\hat{r}\cdot\hat{n}_{\theta_-}) \\ &+p_{\phi_+}A_{\phi_+}(\hat{r}\cdot\hat{n}_{\phi_+}) + p_{\phi_-}A_{\phi_-}(\hat{r}\cdot\hat{n}_{\phi_-})\big\}.\end{aligned} \tag{2.18}$$

Interpolating the surface values of p using the values at the centers of adjacent cells, we obtain

$$\begin{aligned}(\nabla p)_r^{(k,l)} = &\frac{r_+^2}{2r^2\Delta r}p^{(k+1,l)} - \frac{r_-^2}{2r^2\Delta r}p^{(k-1,l)} - \frac{\sin\theta_+}{4r\sin\theta}p^{(k,l+1)} \\ &- \frac{\sin\theta_-}{4r\sin\theta}p^{(k,l-1)} - \frac{\sin\theta_+ + \sin\theta_-}{4r\sin\theta}p^{(k,l)}.\end{aligned} \tag{2.19}$$

This expression appears similar to a finite difference operator, but correctly accounts for the spherical geometry of the domain and does not introduce coordinate singularities at the north and south poles. The $\hat{\theta}$ component of the pressure gradient is derived in a similar manner and results in a similar expression. The $\hat{\phi}$ component is somewhat simpler because we use the Fourier series to interpolate values onto the ϕ-faces of the cell. Adopting the small angle approximation $\sin\Delta\phi/2 \approx \Delta\phi/2$, the expression for $(\nabla p)_\phi$ simplifies into

$$(\nabla p)_\phi^{(k,l)} = \left(\frac{im}{rsin\theta}\right)p^{(k,l)} \tag{2.20}$$

where m represents the Fourier mode.

Expressions for all other terms in the governing equations are derived in a similar manner. We introduce short-hand notation for the derived numerical operators to simplify notation. For example, the divergence operator can be represented as

$$\nabla\cdot\vec{v} = \nabla_r v_r + \nabla_\theta v_\theta + \nabla_\phi v_\phi \tag{2.21}$$

where $\nabla_r, \nabla_\theta, \nabla_\phi$ represent numerical operators that include terms due to the spherical geometry of the problem (e.g. $\nabla_r \neq \partial_r$). Details of these derivations and the resulting operators can be found in the supplement.

2.1.5 Eigenvalue Formulation

Perturbations in the fields are constrained to vary periodically in time and longitude with complex time frequency ω and longitudinal wavenumber m:

$$\begin{bmatrix} \vec{v}(r,\theta,\phi,t) \\ b_{\theta,\phi}(r,\theta,\phi,t) \\ p(r,\theta,\phi,t) \\ u_r(r,\theta,\phi,t) \end{bmatrix} = \begin{bmatrix} \vec{v}(r,\theta) \\ b_{\theta,\phi}(r,\theta) \\ p(r,\theta) \\ u_r(r,\theta) \end{bmatrix} e^{i(\omega t + m\phi)}. \tag{2.22}$$

Applying this constraint and introducing the notation from section 2.1.4, the final governing equations for the model are

$$0 = -(\nabla p)_r - N_\Omega^2 u_r \tag{2.23a}$$

$$i\omega v_\theta = -(\nabla p)_\theta + \frac{E}{P_m}(\nabla \cdot T_l)_\theta + E(\nabla^2 \vec{v})_\theta + 2\cos\theta\, v_\phi \tag{2.23b}$$

$$i\omega v_\phi = -(\nabla p)_\phi + \frac{E}{P_m}(\nabla \cdot T_l)_\phi + E(\nabla^2 \vec{v})_\phi - 2\cos\theta\, v_\theta \tag{2.23c}$$

$$i\omega b_\theta = (\nabla \times \vec{v} \times B_r \hat{r})_\theta + \frac{E}{P_m}(\nabla^2 \vec{b})_\theta \tag{2.23d}$$

$$i\omega b_\phi = (\nabla \times \vec{v} \times B_r \hat{r})_\phi + \frac{E}{P_m}(\nabla^2 \vec{b})_\phi \tag{2.23e}$$

$$0 = \nabla_r v_r + \nabla_\theta v_\theta + \nabla_\phi v_\phi \tag{2.23f}$$

$$i\omega u_r = v_r. \tag{2.23g}$$

Note that we do not explicitly solve for b_r because its effect on the dynamics of the fluid is very small. However, the magnetic induction equations (2.23d)-(2.23e) in combination with mass continuity (2.23f) enforce the condition $\nabla \cdot \vec{b} = 0$ when the initial field is solenoidal, and b_r can always be recovered from the solution using the solenoidal condition.

2.1.6 Boundary Conditions

Boundary conditions are needed at the top and bottom radial surfaces of the layer to close the equations. However, we do not need conditions at $\theta = 0$ and $\theta = \pi$ in the FVF method because the area of the face of the cell adjoining the north and south pole vanishes and thus does not contribute to the surface integral.

At the CMB we impose no radial motion and adopt (viscous) stress-free boundary conditions because viscous boundary layers are not expected to play a large role in the dynamics of the waves when the Ekman number (E) is small. Consequently, the boundary conditions on velocity at the CMB are

$$v_r = 0, \qquad \frac{\partial v_\theta}{\partial r} = 0, \qquad \frac{\partial v_\phi}{\partial r} = 0. \tag{2.24}$$

The conditions at the bottom boundary of the layer are more complex. Viscous stress-free conditions are reasonable when E is small, but it is not obvious that the radial motion should vanish. Numerical calculations show that the radial motion is indeed small for zonal MAC waves when the underlying region is geostrophic (Buffett, 2014). Braginsky also argued for no radial motion at the bottom boundary for non-zonal waves by introducing a density jump at the base of the layer (Braginsky, 1998). When the density jump is large enough the associated buoyancy suppresses radial motion at the boundary. Gravity waves can propagate along the interface, but the periods are short compared with the period of non-zonal MAC waves, so the motion is effectively decoupled. As long as the timescale of dynamics in the interior is different enough from the period of waves in the layer, then it seems reasonable to decouple the motion in these two regions. We do this by adopting (2.24) as boundary conditions on the base of the layer.

These conditions are incorporated directly into FVF discretization for cells adjoining the top and bottom boundaries, with details found in the supplement.

The appropriate conditions on pressure follow directly from (2.23a). When either the radial motion or the stratification (N) vanishes, we require

$$\frac{\partial p}{\partial r} = 0 \tag{2.25}$$

at the top and bottom boundary of the layer. These are again implemented directly into the FVF operators, with details in the supplement.

A natural choice of boundary conditions for the magnetic field at the CMB is to match the numerical solution to a potential field outside the core. These boundary conditions are not easily implemented in a finite volume formulation, but fortunately the pseudo-vacuum boundary conditions

$$b_{\phi,\theta}|_{CMB} = 0 \tag{2.26}$$

are a good approximation. Braginsky (1998) offers a detailed discussion of these boundary conditions for waves in a thin layer, but they can be justified with a simple physical argument. In the mantle, horizontal and radial components of a potential magnetic field perturbation are of the same order $b_{\theta,\phi}|_{\text{mantle}} \sim b_r|_{\text{mantle}}$. However, in a thin layer, horizontal perturbations to the magnetic field are much larger than the radial perturbations due to large horizontal fluid motions, $b_{\theta,\phi}|_{\text{layer}} >> b_r|_{\text{layer}}$. The magnetic field must be continuous, so at the CMB, $b_{\theta,\phi}$ must be similar in magnitude to b_r. Thus, $b_r|_{\text{CMB}} \sim b_{\theta,\phi}|_{\text{CMB}} << b_{\theta,\phi}|_{\text{layer}}$. Therefore, the horizontal perturbation of the magnetic field is much smaller at the CMB than within the layer so we can adopt the conditions shown in (2.26) without significantly affecting the wave dynamics.

At the bottom of the layer, the boundary conditions for the magnetic field must match the solution for a perturbation in the conductive fluid deeper inside the core. The waves we wish to study require buoyant stratification to propagate and thus decay in the region below where there is no buoyant restoring force. However, these waves do interact with the convective fluid in the bulk of the core through magnetic induction and pressure and potentially couple to modes of oscillations in the bulk of the core. To fully treat this problem would require a description of motion through the whole core, which is beyond the scope of this work. Instead, we choose to simulate only the stratified layer region and approximate the bulk of the core fluid as stationary, allowing the magnetic perturbation to propagate into the core with a skin depth dependent on the period of oscillation.

To implement this boundary condition in our model, we require the magnetic field to be continuous across the bottom boundary and integrate the induction equation across the interface, assuming that horizontal gradients in the magnetic field are negligible compared to radial gradients. The continuity condition becomes

$$B_r[v_{\theta,\phi}]^+_- + \frac{E}{P_m}[\partial_r b_{\theta,\phi}]^+_- = 0 \tag{2.27}$$

where $[\,]^+_-$ denotes the discontinuity in quantities above (+) and below (−) the bottom layer boundary. The velocity above the boundary does not vanish because we impose viscous stress free conditions. Below the boundary, $v^-_{\theta,\phi} = 0$ and the magnetic perturbation inside the core obeys a diffusion equation. The solution below the layer is

$$b^-_{\theta,\phi}(r - r_b) = b^+_{\theta,\phi}(r_b) e^{[(1+i)(r-r_b)/\delta]} e^{i(\omega t + m\phi)} \tag{2.28}$$

where r_b denotes the radial location of the bottom layer boundary and δ denotes the dimensionless magnetic skin depth

$$\delta = \sqrt{\frac{2E}{\omega P_m}}. \tag{2.29}$$

Note that all values are dimensionless, but a typical eMAC wave with a period of 8 years gives a magnetic skin depth of ~ 8 km.

Using (2.28) to evaluate the boundary condition in (2.27) gives

$$B_r v^+_{\theta,\phi} + \frac{E}{P_m}\partial_r b^+_{\theta,\phi} - \frac{(1+i)}{\delta} b^+_{\theta,\phi} = 0\,. \tag{2.30}$$

When the magnetic perturbation at $r = r_b$ is mainly due to the velocity discontinuity at the base of the layer, it is reasonable to approximate $\partial_r b^+_{\theta,\phi}$ using the diffusive solution complementary to (2.28). In this case, the boundary condition reduces to

$$b^+_{\theta,\phi} = \frac{\delta B_{0r} P_m}{2(1+i)E}\, v^+_{\theta,\phi} \tag{2.31}$$

with further details found in the supplement.

As the magnetic skin depth depends upon the period of the wave, these boundary conditions require knowledge of the period of the waves prior to solving the eigenvalue problem. Thus, we use an iterative approach: an estimate of the wave period is used for the initial calculation, then the solution is recomputed using the updated wave period. Typically, convergence requires only a few iterations.

2.1.7 Solving the Eigenvalue Problem

Incorporating boundary conditions into the discrete operators, the governing equations (2.23) are cast into the form of a generalized eigenvalue problem $\omega\mathbf{B}\mathbf{x} = \mathbf{A}\mathbf{x}$ where $\mathbf{A}$ and $\mathbf{B}$ are sparse matrices, ω is the eigenvalue, and $\mathbf{x}$ is the eigenvector containing the wave structure for each variable. We let

$$\mathbf{x}^T = [v_r, v_\theta, v_\phi, b_\theta, b_\phi, p, u_r]\,. \tag{2.32}$$

where each variable is indexed first by cell radial coordinate k, then cell latitudinal coordinate l. In other words, the first two elements of v_r are $v_r(k=0, l=0)$ and $v_r(k=1, l=0)$. Thus, $\mathbf{x}$ is a vector with $7 \times N_r \times N_\theta$

components, where N_r and N_θ are the number of radial and latitudinal cells in the model, respectively. With this formulation, $\mathbf{B}$ is a singular semi-positive definite mass matrix consisting only of ones and zeros on the diagonal representing time derivatives and $\mathbf{A}$ is a sparse block matrix containing the rest of equation dynamics and boundary conditions.

Typical model runs have $N_r \sim 40$ and $N_\theta \sim 200$, so that $\mathbf{x}$ has $\sim 56,000$ components. The matrices are extremely sparse; most sub-matrices only require storing a few terms near the diagonal. Although $\mathbf{A}$ is a $(7N_rN_\theta \times 7N_rN_\theta)$ matrix with $(7N_rN_\theta)^2 \sim O(10^9)$ possible components, it only requires the storage of $O(100 \times 7N_rN_\theta) \sim O(10^6)$ terms due to the sparsity of the discretized FVF operators.

Matrices are assembled in the Python language using the sparse matrix toolkits included in the SciPy and NumPy packages (Van Der Walt et al., 2011; Jones et al., 2001). After the matrices are assembled in Python, the eigenproblem is solved using the Scalable Library for Eigenvalue Problem Computations (SLEPc) (Hernandez et al., 2005). A desired wave frequency ω_0 is targeted using the shift-invert technique. The shifted eigenproblem is then solved using an iterative Krylov-Schur method, finding the requested number of solutions with frequencies closest to the desired wave frequency ω_0. The Krylov-Schur method normalizes the eigenvector each iteration, minimizing the pressure term and removing its extra degree of freedom (recall that the boundary conditions on p leave the average amplitude unconstrained). The eigenvector contains information about the structure of the wave, and the eigenvalue specifies the wave period and decay rate. Since the eigenvector is unconstrained up to a constant factor, the amplitude of the wave is determined by defining an excitation or by comparison to observed secular variation and inferred core fluid velocities.

2.2 Validation

Using the FVF method, we are able to examine the effect of different magnetic field configurations on magnetohydrodynamic waves in Earth's core. We first verify the technique by deriving global waves with a reduced subset of the equations. We choose global barotropic Rossby waves because they have an exact analytical solution to compare against and they demonstrate that our formulation allows flow directly across the north and south poles. Next, we examine the effect of non-dipolar fields on the structure of zonal

MAC waves and compare to the results of Braginsky (1993) and Buffett (2014). Finally, we study the effects of varying magnetic field strength and structures on the spatial extent and characteristics of non-zonal MAC waves, with relevance to recent observations by Chulliat (2015).

2.2.1 Global Barotropic Rossby Waves

Barotropic Rossby waves arise in a thin spherical shell of fluid due to interactions between inertia, pressure, and the Coriolis force:

$$\frac{\partial \vec{v}}{\partial t} = -\frac{1}{\rho}\nabla p - 2\Omega \times \vec{v}. \tag{2.33}$$

Solutions for Rossby waves are well studied (e.g. Platzman et al., 1968) and can be expressed in terms of a stream-function formulation for the velocity field

$$\vec{v} = \nabla \times \Psi \hat{r}. \tag{2.34}$$

The radial component of the curl of the governing equation (2.33) can be written in terms of the stream-function as

$$\frac{\partial \nabla^2 \Psi}{\partial t} = -\frac{2\Omega}{r^2}\partial_\phi \Psi \tag{2.35}$$

which for vertically invariant fluid motions admits solutions of

$$\Psi = C P_\ell^m(\cos\theta) e^{i(m\phi + \omega t)} \tag{2.36}$$

where $P_\ell^m(x)$ are the associated Legendre polynomials and C is an arbitrary constant. Note that degree ℓ is distinct from index l, which is used previously to denote latitudinal grid cell in the FVF method. Substituting (2.36) into (2.35) gives an expression for the wave frequency

$$\omega_{\text{Rossby}} = \frac{2m}{\ell(\ell+1)}\Omega. \tag{2.37}$$

Rossby waves emerge from our numerical model by removing the influence of magnetic field and fluid stratification. Figure 2.2 shows numerical solutions for two wave modes: one specified by $\ell = 1$, $m = 1$ and the other by $\ell = 3$, $m = 2$. Numerical and analytical solutions were found to agree precisely with a grid size of 20 radial and 120 latitudinal cells, with a maximum root

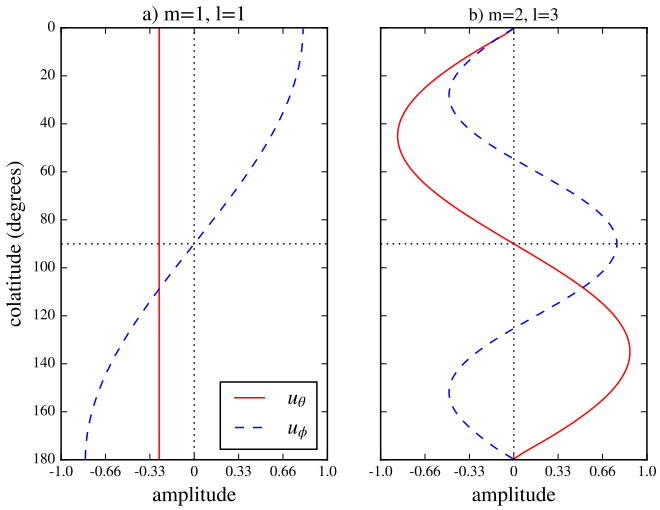

Figure 2.2: Longitudinal slices of velocity fields for Rossby wave modes with peak velocity normalized to 1. (a) $\ell = 1, m = 1$ and (b) $\ell = 3, m = 2$. Note that (a) includes non-zero flow at the poles – no modifications to the method are required to handle this case.

mean squared error between normalized velocity fields of 1.6×10^{-4} and wave periods in agreement to four significant digits. Note that the FVF model correctly computes the Rossby wave with $\ell = 1$, $m = 1$ which represents a solid-body rotation around an equatorial axis and includes flow across the north and south poles.

2.2.2 Zonal Magnetic Archimedes Coriolis (MAC) Waves

Analytical solutions for zonal MAC waves were given by Braginsky (1993). He adopted a constant buoyancy frequency through the layer and used the radial component of a dipole as the background magnetic field. He proposed the same boundary conditions as those assumed in our FVF model, although he relaxes the bottom boundary conditions to pseudo-vacuum conditions to derive the leading-order analytical solution. His lowest frequency wave (at latitudinal degree $\ell = 2$) is compared with the results of our FVF model in figure 2.3. Wave structures are nearly identical, with very small ($< 2\%$) differences in the amplitudes of the flow components. Braginsky's expression

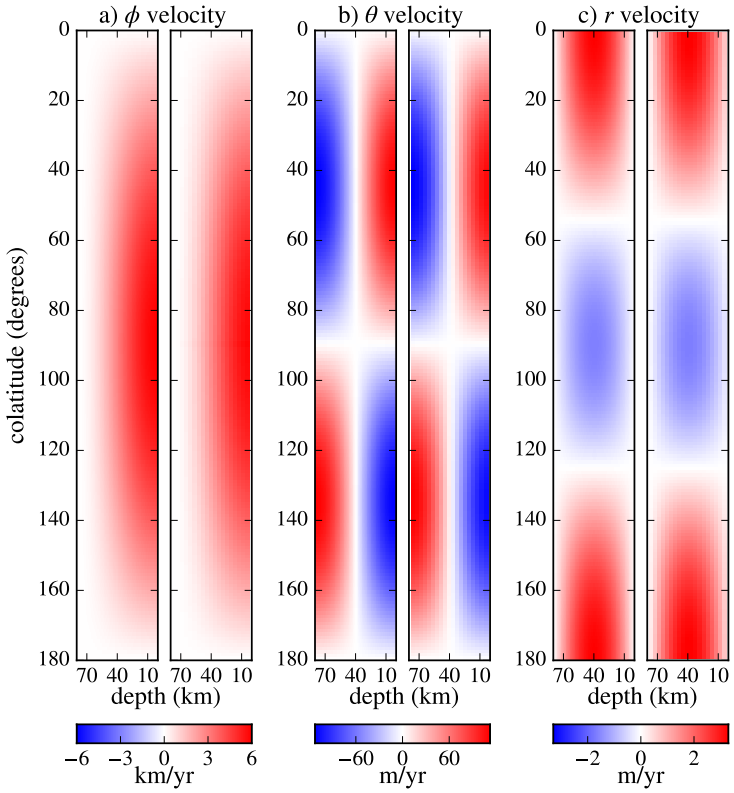

Figure 2.3: Comparison of Braginsky analytical (left) and FVF numerical (right) solutions for zonal MAC waves with Braginksy's preferred parameters H=80 km, N=2Ω, $\eta = 2\,m^2/s$, $B_d = 0.5\,mT$. Longitudinal (a), latitudinal (b), and radial (c) components of flow are shown for a meridional slice through the stable layer, with (a) offset 90° in phase. The relative amplitudes of the flow are fixed in the solution, but the overall magnitude is unconstrained. A representative estimate for v_ϕ is chosen for comparison to waves in Earth's core.

for the wave period gives 63.42 years with his preferred layer parameters (see figure 2.3 caption), while the FVF model gives 72.8 years. Most of this discrepancy arises because Braginsky discards diffusion when deriving his expression for the wave period. When we reduce the magnetic diffusivity in our model by a factor of four the wave period becomes 63.34 years, a difference of only $\sim 0.1\%$.

Our FVF model is also able to reproduce numerical MAC wave results from a previous spectral model (Buffett, 2014). The two lowest-order MAC waves for the case of constant buoyancy and constant radial magnetic field were compared for two different values of N_Ω. Wave structures and periods converged to a stable solution with a resolution of 20 radial by 120 latitudinal cells, with RMS error of the wave structures within 1% and wave periods and quality factors ($Q = \Re(\omega)/2\Im(\omega)$) within 2% for both modes.

2.3 Summary

In this chapter, we have developed a numerical model to calculate the structure and period of waves in a stratified layer at the top of the core. The method of solution is a hybrid of finite-volume and Fourier methods and is constructed as an eigenvalue problem. The formulation allows general descriptions of the stratification structure of the layer and for radial and latitudinal variation in magnetic field strength. In the following sections, we use this method to study the properties of these waves and to search for evidence of their existence in geomagnetic observations.

Chapter 3

eMAC Waves

The FVF model reveals a class of equatorially-trapped MAC waves that propagate to the east with sub-decadal periods. We refer to these waves as eMAC waves, and investigate them as a potential source of strong, short-period oscillations in secular acceleration observed in near Earth's equator (Chulliat et al., 2015). These waves bear a resemblance to equatorially-trapped Rossby waves and inertio-gravity waves that propagate in Earth's oceans and atmospheres, but have substantially different behavior due to the inclusion of magnetic forces. Bergman (1993) derived solutions for equatorially-trapped waves in a stratified layer in Earth's core, but our solutions differ substantially from his. Notably, Bergman's solutions propagate only to the west, not east, and his dispersion relationship is different from the behavior we observe in our eMAC waves. In addition, we are unable to find waves that match the properties derived by Bergman after an extensive numerical search. There are several possible reasons for this discrepancy. Approximations used by Bergman to derive analytical solutions lead to purely damped perturbations (see eq. 3.16 in that study). Bergman also performs numerical computations (figures 2 and 3 in that study), but only finds propagating waves with periods of several moths or less using unrealistically strong stratification and weak magnetic fields. Bergman recognizes this when he states "...we do not know the relevance of the solutions to the H layer" (Bergman, 1993).

3.1 Wave Structure

The eMAC waves derived in this work arise due to interactions between buoyancy, Lorentz forces, and Coriolis forces. Convection in the outer core causes buoyant fluid parcels to rise and impact the bottom of the stably-stratified layer. These motions cause pressure gradients that drive meridional flow across the equator, as can be seen in in the r-displacement and θ-velocity subplots of figure 3.1. Off the equator, these pressure gradients drive cyclonic flows due to the Coriolis force, as seen in the ϕ-velocity subplot. Both of these flows are opposed by the radial magnetic field, which provides the restoring force through field gradients (b_θ and b_ϕ) and by its interaction with the bulk conductive core.

We describe the wave shown in figure 3.1 as having a radial wavenumber of k=1, as the wave components have one zero-crossing in the radial direction. Likewise, we describe this wave as having a latitudinal wavenumber of l=0, as this is the simplest latitudinal wave structure observed and v_θ and b_θ have no zero-crossings in the latitudinal direction. Note that for this wave, the radial displacement, b_ϕ, and v_ϕ have one latitudinal zero-crossing. In general, these variables have l+1 latitudinal zero-crossings, and so have the opposite equatorial symmetry to v_θ and b_θ. This wave has a longitudinal wavenumber of m=6, which is prescribed in the FVF calculation. Note that the amplitude of the wave is undetermined due to the construction of the FVF model as a eigenvalue problem. Unless otherwise specified, amplitudes of the waves shown in figures are set to a typical value so that the eMAC fluid motions acting on Earth's observed field produce SA of approximately the same magnitude as that observed in Earth's equatorial region.

We describe the l=0 wave mode as a "symmetric" eMAC wave due to the equatorial symmetry of SV and SA signals that the wave produces when advecting a dipole background magnetic field. In general, all eMAC waves with even l produce equatorially symmetric signals when advecting a dipole magnetic field, while all odd l produce asymmetric signals. We show in figure 3.2 the CMB surface flows for the fundamental symmetric (l=0) and asymmetric (l=1) eMAC waves. These waves are computed with k=1 and m=6. Note that the waves include both surface advection shown by arrows and horizontal divergence, shown by the red and blue colors on the plot. Both of these terms act to advect background magnetic field and produce observable SV and SV (see section 4.1.1). We show the full solutions for all variables in the FVF model for these two modes in figures 3.3 and 3.4.

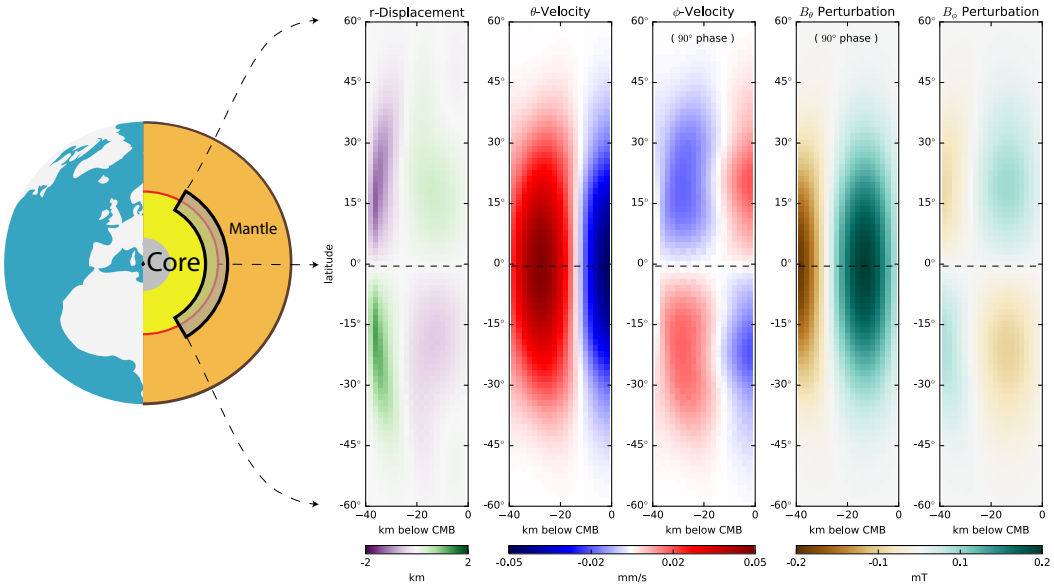

Figure 3.1: Representation of typical eMAC wave, including stratified layer location with Earth. This wave is computed with a constant radial magnetic field and constant layer stratification. However, the general structure of the eMAC waves remains the same if layer stratification is allowed to vary with radius or the radial magnetic field strength is allowed to vary with latitude.

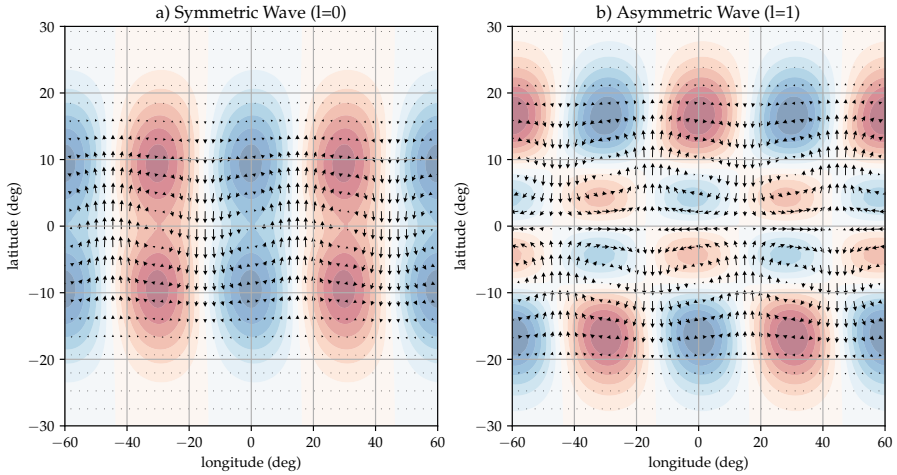

Figure 3.2: Horizontal wave structures for two equatorial wave modes using Hermite fits derived from our FVF numerical model solutions. Structures shown have $\delta_\theta = 30°$. Colors represent divergence (red) and convergence (blue), and arrows show horizontal flow structure. Waves are denoted "symmetric" (a) and "asymmetric" (b) in reference to the SV and SA they produce when advecting a pure dipole magnetic field.

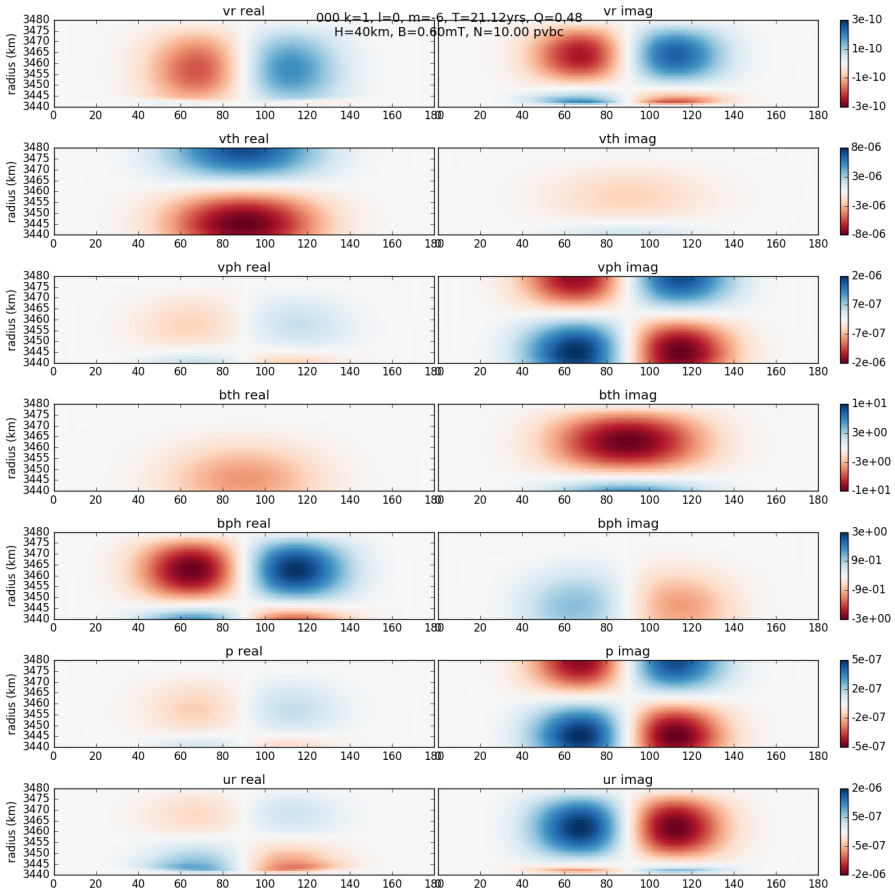

Figure 3.3: Symmetric eMAC Wave showing all variables in model. Wave has radial wavenumber k=1, latitudinal wavenumber l=1, and longitudinal wavenumber m=6, computed with H=40 km, a constant N=10Ω, with a dipole field with B_d = 0.6 mT, B_{noise} = 0.3 mT.

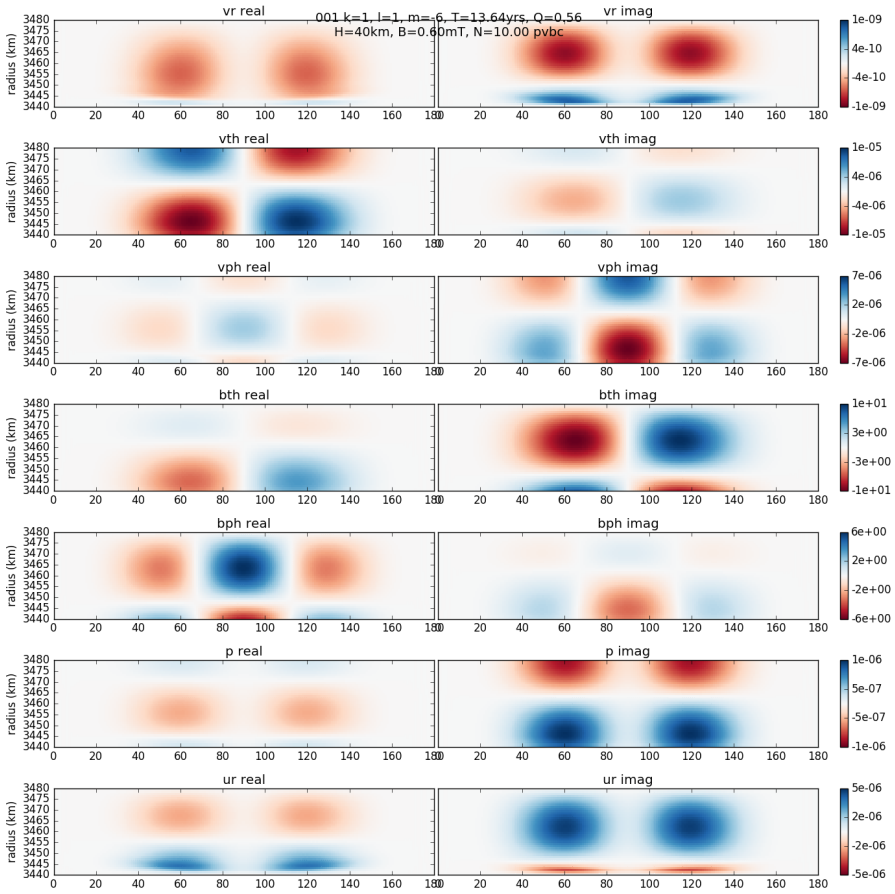

Figure 3.4: Asymmetric eMAC Wave showing all variables in model. Wave has radial wavenumber k=1, latitudinal wavenumber l=1, and longitudinal wavenumber m=6, computed with H=40 km, a constant N=10Ω, with a dipole field with $B_d = 0.6$ mT, $B_{noise} = 0.3$ mT.

3.2 Period and Quality Factor of Waves

We wish to examine the general behavior of eMAC wave periods and quality factors. We perform a numerical search of the relevant parameter space which allows us to examine the wave dependence on several relevant variables. Notably, an analytical solution for the dispersion relationship for these waves has recently been found which largely matches the results obtained in this section (Buffett and Matsui, 2019). However, the full dispersion relation was derived after this work was performed, so is not utilized. We use a simplified model with pseudo-vacuum boundary conditions (PVBC) on both the top and bottom boundary of the layer to improve our ability to resolve waves and reduce computation time for this parameter space search. This change in boundary conditions only has a small effect on the structure of the waves near the bottom layer boundary. Results for the the standard EM boundary conditions are shown in 3.3 and 3.4 for a symmetric and asymmetric wave, while introducing PVBC produces results shown in 3.5 and 3.6. Comparing these results, we see that the choice of EM boundary conditions has a minimal effect on the period of the waves, but does affect the quality factor. This will be examined in more detail in section 3.2.9.

We use a default set of parameters specified in table 3.1, with a constant radial magnetic field B and constant buoyancy frequency, N, through the layer.

3.2.1 Layer Thickness (H)

We vary the layer thickness H from 20 km to 180 km in figure 3.7. We find that eMAC wave periods increase with layer thickness, such that

$$\omega \propto H^{-2} .$$

Parameter	Description	Value
H	layer thickness	40 km
B	radial magnetic field strength	0.6 mT
N	buoyancy frequency	10 Ω
η	magnetic diffusivity	0.8 m^2/s
ν	momentum diffusivity	0.8 m^2/s
m	longitudinal wavenumber	6

Table 3.1: Default layer parameters for eMAC wave parameter space search

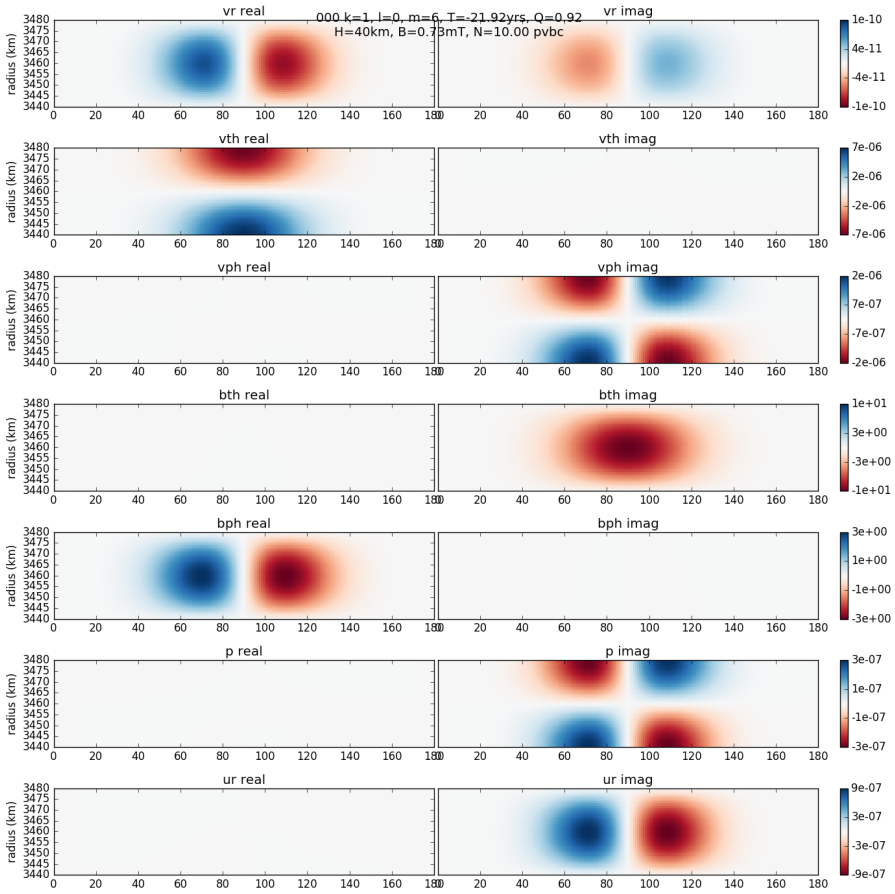

Figure 3.5: Symmetric eMAC wave computed using PVBC showing all variables in model. Wave has radial wavenumber k=1, latitudinal wavenumber l=1, and longitudinal wavenumber m=6, computed with H=40 km, a constant N=10Ω, with a dipole field with $B_d = 0.6$ mT, $B_{noise} = 0.3$ mT.

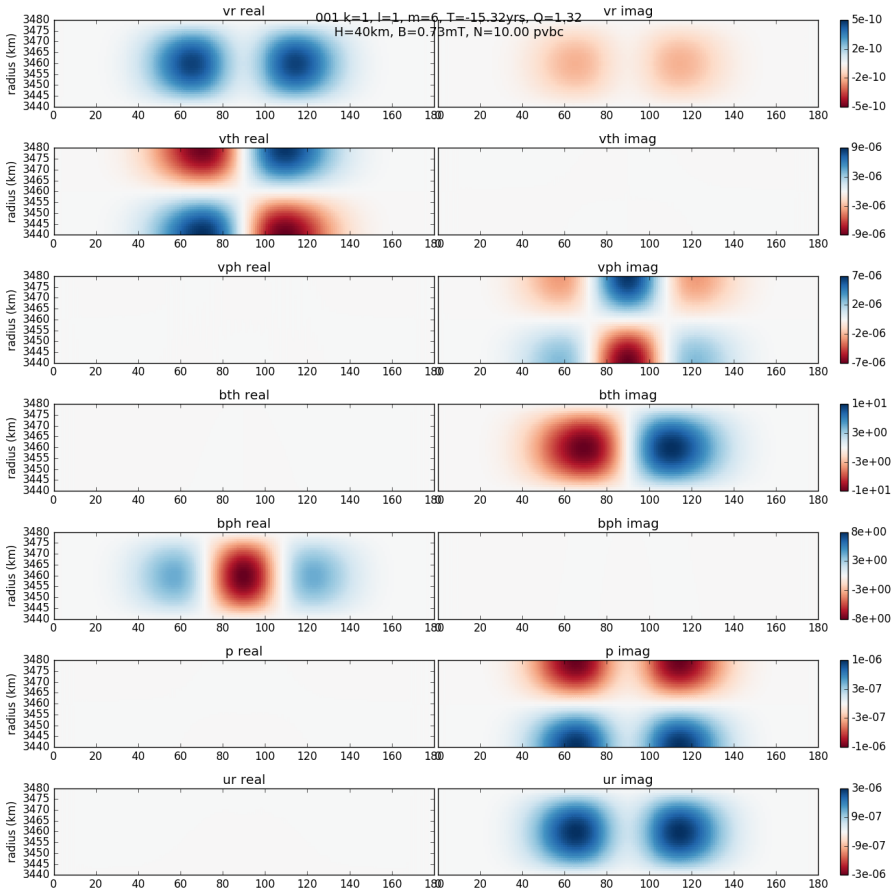

Figure 3.6: Asymmetric eMAC wave computed using PVBC showing all variables in model. Wave has radial wavenumber k=1, latitudinal wavenumber l=1, and longitudinal wavenumber m=6, computed with H=40 km, a constant N=10Ω, with a dipole field with B_d = 0.6 mT, B_{noise} = 0.3 mT.

Quality factors are not influenced by the layer thickness

$$Q \not\propto H\,.$$

3.2.2 Buoyancy Frequency (N)

We examine the effect of strength of layer stratification on eMAC waves by varying the radially-constant buoyancy frequency, N, from 0.5 Ω to 20 Ω in figure 3.8. We find that eMAC wave periods and quality factors exhibit a transition in behavior around a threshold value of N which depends on latitudinal wavenumber l. Above the threshold, eMAC waves take on the typical structure shown in figure 3.1 and their period and quality factor are insensitive to variations in N. Below the threshold N, eMAC wave periods begin to have a strong dependence on N, with their period increasing with smaller N and their quality factor decreasing. As the the layer stratification becomes weaker, the eMAC waves also have an increasing amount of their power at higher latitudes and eventually escape their equatorial trapping and have the majority of their power and high latitudes for very weak stratification. The transition point between large-N and small-N eMAC regimes seems to occur near N$\sim$1 for l=0 and increase to N$\sim$3 for l=3.

Compositionally stratified layers in Earth's core have proposed buoyancy frequencies N>10, putting these layers firmly in the large-N regime of eMAC wave behavior. On the other hand, thermally stratified layers have proposed buoyancy frequencies near N=1, making this these small-N waves and the transition between regimes an important subject to examine. However, because small-N waves are no longer equatorially-trapped, they cannot explain the strong observed SA near the equator and so we do not address them in detail in this study. Thus, for equatorially-trapped eMAC waves,

$$\omega \not\propto N\,,$$
$$Q \not\propto N\,.$$

3.2.3 Magnetic Field Strength (B)

We vary the constant radial magnetic field strength from 0.1 mT to 0.9 mT while keeping the other default values constant and plot the period and

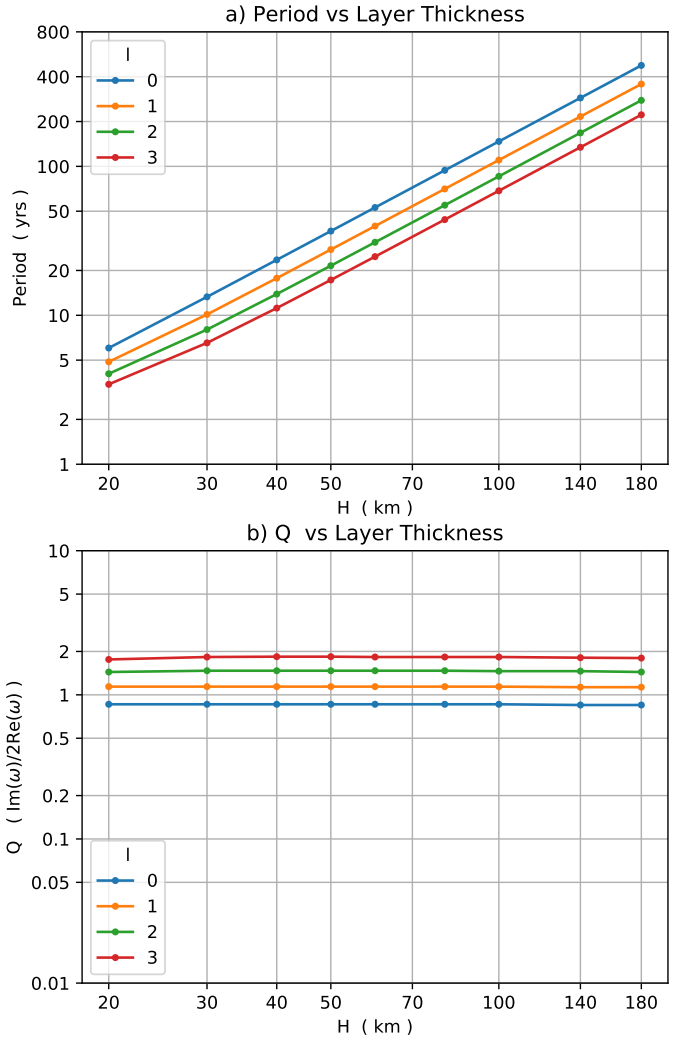

Figure 3.7: eMAC wave period (a) and quality factor (b) dependence on layer thickness (H).

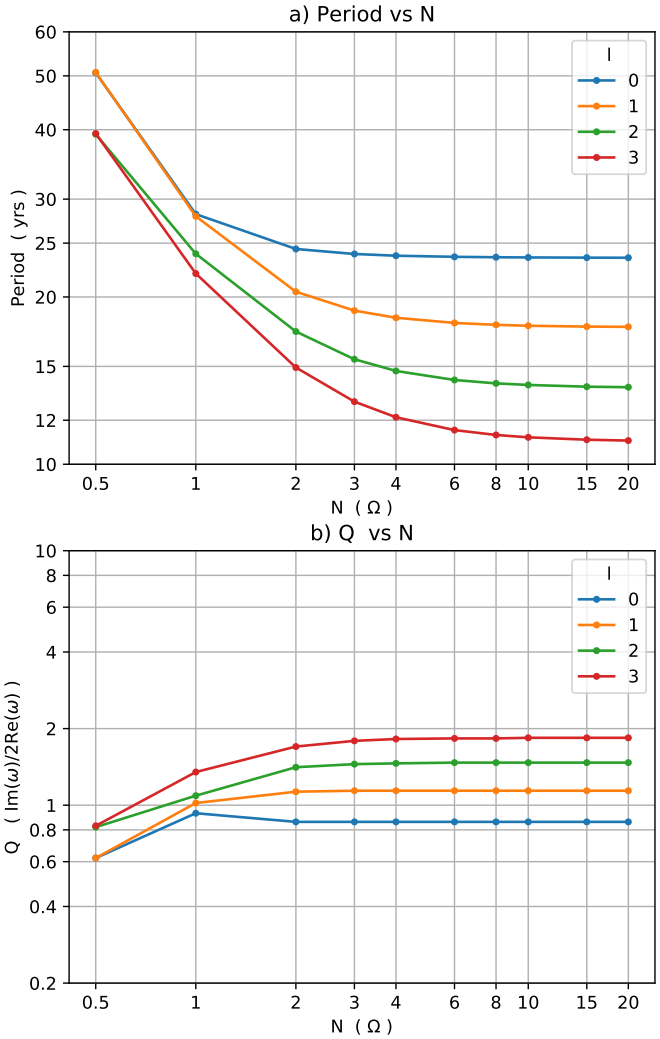

Figure 3.8: eMAC wave period (a) and quality factor (b) dependence on strength of layer buoyancy (N).

quality factor in figure 3.9. We find that the wave period varies with the inverse square of the magnetic field strength, which means that frequency

$$\omega \propto B^2 \,.$$

Quality factor also varies as

$$Q \propto B^2 \,.$$

3.2.4 Radial Wavenumber (k)

We are able to find eMAC waves with various radial wave-numbers, which we denote k. We find that increasing radial structure decreases the wave period and increases the quality factor of the waves, as shown in figure 3.10. Between k=1 and 3, the period decreases with k such that

$$\omega \propto k^2$$

for small k. For k = 1,2,3, the quality factor Q does not change with radial wavenumber

$$Q \not\propto k \,.$$

For higher values of k, the waves begin to have more of their power at higher latitudes and are no longer equatorially trapped. They also diverge from the ω and Q relationships established at lower values of k. Both of these indicate that the waves are then transitioning into a different, non-eMAC wave mode in the layer for higher k.

3.2.5 Latitudinal Wavenumber (l)

We examine waves with various latitudinal wave-numbers in the same default layer in figure 3.11. We find that the period decreases as latitudinal wavenumber increases. However, the precise behavior depends on the particular longitudinal wavenumber examined. For m=1,2 the decrease in period and increase in quality factor with l is faster than for m=3,6,9. In addition, the trends with m=3,6,9 seem to converge for higher values of l, while m=1,2 show distinct behavior even at higher values of l.

The quality factor of the eMAC waves depends on latitudinal wavenumber in a similar but opposite manner to the period. The quality factor generally increases with latitudinal wavenumber, but the increase is faster for smaller m and more gradual for larger m.

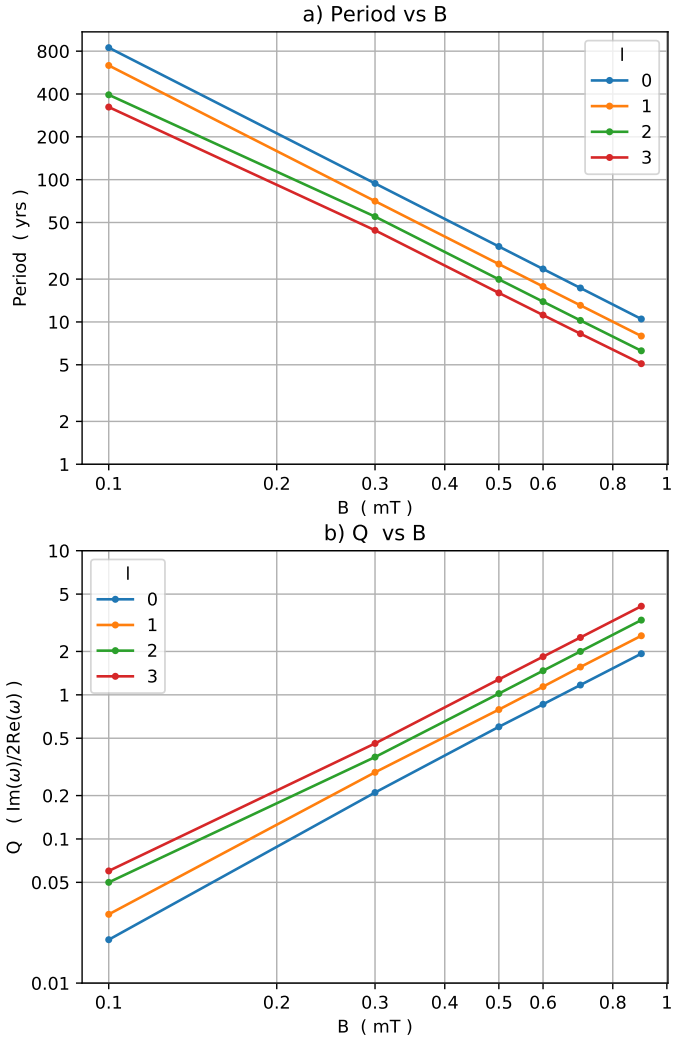

Figure 3.9: eMAC wave period (a) and quality factor (b) dependence on radial magnetic field strength (B).

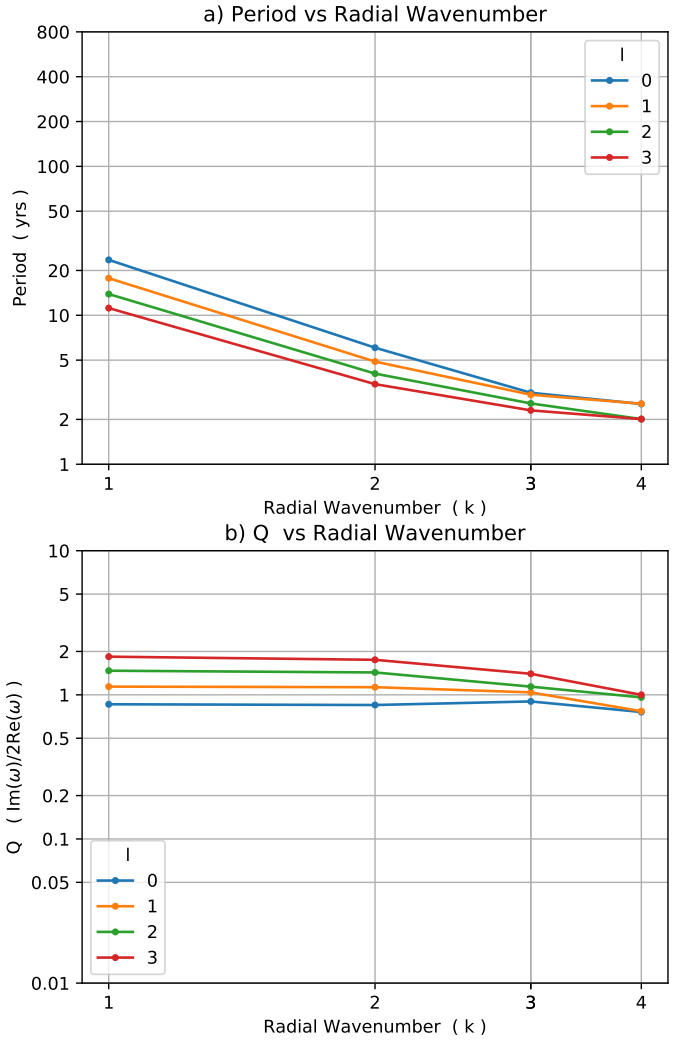

Figure 3.10: eMAC wave period (a) and quality factor (b) dependence on radial wavenumber (k).

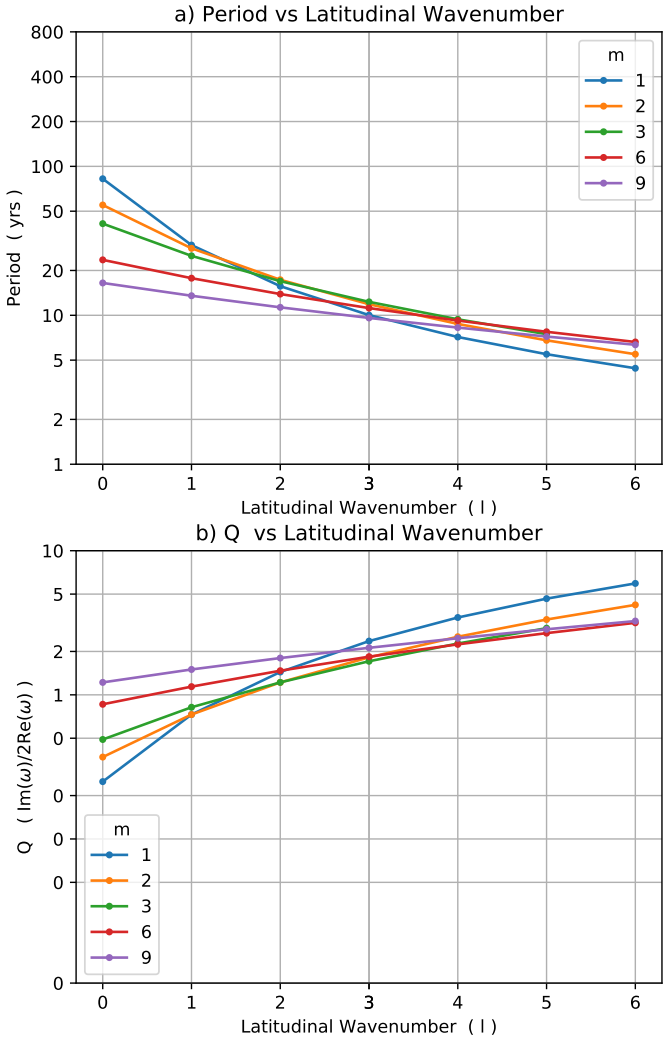

Figure 3.11: eMAC wave period (a) and quality factor (b) dependence on latitudinal wavenumber (l).

3.2.6 Longitudinal Wavenumber (m)

We examine waves with various longitudinal wave-numbers in the same default layer in figure 3.12. We find that the period generally decreases for waves with low latitudinal wave-numbers ($l = 0, 1$). However, the dependence is not a constant power, and higher latitudinal wavenumber waves have periods that increase from m=1 to m=3 before beginning to decrease with larger m. All values of l seem to be converging to an inverse relationship between period and wavenumber, resulting in

$$\omega \sim m$$

for large values of m.

The quality factor of the eMAC waves depends on longitudinal wavenumber in a similar but opposite manner. The quality factor generally increases with m for waves with low latitudinal wave-numbers ($l = 0, 1$). However, the dependence is not a constant power, and higher latitudinal wavenumber ($l = 2, 3$) show a decrease in quality factor from m=1 to m=3 before beginning to increase with larger m. All values of l seem to be converging to an direct relationship between quality factor and wavenumber, resulting in

$$Q \sim m$$

for large values of m.

3.2.7 Magnetic Diffusivity (η)

There is currently considerable debate about the correct value for magnetic diffusivity in the core (see section 1.1.2). We vary the magnetic diffusivity used in our model from $\eta = 0.2m^2/s$ to $1.6^2/s$ and show the results in figure 3.13. We find that the period does not change with magnetic diffusivity in this range

$$\omega \not\propto \eta$$

but that η does have an inverse relationship with the quality factor

$$Q \sim \eta^{-1}\,.$$

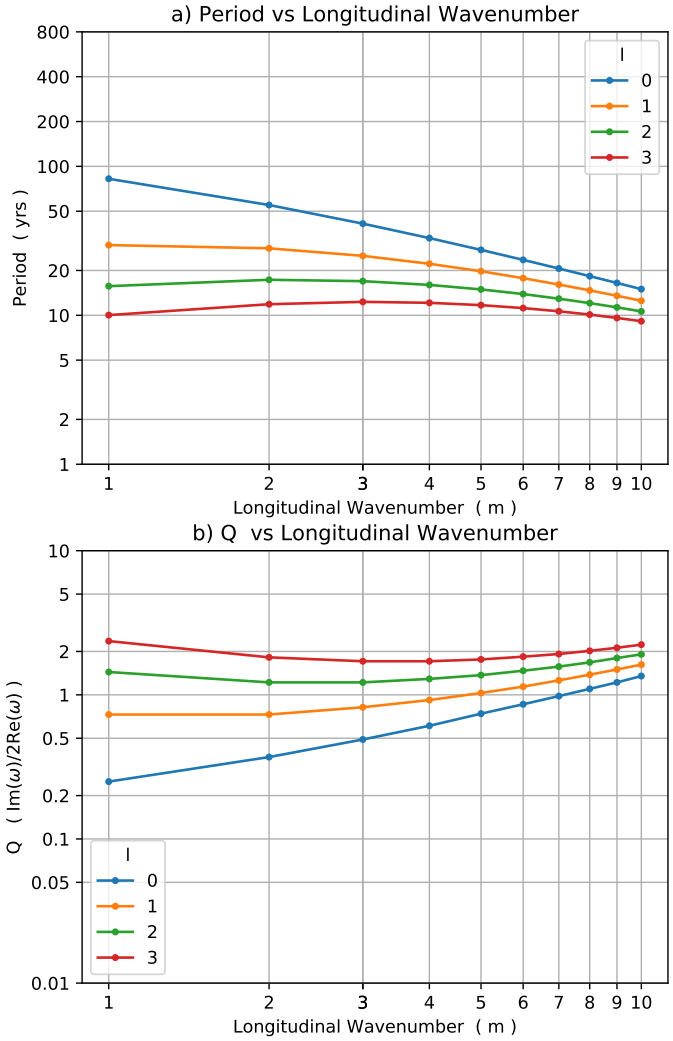

Figure 3.12: eMAC wave period (a) and quality factor (b) dependence on longitudinal wavenumber (m).

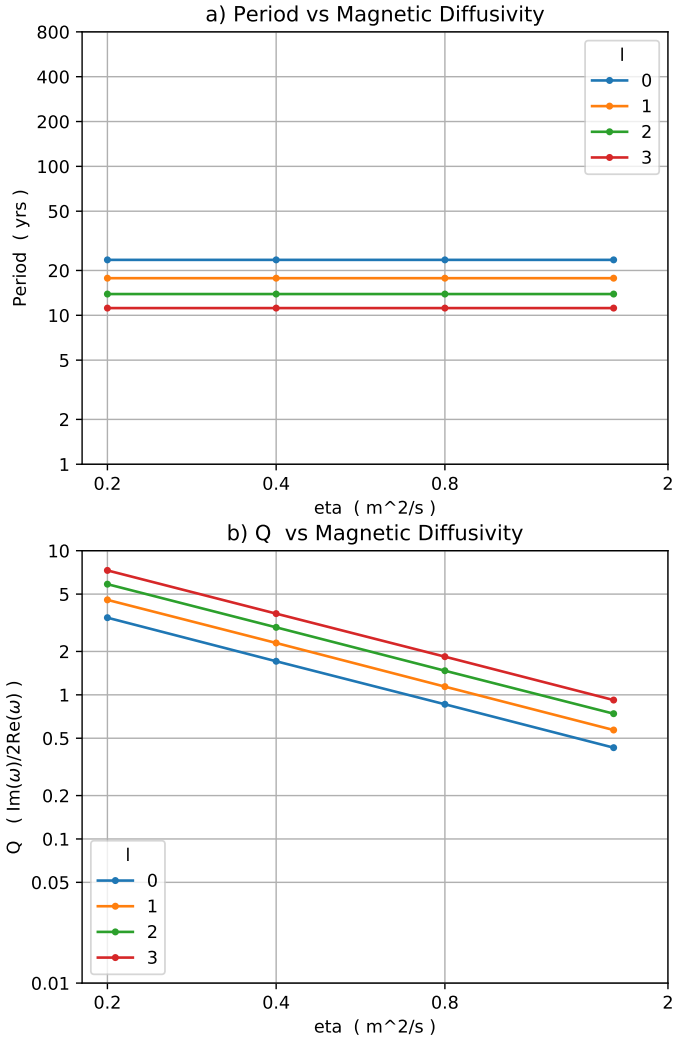

Figure 3.13: eMAC wave period (a) and quality factor (b) dependence on the magnetic diffusivity (η) of the core fluid.

3.2.8 Momentum Diffusivity (ν)

Although the momentum diffusivity (ν) of the core is unknown to within several orders of magnitude, we find that the effect of this variable is insignificant for the structure, frequency, or quality of eMAC waves.

$$\omega \not\propto \nu \,,$$

$$Q \not\propto \nu \,.$$

3.2.9 Magnetic Coupling to the Bulk Core Fluid

We examine the effect of changing boundary conditions on eMAC waves, including pseudo vacuum boundary conditions (PVBC) vs electromagnetic coupling (EMBC) at the bottom boundary of the stratified layer, as well as the influence of the period used to compute the EMBC (see chapter 2). We compute eMAC waves using PVBC, as well as EMBC using periods ranging from 3 years to 24 years. We plot the periods for eMAC waves with m=6, and l ranging from 0 to 5 in figure 3.15 using default parameters listed in table 3.1. We find that wave periods obtained for a particular eMAC mode can differ by up to 25% depending upon the choice of period used to compute the EM coupling with the bulk core fluid. This is a relatively small error, even when using EM coupling periods very far from the wave period. Even using PVBC gives fairly accurate results for the wave period for low latitudinal wave-numbers. For l=0 the eMAC wave period with EMBC is $\sim$21 years while using PVBC gives a period of 23.5 years, an error of only 12%. For l=1 the EMBC period is $\sim$14.5 years while PVBC gives 17.75 years, an error of 22%.

We also examine the effect of boundary conditions on eMAC quality factors. We plot the quality factor of eMAC waves for m=6, l=0 to 5 in figure 3.16, again using default parameters listed in table 3.1. We find that the quality factor of eMAC waves is relatively insensitive to the choice of period used for computing the EMBC, with differences typically under 25% between the EMBC value and the most extreme errors. However, we find a large difference between the quality factors obtained using PVBC and quality factors obtained using EMBC. For l=0, the EMBC gives Q$\sim$0.5, while PVBC gives Q=0.9, a difference of 80%. For l=1, EMBC gives Q$\sim$0.6 and PVBC gives Q=1.14, a 90% difference. The error increases with l, such that for l=5, EMBC gives Q$\sim$1.0 while PVBC gives Q=2.68, a difference of 168%.

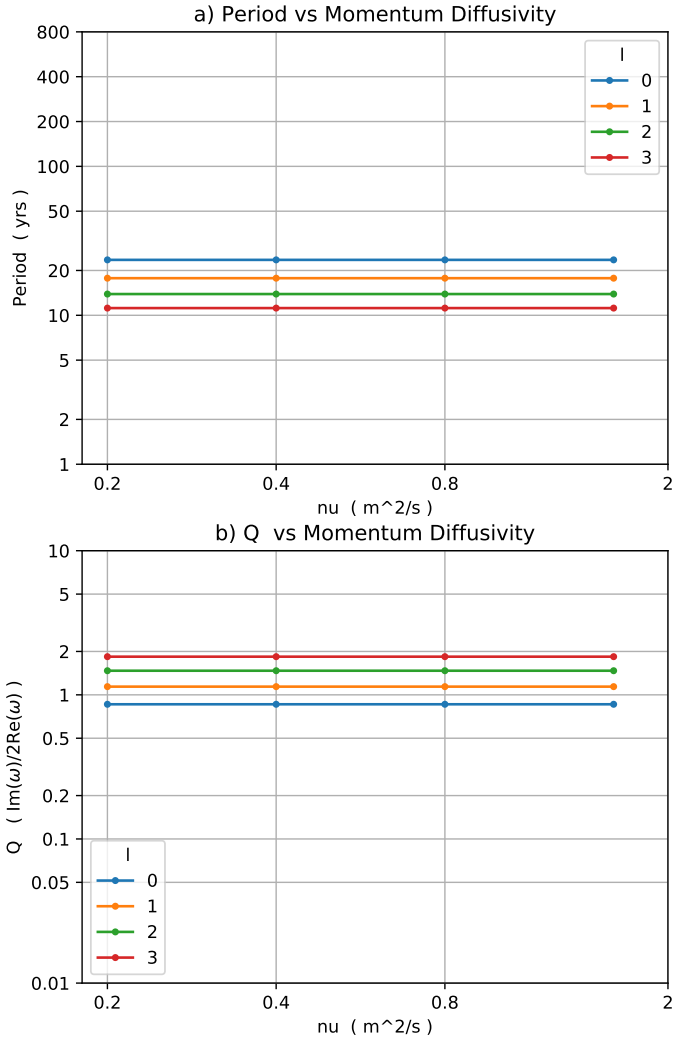

Figure 3.14: eMAC wave period (a) and quality factor (b) dependence on the momentum diffusivity (ν) of the core fluid.

The large differences in quality factor obtained using PVBC likely arise due to the extremely thin layer in which eMAC waves propagate in this study ($\sim$40 km). Because electromagnetic forces couple wave motions near the bottom of the stratified layer to the quasi-stationary bulk core fluid, EMBC applies a strong damping force to the wave motions. Assuming PVBC at the bottom boundary of the layer allows for the fluid at the base of the stratified layer to move freely without experiencing the damping from electromagnetic coupling with the bulk fluid layer. This allows the waves to obtain much higher quality factors.

There are a variety of mechanisms that could allow eMAC waves to propagate in the core with sub-decadal periods despite the low quality factors obtained using EMBC. First, higher radial wavenumbers (k) can decrease the eMAC wave period while maintaining their quality factor (see section 3.2.4). Thus, a thicker layer could allow for sub-decadal waves with k>1 to propagate with quality factors substantially larger than 1. On the other hand, energy could be continuously pumped into the system due to the vigorous dynamo convection beneath the stratified layer, which could continuously excite eMAC waves despite their low quality factors. The question of excitation and propagation of eMAC waves is complicated by the results in section 3.3.2 using varying layer stratification, as it shows a mixing of modes much more complex behaviors of eMAC waves. The implications of the low eMAC quality factors obtained are discussed further in section 6.3.

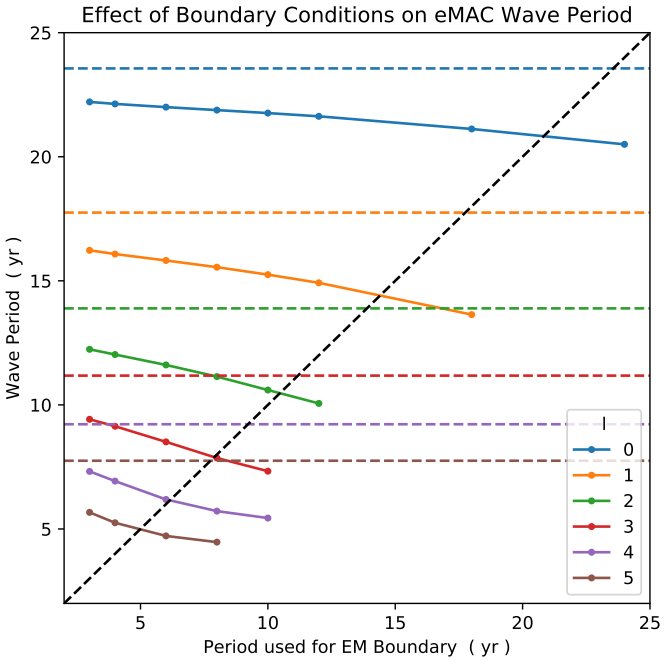

Figure 3.15: eMAC wave period vs period used for EM coupling at base of stratified layer for l = 0 to l = 5, using default parameters listed in table 3.1. Solid lines represent results obtained using EM coupling at the base of the stratified layer, as detailed in chapter 2. Colored dotted lines represent periods obtained using pseudo-vacuum boundary conditions (PVBC) on both the top and bottom boundary. The diagonal black dotted line represents the physically relevant case when the wave period matches the period used to compute the EMBC exactly.

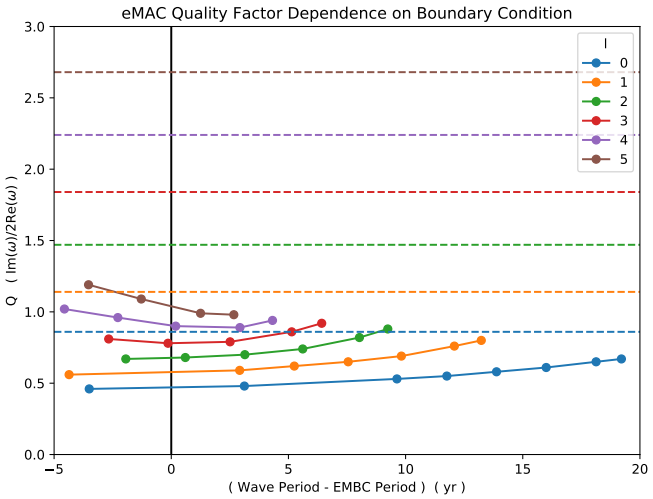

Figure 3.16: eMAC wave quality factor (Q), plotted versus the mismatch between the wave period and the period used for EM coupling at base of stratified layer. Waves shown for latitudinal wave-numbers $l = 0$ to $l = 5$, with parameters listed in table 3.1 used for all other values. Solid lines represent results obtained using EM coupling at the base of the stratified layer, as detailed in chapter 2. Dotted lines represent quality factors obtained using pseudo-vacuum boundary conditions (PVBC) on both the top and bottom boundary.

3.3 Wave Structure Variation

The CMB magnetic field and layer properties influence the structure of eMAC waves in addition to their period and quality factor. In particular, the distribution of magnetic field strength at the CMB has a large influence on the degree to which eMAC waves are equatorially trapped. In addition, while we find that the magnitude of the layer buoyancy does not influence the structure of eMAC waves, any deviation from a constant layer stratification does have a strong influence on the radial structure of eMAC waves.

3.3.1 Magnetic Field Distributions

The FVF model permits the study of more general background magnetic field configurations than just constant or dipole fields. Earth's observed field is neither constant nor a perfect dipole, but instead has a dominant dipole structure with a significant amount of higher-order structure overlaid. As the Lorentz force takes the form $\vec{B} \cdot \nabla(\vec{B})$ in the magnetohydrodynamic approximation, it is insensitive to the polarity of the field. Then, as waves in a thin layer are mainly sensitive to the radial magnetic field, it is appropriate to examine the root-mean-square (RMS) radial magnetic field strength as a function of latitude. It can be seen in figure 3.17a that historical observations of the average magnetic field strength by latitude at the CMB show a RMS field strength of ∼0.5 mT at high latitudes and ∼0.3 mT near the equator (Jackson et al., 2000). This represents a lower bound on the total field at the CMB, as unobserved small-scale features likely contribute to the total RMS field at the CMB. To approximate the structure of the total field at the CMB, we add white noise to a dipole field and take the root-mean-square of the distribution, giving

$$B_r^{rms}(\theta) = \sqrt{B_d^2 \cos^2\theta + \sigma^2}. \tag{3.1}$$

Values of $B_d = 0.5$ mT and $\sigma = 0.3$ mT are chosen to approximate Earth's observed CMB field with a small amount of unobserved noise (figure 3.17a). Braginsky (1998) used the same value for his dipole but did not include noise, resulting in zero field strength at the equator. The core's internal radial magnetic field is also likely to vary with radius. While our model can accommodate radial variations, the details of these variations are unknown and likely to be small in a thin layer, so we simply use the CMB field throughout the layer depth.

3.3.1.1 Zonal MAC Waves

First, we examine the influence of magnetic field structure on the global zonal MAC waves described in section 2.2.2. The dipole with noise approximation of the total field produces zonal MAC waves with peak zonal flows at mid-latitudes and no flow at the equator, in stark contrast to MAC waves derived using a dipole, which have peak flow on the equator. A dipole permits flow at the equator because the force balance between the Lorentz and Coriolis forces are perfectly maintained as they become weaker near the equator. However, non-zero field strength at the equator alters the force balance in the ϕ-component of the momentum equation. To a first approximation, we have a balance between the Coriolis force $2\Omega\cos\theta\, u_\theta$ and the Lorentz force $B_r\partial_r b_\phi$. When B_r is dipolar, we can achieve a balance between the Coriolis and Lorentz forces with a non-zero $\partial_r b_\phi$ at the equator. Otherwise, if B_r is finite at the equator, $\partial_r b_\phi$ must vanish at the equator to maintain the force balance, which precludes any source of generation due to u_ϕ. Consequently, u_ϕ must be zero at the equator for these wave motions.

This result demonstrates the importance of magnetic field configurations when studying waves in Earth's core. Braginsky's MAC wave solution is only valid due to the precise balance between Coriolis and Lorentz forces near the equator resulting from a perfect dipole field, and even small perturbations to B_r alter the basic structure of the solution significantly. Because Earth's field includes significant power near the equator, a constant radial field seems to be a better approximation than a dipole field for MAC waves, as it produces a similar basic wave structure. However, both the dipole and constant field approximations give very different wave structures and properties to those derived using a more realistic magnetic field configuration with our FVF method.

3.3.1.2 eMAC Waves

We next examine how the distribution of magnetic field strength near Earth's equator influences the structure of eMAC waves. As shown in section 3.2.3, the period of eMAC waves is influenced by the strength of the radial magnetic field at the CMB, with stronger fields producing shorter periods. Notably, the spatial structure of the waves is largely insensitive to changes in the total RMS field. Instead, the spatial distribution of background magnetic field has a large influence on the latitudinal extent of the waves. We compute

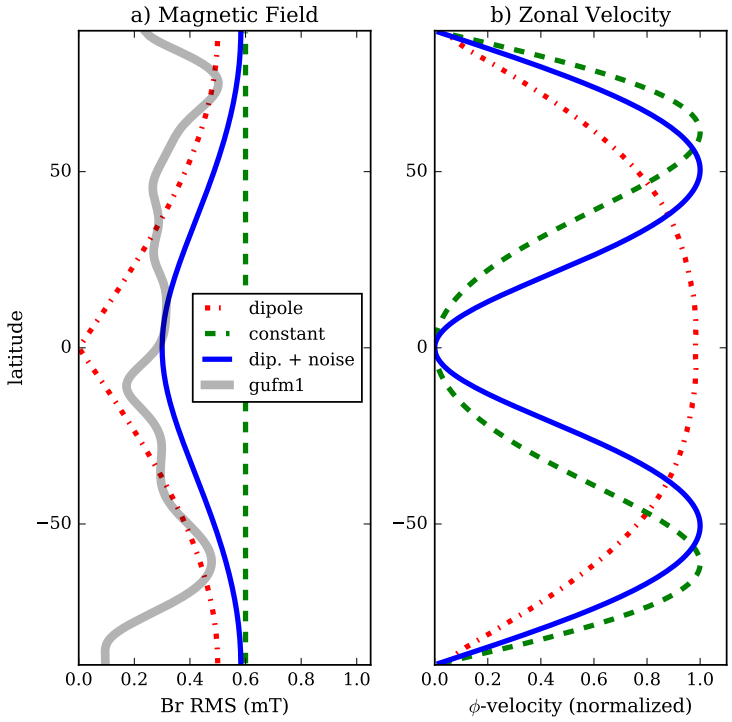

Figure 3.17: Comparison of MAC wave zonal flow velocities (v_ϕ) for three choices of radial magnetic field. We include a dipole field (Braginsky, 1993), a constant field, and a dipole plus noise (see text), which is intended to approximate gufm1 at 1990 (Jackson et al. 2000). All runs use H=80 km, N=2 Ω. Note that a finite magnetic field strength at the equator causes v_ϕ to vanish.

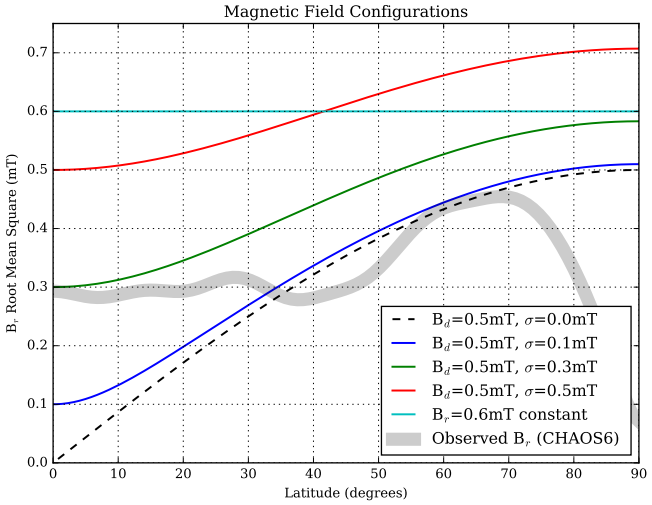

Figure 3.18: Magnetic field distributions used for MAC wave solutions in figure 3.17 and figure 3.19. Note that small noise values have relatively high (low) field strength at high (low) latitudes, while large noise values results in field structures more evenly distributed across latitude. Included for comparison is the observed zonal-averaged RMS radial core field in 2010 from the CHAOS-6 field model (Finlay et al., 2016).

several wave solutions using (3.1) to construct a range of simple models for the radial magnetic field, including a dipole with several different amounts of noise and a constant radial field (see figure 3.18). We then compute the wave structures for the same wave mode using a 40 km thick layer with a constant N=10 Ω, and show the eastward fluid velocity structure by latitude in figure 3.19. A nearly dipolar field with only 0.1mT noise produces strong equatorial trapping, with peak flow near the equator. Larger amounts of noise result in stronger relative field strengths in the equatorial region and produce waves that are less confined to the equator. In the limit of a constant radial field, the peak flow velocities occur at mid-latitudes. Because the spatial distribution of magnetic field strength is important in determining the spatial structure of the waves, the spatial extent of oscillations in observed secular acceleration could provide a constraint on distribution of total magnetic field strength at the CMB, including small scale structures unable to be observed directly.

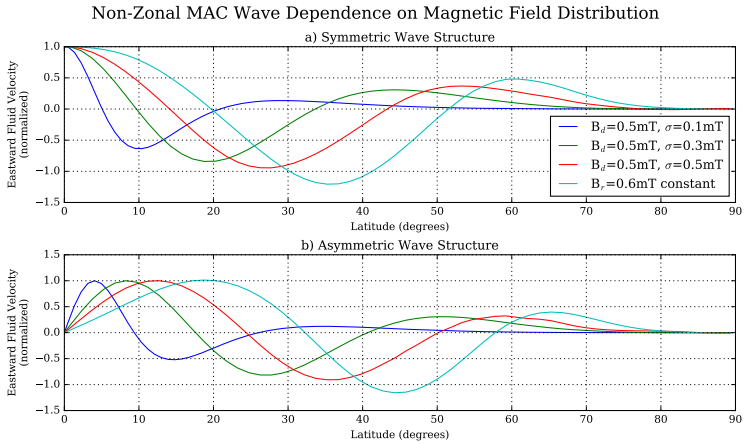

Figure 3.19: Comparison of wave structures of four non-zonal eMAC waves computed using four different magnetic field distributions (shown in figure 3.18). Note that as the field structure changes between a dipole field and a constant field, flow moves to progressively higher latitudes.

3.3.2 Layer Stratification Structure

The majority of eMAC waves shown in this section have been computed using a constant layer buoyancy, which represents a linear decrease with radius in the density perturbation below the adiabat. However, a perfect linear density increase is unlikely to arise in the physical core. Instead, diffusive processes may produce an approximately exponentially decaying density contrast from the CMB to the base of the stratified layer (Buffett and Seagle, 2010; Buffett, 2014). To approximate this, we can use a buoyancy frequency that varies with radius instead of a constant buoyancy frequency through the layer. The simplest form we can use is to vary N linearly with radius, which approximates an exponential density increase with radius. We use a buoyancy frequency that varies from N=0 Ω at the base of the layer to N=10 Ω at the CMB to compute eMAC waves. We are able to find results that closely match those derived using constant buoyancy, and show the (k=1, l=0, m=6) eMAC wave in figure 3.20. The changing stratification changes the functional form of the radial fluid motion v_r, but does not significantly affect the period, quality factor, or functional form of the other components of the wave structure.

However, a radially-varying N does admit many further solutions that

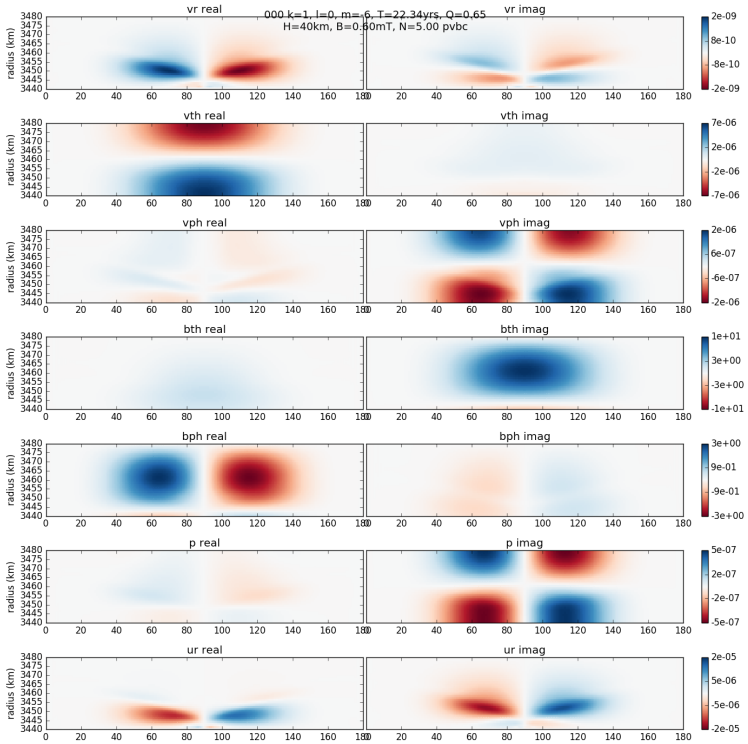

Figure 3.20: eMAC wave propagating in a layer with a linearly-varying buoyancy from N=0 at the base of the layer to N=10Ω at the CMB. eMAC wave has wave-numbers k=1, l=0, m=6, and uses the default parameters listed in table 3.1 for all values except N, with EMBC at the bottom boundary. This wave has a period of 22.34 years and a quality factor of 0.65.

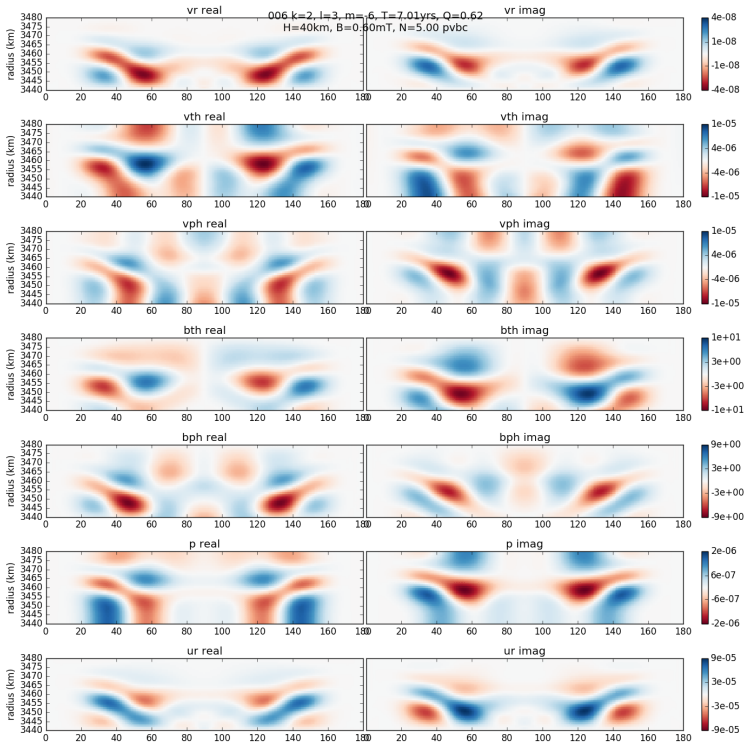

Figure 3.21: eMAC wave propagating in a layer with a linearly-varying buoyancy from N=0 at the base of the layer to N=10Ω at the CMB. This eMAC mode is asymmetric (see e.g. the b_θ term), and has a longitudinal wavenumber of m=6, but an appropriate radial or latitudinal wavenumber cannot be readily identified. This wave has a period of 7.01 years and a quality factor of 0.62.

take the general form of eMAC waves but are not readily classified with particular wave-numbers. One example is shown in figure 3.21. This wave is again computed using the default values listed in table 3.1 except for N, with EMBC. The structure of this wave is asymmetric with respect to the equator, but an appropriate radial or latitudinal wavenumber cannot be readily identified. An effective categorization or parameterization scheme has eluded identification for these modes, despite extensive examination and search of the parameter space. Thus, the remainder of this study will focus on the simple form of eMAC waves identified using constant N.

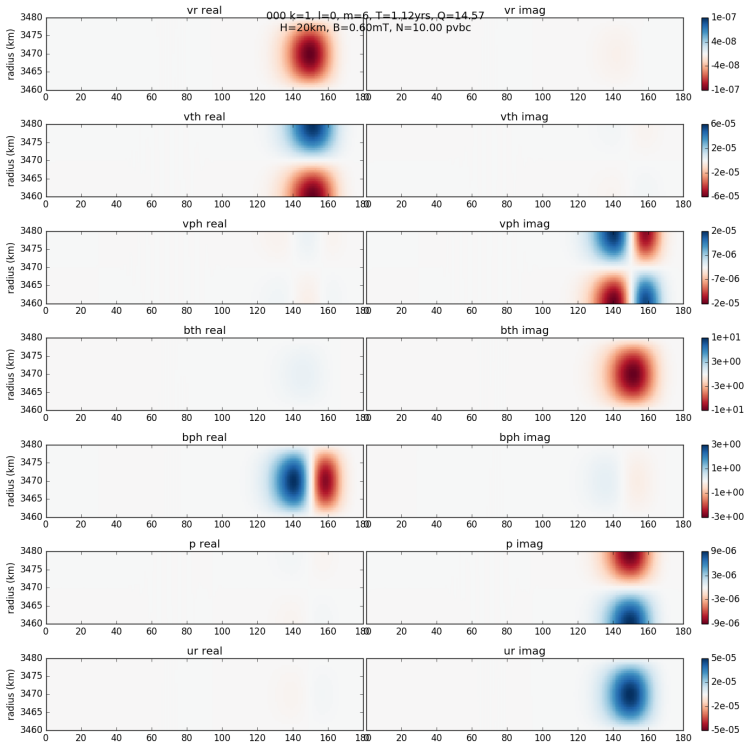

Figure 3.22: MAC wave propagating to the west at high latitudes with wavenumbers of k=1, l=0, m=6. This waves has a high quality factor of Q $\sim$ 15 and short period of only $\sim$ 1 year. Layer properties are the defaults listed in table 3.1 except for the layer thickness which has been reduced to 20 km.

3.4 Other Observed Wave Modes

During the investigation of eMAC wave modes, other wave modes are found to propagate in the layer. Notably, there are waves that propagate to the west in the mid- and high- latitudes with very high quality factors. We show two examples of the first two modes in figures 3.22 and 3.23. These waves will not be the focus of this thesis, but could warrant further study, as discussed in chapter 6. In addition, numerical results for the dependence of these waves on layer structures can be found in appendix D.

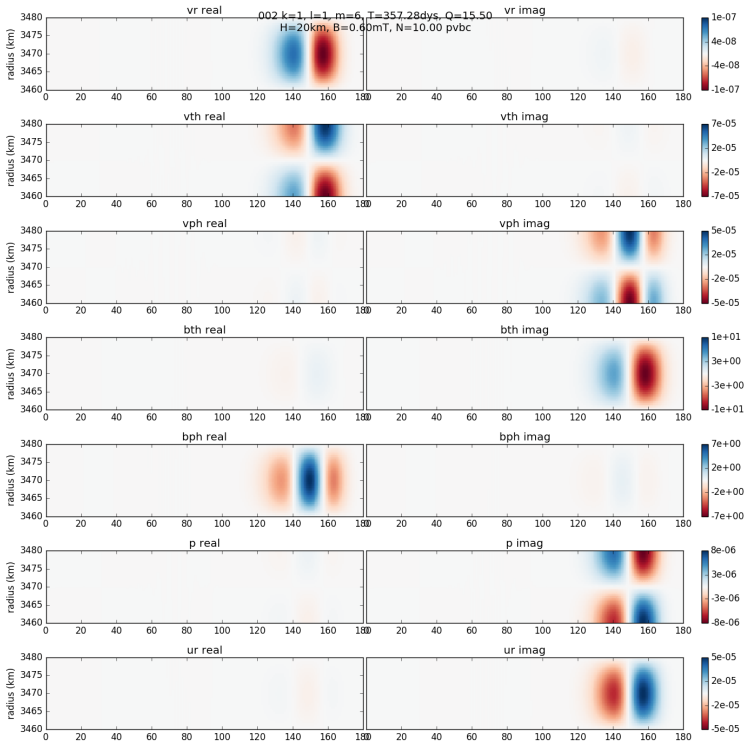

Figure 3.23: MAC wave propagating to the west at high latitudes with wavenumbers of k=1, l=1, m=6. This wave has a high quality factor of Q $\sim$ 15 and short period of only $\sim$ 1 years. Layer properties are the defaults listed in table 3.1 except for the layer thickness which has been reduced to 20 km.

Chapter 4

Methods to Detect Waves

To quantitatively assess the limits of our ability to observe eMAC waves in Earth's magnetic field, we use the eMAC waves produced by our numerical model to create synthetic SA and SV signals (section 4.1.1). We then use these signals with known origins to assess the effectiveness of various methods used to study waves in Earth's core (section 4.2.1). We focus on eMAC waves with periods and spatial structures relevant to observed oscillatory signals in equatorial SA and SV (e.g. Finlay et al., 2016; Chulliat et al., 2015). We propose an improved technique for detecting waves in geomagnetic observations of SV as well as SA (section 4.2.2 and 4.3.1). We also construct a noise model to demonstrate that the technique is robust to data uncertainties and other sources of error in SV (section 4.3.2) and SA.

4.1 eMAC Wave Parameterization

We use the hybrid finite-volume and Fourier (FVF) model described in chapter 2 to study equatorial waves in Earth's core with various magnetic fields and stratification structures. We find the eMAC waves described in chapter 3 have consistent patterns of wave motion for a variety of layer properties and magnetic fields. However, details like the period, latitudinal extent, and quality factor do change with the properties of the layer and field.

We derive a flexible representation of the eMAC wave structure in order to efficiently study the geomagnetic signals produced by eMAC waves propagating in a wide variety of SOC structures in Earth's core. Computing wave solutions for a wide variety of layer parameters using our FVF model

is computationally expensive, and we wish to be able to have fine control over the latitudinal extent and longitudinal wavenumber of synthetic eMAC waves. Therefore, we compute wave structures for a set of layer and field structures and fit the flow fields to obtain a flexible parametric representation of eMAC flow structures at the CMB. This essentially translates the structure of eMAC waves from the discrete representation of the FVF model to a functional parametric representation. Then, by adjusting the parameters of this representation, we can adjust the flow structure and period of the waves over a wide range of conditions without having to re-compute the waves with our FVF model for each specific set of layer parameters.

A natural choice to to capture the functional form of the eMAC waves are the Hermite basis functions indexed by n,

$$\psi_n(x) = (-1)^n (2^n n! \sqrt{\pi})^{-\frac{1}{2}} e^{\frac{x^2}{2}} \frac{d^n}{dx^n} e^{-x^2} \tag{4.1}$$

because they are concentrated near $x = 0$, corresponding to the equator, and decay away from the equator. These functions are adapted from Hermite polynomials to provide an orthonormal basis over space without any weighting function.

To use them for waves on a sphere, we choose a parameter δ_θ such that $x = \theta/\delta_\theta$ where θ is latitude. Thus, δ_θ describes the width of the waves in degrees latitude.

The FVF model is formulated as an eigenvalue problem, which produces wave solution vectors that describe the real and imaginary components of flow velocity $\hat{v}_{\theta,\phi}$ at each latitude θ on a grid. These are used to compute the velocity at the core-mantle boundary for particular longitude ϕ through

$$v_{\theta,\phi}(\theta,\phi) = \Re\left\{\left[v^{\Re}_{\theta,\phi}(\theta) + i v^{\Im}_{\theta,\phi}(\theta)\right] e^{im\phi}\right\} . \tag{4.2}$$

We recover a flexible representation of the flow which we denote $\hat{v}$ using the Hermite basis functions

$$\hat{v}^{\Im}_{\theta}(\theta) = \sum_n c^{\Im}_{\theta,n} \psi_n(\theta/\delta_\theta) \tag{4.3}$$

$$\hat{v}^{\Re}_{\theta}(\theta) = \sum_n c^{\Re}_{\theta,n} \psi_n(\theta/\delta_\theta) \tag{4.4}$$

$$\hat{v}^{\Im}_{\phi}(\theta) = \sum_n c^{\Im}_{\phi,n} \psi_n(\theta/\delta_\theta) \tag{4.5}$$

$$\hat{v}^{\Re}_{\phi}(\theta) = \sum_n c^{\Re}_{\phi,n} \psi_n(\theta/\delta_\theta) \tag{4.6}$$

where $c^i_{j,n}$ and δ_θ are fit coefficients. These coefficients are found by minimizing

$$\sum_{i,j}(v^i_j - \hat{v}^i_j(c^i_{j,n}, \delta_\theta))^2$$

where $i = [\Re, \Im]$, $j = [\theta, \phi]$, and n is the Hermite basis function degree.

Although these waves have radial variation in their flow, fluid motions below the CMB do not produce significant observable SA and SV when the effects of magnetic diffusion are small. Therefore, we only fit flow at the core-mantle boundary with this representation.

Our FVF model produces two classes of eMAC waves with different equatorial symmetries of their flow. We denote these classes "symmetric" and "asymmetric" waves in reference to the equatorial symmetry of the geomagnetic signal they produce when advecting a pure dipole field, and examine the fundamental mode (in radial and latitudinal structure) of each class (see figure 3.2). Symmetric waves correspond to even latitudinal wave-numbers (l), while asymmetric waves correspond to odd l.

We fit the CMB flows obtained from the FVF model for these waves to Hermite basis functions and find that the complex coefficients $c^i_{j,n}$ are consistent across a range of realistic layer and magnetic field structures. Only the period, quality factor, and latitudinal extent (δ_θ) vary significantly as we change layer and field properties. Thus, we are able to construct a set of symmetric and asymmetric complex coefficients $c^i_{j,n}$ that can be used to describe the complete flow structure of the wave across the CMB. These symmetric and asymmetric waves have most of their power in a single Hermite polynomial, making the flow structure of these two classes nearly orthogonal to each other. However, for accuracy, we fit each wave using the first seven Hermite basis functions to guarantee that they are well-described.

These fits can then be used to describe general symmetric and asymmetric waves by choosing a particular set of parameters including the longitudinal wavenumber m, period T, and width parameter δ_θ for the wave. Typical values of δ_θ for the waves derived using our FVF model are in the range $\delta_\theta = 10^\circ$ to 30°, and this parameter's influence on a single wave component can be seen in figure 4.1. The flow velocity of the wave must also be set. Because the FVF model is constructed as an eigenvalue problem, the amplitude of the solutions and therefore the wave velocities are unconstrained. We find that peak flow velocities of 1-2 km/yr produce SA consistent with the magnitude of observed SA, and therefore use values in this range in our analyses. The

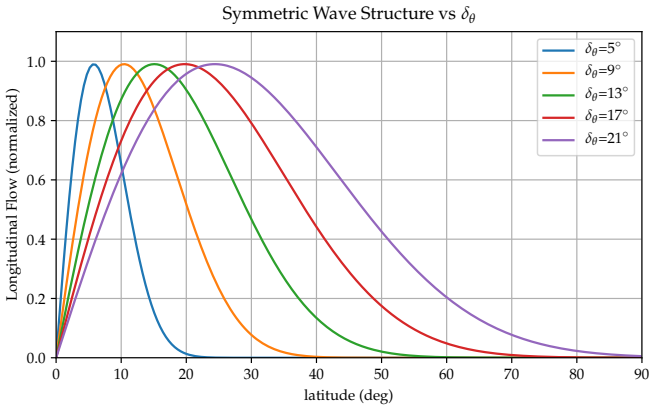

Figure 4.1: Longitudinal flow (v_ϕ) structure variation for the symmetric wave with different values of δ_θ. Peak flow velocity normalized to one.

final parameter we must fix to fully describe these waves is their longitudinal position or phase ϕ_0 at a particular point in time. A full description of the wave solution is given by

$$v_{\theta,\phi}(\theta,\phi,t) = \Re\left\{\left[v^{\Re}_{\theta,\phi}(\theta) + iv^{\Im}_{\theta,\phi}(\theta)\right] e^{im(\phi+\phi_0)+i\omega t}\right\} . \tag{4.7}$$

where t is time and $\omega = 2\pi/T$ is the wave frequency. The representation in (4.7), based on fits to the numerical model, gives a complete and flexible description of the CMB fluid flow for eMAC waves, which we use throughout the remainder of this chapter.

4.1.1 Generation of Secular Variation and Acceleration

Fluid motions at the core-mantle boundary advect the main magnetic field, contributing to geomagnetic secular variation (SV) and secular acceleration (SA). Secular variation (i.e. $\partial_t B_r$) is governed by the induction equation

$$\partial_t B_r = -\nabla_H \cdot (\vec{v}_H B_r) + \frac{\eta}{r}\nabla^2 r B_r \tag{4.8}$$

where B_r is the radial field at the CMB, $\vec{v}_H$ is the horizontal fluid velocity, and η is magnetic diffusivity (Holme, 2015). We ignore radial fluid motions v_r, as they vanish at the CMB and $v_r \ll v_H$ within the stratified layer below.

In a stratified layer the diffusion term is dominated by the radial length scale L_r. Typical layers examined have $L_r \sim 50$ km to 300 km, while typical horizontal scales are $L_H \sim R/m \sim 300$ km for $m = 6$, where R is the radius of the core. We obtain a characteristic timescale for magnetic diffusion of $\tau \sim L_r^2/\eta \sim 80$ yrs for the thinnest layers and 316 yrs for the thickest layers, both much larger than the ~ 8 yr period of waves examined. This indicates the error introduced by ignoring magnetic diffusion should be small for periodic motions like these waves. Barrois et al. (2017) finds that diffusion contributes up to 20% of SV across all scales, placing an upper bound on the error introduced by this approximation. Expanding the horizontal divergence in (4.8),

$$\partial_t B_r = \vec{v}_H \cdot \nabla_H B_r + B_r \nabla_H \cdot \vec{v}_H \tag{4.9}$$

explicitly shows the advection and divergence terms.

Secular acceleration is similarly generated by fluid motions and can be computed by taking the time derivative of secular variation in (4.8). When the diffusive term is dropped for the reasons outlined above, we obtain

$$\partial_t^2 B_r = \nabla_H \cdot (\vec{a}_H \, B_r) + \nabla_H \cdot (\vec{v}_H \, \partial_t B_r) \tag{4.10}$$

where $\vec{a}_H = \partial_t \vec{v}_H$. With terms expanded we compute secular acceleration using

$$\partial_t^2 B_r = \vec{a}_H \cdot \nabla_H B_r + B_r \nabla_H \cdot \vec{a}_H + \vec{v}_H \cdot \nabla_H \partial_t B_r + \partial_t B_r \nabla_H \cdot \vec{v}_H \tag{4.11}$$

One key aspect of these equations is that the SA and SV depends upon the fluid velocities ($\vec{v}_H$) and accelerations ($\vec{a}_H$) of the wave as well as the structure of the background magnetic field B_r. When the background B_r has a simple structure such as a pure dipole field, the waves described in section 4.1 produce signals from which it is easy to determine their longitudinal wavenumber and symmetry across the equator (see figure 4.2a and b). This allows one to easily assess the structure of these wave directly from the observed SV and SA. However, when the same waves are produce SV and SA by advecting the observed B_r up to degree 14 from the CHAOS-6 model (Finlay et al., 2016) they produce complex signals from which neither the longitudinal wavenumber or equatorial symmetry are readily apparent (see figure 4.2c,d). This effect is similar to that observed by Cox et al. (2016), who explore whether global torsional waves can couple with heterogeneous background magnetic fields to produce localized signals in SV resembling geomagnetic jerks.

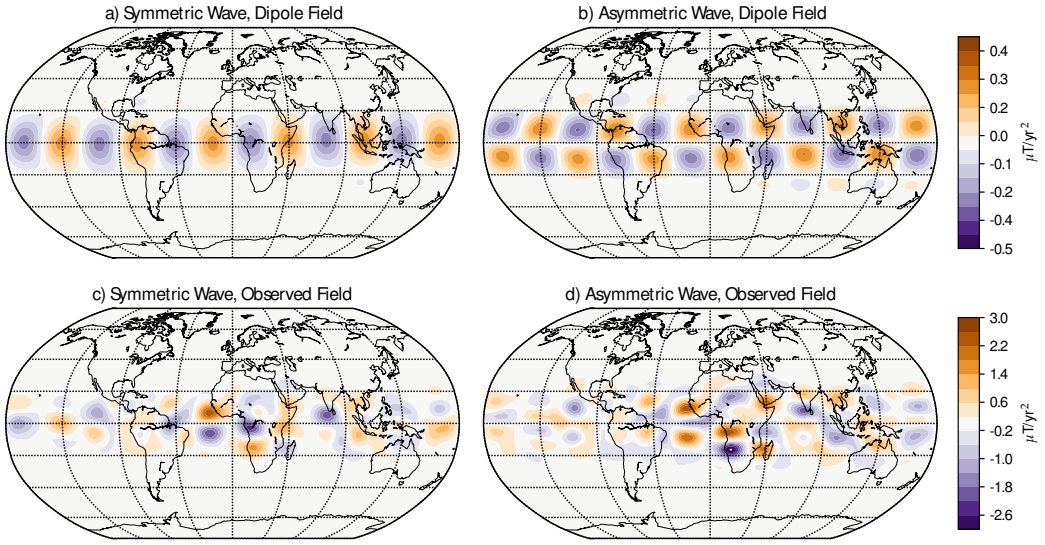

Figure 4.2: Secular acceleration produced by symmetric (a,c) and asymmetric (b,d) wave mode advecting a pure dipole field (a,b) and the observed geomagnetic field (c,d) in 2010 (Finlay et al. 2016). Note that the simple waves couple to small-scale structures in the geomagnetic field to produce complex signals.

Coupling between flows and the background magnetic field also introduce errors into these calculations because we only observe the main field up to degree ~ 14. Shorter wavelength components of the main field with degree > 14 will couple to the flow and contribute to observed low-degree SV. The magnitude of the error introduced from this contribution is unknown, but expected to be modest compared to other sources of error.

4.2 Wave Detection Using Secular Acceleration

4.2.1 Period-Wavenumber Observations

Previous attempts to overcome the complexities in SV and SA have relied on a two-dimensional Fourier transform to convert the data from a time-longitude domain to period-wavenumber (PWN) space. Chulliat et al. (2015)

used this method to examine signals near the equator by summing (or differencing) time-longitude slices of observed SA at 5, 10, and 15 degrees latitude above and below the equator to compute the amplitude of symmetric (asymmetric) waves in PWN space. They then attribute peaks in these symmetric (asymmetric) SA PWN plots to symmetric (asymmetric) equatorial waves in Earth's core. However, the results of the previous section raise questions about the correspondence between peaks in PWN space and the presence of waves in the core. We can assess the validity of this approach using known wave motion.

To compute a PWN plot, the input data must only have dimensions of time and longitude. Chulliat et al. (2015) select SA data at 0, 5, 10, and 15 degrees latitude and sums and differences the values north and south of the equator to examine symmetric and asymmetric waves. This approach discards data from all other latitudes, including those near the equator that should contain information about wave motions. In order to fully utilize this information, we generalize this approach by adopting continuous weight functions over latitude that are either symmetric or asymmetric across the equator. We use the first (n=0) Hermite basis function (4.1)

$$\psi_0(x) = \pi^{-\frac{1}{4}} e^{-\frac{1}{2}x^2} \tag{4.12}$$

for symmetric waves and the second (n=1) function

$$\psi_1(x) = \sqrt{2}\pi^{-\frac{1}{4}} x e^{-\frac{1}{2}x^2} \tag{4.13}$$

for asymmetric waves, where $x = \theta/\delta_\theta$. With these weight functions, we can adjust δ_θ to maximize the amount of data from wave motions included in our analysis and exclude signals far from the equator unlikely to be due to waves.

To test whether it is possible to reliably differentiate between symmetric and asymmetric waves using a PWN transform, we compute the PWN of the SA for different combinations of wave symmetry and weighting function symmetry (figure 4.3). For this analysis, all parameters other than symmetry are held constant between the two waves, including the peak wave velocity and latitudinal extent.

A symmetric wave examined using a symmetric weight function (4.12) produces a single strong signal at the correct period and wavenumber (figure 4.3a). Likewise, an asymmetric wave examined using an asymmetric weight

function (4.13) recovers the correct wave parameters (figure 4.3d). However, an asymmetric wave also produces significant power in the PWN plot when using a symmetric weight function, as seen in (figure 4.3c). In fact, there are multiple peaks of similar magnitude at various wave-numbers, with very little power at the correct wavenumber. One small piece of good news is that these spurious peaks are all a factor of five smaller than the true peak observed from the symmetric wave in using a symmetric weight function. However, when a symmetric wave is examined using an asymmetric weight function, it produces multiple spurious peaks in the PWN spectrum (figure 4.3b), many of which have a similar magnitude to the single peak obtained from an asymmetric wave.

This result illustrates that the PWN transformation cannot reliably distinguish signals from symmetric and asymmetric equatorial waves, even in the simplest possible case of only a single wave mode. This result is robust when using a wide variety of weight-functions, including constant weight with latitude, square functions, and averaging observations at particular latitudes north and south of the equator as used in (Chulliat et al., 2015).

The situation is worse when multiple waves are present (as is likely in Earth's core), as it becomes impossible to determine if a signal arises from a single asymmetric wave (fig. 3d) or multiple symmetric waves (fig. 3b). In addition, the strength of the FFT is directly related to the amplitudes of the waves, so even the weak signals seen in fig. 3c could be interpreted as either the result of a single asymmetric wave (as in this case) or multiple low-amplitude symmetric waves.

4.2.2 Wave Correlations with Observations

Instead of simply transforming observed SA to look for wave signals, we can utilize our knowledge of the structure of our equatorial waves to look for correlations between signals produced by our waves and observed SA. First, we select the wave by specifying a representative value for δ_θ and choose the wavenumber (m), period (T), and phase (ϕ_0). Then we compute the SA_{wave} for our choice of wave and evaluate the correlation with the observed $SA_{obs.}$.

We evaluate the correlation between $SA_{obs.}$ and the SA_{wave} by first applying a weight function w_θ across latitude to each to obtain $X = w_\theta \cdot SA_{obs.}$ and $Y = w_\theta \cdot SA_{wave}$. Then, we compute the correlation between the weighted

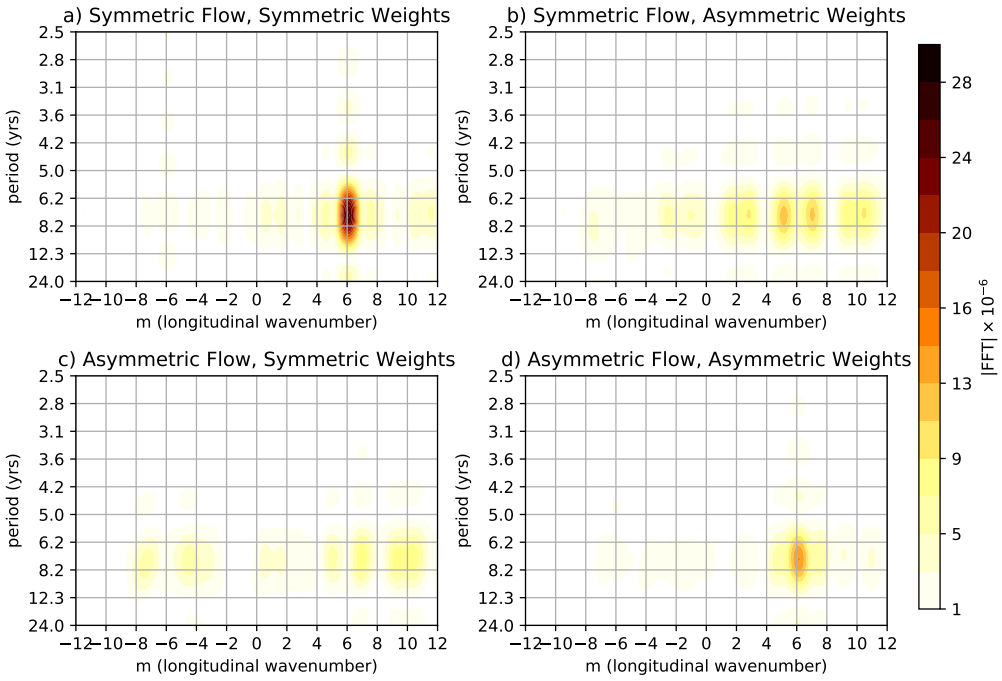

Figure 4.3: Period-wavenumber (PWN) transformations of SA produced by waves advecting the observed geomagnetic field. Waves were computed with m=6, period=7.5 yrs, $\delta_\theta = 14°$; and are either symmetric (a,b) or asymmetric (c,d). PWN transformations were computed using weighting functions that are symmetric (a,c) or asymmetric (b,d). Note that the symmetric flow transformed with a symmetric weight function gives a single strong signal recovering the wave properties, but that the same wave also produces weaker signal in many wave-numbers when examined with an asymmetric weighting function. Likewise, the asymmetric wave produces power in many wave-numbers when examined with a symmetric weight function, and only produces a weak signal of similar magnitude to the symmetric wave using asymmetric weights.

data sets using

$$\rho_{X,Y} = \sum_{\theta,\phi,t} \frac{(X - \mu_X)(Y - \mu_Y)}{\sigma_X \sigma_Y} \tag{4.14}$$

where μ and σ are the mean and standard deviation of each weighted dataset. We evaluate this cross-correlation across a range of periods T, wave-numbers m, and the full range of phases ϕ_0 from 0 to 2π. This allows us to find the peak correlation across these three parameters in the ranges of interest. With this method, we can focus on either symmetric or asymmetric waves by choosing only one type of wave to generate the SA_{wave}.

To demonstrate this method, we create 15 years of synthetic observations of SA using four waves to simultaneously advect the observed geomagnetic field. Two waves are symmetric and have periods and wave-numbers of T=7.5 yrs, m=6 and T=8.5 yrs, m=-4, respectively. The other two waves are asymmetric with T=10.5 yrs, m=6 and T=9.5 yrs, m=-3. All waves have $v_0 = 1$ km/yr, while their δ_θ are randomly chosen between from 8° to 16° and phases distributed uniformly between 0° and 360°. The computed correlations are shown in figure 4.4 and show clear recovery of all four wave modes. Other peaks in T and m have much less power.

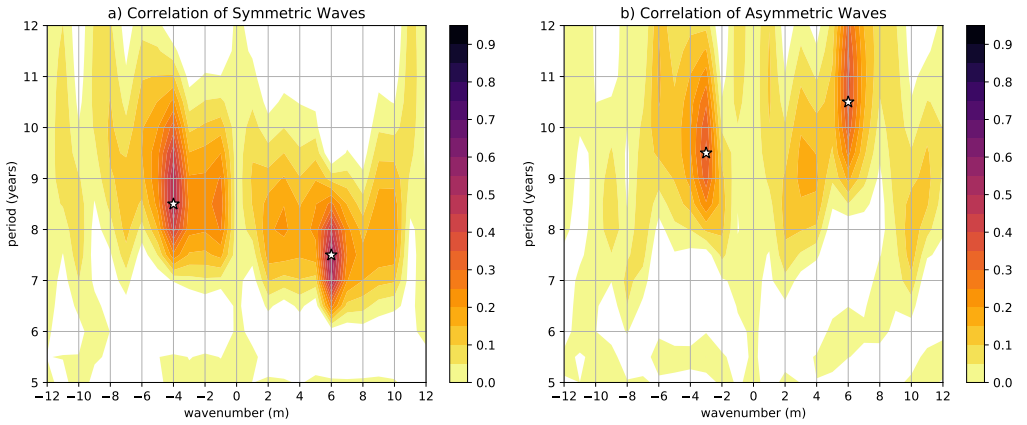

Figure 4.4: Correlation of symmetric (a) and asymmetric (b) waves across different wave-numbers and periods with a single SA signal produced by advecting the observed field using four different waves (see text). The period and wavenumber for each wave is marked on the plot with a star. Note that both plots are produced using the same SA signal, yet symmetric and asymmetric waves are clearly distinguished with this method, with little spurious power bleeding between symmetries.

4.3 Wave Detection Using Secular Variation

4.3.1 Steady Flow Removal

The correlation analysis from section 4.2 can also be applied to SV. There are several reasons for examining SV in addition to SA. First, we can obtain a check against random noise producing spurious wave detections as SV is more well-resolved than SA at smaller length scales and suffers fewer artifacts near the start and end of the time series in models that regularize their solutions (Finlay et al., 2016). Second, a simultaneous detection of waves with identical properties in both SA and SV is much less likely to occur due to chance. To see why, note that some processes in the core, such as steady fluid motions, produce power dominantly in SV. Likewise, other processes such as small-amplitude transient fluid motions produce little SV but significant SA. Each of these processes might individually produce signals in either SA or SV that could be interpreted as wave motions. However, simultaneous wave correlations in both SA and SV must result from a process that has a very specific relationship between fluid velocity and acceleration (e.g. $\partial_t v = i\omega v$).

To apply the correlation analysis to SV, we first need to account for the contribution from large-scale steady fluid motions in the core. While these fluid motions do not significantly contribute to observed SA, a large fraction of SV can be explained with a large-scale steady flow (see Section 4.1.1). These flows have been estimated to have peak velocities on the order of $\sim$ 10-20 km/yr (Holme, 2015). For comparison, equatorial waves with periods of $\sim$ 10 years and m=6 require peak flow velocities of only $\sim$ 1 km/yr to produce a representative $|SA| \sim 2$ μT/yr in the equatorial region of Earth's core. As this velocity is an order of magnitude less than estimates for large-scale steady flows, we might expect steady flow to obscure signals from wave motions in observed SV.

To examine whether this is true, we first fit a steady flow to the CHAOS-6 field model (Finlay et al., 2016) using the method described by Holme (2015). We choose a damping parameter to produce a fairly smooth flow structure and minimize the residual at the CMB as this is the region we are interested in studying. The resulting steady flow velocity can be seen in figure 4.5. Then, we use this steady flow to advect the observed geomagnetic field to produce SV and SA. Finally, we compare this result to SV and SA produced by representative equatorial waves. We show in figure 4.6 that steady flow produces strong SV and little SA, while the opposite is true for

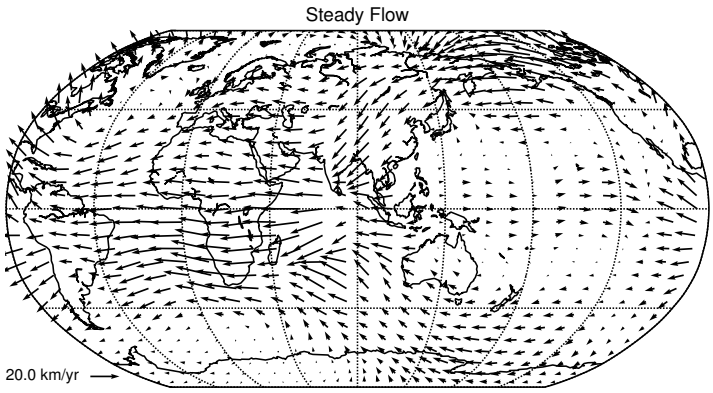

Figure 4.5: Steady flow structure fit to explain changes in the observed geomagnetic field model CHAOS-6 from 2001 to 2015.

wave motions. In fact, the SA produced by equatorial waves is an order of magnitude larger than that produced by steady flow, even thought the wave flow velocity is much smaller. The opposite is true for SV. This is easily explained by examination of equations (4.9) and (4.11). Steady motions have large magnitude $\vec{v}$, compared to waves, so they would produce greater SV. On the other hand, steady flow by definition has $\vec{a} = 0$, so they produce very little SA.

Because only a small portion of total SV originates from wave motions, we seek to remove the contribution of large-scale steady flow from the total SV in order to examine wave motions. To do this, we compute the SV produced by our steady flow fit, then subtract this from the total SV to obtain

$$SV_{\text{residual}} = SV_{\text{observed}} - SV_{\text{steady flow}} .$$

This could include SV produced by the wave motions and transient motions unrelated to waves; it could also reflect the effects of magnetic diffusion within the core (Barrois et al., 2017). In addition, SV_{residual} will have errors introduced due to the small-scale flows and the imperfect steady-flow fit resulting from the limited temporal and spatial resolution of SV observations

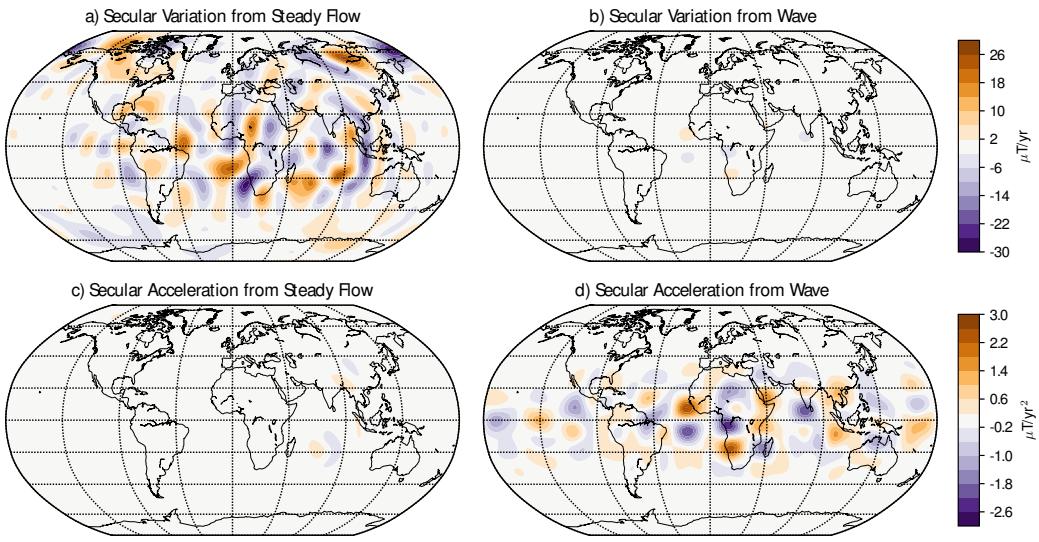

Figure 4.6: SV and SA produced by steady flow and wave motions (wave parameters: symmetric, m=6, period=8.5 yrs, peak velocity = 2 km/yr, δ_θ = 10^o). Note that steady flow produces strong SV and little SA, while wave motions produce strong SA and little SV.

(Baerenzung et al., 2016; Pais and Jault, 2008; Gillet et al., 2015a). We group all of these effects into a noise term SV_{noise} which gives

$$SV_{\text{residual}} = SV_{\text{wave}} + SV_{\text{noise}} \,.$$

The noise can potentially obscure any wave signals that exist in the data or causing spurious correlations that could be interpreted as waves. Indeed, applying our wave correlation method to the SV_{residual} results in strong correlations for a large number of waves across a variety of wave properties. In order to confidently identify waves, we need to quantify the extent to which SV_{noise} contributes to the wave correlation.

4.3.2 Noise Model

We construct a stochastic noise model SV^*_{noise} to represent non-wave processes in SV_{residual}. We aggregate many realizations of this model to determine the baseline level of wave correlation expected when no waves are present. Then, correlations above this baseline can be attributed to waves with greater confidence.

Stochastic methods have been used in the past to study uncertainties in observations of Earth's magnetic field (e.g. COV-OBS.x1, Gillet et al., 2015a) and large-scale flow in the core (Gillet et al., 2015b). These techniques have been used with great success, but they are not directly applicable to the question of characterizing SV_{noise}. Instead, these models are intended to represent time variations in the total field, including contributions from steady flow, waves and other non-steady influences. However, we wish to evaluate signals arising in SV_{residual} with contributions from steady flow removed, which has not been previously considered in the literature.

Instead, we construct our SV^*_{noise} model by generating random gauss coefficients with an appropriate power spectrum in both space and time. The spatial power spectrum of total observed SV at the CMB has been well studied (see e.g. Finlay et al., 2016, fig. 8). However, much of this power can be explained by large-scale steady flow in the core, which we remove in our analysis and therefore do not wish to simulate in our noise model. Examining just the portion of SV unexplained by steady flow (SV_{residual}), we find that the power increases with degree l and is fairly constant across order m (see figure 4.7).

We must then find an appropriate way to treat the temporal variations of SV_{noise}. Previous authors have used an AR(1) stochastic process to find

that the frequency spectrum of the total SV follows a power law distribution with exponent -2 (Lesur et al., 2018). However, as the authors of that study point out, AR(1) processes produce significant high-frequency noise which would need to be filtered to represent realistic observed SV. In addition, the frequency spectrum of the total observed SV does not necessarily reflect the frequency spectrum of the SV_{noise} we wish to model.

We instead adopt an approach based on a Fourier expansion of the gauss coefficients of SV_{residual} to examine its temporal variation. This results in complex Gauss-Fourier coefficients $c_r(l, m, t)$ which are related to SV_{residual} through

$$SV_{\text{residual}}(\theta, \phi, t) = \frac{1}{T} \sum_{l=0}^{N_l} \sum_{m=-l}^{l} \sum_{k=0}^{N_k} c_r(l, m, k)\, Y_l^m(\theta, \phi)\, e^{i2\pi k/T} \tag{4.15}$$

where l and m are spherical harmonic degree and order, k is Fourier frequency, $Y_l^m(\theta, \phi)$ is the complex spherical harmonic function, θ is co-latitude, ϕ is longitude, t is time, and T is the duration of the time series. This transformation allows us to examine the spatial and temporal spectrum of SV_{residual} simultaneously.

We find that the magnitude of the coefficients increase linearly with degree l for $k = 0$, while magnitudes for $k \neq 0$ increase with l to $l \sim 12$ before beginning to decrease. Magnitudes are fairly evenly distributed across order m, and decrease with temporal frequency k (see figure 4.7). On the other hand, the phase of coefficients (i.e. the relative magnitude and sign of $g_n(l, m, k)$ and $h_n(l.m, k)$) are uniformly distributed across all possible values with no clear trends with l, m, or k.

We use the Gauss-Fourier coefficients of SV_{residual} as the basis for our SV^*_{noise} model. This approach might include contributions from waves in the core, which we would ideally exclude from our noise model. However, their inclusion would have the effect of raising the threshold for detection and so would not cause spurious detections. We assume that the Fourier components of the complex Gauss coefficient are drawn from a normal distribution where the mean and variance (denoted μ_{fit} and σ^2_{fit}) are inferred from the complex coefficients of SV_{residual} for the CHAOS-6 model (specific details are given below). Thus the amplitude of the coefficients of the noise model (denoted $c_n(l, m, k)$) are drawn from a normal distribution

$$|c_n(l, m, k)| \sim \mathcal{N}\left(\mu_{fit}(l, k)\,,\, \sigma^2_{fit}(l, k)\right). \tag{4.16}$$

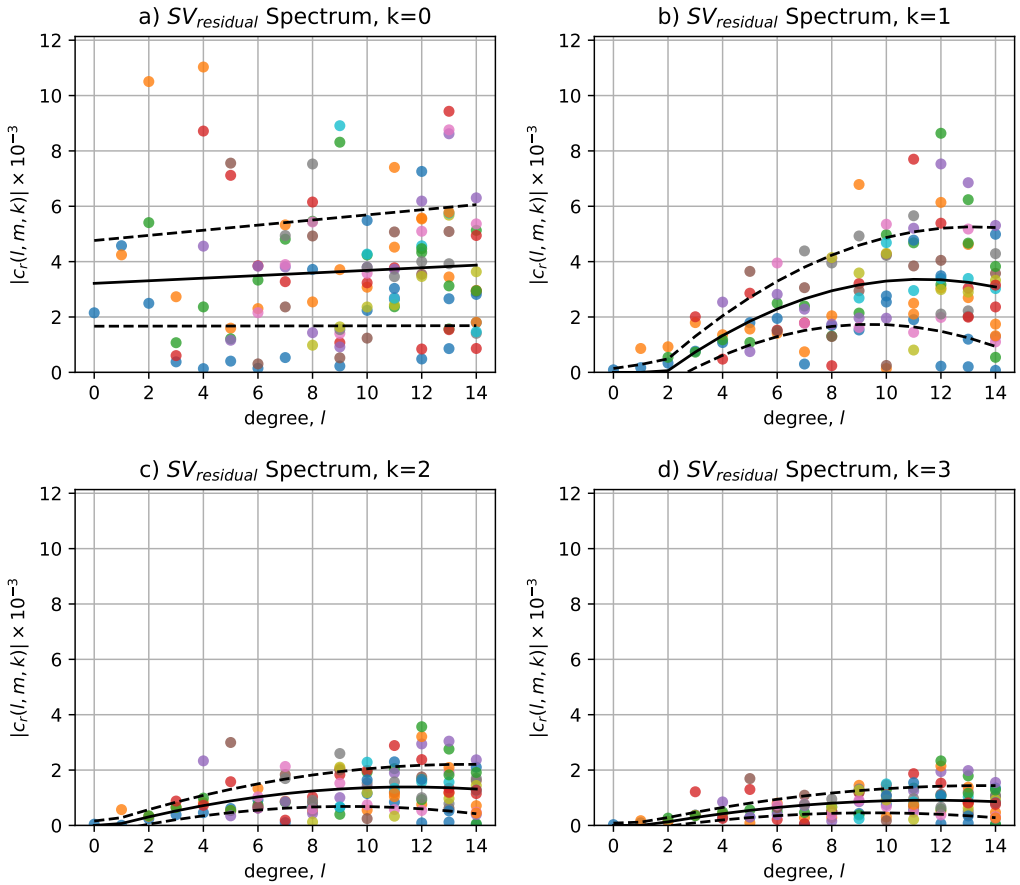

Figure 4.7: Spectrum of the SV_{residual}. Each dot is the magnitude of an individual $c_r(l, m, k)$ (see (4.15)), plotted with respect to degree l and colored by order m. Subplots show Fourier frequencies $k = 0, 1, 2, 3$. Clear trends are seen in l and k, but no trend is seen with m (colors). Solid lines represent the trend of the mean magnitude of coefficients with l, while dotted lines show bounds of one standard deviation (see text for details).

The phase of the coefficients $\psi(l, m, k)$ are then drawn from a uniform distribution on the interval 0 to 2π

$$\psi(l, m, k) \sim Unif[0, 2\pi)\,. \tag{4.17}$$

This allows us to construct our model without knowledge of the temporal power spectrum of SV_{residual} a-priori, and does not introduce spurious high-frequency noise as an AR(1) process would.

There is considerable scatter in the means and variances computed from the coefficients at fixed l and k and variable m. More importantly, there are relatively few m values at low degree. Consequently, we adopt simple functional forms for μ_{fit} and σ_{fit} that depend on degree l and frequency k. We compute the mean $\mu(l, k)$ of the magnitude of each observed coefficient across m for each l and k. Then, we fit these means with a linear fit vs l for the constant Fourier term ($k = 0$) and a quadratic fit vs l for the time-varying ($k \neq 0$) terms, weighted by the number of m coefficients at each degree l.

$$\mu_{fit}(l, k) = \begin{cases} \alpha_0 + \alpha_1\, l & \text{for } k = 0 \\ \alpha_0 + \alpha_1\, l + \alpha_2\, l^2 & \text{for } k \neq 0 \end{cases}$$

We perform a similar analysis for the standard deviation σ. We compute the sample standard deviation $\sigma(l, k)$ around $\mu(l, k)$ to provide an estimate of the coefficient variance across order m. We assume the standard deviation varies linearly across l to find $\sigma_{fit}(l, k)$, again weighted by the number of m coefficients at each l.

Using $\mu_{fit}(l, k)$ and $\sigma_{fit}(l, k)$ in (4.16), we generate a random magnitude for each complex coefficient of the noise model $c_n(l, m, k)$. We combine these magnitudes with a random phases from (4.17) to obtain a set of coefficients

$$c_n(l, m, k) = |c_n(l, m, k)|e^{i\psi(l,m,k)}$$

which are then transformed to physical space and time using (4.15). Finally, an additional constraint is imposed that the root-mean-square amplitude of the generated SV^*_{noise} must match that of the observed SV_{residual} in the equatorial region by scaling the coefficients of each realization by a constant factor.

To determine whether wave signals are visible in SV_{residual} over this background noise, we produce 20 realizations of our SV^*_{noise} model with no synthetic waves added and compute the wave correlation across m and period.

Then, for each point in (m, T) space we fit a normal distribution to the histogram of these computed correlations to estimate the 95% quintile of correlation when no waves are present, which we plot in figure 4.8. This represents a floor for detection of wave motions using the wave correlation analysis for SV_{residual}. Any correlation below this threshold can likely be attributed to spurious correlations with SV_{noise}, not the SV_{wave} we wish to find. The detection threshold varies from around 0.01 for wave periods of 5 years to 0.1 for wave periods of 12 years.

We use this detection threshold to examine the minimum wave velocity required for detection in SV by computing the signal-to-noise ratio of SV_{residual} correlation to SV^*_{noise} correlations. Using a peak fluid velocity of 1 km/yr, we find a signal-to-noise ratio of almost 2 when recovering the synthetic wave properties. In this analysis, there are only a few places elsewhere on the plot where the signal to noise ratio barely rises above one due to signals arising from the SV^*_{noise} model (see figure 4.9). Repeating this calculation across a range of velocities, we find that a peak wave flow velocity of approximately 0.3 km/yr is required for a wave with these parameters to appear above the background 95% noise level. This compares favorably with the $|v| \sim 1$ km/yr needed to explain the magnitude of observed equatorial SA. We find that the wave velocity needed for detection does not vary with the longitudinal wavenumber m, but does change with the wave period. We find that the wave velocity needed to rise above our detection threshold remains around 0.3 km/yr for wave periods between 3 and 7 years, then increases approximately linearly with period to ~ 0.7 km/yr for waves with a 12-year period.

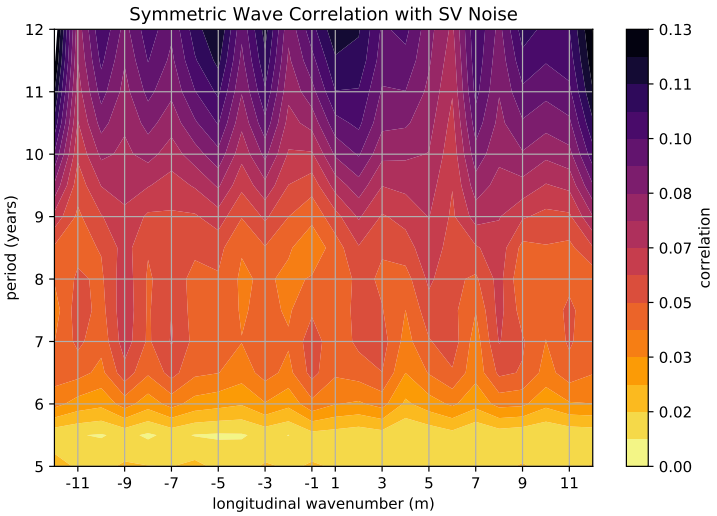

Figure 4.8: Period-wavenumber plot showing the threshold at which a correlation with SV_{residual} is likely to be a wave. Values shown are the 95% quintile of correlation with the synthetic noise model representing SV_{residual}. See text for details.

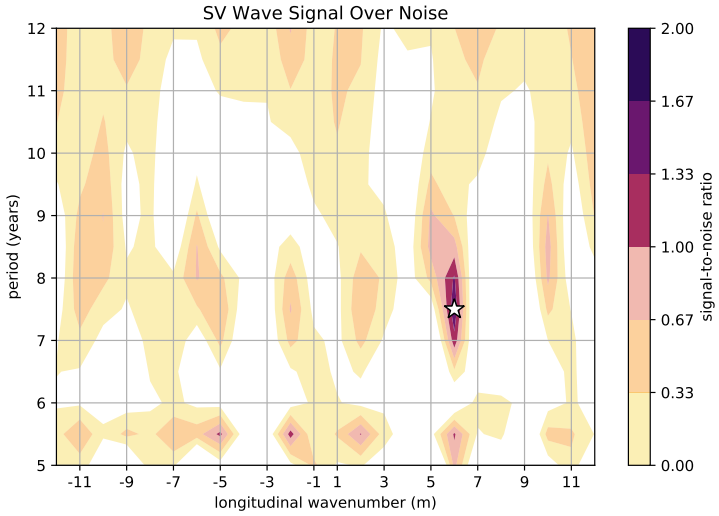

Figure 4.9: Period-wavenumber plot showing the signal-to-noise ratio for a wave with a period of 7.5 years, m=6, peak velocity of 1 km/yr, and includes one realization of the residual SV^*_{noise} model. The background correlation threshold is a smoothed version of that shown in figure 4.8. Note that signal is nearly twice the background correlation for the wave, with only small locations elsewhere where the ratio rises above one near the bottom of the plot.

.

4.4 Conditions for Wave Detection

The methods described above are shown to be able to recover wave period (T), longitudinal wavenumber (m), and equatorial symmetry from both SA (figure 4.4) and SV (figure 4.9). We show below that this technique can also accurately recover latitudinal extent (δ_θ) (section 4.4.1), phase (ϕ_0) (section 4.4.2), and peak flow velocity (v_0) (section 4.4.3) for each wave in a set of waves.

4.4.1 Latitudinal Extent of Waves

The latitudinal extent δ_θ of the equatorial waves can vary greatly depending upon the layer and magnetic field properties. This means that the reliable recovery of the latitudinal extent of the waves can provide important insights. In addition, an accurate estimate is required to obtain useful results from the wave correlation analysis described in section 4.2.2. To estimate the latitudinal extent of these waves, we simply find the peak correlation across an array of values for δ_θ at the period, wavenumber, and phase corresponding to a particular wave. We show this technique for two wave-numbers in figure 4.10. These results were obtained using the synthetic SA produced by four simultaneous waves. All waves have periods around 8 years, amplitudes of 1 km/yr, δ_θ between 8° and 20°, longitudinal wave-numbers of -6, 3, 2, and 6, and uniformly random phases. We show the strength of correlation for one symmetric wave with a true $\delta_\theta = 8°$ and one asymmetric wave at $\delta_\theta = 15°$ as we vary the latitudinal width of waves with the same period, wavenumber, and symmetry. The latitudinal extent of the symmetric wave is recovered precisely by the peak correlation, while peak correlation of the asymmetric wave occurs very close to the actual value of $\delta_\theta = 14°$. By repeating this analysis for a large sample of waves with random parameters, we find that this technique recovers the true δ_θ within 2° for all wave periods, longitudinal wavenumbers, and equatorial symmetries examined in this study.

Notably, the strength of correlation declines away from the peak value much more quickly for the asymmetric wave compared to the symmetric wave. We believe this is because asymmetric waves have more complex flow structures than symmetric waves – small changes in δ_θ create larger discrepancies in the direction and magnitude of flow at any particular point, leading to a faster decline in the correlation with changes in δ_θ.

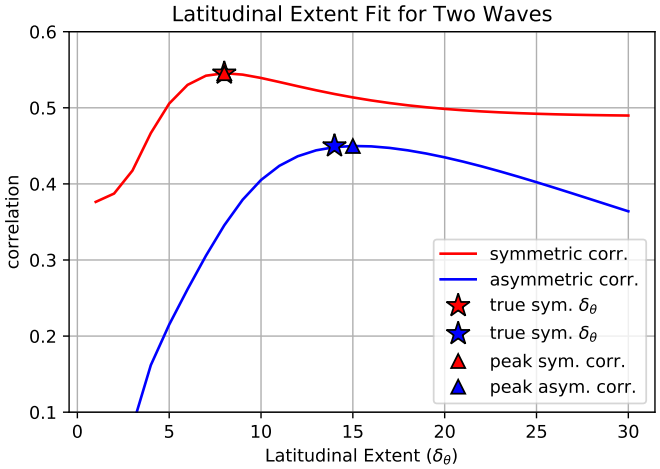

Figure 4.10: Recovery of latitudinal extent (δ_θ) of a symmetric and asymmetric wave from correlations with synthetic SA. The synthetic SA includes two symmetric and two asymmetric waves with periods around 8 years, amplitudes 1 km/yr, δ_θ between 8° and 20°, and various longitudinal wave-numbers and phases. The symmetric wave examined has a true $\delta_\theta = 8°$, which is recovered precisely by the peak correlation. For the asymmetric wave, peak correlation occurs for $\delta_\theta = 15°$, very close to the actual value of $\delta_\theta = 14°$.

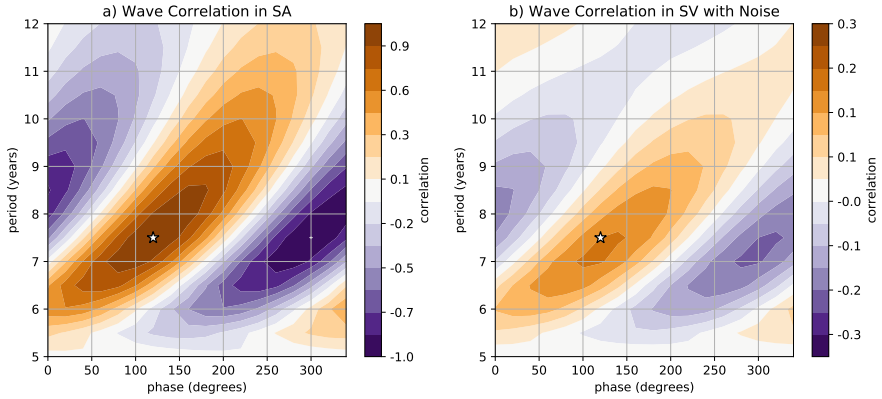

Figure 4.11: Correlation in SA and SV with one realization of the noise model, as a function of phase and period. The synthetic SA and SV datasets are produced using a single symmetric wave with T=7.5 yrs, $\phi_0 = 120°$ (marked on each plot with a star), and $v_0 = 1$ km/yr. The correlation is computed using a symmetric wave. Note that the peak of the correlation occurs at the same period and phase in both SA and SV, despite the fact that the peak correlation in SV is only ~ 0.25 due to the inclusion of noise.

4.4.2 Phase Determination

Independent estimates of the wave phase can be recovered by applying the correlation analysis described in section 4.2.2 to both SA and SV. While the correlation in the SV signal is general lower than with SA due to the additional sources of noise described in section 4.3.1, the shape of the peak correlation between SA and SV are remarkably similar. We show the correlation analysis for SA and SV produced by a wave with m=6, period of 7.5 years, and a phase of 120° in figure 4.11, demonstrating clear recovery of the correct wave properties, even with the inclusion of SV noise.

Consistent values for the wave phase between SA and SV are unlikely to arise by chance, so can be a robust indicator of waves. The observations have limited resolution in space ($l <\sim 14$) and time (periods ~ 3 to 19 years), so resolution improves at larger time and spatial scales. On the other hand, detection of oscillations becomes more confident with more observed wave periods, so short-period waves are able to be detected with greater confidence. Thus, we might expect to preferentially detect waves with intermediate pe-

riods $T \sim 10$ yrs and low spatial wave-numbers (e.g. m $<\sim$ 6). This is precisely where waves are reported. Transient process in the core produce both SA and SV, leading to the possibility of non-waves producing signals that correlate with similar wave-numbers and periods in both SA and SV. Also, equatorial processes unrelated to waves might give similar estimates for the latitudinal extent. However, observational constraints do not bias any particular value of phase, allowing for all phases to appear uniformly when computing wave correlations with random SA and SV data. Thus, it is unlikely that the computed phase would match between SA and SV unless the observations were actually generated by a wave.

To see why, note that general fluid motions in the core create SA and SV through (4.9) and (4.11), which couple all the Fourier coefficients describing the flow with all the coefficients of the background magnetic field magnitude and gradients. Because of this coupling, components across all m and l values could potentially contribute to a correlation analysis performed at a single wavenumber m, causing peak correlations at random phases for any particular set of wave parameters examined. Thus, if the same phase is obtained for a particular set of wave parameters in both SA and SV, it provides very strong evidence of wave motion.

4.4.3 Peak Flow Velocity Determination

The last parameter needed to describe a set of observed waves are the amplitudes or peak flow velocity of each wave mode. Under the assumptions made in section 4.1.1, the total SA produced by a set of waves is simply a linear combination of the SA_n produced by each wave mode n. Thus, in order to find the best-fit amplitudes C_n for a set of N waves, we simply find the best-fit coefficients to minimize the residual

$$Err = \left\langle SA_{\text{obs.}}(\theta, \phi, t) - \sum_n C_n SA_n(\theta, \phi, t) \right\rangle_{rms} \tag{4.18}$$

where $SA_{\text{obs.}}$ is the observed secular acceleration, and SA_n is the secular acceleration produced for each wave, with wavenumber, period, phase, and latitudinal extent determined using the methods described in previous sections. Then, it is straightforward to convert from the amplitude C_n to the peak wave velocity of each mode. Because the computed wave modes each have most ($\sim 85\%$) of their power in a single Hermite function, they are

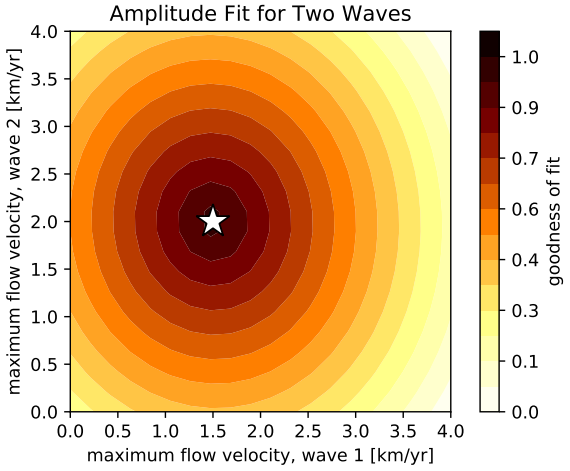

Figure 4.12: Wave velocity fit using SA produced by two waves. The true amplitudes of the synthetic waves marked by a white star denoting 1.5 and 2.0 km/yr peak flow velocities. The goodness of fit is calculated as the minimum error divided by the error at a particular point, so that a value of 1.0 denotes the best-fit, and smaller values have increasing error. Note that because the system is linear and the waves are mostly orthogonal, the residual is convex in amplitude space with only one global best fit. Two waves are shown for visualization purposes, but this fit method can be easily extended to multiple dimensions to fit several waves.

nearly orthogonal. Therefore, there is very little interaction between wave modes when fitting their amplitudes, and there exists a global, convex minimum for the residual RMS SA or SV. We demonstrate this in figure 4.12, showing the smoothly concave residual for the amplitudes of two waves, with the minimum recovering the amplitude of each synthetic wave precisely. This technique is easily extended to as many wave modes as required, as they are pairwise orthogonal. The orthogonal structure of the waves also means that we are unlikely to recover large amplitudes for waves that do not exist using this method. In fact, if we fit five waves to the same synthetic SA produced above using four waves, the analysis finds a best fit that precisely recovers the four nonzero wave amplitudes with zero amplitude for the extraneous wave.

Chapter 5

Observed Waves in Earth's Core

Several strong patches of secular acceleration near Earth's equator seem to drift and fluctuate rapidly in recent observations of Earth's geomagnetic field. We wish to examine whether these arise from eMAC waves by applying the methods described in chapter 4 to the CHAOS-6 geomagnetic field model (Finlay et al., 2012).

eMAC waves are equatorially trapped, so we isolate the signal near the equator by excluding SA and SV at mid and high latitudes. To do this, we apply a window function by latitude to our correlation analysis, shown in figure 5.1. This window function is simply a zeroth-order Hermite polynomial with a latitudinal width of $\delta_\theta = 10°$. This value was chosen to capture the majority of the oscillatory signal observed near the equator while excluding SA and SV at mid- and high-latitudes which is unlikely to originate from eMAC waves. Figure 5.1 shows both the window function as well as the oscillatory power observed by taking a 2D FFT at each latitude and averaging the magnitude of the FFT over wave periods from 5 to 10 years and longitudinal wavenumbers from 5 to 7. This attempts to capture the amplitude of oscillator signal by latitude, and is similar to the 2D FFT technique described in section 4.2.1 as a "Period-Wavenumber" transform. Although this technique cannot reliably distinguish which wave mode produces the observed FFT power, it does allow us to to determine the latitudinal location of oscillatory motions. Thus, we choose the window function to capture the majority of this power.

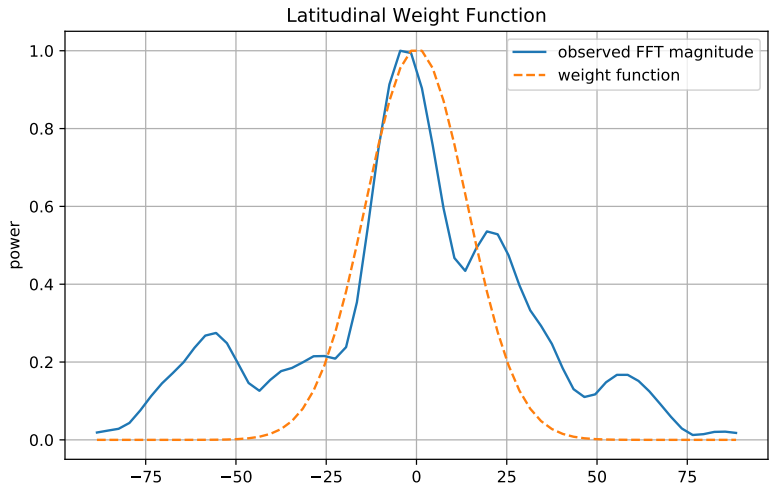

Figure 5.1: Latitudinal weight function used to examine global waves, derived using a Hermite polynomial with a $\delta_\theta = 10°$. Also plotted is the Period-wavenumber transform power for eastward traveling waves, averaged over m=5 to 7 and periods 5 to 10 years. This magnitude is computed at each latitude, then plotted.

5.1 Global Waves

We apply our correlation analysis for the l=0 symmetric and l=1 asymmetric waves modes described in chapter 3. We compute the correlations for periods between 3 and 15 years, longitudinal wavenumbers (m) from -11 to 11, and phases (ϕ_0) from 0° to 360° in intervals of 10°. We also vary the latitudinal width parameter for the synthetic waves (δ_θ) from 5° to 20°. These computed correlations are then compared to the expected noise level, as described in section 4.3.2 for SV and using the same method to define a noise threshold for SA.

We show the results for this correlation analysis in figures 5.2 and 5.3 for l=0 and l=1 wave modes, respectively. We see in figure 5.2a that correlations in secular acceleration show evidence for one eastward-traveling wave at l=0, m=-7, while SV shows one eastward wave with l=0, m=-5. Both SA and SV indicate a westward traveling wave with l=0, m=7. For the asymmetric (l=1) mode, correlations show a m=-10 wave in both SA and SV, and a m=-6 wave in SV, with correlation just under significance in SA. The asymmetric wave also shows correlations for a westward-traveling mode with m=3 for SV and m=7 for both SA and SV.

In order to determine whether these correlations represent waves, we examine the phase of the observed waves in SA and SV using the techniques described in section 4.4.2 and list the results in table 5.1. We list a best estimate of the wave phase as ϕ_0, which we obtain by averaging the phase obtained from SA and SV. Then, we also list the difference between the phase derived from SA and that from SV as $\Delta\phi$. Through synthetic SA and SV experiments, we find that we are able to recover the phase of eMAC waves advecting Earth's observed field within an accuracy of $\Delta\phi < 25°$ in both SA and SV. Thus, the (l=1, m=-6) mode as well as the (l=0, m=5) and (l=1, m=7) westward traveling modes seem to provide evidence of waves with phases that are consistent between SA and SV. On the other hand, the (l=0, m=-7), (l=1, m=-10), and (l=1, m=3) modes give phases that are inconsistent between SA and SV, indicating that the correlations observed are not robust indications of the presence of eMAC waves.

We then compute the amplitudes of these waves using the method described in section 4.4.3 to obtain the peak flow velocities of these waves. We find that the (l=1, m=-6) wave produces a peak flow velocity of only 0.09 km/yr, which is quite low and would likely not produce observable SA. On the other hand, we find that the analysis gives stronger wave amplitudes for

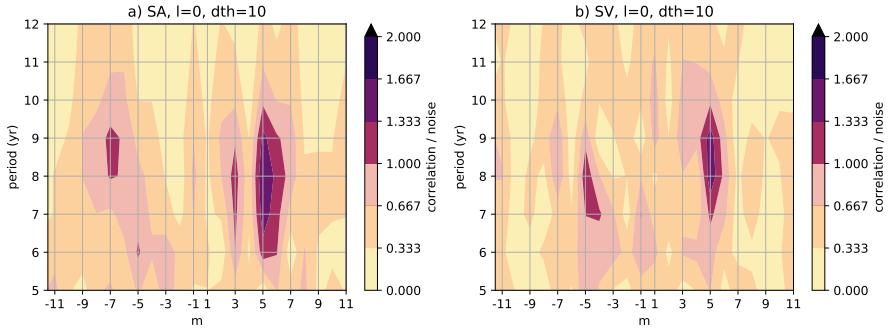

Figure 5.2: Symmetric (l=0) eMAC Wave correlation above noise for secular acceleration and secular variation, using global data and a symmetric window function with $\delta_\theta = 10°$

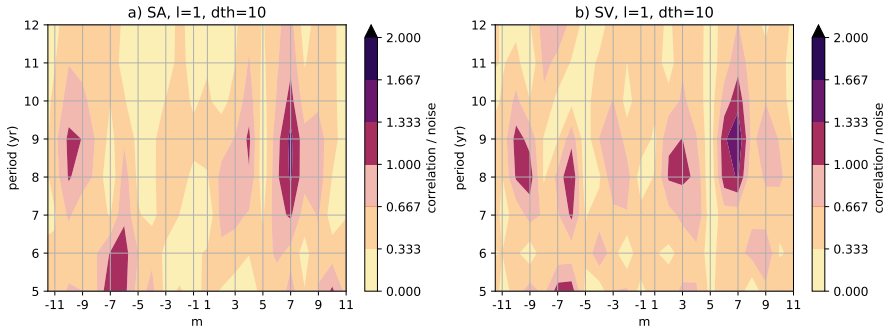

Figure 5.3: Asymmetric (l=1) eMAC Wave correlation above noise for secular acceleration and secular variation, using global data and a symmetric window function with $\delta_\theta = 10°$

eastward-traveling waves						
l	m	period (yrs)	v_{max} (km/yr)	ϕ_0	$\Delta\phi$	δ_θ
0	-7	9	0.12	190°	4.9°	8°
0	-5	7	0.20	111°	41°	8°
1	-6	8	0.09	6.4°	5°	8°
1	-10	7	0.08	66.1°	35°	12°
westward-traveling waves						
l	m	period (yrs)	v_{max}	ϕ_0	$\Delta\phi$	δ_θ
0	5	8	0.41	74°	18°	8°
1	3	8	0.06	227°	34°	8°
1	7	8.5	0.40	222°	11°	10°

Table 5.1: eMAC waves proposed in Earth's core using global equatorial observations.

the westward-traveling modes of (l=0, m=5) and (l=1, m=7) at around 0.4 km/yr.

Finally, we examine the change in correlation with latitudinal width. We find that the strength of correlation is highest for most wave modes for a δ_θ between 8° and 12°, with a drop-off in correlation strength at $\delta_\theta = 5°$ and $\delta_\theta = 20°$. However, correlations are similar in magnitude across the range between 8° and 12°, so a precise determination of latitudinal extent is not possible.

These results seem to provide only weak evidence of the existence of global eMAC waves. The strongest correlations and most robust observations are for the hypothetical equatorial waves that propagate to the west and for which we do not find solutions in our numerical model. While our numerical model does produce westward traveling modes with reasonable SOC parameters, they are not equatorially trapped and often have the majority of their power at mid- and high-latitudes, so they are not considered to be strong candidates to explain these signals.

A more likely explanation for these weak correlations for eMAC waves arises from the low quality factors obtained in our numerical simulations. We commonly find quality factors on the order of 1-4 for many of the eMAC waves in our numerical simulations. If we assume a localized excitation source, these

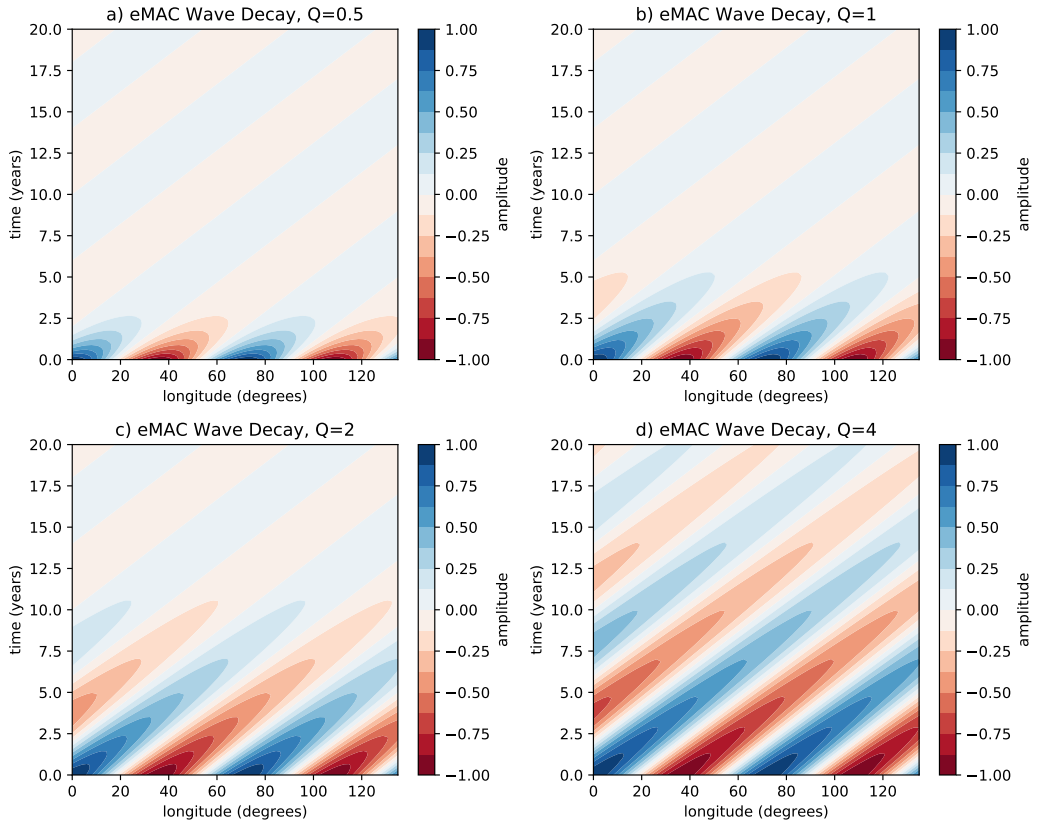

Figure 5.4: Propagation distances for various quality factors of eMAC waves.

eMAC waves would only propagate for a limited distance around the core before dissipating. This can be seen in figure 5.4, which plots the decay of an eMAC wave with an instantaneous excitation source over time and longitude for several representative quality factors. This decay of eMAC waves would render global correlation studies invalid, as waves excited in separate regions around the globe would be unlikely to propagate beyond their local region. Thus, multiple waves around the equator would be unlikely to have matching phases, and therefore any single global wave would not correlate strongly with all regions simultaneously.

There are many localized sources that could excite eMAC waves in particular regions, such as an upwelling parcel of fluid or local CMB topography. Observations of the SA signals may also offer evidence for local excitation of

eMAC waves. There are two equatorial regions of strong oscillatory signal separated by relatively little SA signal across the entire time-series. These two regions fall generally under the Americas and under south-east Asia. If these regions have separate excitation sources, they may produce distinct eMAC wave modes. Thus, we investigate eMAC wave correlations in these regions individually.

5.2 America

We wish to investigate the presence of eMAC waves under the equatorial region of the Americas alone. We use the same latitudinal window function described in the previous section, and apply a window function for longitude as well to isolate the Americas. We again use the zeroth-order Hermite function, but this time centered at -35° longitude (35°W), with a width of $\delta_\phi = 45°$. This produces the window function shown in figure 5.5.

Applying this window function to the observed SA, we see strong patches of SA that appear to oscillate in polarity near the equator, as show in figure 5.6. To a first order, this appears as a standing wave, and might be interpreted to indicate the presence of both eastward and westward propagating waves near the equator.

We perform our correlation analysis with eMAC waves using observed SA and SV data from this region to obtain results for l=0 and l=1 shown in figures 5.7 and 5.8. We see that the symmetric l=0 mode shows strong correlations in both the eastward and westward direction, with correlation power centered at (l=0, m=-6) and (l=0, m=6). For the asymmetric eMAC waves there are several wave modes with significant correlations, including (l=1, m=-7), (l=1, m=4), and (l=1, m=7).

The correlation power in these plots is spread into the neighboring longitudinal wavenumbers (m=4 and 6) much more strongly than for the global analysis, producing diffuse blobs of signal rather than sharp peaks. This is to be expected, as we have constrained the dataset in longitude, reducing the angular resolution and allowing a greater range of longitudinal wavenumbers to produce signals consistent with observations.

In addition, the correlations observed are much stronger in the global wave modes, with the signal-to-noise ratio rising close to 2 in multiple locations, rather than hovering closer to 1 as for the global analysis in the previous section. Because we are using a smaller domain, this would again naturally

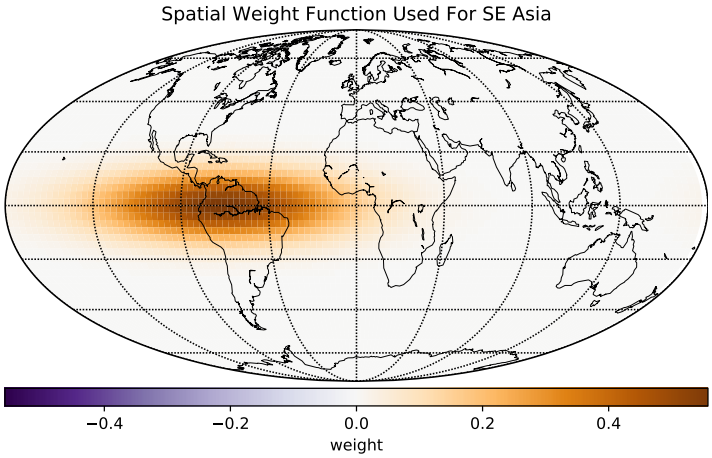

Figure 5.5: Spatial weight function used to examine wave signals under America. $\delta_\theta = 10°$, $\delta_\phi = 45°$, centered at -35 degrees longitude.

occur as a our eMAC waves are compared to a smaller amount of data. This reduces the amount of random noise, therefore enhancing the signal to noise ratio and producing stronger correlations on average.

We again perform our analysis for the phase of the wave in SA and SV, as well as fitting amplitudes to the waves. We find that all waves in this analysis give coherent phase results between SA and SV. Also, all of these wave modes show significant wave velocities except the (l=1, m=-7) mode. The two largest amplitude waves are the (l=0, m=-6) and (l=0, m=6), both with periods of eight years. These waves would set up a standing wave and produce oscillating patches of SA and SV, which matches our initial expectations from a visual analysis of the SA signal. However, the westward-traveling modes are unexplained by eMAC waves, which propagate only to the east.

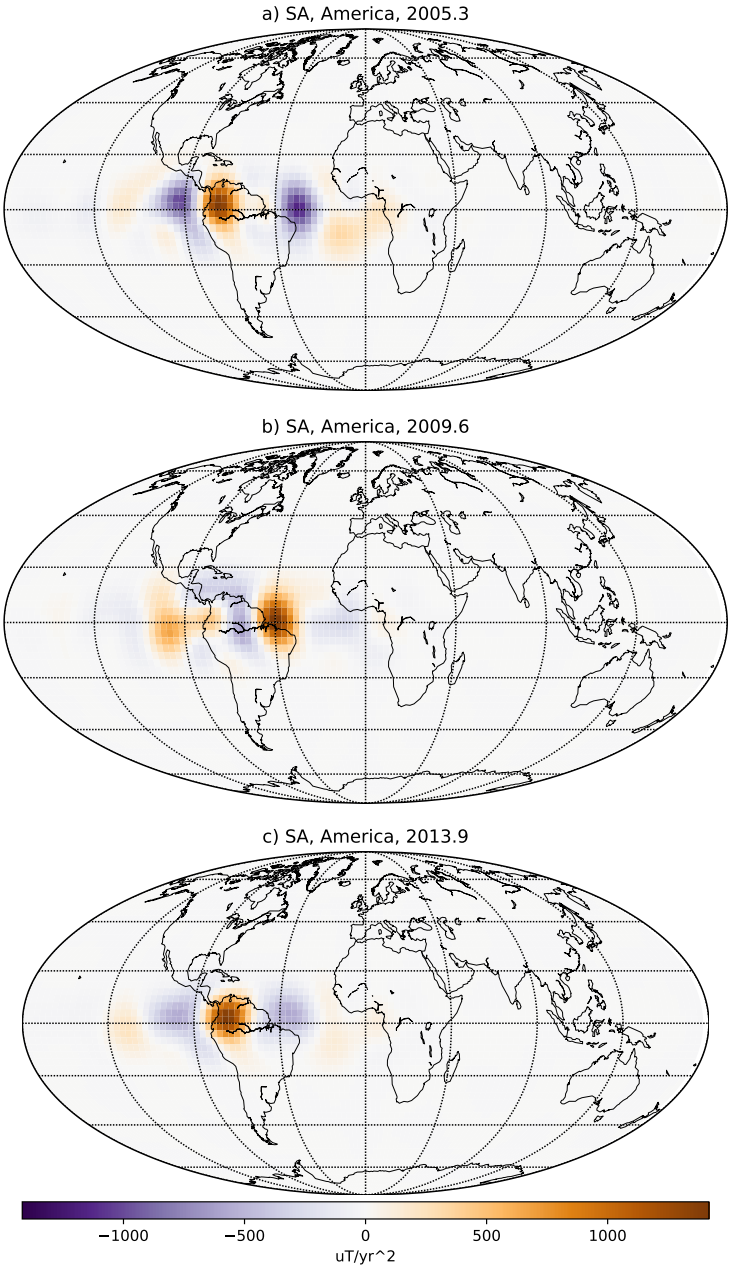

Figure 5.6: Secular Acceleration under America over time, selected using the weight function shown in 5.5. Note the orange and purple patches seem to oscillate in their locations, but that there is not as clear of a signal for traveling waves in either direction as under SE Asia.

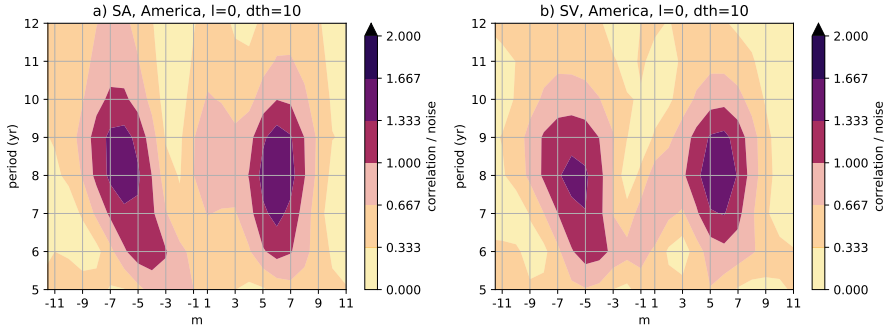

Figure 5.7: Symmetric (l=0) eMAC Wave correlation above noise for secular acceleration and secular variation, using data in the region of America and a symmetric weight function with $\delta_\theta = 8°$

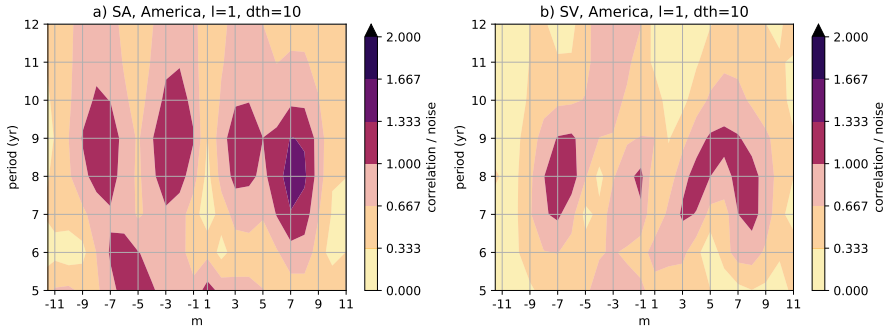

Figure 5.8: Asymmetric (l=1) eMAC Wave correlation above noise for secular acceleration and secular variation in the region of America, with data and a symmetric weight function with $\delta_\theta = 8°$

eastward-traveling waves						
l	m	period (yrs)	v_{max}	ϕ_0	$\Delta\phi$	δ_θ
0	-6	8	0.33	334°	22°	10°
1	-7	8	0.02	256°	16°	12°
westward-traveling waves						
l	m	period (yrs)	v_{max}	ϕ_0	$\Delta\phi$	δ_θ
0	6	8	0.47	318°	13°	12°
1	4	8	0.24	332°	18°	14°
1	7	8	0.43	240°	18°	10°

Table 5.2: eMAC waves observed in the America region of Earth's core.

5.3 South-East Asia

The second region in which we see strong oscillating SA patches is under the equatorial region of south-east Asia. We use a longitudinal window function centered on 45°E, with a width of $\delta_\phi = 55°$. This produces the window function shown in figure 5.9. Using this window function, we examine the SA signal in this region and see patches of SA drifting to the east, as shown in figure 5.10.

To examine whether these patches originate due to the presence of eMAC waves, we perform our correlation analysis on this region to obtain figures 5.11 and 5.12. We see strong correlation for single eastward-propagating symmetric wave in the SA and SV with (l=0, m=-6). There is also a weak correlation for a wave with (l=0, m=-11). For the asymmetric waves, we see correlations for wave propagating to the east and west, with (l=1, m=-4) and (l=1, m=4) appearing to have the strongest correlations overlapping between SA and SV.

We find the peak phase for each of these waves, and find that the (l=0, m=-11) wave does not have a consistent phase between SA and SV, indicating it is probably a spurious correlation. Indeed, when we compute the amplitudes, we find that the best fit gives a negligible amplitude to this wave. However, the other waves observed have both consistent phases between SA and SV and significant amplitudes. Indeed, the eastward propagating modes have a significantly stronger amplitude than the westward propagating mode,

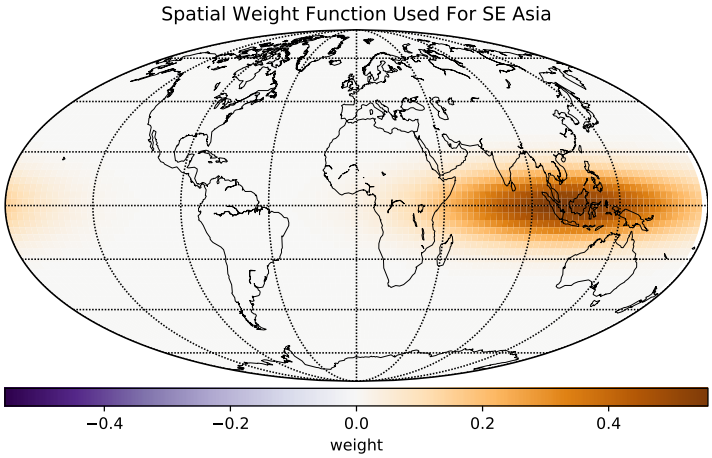

Figure 5.9: Spatial weight function used to examine wave signals under south-east Asia. $\delta_\theta = 10°$, $\delta_\phi = 55°$, centered at 45 degrees longitude.

which indicates that a large portion of the signal observed in the SE Asian region can be explained by two eMAC waves modes alone with (l=0, m=-5) and (l=1, m=-4).

5.3.1 Synthetic eMAC SA

As a rationality check on our analysis, we compute the SA produced by the (l=0, m=-5) and (l=1, m=-4) waves listed in table 5.3 for comparison to the observed SA in the S.E. Asian equatorial region. First, we show the signals produced by these two eMAC waves advecting the observed CMB field for three snapshots in time in figures 5.13 and 5.14. Although these waves have opposite equatorial symmetry, they produce both equatorially symmetric and asymmetric signals due to their interaction with the background CMB magnetic field gradients.

We then compare the SA produced using both of these waves simultaneously to the observed SA for three snapshots in time in figure 5.15. Many similar features can be observed in these comparisons, such as the location and shape of negative and positive patches of SA and their motion across time. However, there are still many differences, and the results do not match

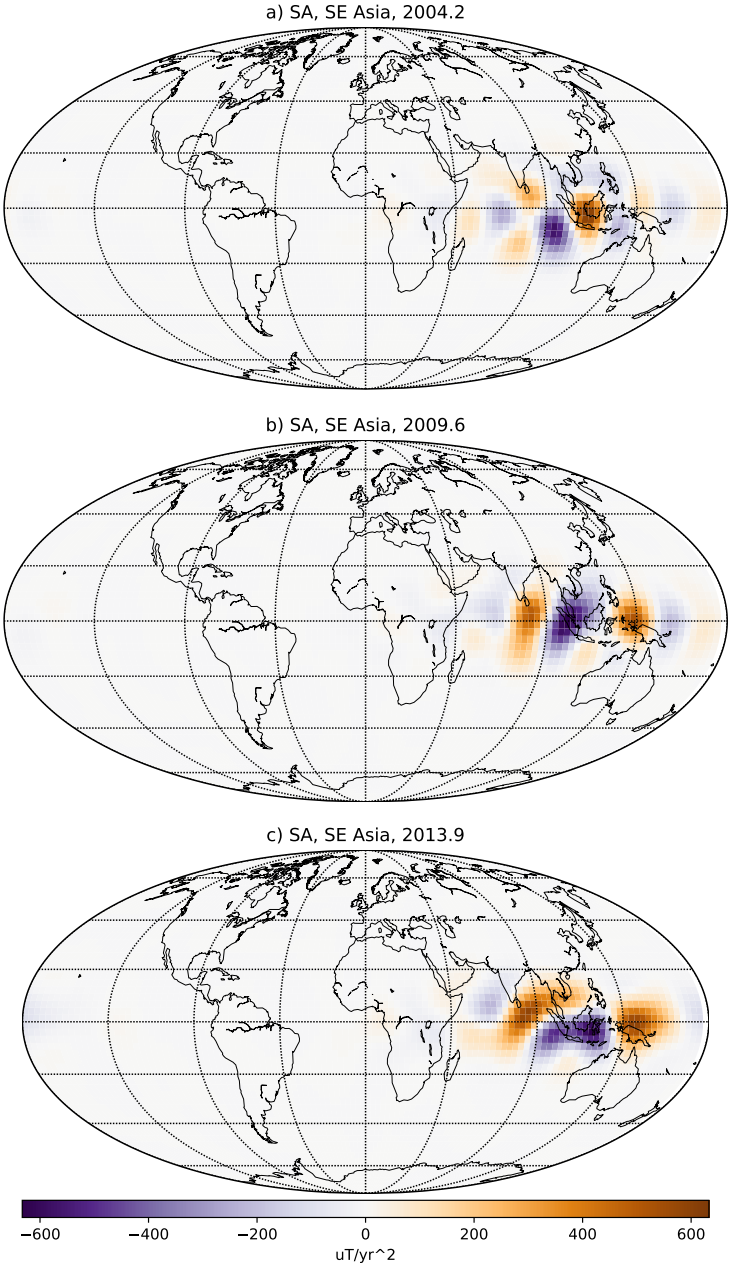

Figure 5.10: Secular Acceleration under SE Asia over time, selected using the weight function shown in 5.9. Note the orange patch that seems to travel to the East over the roughly ten years spanned by these figures.

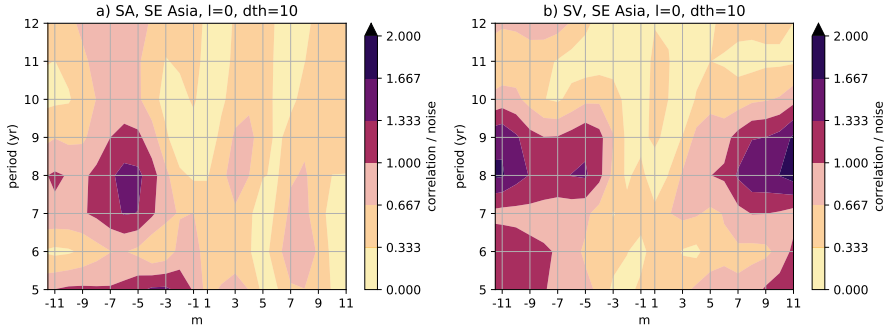

Figure 5.11: Symmetric (l=0) eMAC Wave correlation above noise for secular acceleration and secular variation, only data under south-east Asia and a symmetric weight function with $\delta_\theta = 10°$

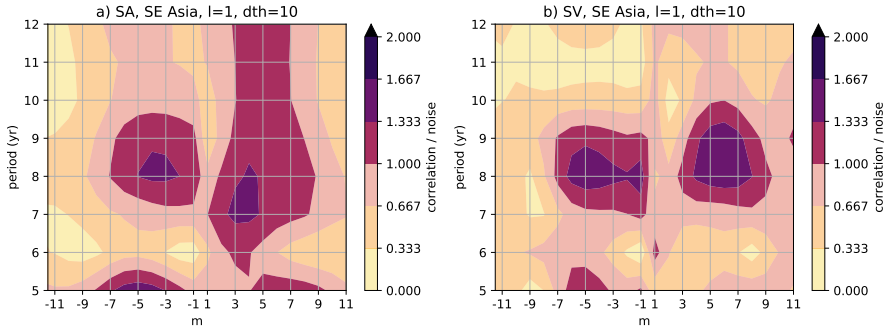

Figure 5.12: Asymmetric (l=1) eMAC Wave correlation above noise for secular acceleration and secular variation, only data under south-east Asia and a symmetric weight function with $\delta_\theta = 10°$

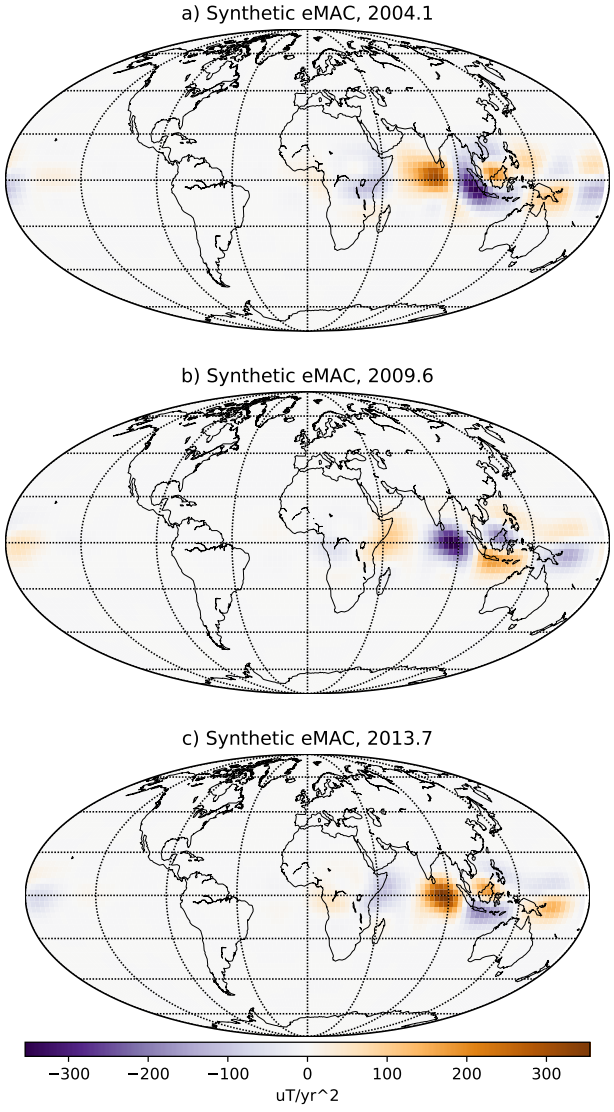

Figure 5.13: Synthetic SA produced by l=0, m=-5 eMAC wave with parameters listed in table 5.3.

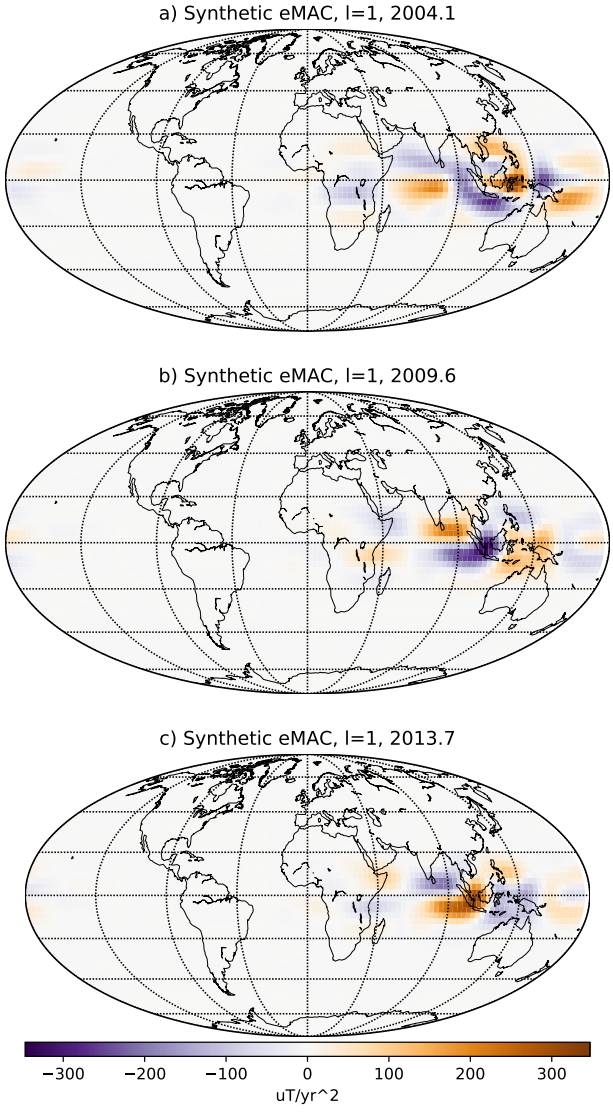

Figure 5.14: Synthetic SA produced by l=1, m=-4 eMAC wave with parameters listed in table 5.3.

eastward-traveling waves						
l	m	period (yrs)	v_{max}	ϕ_0	$\Delta\phi$	δ_θ
0	-5	8	0.85	21°	11°	14°
0	-11	8	0.02	212°	64°	12°
1	-4	8	0.44	198°	14°	12°
westward-traveling waves						
l	m	period (yrs)	v_{max}	ϕ_0	$\Delta\phi$	δ_θ
1	4	8	0.33	349°	11°	10°

Table 5.3: eMAC waves observed in the south-east Asia region of Earth's core.

perfectly. This could be due to many factors, including additional eMAC waves present in the core but not in our analysis; errors introduced by our imperfect observations of the background magnetic fields at the core; or inaccuracies in the derived structure of our eMAC waves.

Note that we have used larger peak flow velocities of 1.5 km/yr for (l=0, m=-5) and 1 km/yr for (l=1, m=-4) to produce this comparison in order to match the amplitude of observed SA. Because our method for fitting the wave amplitude uses the absolute RMS difference between SA produced by the waves and the observed SA, any difference in spatial structure of our simulated waves compared to the observed SA will penalize the best-fit amplitude of the wave modes. This makes it likely that this method of fitting amplitude will under-estimate rather than over-estimate the true value. Thus, these increased peak flow velocities used to plot have been chosen to approximately fit the the RMS power of the observed SA while maintaining the relative amplitudes of the two eMAC wave modes.

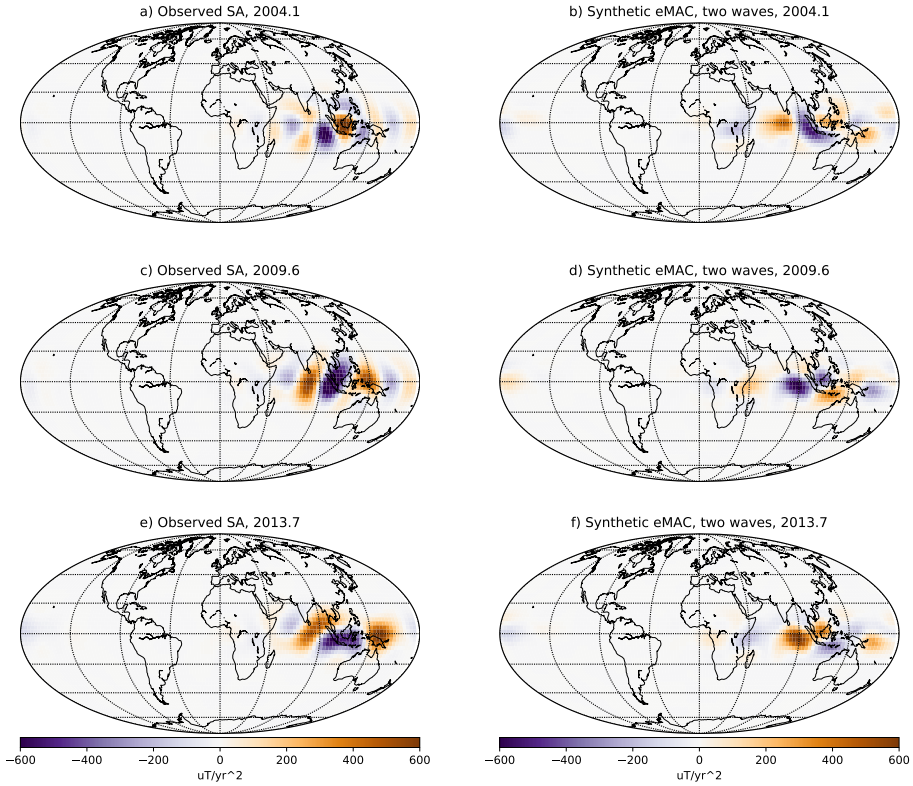

Figure 5.15: Synthetic SA produced by both l=0, m=-5 and l=1, m=-4 eMAC waves. Parameters used are those listed in table 5.3, except for wave amplitudes, which have been increased to 1.5 km/yr for l=0, m=-5 and 1 km/yr for l=1, m=-4 to roughly match the magnitude of observed SA.

Chapter 6

Discussion

In previous chapters, we derived a numerical model to study magnetic waves in the stratified ocean of Earth's core and described a class of waves that propagate to the east in the equatorial region on decadal timescales, which we term eMAC waves. We then derived and validated a method for observing these waves and were able to find evidence for three eMAC waves in Earth's core, whose properties are listed in table 6.1. The observed period and structure of these waves can therefore now be used to constrain the properties of the SOC, as well as the structure of the radial magnetic field at the CMB.

l	m	period (yrs)	v_{max} (km/yr)	ϕ_0	$\Delta\phi$	δ_θ
South-East Asia						
0	-5	8	0.84 - 1.5	21°	11°	14°
1	-4	8	0.44 - 1	198°	14°	12°
America						
0	-6	8	0.33	334°	22°	10°

Table 6.1: eMAC waves observed in Earth's core.

6.1 Comparison to Previous Results

Our observation of equatorial waves with periods of around eight years are similar to the results obtained by Chulliat et al. (2015). Both studies find evidence for wave modes both symmetric and asymmetric across the equator, and that observations support several waves propagating with periods between five and ten years. In addition, both studies find several modes propagating to the east with longitudinal wave numbers between m=-3 and -6. Finally, both studies also find evidence in geomagnetic signals for equatorial wave modes propagating to the west with wave numbers between m=3 and 7.

However, there are notable differences between the results obtained by Chulliat et al. (2015) and the results of this study. First, the longitudinal wave numbers of observed waves obtained between the two studies do not match precisely. In particular, Chulliat finds a single strong asymmetric wave mode propagating to the west with a longitudinal wavenumber of m=2. On the other hand, we find no evidence of waves with a longitudinal wavenumber $|m| < 3$ of any mode. However, Chulliat et al. (2015) admits that precise values for longitudinal wave numbers are not well-defined.

In addition, Chulliat's observations are performed using period-wavenumber transformations which do not take into account the coupling of wave structures and the background magnetic field, so differences in our results should be expected. As noted in chapter 4, eMAC wave motions couple with the complex background magnetic field at the CMB equator and produce complicated signals. These signals can easily be interpreted as evidence for waves with incorrect wavenumbers, propagation speeds, or even directions of propagation when examined using time-longitude or FFT-methods such as those employed by Chulliat et al. (2015). On the other hand, our method accounts for these complications, so differences in results obtained may be expected.

We also find that our magnetic equatorial waves have different behaviors than derived by previous authors. Our eMAC wave periods do not display the same dependence on layer thickness, magnetic field strength, or buoyancy frequency as the solutions obtained by Bergman (1993). In addition, his solutions propagate to the west, while we are only able to find equatorial waves that propagate to the east after an extensive numerical search of plausible SOC structures and background magnetic fields. These differences are significant, and may arise due to simplifications Bergman uses in the derivations of those results which raise questions about their applicability to the

SOC (see section 1.4.2).

However, our unsuccessful attempt to find solutions for westward propagating equatorial waves is surprising for other reasons. First, westward propagating equatorial modes are well-studied and widely observed in non-magnetic thin-layer fluids (e.g. Gill, 1982). By analogy we may then also expect to find westward-propagating magnetohydrodynamic waves. Second, both visual inspection of time-longitude plots of the equatorial region (e.g. Chulliat and Maus, 2014, figs. 3,4), and our correlation results (see chapter 5) seem to show indications of westward propagating waves. These apparent westward-propagating signals are unexplained by the eMAC waves described in this thesis, and deserve further study as discussed in section 6.4.1.

6.2 Implications

6.2.1 Stratified Layer

The eMAC waves detected all have wave periods between seven and ten years. A SOC layer with thickness of ∼20 km can produce waves with these periods for the observed m=-4,-5,-6 modes. However, SOC thickness is impossible to precisely constrain due to possible presence of higher radial overtones of eMAC waves. We can only observe the period and flow of eMAC waves at the surface of the core, and a thicker SOC could support eMAC waves with a higher radial wavenumber (k) that produce precisely the same spatial wave structure at the CMB with the same wave period. We show in section 3.2.4 that

$$\omega \propto k^2$$

so that an eMAC wave with k=1 in a 20 km layer, k=2 in 40 km layer, and k=3 in 60 km layer would all produce similar CMB flow patterns and periods.

With this caveat in mind, a ∼20 km thick SOC with strong stratification is still the most likely explanation for our observations for a variety of reasons. First, the lowest radial overtone eMAC wave has the simplest structure, and so in one sense, it is the simplest wave to explain the observations. In addition, the Brunt-Väisälä frequency is likely to vary with radius in Earth's SOC. This variation is more likely to negatively affect the propagation of waves with high radial wavenumbers, as their relatively shorter radial wavelengths would interact with different local buoyancies and possibly cause the features to decohere (see e.g. figure 3.21). Waves with simpler

radial structures may be relatively less affected by radial variations in buoyancy and continue to propagate coherently, as their large-scale motions could more easily overcome small-scale differences in buoyancy. Thus, the simplest explanation is that the signals observed arise from eMAC waves with fundamental radial overtones, and therefore that the SOC supporting these wave motions has a thickness ∼20 km.

The SOC must also have relatively strong stratification for these eMAC waves to propagate. eMAC waves with the periods and structures observed fail to propagate below a threshold value of N ∼10, as shown in section 3.2.2. Thus, the SOC supporting these waves must have at least this strength of buoyancy. However, the buoyancy could be considerably stronger than this value (e.g. Buffett and Seagle, 2010), as eMAC waves are insensitive to the precise strength of buoyancy above this threshold value.

Thus, we propose a relatively thin SOC, with a thickness of 20-40 km and a buoyancy frequency of N$\geq$ 10Ω as our preferred layer to explain the observed eMAC waves. This result is consistent with some seismic observations which propose a thin, strongly-stratified layer near the CMB (Eaton and Kendall, 2006). In addition, this strength of buoyancy can plausibly arise from compositional stratification, perhaps due to chemical interactions with the mantle (Buffett and Seagle, 2010).

On the other hand, this thin, strongly stratified SOC is at odds with the results of many other studies. Many seismic studies detect a much larger region with anomalous seismic wave speeds, near $\sim$ 200 km thick (see 1.2.1), which are proposed to arise due to a SOC of similar thickness. In addition, Buffett (2014) detects signals of zonal MAC waves that require the SOC to be ∼140 km thick with a relatively weak buoyancy frequency of N ∼1 Ω.

One possible resolution to these contradictory results would be a thin, strongly-stratified layer embedded within a thicker weakly-stratified layer. A representation of this situation can be seen in figure 6.1, showing a 20 km thick layer with N=10Ω, as well as a 140 km thick layer with a linearly-varying N from 0 to 1 Ω as proposed by Buffett (2014).

A thin, strongly-stratified layer could plausibly arise within a thicker weakly-stratified layer by several mechanisms. First, a thick stratified layer with H $\sim$ 140 km and N $\sim$ 0 to 2 Ω could arise through thermal origins (see section 1.1.2.1). Then, an additional layer of enhanced compositional stratification could arise near the CMB through a local enrichment of light elements. This local enrichment could occur due to chemical interactions with the mantle or through barodiffusion. The effectiveness of both of these pro-

cesses to produce thin, strongly buoyant layers may even be enhanced by the overlying stratified layer. This is because the overlying stratification would suppress radial fluid motions and prevent turbulent mixing due to convection. Thus, these processes would tend to produce a region of concentrated buoyancy near the CMB.

Previous studies have shown that barodiffusion could produce a SOC with $N \sim 20\,\Omega$ (Gubbins and Davies, 2013). However, this stratification occurs in a SOC $\sim$ 100 km thick, which is much larger than the 20-30 km SOC required for eMAC waves to propagate. The particular light elements or presence of an overlying stratified layer may impact the formation of stratification by barodiffusion, potentially allowing it to produce strong stratification in a thin layer as required for eMAC waves. On the other hand, chemical interactions with the mantle have been shown to be able to produce both the strength of stratification (Buffett and Seagle, 2010) and the thickness (e.g. Helffrich and Kaneshima, 2013, fig. 3) required to support the observed eMAC waves. Thus, either of these processes could potentially give rise to a double-layer SOC structure that could simultaneously explain both the eMAC waves and many other observed signals.

One question that naturally arises is how the addition of a thin, strongly-stratified layer affects the propagation and visibility of zonal MAC waves in the thick, weakly-stratified layer. Numerical experiments using the FVF model described in chapter 2 with the layer structure shown in figure 6.1 show that zonal MAC waves in the thick stratified layer easily propagate through the overlying thin layer with only minor suppression of the latitudinal flows. Therefore, the conclusions of Buffett (2014) remain largely the same, even with the addition of a overlying thin, strongly-stratified layer.

This proposed layer structure can also potentially explain contradictory seismic results from multiple authors. Several authors show seismic results that indicate a thick layer near the CMB with slow seismic wave-speeds (e.g. Garnero et al., 1993; Helffrich and Kaneshima, 2010; Lay and Young, 1990; Tanaka, 2007). However, Eaton and Kendall (2006) detect a thin $\sim$12 km thick region near the CMB with fast seismic wave-speeds. These results could potentially be reconciled by our proposed two-layer SOC. The thick layer could arise due to thermal buoyancy and/or light element enrichment and create a roughly 100-200 km thick region with weak stratification and anomalously slow seismic wave-speeds (e.g. Helffrich, 2012). Then, a thin region near the CMB roughly 20-30 km thick with strong stratification could arise through a separate mechanism, perhaps from chemical interactions with

the mantle. Because it has a distinct origin, it is plausible to expect the composition of this thin region to be distinct from the overlying thick layer, potentially creating a region with fast seismic wave-speeds (e.g. Buffett and Seagle, 2010).

The layered SOC might be expected to require unrealistic density deficits due to the combination of a thick, weakly buoyant layer in addition to a thin, strongly buoyant layer near the CMB. However, figure 6.1b shows that the required buoyancy profile can be produced from an SOC with a total density deficit of only 0.1% under the adiabatic density profile of the core. This value is well within those proposed by many previous authors (e.g. Lister and Buffett, 1998), and is likely consistent with observations of core flows from geomagnetic evidence (see section 1.2.2).

6.2.2 CMB Magnetic Field

We are also able to use the properties of observed eMAC waves to draw conclusions about the CMB magnetic field. First, the total RMS strength of the radial magnetic field near the core has a large influence on both the period and quality factor of eMAC waves, as shown in section 3.2.3. In general, stronger fields are associated with shorter wave periods and higher quality factors, varying according to

$$\omega \propto B^2$$

and

$$Q \propto B^2 \,.$$

We find that a RMS radial magnetic field near 0.6 mT is sufficient to explain eMAC wave periods observed. However, we note that with this field strength, these waves are fairly heavily damped, and thus would require a strong and consistent excitation mechanism. Stronger RMS radial magnetic fields alleviate this problem by causing these waves to propagate with higher quality factors. However, the total RMS radial field near the CMB is likely $<$1 mT based on evidence from numerical geodynamo simulations (Christensen, 2011), observations of the geomagnetic field (Finlay et al., 2016), and observed periods of torsional oscillations (Gillet et al., 2010). Thus, a slightly higher field strength may be preferred to allow these waves to propagate, but plausible field strengths could only increase the quality factor of these waves

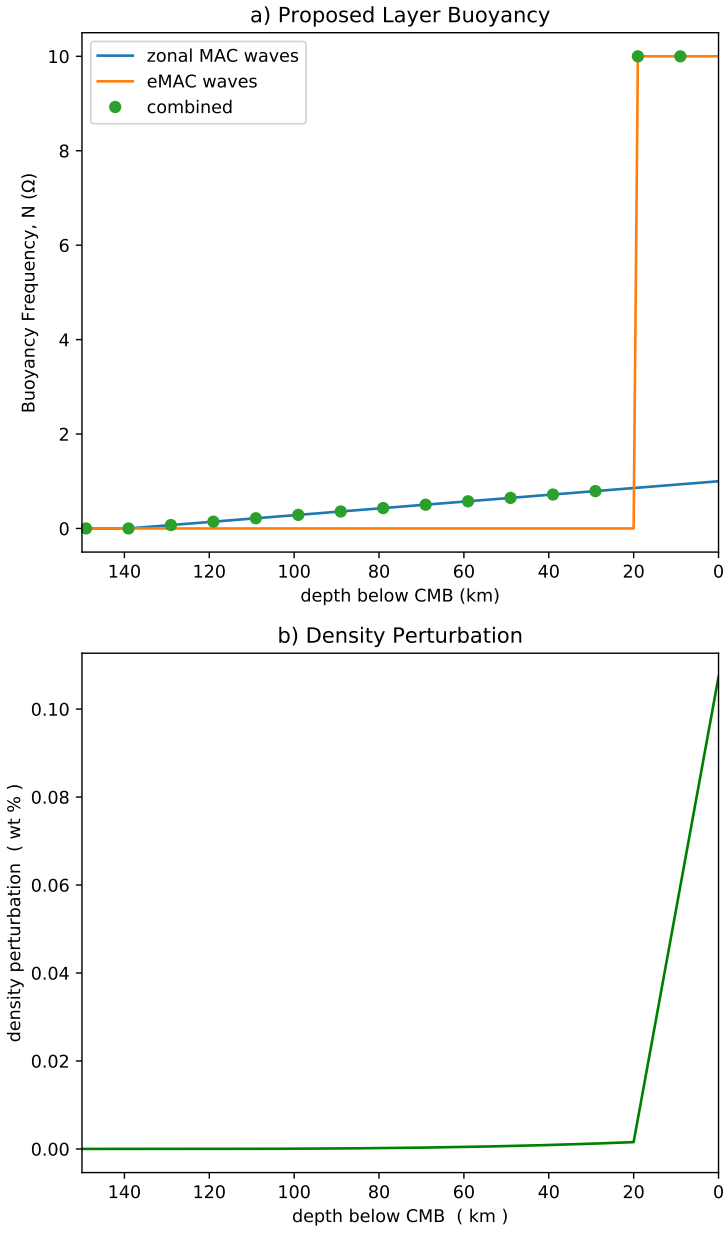

Figure 6.1: Proposed double-layered SOC, showing buoyancy frequency (a) and density perturbation off of the adiabatic density gradient (b). This plot shows a thin, 20 km thick, N = 10 Ω layer which would allow eMAC waves to propagate with values observed in this study. It also shows a thick, thermally stratified layer 140 km thick with N varying from 0 to 1 Ω as proposed by Buffett (2014) to explain zonal MAC wave observations.

by a factor of ∼2 (see chapter 3). This issue is discussed further in section 6.3.

We can also obtain information about distribution of radial magnetic field at the CMB by latitude as the field structure impacts the eMAC wave structure (see sections 3.3.1.2 and 4.4.1). The observed eMAC waves have a δ_θ somewhere between 10° and 15 °. Waves of this width require a depression in the strength of the radial magnetic field near the equator to narrowly constrain their flow structure, as detailed in section 3.3.1. The observed radial magnetic field near the equator has a RMS value ∼0.3 mT. Higher-order spatial structures can only increase the RMS field value, so this represents the minimum possible RMS value. Thus, we propose a RMS B_r of 0.3 mT at the equator and a RMS $B_r \sim 0.6$ mT just off the equator to produce eMAC waves with the observed latitudinal width, periods, and quality factors. This additional unobserved radial field strength could be explained by small-scale field structures which are prominent in many of the latest geodynamo simulations (e.g. Schaeffer et al., 2017).

We compare three proposed B_r magnetic field distributions to the observed RMS B_r at the CMB in figure 6.2. These field structures are generated by subtracting a zeroth-order Hermite polynomial from a constant radial field. This representation is chosen to achieve smooth variation near the equator so as not to introduce sharp artifacts into the structure of eMAC waves obtained with the FVF model. These structures produce eMAC waves with latitudinal widths similar to the δ_θ the describes the width of the equatorial depression in the radial field. Our results in chapter 5 imply that the observed eMAC waves have a δ_θ between 10° and 15° which correspond to the orange and green distribution in figure 6.2. However, note that it is impossible to rule out narrower eMAC waves and thus magnetic field structures due to the limitations of our geomagnetic observations. Observations of the core field are limited to a spherical harmonic degree of l∼14, so signals from very narrow eMAC waves would produce signals that appear to have a wider latitudinal width closer to $\delta_\theta = 10°$ due limitations of the resolution of our observations. Note also that the representative field structures shown in figure 6.2 are only relevant near the equator, as eMAC waves only give information in this region. Thus, the RMS B_r at high latitudes is entirely unconstrained by this study.

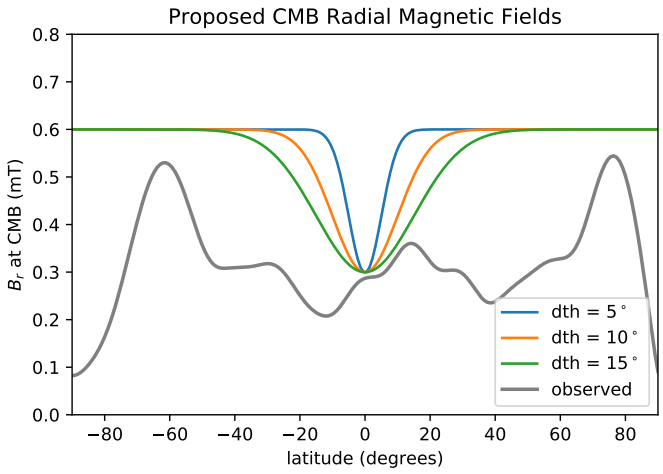

Figure 6.2: Proposed distribution of total B_r RMS at the CMB, including small-scale unobserved field strength.

6.3 Quality Factor

One major argument against eMAC waves as the origin of the observed equatorial SA signals is their relatively low quality factors. For example, the fundamental symmetric eMAC mode with m=6 has a quality factor <1 for many of the layer structures examined in chapter 3. Such a low quality factor would mean that these eMAC waves would decay within around five years and only propagate across ∼40 degrees of longitude (see figure 5.4). Indeed, with Q<1, it is perhaps more accurate to refer to these as "decaying fluid oscillations" rather than "waves". With this low quality factor, some process must continually excite these waves to be consistently observed across the >10 year time period of the CHAOS-6 geomagnetic field model. This excitation could arise from flow over CMB topography, similarly to non-magnetic Rossby waves in the ocean (e.g. Rhines and Bretherton, 1973). Alternatively, these waves could be continuously excited by stochastic motions of convection in the bulk outer core, a similar mechanism to that proposed by Buffett and Knezek (2018) to generate MAC waves.

On the other hand, the low quality factor of eMAC waves may fit with our observations of eMAC waves in geographically limited regions. If the quality factor of eMAC waves were very high they would likely propagate around the

entire globe, reinforcing themselves and producing high correlations in the global eMAC analysis performed in section 5.1. Because we observe different eMAC waves in the regions of America and South East Asia, it is plausible that eMAC waves do not propagate between these regions. The separation of these two regions constrains the quality factors of the observed eMAC waves to around Q<10, and Q∼2 is sufficient for eMAC waves to propagate across the American and SE Asia regions studied.

Although the fundamental eMAC modes obtained in our model have Q<2, there are many plausible mechanisms by which eMAC waves could propagate with Q≥2. First, many eMAC waves with higher latitudinal-degree have quality factors between 2 to 4 (see figure 3.11), so observed signals could arise due to wave modes with l>1. In addition, the quality factor for the fundamental mode l=0 can easily be increased by slightly changing the parameters used to simulate the eMAC waves. For example, increasing the radial CMB magnetic field strength in the model to 0.9 mT produces Q∼2 for l=0. In addition, decreasing the magnetic diffusivity from 0.8 m^2/s to 0.4 m^2/s also improves the quality to Q∼2 for l=0. A combination of smaller changes to each of these parameters could likewise increase the quality factor of all eMAC modes enough to explain the observations.

The construction of our model could also bias the quality factors to be lower than in reality. Waves derived with electromagnetic boundary coupling to the bulk core fluid are much more heavily damped than those derived with pseudo-vacuum boundary conditions. This is because we constrain the fluid beneath the SOC to be stationary and only allow the magnetic perturbation to propagate into the bulk core. While this simplification is necessary for numerical tractability, in reality some of the fluid motion would also propagate into the fluid below the layer, resulting in non-zero fluid motions beneath the boundary and possibly allowing the eMAC waves to propagate more freely and with higher quality factors. Indeed, even using pseudo-vacuum boundary conditions at the bottom boundary may underestimate the quality factor of the derived eMAC waves, as this constrains the magnetic perturbation at the bottom boundary and therefore increases the radial gradients of the wave. This increases the magnetic diffusion and therefore potentially increases the damping of the eMAC waves. With these considerations, it is at least plausible that eMAC waves could propagate with the required quality factors to fit observations.

6.4 Future Work

The results presented in this thesis present an enormous amount of additional information pertinent to studies of the SOC. However, this work represents just a minute portion of the possible work to be done on this topic.

6.4.1 Westward-Propagating Equatorial Waves

Perhaps the largest question left unanswered by this thesis is the origin of the apparent westward-propagating signals observed in the equatorial region of Earth's geomagnetic field. Results of previous work (Chulliat et al., 2015) and this thesis (chapter 5) seem to indicate the presence of westward-propagating equatorial waves with sub-decadal periods in Earth's core. It is possible that these observations could arise due to multiple eMAC waves advecting the complex background magnetic field. However, our correlation analysis seems to provide strong evidence against this explanation and instead indicate that these signals arise due to westward-propagating waves of some form.

We were unable to obtain solutions for westward-propagating equatorial waves with the observed properties after an extensive numerical search with plausible SOC parameters. However, we did find solutions for westward-propagating waves with appropriate periods at mid- to high-latitudes (e.g. figure 3.22). It is possible that more complicated layer buoyancy structures (e.g. figure 3.21), or influence from the unobserved CMB magnetic field structure could cause these westward modes to produce signal near the equator by modifying their propagation structure or by causing them to couple with other modes near the equator. However, this possibility has not been explored in-depth. It is also possible that these signals could also arise by coupling westward-propagating waves in the bulk outer core to flows in the SOC (e.g. Hori et al., 2015; Takehiro and Sasaki, 2018; Vidal and Schaeffer, 2015). However, known wave modes in the bulk outer core are unlikely to produce the observed wave periods or structures (see section 1.2.3). Both of these possible explanations deserve further study, especially as many of our analyses show stronger evidence for westward-propagating modes than their eastward-propagating counterparts derived by our FVF model.

6.4.2 Further Wave Modes

Other wave modes beyond eMAC waves are observed propagating in the SOC using our FVF model. These include both very short-period equatorial waves and long-period mid-latitude waves that propagate to the west (see section 3.4). The long-period mid-latitude waves are of particular interest, as they have relatively high quality factors and have long enough wave periods that they may be visible in geomagnetic observations. Not only would detection of these waves provide additional confirmation of the existence of the SOC, their periods are also more sensitive to layer stratification and so could provide a tighter constraint on the layer structure.

Further work is needed to know whether these mid-latitude waves are observable. Initial studies indicate that they have much shorter wave periods of about 1 year for the layer structures proposed for eMAC waves (see appendix D), which would likely mean they are unobservable with current technology. However, these waves have periods on the order of a decade when propagating in an SOC with H $\sim$ 140 km, N $\sim$ 1 Ω as proposed for zonal MAC waves. Therefore, if our double-layer SOC proposal is correct, it may be possible to observe these waves propagating in the thick underlying layer. In addition, as noted above, these waves are key candidates regarding the origin of observed westward-propagating equatorial signals.

Indeed, our investigations indicate that there may be a host of other wave modes that propagate in the SOC. However, the many of these wave modes would have periods that are either too short or too long to be detected with current observations. Current geomagnetic observations can potentially resolve small-scale (m$\sim$6) with a minimum period of perhaps two years, and this is unlikely to improve much due to physical limitations on observations (see section 1.5.1 and 1.5). However, as satellite missions continue to collect data over time, it will allow us to resolve waves with increasingly long periods. Thus, within the next few decades, it may be possible to observe many different classes of wave modes in the SOC with periods from years to several decades, precisely constraining its structure and properties.

6.4.3 Layer Structure and Buoyancy

There is also much work to be done to examine the effect of radially-varying layer buoyancy on the structure of eMAC waves. We show in section 3.3.2 that eMAC modes can propagate with radial variations in layer buoyancy,

but that radial variation introduces complex wave modes that are not easily classified or categorized. These complex modes seem to represent a coupling of many different types of eMAC waves, perhaps due to local interactions with varying buoyancy. However, they also seem to vary with latitude, perhaps due to the spherical geometry of the layer. The behavior or eMAC waves in SOCs with varying buoyancy is an important area of study, as the buoyancy in Earth's SOC is very likely to vary with radius (see section 1.1.3).

In addition, further work is needed to explore the dynamics of a two-layer SOC composed of a thin, strongly buoyant layer atop a thick, weakly-buoyant layer. Preliminary studies show that MAC waves propagating in the thick underlying layer are only slightly modified by the addition of a thin stratified layer near the CMB. However, our FVF was unable to resolve eMAC waves propagating in the thin overlying layer when computing waves in a two-layer SOC. This may be due to the eigenvalue solver used, which prioritizes wave solutions with the largest amplitudes. Regions with weaker stratification naturally allow stronger radial wave motions, so the amplitude of the wave vector in our numerical model is larger. Thus, our solver preferentially finds wave modes with the majority of their motion in the more weakly-buoyant region. Further investigation is needed to resolve both MAC and eMAC waves in a layer with two stratification regimes to verify that both wave modes can coexist in a single SOC.

6.4.4 Excitation Mechanisms

This study has shown the existence of eMAC waves in Earth's core, but leaves open the question of their excitation mechanism. There are several possible mechanisms through which these waves could be excited. First, the convective fluid motions in the bulk core fluid could excite eMAC waves in the stratified layer through buoyancy, Lorentz, or magnetic induction forces (Buffett and Knezek, 2018; Jaupart and Buffett, 2017). However, the addition of an overlying stratified layer complicates this mechanism for eMAC waves in a double-layered SOC. Further study is needed to investigate whether these excitation mechanisms could excite eMAC waves despite the thick, weakly-buoyant layer shielding it from direct interactions with the bulk convecting core.

On the other hand, it has been shown that some fluid motions in the bulk core such as torsional oscillations (TO) can relatively easily propagate through the SOC (see section 1.1.1.1). Torsional oscillations have been pro-

posed in the bulk outer core with sub-decadal periods (Gillet et al., 2010), so it is worth investigating whether they could serve to excite eMAC waves. On the other hand, TO are zonal (m=0), so they would need some way to transfer energy into m∼6 fluid motions to excite the observed eMAC waves. This could occur to to heterogeneous radial magnetic field strength with an m=6 pattern, as this would couple only portions of the TO flow in the bulk core to the SOC fluid. However, the mechanism by which this field structure would arise, or its ability to and effectiveness to excite eMAC waves has not been examined.

Another possibility is that, fluid flows from TO or other sources could interact with the mantle to excite eMAC waves. Topography or conductivity heterogeneity at the base of the mantle could induce eMAC waves in a similar manner to how topographic Rossby waves in Earth's oceans are excited by structures on the ocean-bottom (e.g. Rhines and Bretherton, 1973). If this mechanism operates in Earth's core, detailed study of eMAC waves could give information on the scale and location of mantle topography or conductivity at the CMB. This is a topic of great interest to mantle dynamics, seismology, and mantle geochemistry, and eMAC waves could represent an entirely new source of data for its study.

6.4.5 Numerical Model Improvements

The FVF model obtains MAC waves and eMAC waves efficiently and with a high degree of flexibility and accuracy. However, the model could be improved in many ways. First, there may be a better method of parameterizing the boundary between the bottom of the stratified layer and the bulk core fluid. The current electromagnetic coupling and pseudo-vacuum boundary conditions are both known to be inaccurate representations of the real system and improved boundary conditions would potentially allow for greater confidence in the results of the model. A more accurate boundary condition might allow both the magnetic field perturbation and fluid momentum to propagate downward into the core, instead of prescribing the bulk core fluid to be stationary. However, an analytical solution for this boundary condition has not be derived, and allowing both momentum and magnetic field perturbations may produce propagating fluid motions that would require simulation of the entire bulk outer core.

Another important improvement would be to allow for variation of the CMB magnetic field with longitude. We know that the CMB magnetic field

includes substantial variation in both longitude and latitude. These variations would impact both the local visibility of eMAC waves due to fluid motions advecting the field, as well as their local propagation due to the field acting as a restoring force. However, our current FVF model only allows background fields and layer structures which are constant around the rotation axis. Allowing variation with longitude would greatly complicate the model and analysis, as it would allow for mixing of eMAC modes of different longitudinal wavenumbers and may require a simulation of the full 3D domain.

Finally, toroidal oscillations are another class of waves of geophysical interest that we could study by extending the FVF model (Cox, 2015; Cox et al., 2014). This could be done by simply adding a set of cells representing axis-aligned cylinders that connect to the bottom of the layer in our FVF model. These cylinders could then allow 2D toroidal oscillations to propagate within the core, and their interaction with and visibility through a stratified layer at the CMB could be studied.

6.5 Final Thoughts

This thesis has advanced the knowledge of equatorial magnetic waves in the stratified ocean of Earth's core (SOC). In particular, it has described a class of equatorial MAC waves (eMAC) waves that propagate to the east and has shown that they could explain many signals observed in Earth's geomagnetic field. These observed eMAC waves give information on the thickness and buoyancy of the SOC as well as the strength and structure of the radial CMB magnetic field. Finally, this study points the way towards several avenues of investigation that could be used to further study the dynamics and structure of the SOC and Earth's magnetic field.

Bibliography

Alexandrakis, C. and Eaton, D. W. (2010). Precise seismic-wave velocity atop Earth's core: No evidence for outer-core stratification. *Physics of the Earth and Planetary Interiors*, 180(1-2):59–65.

Alfvén, H. (1943). On the existence of electromagnetic-hydrodynamic waves. *Arkiv for matematik, astronomi och fysik*, 29:1–7.

Amit, H. (2014). Can downwelling at the top of the Earth's core be detected in the geomagnetic secular variation? *Physics of the Earth and Planetary Interiors*, 229:110–121.

Aris, R. (1962). *Vectors, Tensors and the Basic Equations of Fluid Mechanics*. Dover Books on Mathematics. Prentice Hall, London; printed in USA.

Arveson, S. M., Deng, J., Karki, B. B., and Lee, K. K. M. (2019). Evidence for Fe-Si-O liquid immiscibility at deep Earth pressures. *Proceedings of the National Academy of Sciences*, 116(21):10238–10243.

Asahara, Y., Frost, D. J., and Rubie, D. C. (2007). Partitioning of FeO between magnesiowüstite and liquid iron at high pressures and temperatures: Implications for the composition of the Earth's outer core. *Earth and Planetary Science Letters*, 257(3-4):435–449.

Aubert, J. and Finlay, C. C. (2019). Geomagnetic jerks and rapid hydromagnetic waves focusing at Earth's core surface. *Nature Geoscience*, 12(5):393–398.

Backus, G. and Bullard, E. C. (1968). Kinematics of geomagnetic secular variation in a perfectly conducting core. *Phil. Trans. R. Soc. Lond. A*, 263(1141):239–266.

Badro, J., Siebert, J., and Nimmo, F. (2016). An early geodynamo driven by exsolution of mantle components from Earth's core. *Nature*, 536(7616):1–3.

Baerenzung, J., Holschneider, M., and Lesur, V. (2016). The flow at the Earth's core-mantle boundary under weak prior constraints. *Journal of Geophysical Research: Solid Earth*, 121.

Barrois, O., Gillet, N., and Aubert, J. (2017). Contributions to the geomagnetic secular variation from a reanalysis of core surface dynamics. *Geophysical Journal International*, 211(1):50–68.

Bergman, M. I. (1993). Magnetic Rossby waves in a stably stratified layer near the surface of the Earth's outer core. *Geophysical and Astrophysical Fluid Dynamics*, 68(1-4):151–176.

Bloxham, J. (1990). On the consequences of strong stable stratification at the top of Earth's outer core. *Geophysical Research Letters*, 17(12):2081–2084.

Bloxham, J. (1992). The steady part of the secular variation of the Earth's magnetic field. *Journal of Geophysical Research: Solid Earth*, 97(B13):19565–19579.

Bloxham, J. and Jackson, A. (1990). Lateral temperature variations at the core-mantle boundary deduced from the magnetic field. *Geophysical Research Letters*, 17(11):1997–2000.

Bloxham, J. and Jackson, A. (1992). Time-dependent mapping of the magnetic field at the core-mantle boundary. *Journal of Geophysical Research: Solid Earth*, 97(B13):19537–19563.

Bloxham, J., Zatman, S., and Dumberry, M. (2002). The origin of geomagnetic jerks. *Nature*, 420(6911):65–68.

Braginskiy, S. (1970). Torsional magnetohydrodynamic vibrations in the Earth's core and variations in day length. *Geomagnetism and Aeronomy*, 10:1.

Braginsky, S. I. (1964). Magnetohydrodynamics of the Earth's core. *Geomag. Aeron.*, 4:698–712.

Braginsky, S. I. (1984). Short-period geomagnetic secular variation. *Geophysical & Astrophysical Fluid Dynamics*, 30(1-2):1–78.

Braginsky, S. I. (1993). MAC-Oscillations of the Hidden Ocean of the Core. *Journal of geomagnetism and geoelectricity*, 45(11-12):1517–1538.

Braginsky, S. I. (1998). Magnetic Rossby waves in the stratified ocean of the core, and topographic core-mantle coupling. *Earth, Planets and Space*, 50(8):641–649.

Braginsky, S. I. (1999). Dynamics of the stably stratified ocean at the top of the core. *Physics of the Earth and Planetary Interiors*, 111(1):21–34.

Braginsky, S. I. (2000). Effect of the stratified ocean of the core upon the Chandler wobble. *Physics of the Earth and Planetary Interiors*, 118(3):195–203.

Braginsky, S. I. (2006). Formation of the stratified ocean of the core. *Earth and Planetary Science Letters*, 243(3):650–656.

Braginsky, S. I. (2007). Formation of the stratified ocean of the core: A ternary alloy model. *Earth and Planetary Science Letters*, 253(3):507–512.

Brandon, A. D. and Walker, R. J. (2005). The debate over core-mantle interaction. *Earth and Planetary Science Letters*, 232(3-4):211–225.

Buffett, B. (2014). Geomagnetic fluctuations reveal stable stratification at the top of the Earth's core. *Nature*, 507(7493):484–487.

Buffett, B. and Knezek, N. (2018). Stochastic generation of MAC waves and implications for convection in Earth's core. *Geophysical Journal International*, 212(3):1523–1535.

Buffett, B., Knezek, N., and Holme, R. (2016). Evidence for MAC waves at the top of Earth's core and implications for variations in length of day. *Geophysical Journal International*, 204(3):1789–1800.

Buffett, B. and Matsui, H. (2019). Equatorially trapped waves in Earth's core. *Geophysical Journal International*, 218(2):1210–1225.

Buffett, B. and Seagle, C. (2011). Correction to "Stratification of the top of the core due to chemical interactions with the mantle". *Journal of Geophysical Research*, 116(July):1–10.

Buffett, B. A. (1996). Gravitational oscillations in the length of day. *Geophysical Research Letters*, 23(17):2279–2282.

Buffett, B. A. (2010). Chemical stratification at the top of Earth's core: Constraints from observations of nutations. *Earth and Planetary Science Letters*, 296(3):367–372.

Buffett, B. A. (2015). Core-Mantle Interactions. In Schubert, G., editor, *Treatise on Geophysics*, volume 8, pages 213–224. Elsevier.

Buffett, B. A. and Seagle, C. T. (2010). Stratification of the top of the core due to chemical interactions with the mantle. *Journal of Geophysical Research (ISSN 0148-0227)*, 115(B4):B04407–B04407.

Bullard, E. C., Freedman, C., Gellman, H., and Nixon, J. (1950). The westward drift of the Earth's magnetic field. *Phil. Trans. R. Soc. Lond. A*, 243(859):67–92.

Busse, F. H. (1970). Thermal instabilities in rapidly rotating systems. *Journal of Fluid Mechanics*, 44(3):441–460.

Canup, R. M. (2004). Simulations of a late lunar-forming impact. *Icarus*, 168(2):433–456.

Christensen, U. R. (2006). A deep dynamo generating Mercury's magnetic field. *Nature*, 444(7122):1056–1058.

Christensen, U. R. (2011). Geodynamo models: Tools for understanding properties of Earth's magnetic field. *Physics of the Earth and Planetary Interiors*, 187(3):157–169.

Christensen, U. R. (2018). Geodynamo models with a stable layer and heterogeneous heat flow at the top of the core. *Geophysical Journal International*, 215(2):1338–1351.

Christensen, U. R., Aubert, J., and Hulot, G. (2010). Conditions for Earth-like geodynamo models. *Earth and Planetary Science Letters*, 296(3):487–496.

Christensen, U. R. and Wicht, J. (2008). Models of magnetic field generation in partly stable planetary cores: Applications to Mercury and Saturn. *Icarus*, 196(1):16–34.

Chulliat, A., Alken, P., and Maus, S. (2015). Fast equatorial waves propagating at the top of the Earth's core. *Geophysical Research Letters*, 42(9):3321–3329.

Chulliat, A. and Maus, S. (2014). Geomagnetic secular acceleration, jerks, and a localized standing wave at the core surface from 2000 to 2010. *Journal of Geophysical Research: Solid Earth*, 119(3):1531–1543.

Constable, C. and Korte, M. (2015). 5.09 - Centennial- to Millennial-Scale Geomagnetic Field Variations. In Schubert, G., editor, *Treatise on Geophysics (Second Edition)*, pages 309–341. Elsevier, Oxford.

Corgne, A., Wood, B. J., and Fei, Y. (2008). C- and S-rich molten alloy immiscibility and core formation of planetesimals. *Geochimica et Cosmochimica Acta*, 72(9):2409–2416.

Cox, G., Livermore, P., and Mound, J. (2014). Forward models of torsional waves: Dispersion and geometric effects. *Geophysical Journal International*, 196(3):1311–1329.

Cox, G. A. (2015). *Torsional Alfvén Waves in the Earth's Core*. Phd, University of Leeds.

Cox, G. A., Livermore, P. W., and Mound, J. E. (2016). The observational signature of modelled torsional waves and comparison to geomagnetic jerks. *Physics of the Earth and Planetary Interiors*, 255:50–65.

De Boor, C., De Boor, C., Mathématicien, E.-U., De Boor, C., and De Boor, C. (1978). *A Practical Guide to Splines*, volume 27. springer-verlag New York.

de Koker, N., Steinle-Neumann, G., and Vlček, V. (2012). Electrical resistivity and thermal conductivity of liquid Fe alloys at high P and T, and heat flux in Earth's core. *Proceedings of the National Academy of Sciences*, 109(11):4070–4073.

Eaton, D. W. and Kendall, J.-M. (2006). Improving seismic resolution of outermost core structure by multichannel analysis and deconvolution of broadband SmKS phases. *Physics of the Earth and Planetary Interiors*, 155(1-2):104–119.

Fearn, D. R. and Proctor, M. R. E. (1983). Hydromagnetic waves in a differentially rotating sphere. *Journal of Fluid Mechanics*, 128:1–20.

Ferziger, J. H. and Peric, M. (2002). *Computational Methods for Fluid Dynamics*, volume 3. Springer, Berlin, 3rd edition.

Finlay, C. (2007). Waves in the presence of magnetic fields, rotation, and convection.

Finlay, C. C., Dumberry, M., Chulliat, A., and Pais, M. A. (2010). Short Timescale Core Dynamics: Theory and Observations. *Space Science Reviews*, 155(1):177–218.

Finlay, C. C., Jackson, A., Gillet, N., and Olsen, N. (2012). Core surface magnetic field evolution 2000-2010. *Geophysical Journal International*, 189(2):761–781.

Finlay, C. C., Olsen, N., Kotsiaros, S., Gillet, N., and Tøffner-Clausen, L. (2016). Recent geomagnetic secular variation from Swarm and ground observatories as estimated in the CHAOS-6 geomagnetic field model. *Earth, Planets and Space*, 68(1):112–112.

Friis-Christensen, E., Lühr, H., and Hulot, G. (2006). Swarm: A constellation to study the Earth's magnetic field. *Earth, Planets and Space*, 58(4):351–358.

Garnero, E. J., Helmberger, D. V., and Grand, S. P. (1993). Constraining outermost core velocity with SmKS waves. *Geophysical Research Letters*, 20(22):2463–2466.

Gill, A. E. (1982). *Atmosphere—Ocean Dynamics*, volume 30. Elsevier.

Gillet, N., Barrois, O., and Finlay, C. C. (2015a). Stochastic forecasting of the geomagnetic field from the COV-OBS.x1 geomagnetic field model, and candidate models for IGRF-12. *Earth, Planets and Space*, 67(1):71–71.

Gillet, N., Jault, D., Canet, E., and Fournier, A. (2010). Fast torsional waves and strong magnetic field within the Earth's core. *Nature*, 465(7294):74–77.

Gillet, N., Jault, D., and Finlay, C. C. (2015b). Planetary gyre, time-dependent eddies, torsional waves, and equatorial jets at the Earth's core surface. *Journal of Geophysical Research: Solid Earth*, 120(6):3991–4013.

Gillet, N., Pais, M. A., and Jault, D. (2009). Ensemble inversion of time-dependent core flow models. *Geochemistry, Geophysics, Geosystems*, 10(6).

Gilman, P. A. (2000). Magnetohydrodynamic "shallow water" equations for the solar tachocline. *The Astrophysical Journal Letters*, 544(1):L79.

Glane, S. and Buffett, B. (2018). Enhanced Core-Mantle Coupling Due to Stratification at the Top of the Core. *Frontiers in Earth Science*, 6.

Glatzmaier, G. A., Coe, R. S., Hongre, L., and Roberts, P. H. (1999). The role of the Earth's mantle in controlling the frequency of geomagnetic reversals. *Nature*, 401(6756):885–890.

Glatzmaier, G. A. and Roberts, P. H. (1995). A three-dimensional convective dynamo solution with rotating and finitely conducting inner core and mantle. *Physics of the Earth and Planetary Interiors*, 91(1-3):63–75.

Gomi, H., Ohta, K., Hirose, K., Labrosse, S., Caracas, R., Verstraete, M. J., and Hernlund, J. W. (2013). The high conductivity of iron and thermal evolution of the Earth's core. *Physics of the Earth and Planetary Interiors*, 224:88–103.

Gross, R. (2015). 3.09 - Eath rotation variations – long period. In *Treatise on Geophysics*, volume 3, pages 215–261. Elsevier, Oxford, 2nd edition.

Gubbins, D. (2007). Geomagnetic constraints on stratification at the top of Earth's core. *Earth, planets and space*, 59(7):661–664.

Gubbins, D., Alfè, D., Masters, G., Price, G. D., and Gillan, M. (2004). Gross thermodynamics of two-component core convection. *Geophysical Journal International*, 157(3):1407–1414.

Gubbins, D. and Davies, C. J. (2013). The stratified layer at the core–mantle boundary caused by barodiffusion of oxygen, sulphur and silicon. *Physics of the Earth and Planetary Interiors*, 215:21–28.

Helffrich, G. (2012). How light element addition can lower core liquid wave speeds. *Geophysical Journal International*, 188(3):1065–1070.

Helffrich, G. (2014). Outer core compositional layering and constraints on core liquid transport properties. *Earth and Planetary Science Letters*, 391:256–262.

Helffrich, G. and Kaneshima, S. (2004). Seismological Constraints on Core Composition from Fe-O-S Liquid Immiscibility. *Science*, 306(5705):2239–2242.

Helffrich, G. and Kaneshima, S. (2010). Outer-core compositional stratification from observed core wave speed profiles. *Nature*, 468(7325):807–812.

Helffrich, G. and Kaneshima, S. (2013). Causes and consequences of outer core stratification. *Physics of the Earth and Planetary Interiors*, 223:2–7.

Hernandez, V., Roman, J. E., and Vidal, V. (2005). {SLEPc}: A Scalable and Flexible Toolkit for the Solution of Eigenvalue Problems. *ACM Transactions on Mathematical Software*, 31(3):351–362.

Hide, R. (1966). Free Hydromagnetic Oscillations of the Earth's Core and the Theory of the Geomagnetic Secular Variation. *Philosophical Transactions of the Royal Society A: Mathematical, Physical and Engineering Sciences*, 259(1107):615–647.

Hide, R. (1969). Interaction between the Earth's Liquid Core and Solid Mantle. *Nature*, 222(5198):1055–1056.

Higgins, G. and Kennedy, G. C. (1971). The adiabatic gradient and the melting point gradient in the core of the Earth. *Journal of Geophysical Research (1896-1977)*, 76(8):1870–1878.

Hirose, K., Morard, G., Sinmyo, R., Umemoto, K., Hernlund, J., Helffrich, G., and Labrosse, S. (2017). Crystallization of silicon dioxide and compositional evolution of the Earth's core. *Nature*, 543(7643):99–102.

Hollerbach, R. (1996). On the theory of the geodynamo. *Physics of the Earth and Planetary Interiors*, 98(3):163–185.

Holme, R. (2015). Large-Scale Flow in the Core. In *Treatise on Geophysics*, volume 8, pages 91–113. Elsevier.

Hori, K., Jones, C. A., and Teed, R. J. (2015). Slow magnetic Rossby waves in the Earth's core. *Geophysical Research Letters*.

Huguet, L., Amit, H., and Alboussière, T. (2018). Geomagnetic Dipole Changes and Upwelling/Downwelling at the Top of the Earth's Core. *Frontiers in Earth Science*, 6.

Hulot, G., Sabaka, T. J., Olsen, N., and Fournier, A. (2015). 5.02 - The Present and Future Geomagnetic Field. In Schubert, G., editor, *Treatise on Geophysics (Second Edition)*, pages 33–78. Elsevier, Oxford.

Jackson, A. and Finlay, C. (2015). 5.05 - Geomagnetic Secular Variation and Its Applications to the Core. In Schubert, G., editor, *Treatise on Geophysics (Second Edition)*, pages 137–184. Elsevier, Oxford.

Jackson, A., Jonkers, A. R. T., and Walker, M. R. (2000). Four centuries of geomagnetic secular variation from historical records. *Philosophical Transactions of the Royal Society of London A: Mathematical, Physical and Engineering Sciences*, 358(1768):957–990.

Jault, D., Gire, C., and Mouel, J. L. L. (1988). Westward drift, core motions and exchanges of angular momentum between core and mantle. *Nature*, 333(6171):353–356.

Jaupart, E. and Buffett, B. (2017). Generation of MAC waves by convection in Earth's core. *Geophysical Journal International*, 209(2):1326–1336.

Jeanloz, R. (1990). The nature of the Earth's core. *Annual Review of Earth and Planetary Sciences*, 18:357–386.

Jones, C. A. (2011). Planetary Magnetic Fields and Fluid Dynamos. *Annual Review of Fluid Mechanics*, 43(1):583–614.

Jones, C. A. (2015). 8.05 - Thermal and Compositional Convection in the Outer Core. In Schubert, G., editor, *Treatise on Geophysics (Second Edition)*, pages 115–159. Elsevier, Oxford.

Jones, E., Oliphant, T., Peterson, P., and Others (2001). SciPy: Open Source Scientific Tools for Python.

Kaneshima, S. (2018). Array analyses of SmKS waves and the stratification of Earth's outermost core. *Physics of the Earth and Planetary Interiors*, 276:234–246.

Kaneshima, S. and Helffrich, G. (2013). Vp structure of the outermost core derived from analysing large-scale array data of SmKS waves. *Geophysical Journal International*, 193(3):1537–1555.

Kaneshima, S. and Matsuzawa, T. (2015). Stratification of earth's outermost core inferred from SmKS array data. *Progress in Earth and Planetary Science*, 2(1):15.

Kloss, C. and Finlay, C. C. (2019). Time-dependent low-latitude core flow and geomagnetic field acceleration pulses. *Geophysical Journal International*, 217(1):140–168.

Knezek, N. and Buffett, B. (2018). Influence of magnetic field configuration on magnetohydrodynamic waves in Earth's core. *Physics of the Earth and Planetary Interiors*, 277:1–9.

Knezek, N. R. and Buffett, B. A. (2015). A Numerical Model for Magnetohydrodynamic Waves in a Stably-Stratified Layer in Earth's Core. In *AGU Fall Meeting Abstracts*, volume 41, pages P41A–2037.

Knittle, E. and Jeanloz, R. (1989). Simulating the core-mantle boundary: An experimental study of high-pressure reactions between silicates and liquid iron. *Geophysical Research Letters*, 16(7):609–612.

Knittle, E. and Jeanloz, R. (1991). Earth's Core-Mantle Boundary: Results of Experiments at High Pressures and Temperatures. *Science*, 251(5000):1438–1443.

Kono, M. (2015). 5.01 - Geomagnetism: An Introduction and Overview. In Schubert, G., editor, *Treatise on Geophysics (Second Edition)*, pages 1–31. Elsevier, Oxford.

Konôpková, Z., McWilliams, R. S., Gómez-Pérez, N., and Goncharov, A. F. (2016). Direct measurement of thermal conductivity in solid iron at planetary core conditions. *Nature*, 534(7605):99–101.

Kutzner, C. and Christensen, U. R. (2004). Simulated geomagnetic reversals and preferred virtual geomagnetic pole paths. *Geophysical Journal International*, 157(3):1105–1118.

Labrosse, S. (2015). Thermal evolution of the core with a high thermal conductivity. *Physics of the Earth and Planetary Interiors*, 247:36–55.

Landau, L. D. and Lifshitz, E. M. (1987). *Fluid Mechanics*. Pergamon, Oxford, 2nd edition.

Langel, R. A. (1987). Main field. *Geomagnetism*.

Lay, T. and Young, C. J. (1990). The stably-stratified outermost core revisited. *Geophysical Research Letters*, 17(11):2001–2004.

Lehnert, B. (1954). Magnetohydrodynamic Waves Under the Action of the Coriolis Force. *The Astrophysical Journal*, 119:647.

Lesur, V., Wardinski, I., Baerenzung, J., and Holschneider, M. (2018). On the frequency spectra of the core magnetic field Gauss coefficients. *Physics of the Earth and Planetary Interiors*, 276:145–158.

Lesur, V., Wardinski, I., Hamoudi, M., and Rother, M. (2010). The second generation of the GFZ reference internal magnetic model: GRIMM-2. *Earth, planets and space*, 62(10):6.

Lesur, V., Wardinski, I., Rother, M., and Mandea, M. (2008). GRIMM: The GFZ Reference Internal Magnetic Model based on vector satellite and observatory data. *Geophysical Journal International*, 173(2):382–394.

Lesur, V., Whaler, K., and Wardinski, I. (2015). Are geomagnetic data consistent with stably stratified flow at the core-mantle boundary? *Geophysical Journal International*, 201(2):929–946.

Lister, J. R. and Buffett, B. A. (1998). Stratification of the outer core at the core-mantle boundary. *Physics of the earth and planetary interiors*, 105(1-2):5–19.

Longuet-Higgins, M. S. (1965). Planetary waves on a rotating sphere. II. *Proceedings of the Royal Society of London. Series A. Mathematical and Physical Sciences*, 284(1396):40–68.

Macmillan, S. and Finlay, C. (2011). The International Geomagnetic Reference Field. *Geomagnetic observations and models*, pages 265–276.

Malin, S. and Hodder, B. (1982). Was the 1970 geomagnetic jerk of internal or external origin? *Nature*, 296(5859):726–728.

Márquez-Artavia, X., Jones, C. A., and Tobias, S. M. (2017). Rotating magnetic shallow water waves and instabilities in a sphere. *Geophysical & Astrophysical Fluid Dynamics*, 111(4):282–322.

Maus, S. (2007). CHAMP magnetic mission. *Encyclopedia of Geomagnetism and Paleomagnetism*, pages 59–60.

Maus, S., Lühr, H., Balasis, G., Rother, M., and Mandea, M. (2005). Introducing pomme, the potsdam magnetic model of the earth. In *Earth Observation With CHAMP*, pages 293–298. Springer.

Maus, S., Manoj, C., Rauberg, J., Michaelis, I., and Lühr, H. (2010). NOAA/NGDC candidate models for the 11th generation International Geomagnetic Reference Field and the concurrent release of the 6th generation Pomme magnetic model. *Earth, planets and space*, 62(10):2.

Moffatt, H. K. (1977). Topographic coupling at the core-mantle interface. *Geophysical & Astrophysical Fluid Dynamics*, 9(1):279–288.

Nakagawa, T. (2011). Effect of a stably stratified layer near the outer boundary in numerical simulations of a magnetohydrodynamic dynamo in a rotating spherical shell and its implications for Earth's core. *Physics of the Earth and Planetary Interiors*, 187(3):342–352.

Nimmo, F. (2015). Energetics of the Core. In *Treatise on Geophysics*. Elsevier B.V., second edition.

Ohta, K., Kuwayama, Y., Hirose, K., Shimizu, K., and Ohishi, Y. (2016). Experimental determination of the electrical resistivity of iron at Earth's core conditions. *Nature*, 534(7605):95–98.

Olsen, N., Holme, R., Hulot, G., Sabaka, T., Neubert, T., Tøffner-Clausen, L., Primdahl, F., Jørgensen, J., Léger, J.-M., and Barraclough, D. (2000). Ørsted initial field model. *Geophysical Research Letters*, 27(22):3607–3610.

Olson, P. (2015). Core Dynamics: An Introduction and Overview. In *Treatise on Geophysics*, pages 1–25. Elsevier.

Olson, P., Landeau, M., and Reynolds, E. (2017). Dynamo tests for stratification below the core-mantle boundary. *Physics of the Earth and Planetary Interiors*, 271:1–18.

Olson, P., Landeau, M., and Reynolds, E. (2018). Outer Core Stratification From the High Latitude Structure of the Geomagnetic Field. *Frontiers in Earth Science*, 6.

Olson, P. L., Coe, R. S., Driscoll, P. E., Glatzmaier, G. A., and Roberts, P. H. (2010). Geodynamo reversal frequency and heterogeneous core–mantle boundary heat flow. *Physics of the Earth and Planetary Interiors*, 180(1):66–79.

O'Rourke, J. G., Korenaga, J., and Stevenson, D. J. (2016). Thermal evolution of Earth with magnesium precipitation in the core. *Earth and Planetary Science Letters*, 1:1–10.

Otsuka, K. and Karato, S.-i. (2012). Deep penetration of molten iron into the mantle caused by a morphological instability. *Nature*, 492(7428):243–246.

Ozawa, H., Hirose, K., Mitome, M., Bando, Y., Sata, N., and Ohishi, Y. (2008). Chemical equilibrium between ferropericlase and molten iron to 134 GPa and implications for iron content at the bottom of the mantle. *Geophysical Research Letters*, 35(5).

Ozawa, H., Hirose, K., Mitome, M., Bando, Y., Sata, N., and Ohishi, Y. (2009). Experimental study of reaction between perovskite and molten iron to 146 GPa and implications for chemically distinct buoyant layer at the top of the core. *Physics and Chemistry of Minerals*, 36(6):355–363.

Pais, A. and Hulot, G. (2000). Length of day decade variations, torsional oscillations and inner core superrotation: Evidence from recovered core surface zonal flows, Phys. *Earth Planet. Int*, 118:291–316.

Pais, M. A. and Jault, D. (2008). Quasi-geostrophic flows responsible for the secular variation of the Earth's magnetic field. *Geophysical Journal International*, 173(2):421–443.

Pedlosky, J. (1987). *Geophysical Fluid Dynamics*. Springer, Verlag, 2nd edition.

Platzman, G. W., G.W., P., and Platzman, G. W. (1968). The Rossby wave. *Quarterly Journal of the Royal Meteorological Society*, 94(401):225–248.

Pozzo, M., Davies, C., Gubbins, D., and Alf‘e, D. (2012a). Thermal and electrical conduc- tivity of iron at earth's core conditions. *Nature*, 485:355–358.

Pozzo, M., Davies, C., Gubbins, D., and Alfè, D. (2012b). Thermal and electrical conductivity of iron at Earth's core conditions. *Nature*, 485(7398):355–358.

Pozzo, M., Davies, C., Gubbins, D., and Alfè, D. (2014). Thermal and electrical conductivity of solid iron and iron-silicon mixtures at Earth's core conditions. *Earth and Planetary Science Letters*.

Rhines, P. and Bretherton, F. (1973). Topographic Rossby waves in a rough-bottomed ocean. *Journal of Fluid Mechanics*, 61(3):583–607.

Roberts, P. (2007). *8.03 - Theory of the Geodynamo, in Treatise on Geophysics*. Gerald Schubert, E., Elsevier, Amsterdam. 105, ed. in Chief.

Roberts, P. H. and King, E. M. (2013). On the genesis of the Earth's magnetism. *Reports on Progress in Physics*.

Roberts, P. H. and Stewartson, K. (1974). On finite amplitude convection in a rotating magnetic system. *Philosophical Transactions of the Royal Society of London. Series A, Mathematical and Physical Sciences*, 277(1269):287–315.

Rochester, M. G. (1962). Geomagnetic core-mantle coupling. *Journal of Geophysical Research (1896-1977)*, 67(12):4833–4836.

Rubie, D. C., Nimmo, F., and Melosh, H. J. (2015). 9.03 - Formation of the Earth's Core. In Schubert, G., editor, *Treatise on Geophysics (Second Edition)*, pages 43–79. Elsevier, Oxford.

Sabaka, T. J., Olsen, N., and Purucker, M. E. (2004). Extending comprehensive models of the Earth's magnetic field with Ørsted and CHAMP data. *Geophysical Journal International*, 159(2):521–547.

Sabaka, T. J., Olsen, N., Tyler, R. H., and Kuvshinov, A. (2015). CM5, a pre-Swarm comprehensive geomagnetic field model derived from over 12 yr of CHAMP, Ørsted, SAC-C and observatory data. *Geophysical Journal International*, 200(3):1596–1626.

Schaeffer, N., Jault, D., Nataf, H.-C., and Fournier, A. (2017). Turbulent geodynamo simulations: A leap towards Earth's core. *Geophysical Journal International*, 211(1):1–29.

Schecter, D. A., Boyd, J. F., and Gilman, P. A. (2001). "Shallow-water" magnetohydrodynamic waves in the solar tachocline. *The Astrophysical Journal Letters*, 551(2):L185.

Schumaker, L. (2007). *Spline Functions: Basic Theory*. Cambridge University Press.

Seyed-Mahmoud, B., Moradi, A., Kamruzzaman, M., and Naseri, H. (2015). Effects of density stratification on the frequencies of the inertial-gravity modes of the Earth's fluid core. *Geophysical Journal International*, 202(2):1146–1157.

Shearer, M. J. and H. Roberts, P. (1998). The hidden ocean at the top of Earth's core. *Dynamics of Atmospheres and Oceans*, 27(1):631–647.

Shore, R. M., Freeman, M. P., and Gjerloev, J. W. (2018). An Empirical Orthogonal Function Reanalysis of the Northern Polar External and Induced Magnetic Field During Solar Cycle 23. *Journal of Geophysical Research: Space Physics*, 123(1):781–795.

Shore, R. M., Whaler, K. A., Macmillan, S., Beggan, C., Velímský, J., and Olsen, N. (2016). Decadal period external magnetic field variations determined via eigenanalysis. *Journal of Geophysical Research: Space Physics*, 121(6):5172–5184.

Souriau, A. and Calvet, M. (2015). 1.23 - Deep Earth Structure: The Earth's Cores. In Schubert, G., editor, *Treatise on Geophysics (Second Edition)*, pages 725–757. Elsevier, Oxford.

Soward, A. M. (1979). Convection driven dynamos. *Physics of the Earth and Planetary Interiors*, 20(2-4):134–151.

Sreenivasan, B. and Gubbins, D. (2008). Dynamos with weakly convecting outer layers: Implications for core-mantle boundary interaction. *Geophysical and Astrophysical Fluid Dynamics*, 102(4):395–407.

Sumita, I. and Olson, P. (1999). A laboratory model for convection in Earth's core driven by a thermally heterogeneous mantle. *Science*, 286(5444):1547–1549.

Takehiro, S.-i. and Sasaki, Y. (2018). Penetration of steady fluid motions into an outer stable layer excited by MHD thermal convection in rotating spherical shells. *Physics of the Earth and Planetary Interiors*, 276:258–264.

Tanaka, S. (2004). Seismic detectability of anomalous structure at the top of the Earth's outer core with broadband array analysis of SmKS phases. *Physics of the Earth and Planetary Interiors*, 141(3):141–152.

Tanaka, S. (2007). Possibility of a low P-wave velocity layer in the outermost core from global SmKS waveforms. *Earth and Planetary Science Letters*, 259(3):486–499.

Tanaka, S. and Hamaguchi, H. (1993). Velocities and Chemical Stratification in the Outermost Core. *Journal of geomagnetism and geoelectricity*, 45(11-12):1287–1301.

Tarduno, J. A., Cottrell, R. D., Davis, W. J., Nimmo, F., and Bono, R. K. (2015). A Hadean to Paleoarchean geodynamo recorded by single zircon crystals. *Science*.

Thomson, A. W., Hamilton, B., Macmillan, S., and Reay, S. J. (2010). A novel weighting method for satellite magnetic data and a new global magnetic field model. *Geophysical Journal International*, 181(1):250–260.

Tromp, J. (2015). 1.07 - Theory and Obeservations - Forward Modeling and Synthetic Seismograms, 3D Numerical Methods. In Schubert, G., editor, *Treatise on Geophysics (Second Edition)*, pages 231–251. Elsevier, Oxford.

Tsuno, K., Terasaki, H., Ohtani, E., Suzuki, A., Asahara, Y., Nishida, K., Sakamaki, T., Funakoshi, K.-i., and Kikegawa, T. (2007). In situ observation and determination of liquid immiscibility in the Fe-O-S melt at 3 GPa using a synchrotron X-ray radiographic technique. *Geophysical Research Letters*, 34(17).

Van Der Walt, S., Colbert, S. C., and Varoquaux, G. (2011). The NumPy array: A structure for efficient numerical computation. *Computing in Science and Engineering*, 13(2):22–30.

Vidal, J. and Schaeffer, N. (2015). Quasi-geostrophic modes in the Earth's fluid core with an outer stably stratified layer. *Geophysical Journal International*, 202(3):2182–2193.

Voorhies, C. V. (1984). Magnetic location of Earth's core-mantle boundary and estimates of the adjacent fluid motion. *Ph.D. Thesis Colorado Univ., Boulder.*

Walker, D. (2005). Core Mantle Chemical Issues. *The Canadian Mineralogist*, 43(5):1553–1564.

Whaler, K. A. (1980). Does the whole of the Earth's core convect? *Nature*, 287(5782):528–530.

Whaler, K. A. (1986). Geomagnetic evidence for fluid upwelling at the core-mantle boundary. *Geophysical Journal of the Royal Astronomical Society*, 86(2):563–588.

Wieczorek, M. A. and Meschede, M. (2018). SHTools: Tools for Working with Spherical Harmonics. *Geochemistry, Geophysics, Geosystems*, 19(8):2574–2592.

Wong, J., Davies, C. J., and Jones, C. A. (2018). A Boussinesq slurry model of the F-layer at the base of Earth's outer core. *Geophysical Journal International*, 214(3):2236–2249.

Wood, B. J., Walter, M. J., and Wade, J. (2006). Accretion of the Earth and segregation of its core. *Nature*, 441(7095):825.

Woodhouse, J. H. and Dziewonski, A. M. (1984). Mapping the upper mantle: Three-dimensional modeling of earth structure by inversion of seismic waveforms. *Journal of Geophysical Research: Solid Earth*, 89(B7):5953–5986.

Yan, C. and Stanley, S. (2018). Sensitivity of the Geomagnetic Octupole to a Stably Stratified Layer in the Earth's Core. *Geophysical Research Letters*, 45(20):11,005–11,011.

Yukutake, T. (1981). A stratified core motion inferred from geomagnetic secular variations. *Physics of the Earth and Planetary Interiors*, 24(4):253–258.

Zaqarashvili, T. V., Oliver, R., and Ballester, J. L. (2009). Global shallow water magnetohydrodynamic waves in the solar tachocline. *The Astrophysical Journal Letters*, 691(1):L41.

Zaqarashvili, T. V., Oliver, R., Ballester, J. L., and Shergelashvili, B. M. (2007). Rossby waves in "shallow water" magnetohydrodynamics. *Astronomy & Astrophysics*, 470(3):815–820.

Zatman, S. and Bloxham, J. (1997). Torsional oscillations and the magnetic field within the Earth's core. *Nature*, 388(6644):760–763.

Zhang, N. and Zhong, S. (2011). Heat fluxes at the Earth's surface and core–mantle boundary since Pangea formation and their implications for the geomagnetic superchrons. *Earth and Planetary Science Letters*, 306(3):205–216.

Appendices

Appendix A

Mathematical Notation

This appendix presents a brief overview of the mathematical notation used in this thesis.

A.1 Spherical Harmonics

Throughout this thesis, we utilize spherical harmonics to capture spatial variations in a spherical geometry. In particular, spherical harmonics are used for the geomagnetic field models such as CHAOS-6, as well as to parameterize and describe fluid and wave motions in the core.

For the geomagnetic field, the internal core field can be represented as

$$\mathbf{B}(r,\theta,\phi) = -\nabla\psi(r,\theta,\phi) \tag{A.1}$$

Where r, θ, and ϕ represent the radial, latitudinal, and longitudinal coordinates, and ψ is a magnetic potential field. This magnetic potential field can be described in spherical harmonics as

$$\psi(r,\theta,\phi) = a\sum_{l=1}^{l_{max}}\sum_{m=0}^{l}\left(\frac{a}{r}\right)^{l+1} P_l^m(\cos\theta)(g_l^m\cos m\phi + h_l^m\sin m\phi) \tag{A.2}$$

where a is the mean radius of Earth (6371 km), r,θ, and ϕ are radius, co-latitude, and longitude, P_l^m is the Schmidt-normalized associated Legendre polynomial of degree l and order m, and g_l^m and h_l^m are the real Gauss coefficients describing the field. See (e.g. Langel, 1987), Hulot et al. (2015), section 5.02.3.1, or Finlay et al. (2016) for further details on the use of spherical harmonics to model the geomagnetic field.

Spherical harmonic decompositions can also be represented using complex coefficients. Complex coefficients have some advantages over real coefficients, as they can be manipulated as a single value for each degree and order. This representation is used in section 4.3.2 to model SV noise. These complex spherical harmonics are represented as

$$f(\theta,\phi) = \sum_{l=0}^{\infty} \sum_{m=-l}^{l} f_l^m \, Y_l^m(\theta,\phi), \tag{A.3}$$

where f_l^m is the complex spherical harmonic coefficient, Y_l^m is the corresponding complex spherical harmonic function, θ is co-latitude, ϕ is longitude, and l and m are the spherical harmonic degree and order, respectively. The complex spherical harmonics are defined as

$$Y_l^m(\theta,\phi) = \bar{P}_l^m(\cos\theta)\, e^{im\phi}, \tag{A.4}$$

where the normalized associated Legendre functions for use with the complex 4π-normalized spherical harmonic functions are given by

$$\bar{P}_l^m(\mu) = \sqrt{(2l+1)\,\frac{(l-m)!}{(l+m)!}}\, P_{lm}(\mu), \tag{A.5}$$

. The unnormalized associated Legendre functions are derived from the standard Legendre polynomials using the relations

$$P_{lm}(\mu) = \left(1-\mu^2\right)^{m/2} \frac{d^m}{d\mu^m} P_l(\mu) \tag{A.6}$$

and

$$P_l(\mu) = \frac{1}{2^l l!} \frac{d^l}{d\mu^l} \left(\mu^2 - 1\right)^l. \tag{A.7}$$

See Wieczorek and Meschede (2018) for further details and implementation methods in code.

A.2 B-splines

Earth's geomagnetic field changes over time, and this variation is modeled by allowing the Gauss coefficients to vary over time. A common technique

to capture these changes in a smooth manner is to use B-splines with knots regularly spaced through time (see e.g. Bloxham and Jackson, 1992; Jackson et al., 2000). This method allows each field coefficient to vary independently and smoothly over time and does not impose any functional form on the shape of the long-term variation. B-splines are also local in time, meaning that observations from long ago or far in the future do not affect the components of the present field. Also, B-Splines can be constructed such that as the field has as many continuous time derivatives as desired. That is, the first, second, third, etc. time derivatives can be made to be continuous in time with the proper choice of B-Splines. For example, Finlay et al. (2016) uses sixth-order B-splines to capture variations in Gauss coefficients of the internal geomagnetic field

$$g_l^m(t) = \sum_{k=1}^{K} {}^k g_l^m B_k(t) \tag{A.8}$$

where here K=6, and B_k are spline basis functions. A similar equation is used for $h_l^m(t)$, and values are recorded at 6-month knot spacings with endpoints at t=1997.1 and t=2016.6.

With knots locations at t_0, t_1, ... t_i, then B-spline basis functions of order 1 are defined such that

$$B_{i,1}(t) = \begin{cases} 1 & \text{if } t_i \leq t < t_{i+1} \\ 0 & \text{otherwise.} \end{cases} \tag{A.9}$$

Then, higher-order B-splines are defined recursively from this definition using the Cox-DeBoor algorithm, such that

$$B_{i,k+1} = \frac{x - t_i}{t_{i+k} - t_i} B_{i,k}(x) + \frac{t_{i+k+1} - x}{t_{i+k+1} - t_{i+1}} B_{i+1,k}(x) \tag{A.10}$$

For further information on B-splines, see De Boor et al. (1978) or Schumaker (2007). Commonly, B-splines used for magnetic field models are constructed such that the the magnetic field strength and its first two time derivatives, termed secular variation and secular acceleration, are continuous and smooth (e.g. their derivative is continuous) in time.

A.3 Brunt–Väisälä frequency

The Brunt–Väisälä frequency is a measure of the stability of a parcel of fluid to vertical displacements against a background fluid with a defined density

variation. It is commonly denoted by the value N, with units of radians per time. If this value is real, it defines the angular frequency at which a parcel of fluid will oscillate if displaced slightly from its stationary location and allowed to move freely. However, if N is purely imaginary, then the parcel is unstable and will not oscillate. N is defined using the gradient of the background density ρ_0 as

$$N = \sqrt{-\frac{g}{\rho_0}\frac{\partial \rho_0}{\partial r}} \tag{A.11}$$

where g is the local gravity, and z is the coordinate perpendicular to the density gradient (typically the vertical or radial direction).

The magnitude of N can be used to determine the strength of convection or stratification of a particular region of fluid. As the value depends on both the the local density and density gradient, N is typically not constant, and can vary over space and time with changes in the background fluid. In this thesis, N is often quoted in units of cycles per day, with proposed values of N for the SOC ranging from $\sim$ 1 / day to $\sim$ 70 / day (Braginsky, 1993; Buffett and Seagle, 2011). It should be noted, however, that these frequencies are a measure of the strength of buoyancy, and do not directly control the frequencies of waves that propagate in the SOC. Indeed, the eMAC waves examined in this thesis have frequencies on the order of 1 / decade, not 1 / day.

A.4 Quality Factor

The quality factor or Q factor is a dimensionless measure of the rate at which a wave impulse will decay away. Higher quality factors mean that a wave will propagate further given a constant initial excitation mechanism, while lower quality factors mean that the wave will dissipate more quickly. There are many different ways to define quality factor depending upon the particular scientific or engineering domain. In this thesis, we define the quality factor using the complex frequency ω of a particular wave mode as

$$Q = \frac{|\omega_r|}{2\omega_i} \tag{A.12}$$

where ω_r and ω_i represent that real and imaginary components of the frequency. Thus, if $|\omega_r| >> \omega_i$ the wave will propagate for a long period of time

and Q >> 1. Conversely, if $|\omega_r| << \omega_i$, then Q << 1 and the wave is heavily damped. Note that for all waves examined in this thesis the imaginary component of the frequency is positive, and thus Q is always positive. A negative ω_i would mean that the wave amplitude grows exponentially, which does not represent a physically realistic solution for linear waves in Earth's core.

A.5 Magnetic Fields

Magnetic fields have both a direction and magnitude at each point in space, which we represent as the orientation and magnitude of a vector field $\vec{B}$. This field satisfies a set of rules collectively known as Maxwell's laws, which govern its properties and behavior.

$$\nabla \cdot \mathbf{E} = \frac{\rho}{\varepsilon_0} \tag{A.13}$$

$$\nabla \cdot \mathbf{B} = 0 \tag{A.14}$$

$$\nabla \times \mathbf{E} = -\frac{\partial \mathbf{B}}{\partial t} \tag{A.15}$$

$$\nabla \times \mathbf{B} = \mu_0 \mathbf{J} + \mu_0 \varepsilon_0 \frac{\partial \mathbf{E}}{\partial t} \tag{A.16}$$

$$\tag{A.17}$$

In order, these equations are known as Gauss's laws for electricity and magnetism, Faraday's law, and Ampere's law. Here, $\vec{E}$, and $\vec{B}$ are, respectively, electric and magnetic fields, and $\vec{J}$ is the electric current. The additional terms here are ε_0 electrical permittivity, μ_0 magnetic permeability, and ρ electric charge density.

From these laws, we can see that magnetic fields $\vec{B}$, are both divergence free $\nabla \cdot \vec{B} = 0$ and curl-free $\nabla \times \vec{B} = 0$ in the absence of electrical charges. Thus, in regions with no electrical currents or charges, magnetic fields can be defined as the gradient of a magnetic potential $\vec{B} = \nabla\psi$ where ψ is the magnetic potential. Because the mantle is largely free of magnetic sources or significant electrical currents, this fact can be used to uniquely determine the magnetic potential field from the core through the mantle to the surface of the Earth. In this way, observations at or above the surface of the Earth can be used to determine the geomagnetic field at the CMB (e.g. Hulot et al., 2015).

A.5.1 Induction Equation

In Earth's core, Maxwell's laws can be simplified to be incorporated into magnetohydrodynamic equations of fluid motions. To do this, we first take Faraday's and Ampere's laws

$$\vec{\nabla} \times \vec{E} = -\frac{\partial \vec{B}}{\partial t}, \tag{A.18}$$

and

$$\vec{\nabla} \times \vec{B} = \mu_0 \vec{J}, \tag{A.19}$$

where the displacement current $\mu_0 \varepsilon_0 \frac{\partial \mathbf{E}}{\partial t}$ has been neglected as it usually has small effects in Earth's core. Combining these equations with Ohm's law and eliminating $\vec{E}$ and $\vec{J}$ yields the induction equation for an electrically resistive fluid:

$$\frac{\partial \vec{B}}{\partial t} = \eta \nabla^2 \vec{B} + \vec{\nabla} \times (\vec{v} \times \vec{B}). \tag{A.20}$$

where $\eta = 1/\mu_0 \sigma$ is the magnetic diffusivity.

A.6 Waves

Simple non-magnetic waves can be described by Airy wave theory, also known as linear wave theory, which describes waves in an ideal fluid that is inviscid, incompressible, and irrotational. One of the simplest wave modes in this system is that of a water wave propagating in a horizontal direction across a free surface with a mean water depth of h. In this case, a solution can be found with a dispersion relation of the form

$$\omega^2 = gk \tanh(kh) \tag{A.21}$$

where g is the local gravity, k is the wavenumber, and ω is the wave frequency (e.g. Landau and Lifshitz, 1987).

A.6.1 Rotational and Inertial Waves

Within Earth's core, rotation and inertia acts as additional restoring forces, enabling more types of waves to propagate. To derive these waves, begin by taking the momentum equation in a rotating reference frame

$$\frac{\partial \mathbf{u}}{\partial t} + 2(\mathbf{\Omega} \times \mathbf{u}) = -\frac{\mathbf{1}}{\rho} \nabla \mathbf{p} \tag{A.22}$$

Then, take the curl $\nabla\times$ and denote the vorticity as $\xi = \nabla \times \mathbf{u}$ and we obtain

$$\frac{\partial \xi}{\partial t} = 2(\mathbf{\Omega} \cdot \nabla)\mathbf{u} \tag{A.23}$$

Then, take a further curl and time derivative and perform some substitutions to obtain

$$\frac{\partial^2(\nabla^2 \mathbf{u})}{\partial t^2} = -4(\mathbf{\Omega} \cdot \nabla)^{\mathbf{2}}\mathbf{u} \tag{A.24}$$

which admit solutions of

$$\omega = \pm\frac{2(\mathbf{\Omega} \cdot \mathbf{k})}{|\mathbf{k}|} = \pm 2\Omega \cos\theta \tag{A.25}$$

where θ is the angle between $\mathbf{\Omega}$ and $\mathbf{k}$ and ω varies between 0 and 2Ω. This dispersion relation describes general waves under the influence of rotation and inertia. Specific wave modes can be found by applying additional constraints or taking parameters in this equation to its limits. For example hydrodynamic Rossby waves are a special case of low frequency inertial waves in a spherical geometry when fluid motions are quasi-geostrophic.

A.6.2 Magnetic (Alfvén) Waves

Earth's core consists of a conductive fluid, and this gives rise to a class of waves that rely on the magnetic field as a restoring force. These magnetohydrodynamic waves were first derived by Alfvén (1943), and have been shown to propagate in laboratory experiments as well as Earth's magnetosphere and core. The simplest form of these waves can be derived starting from the momentum equation with only a magnetic field and pressure

$$\frac{\partial U}{\partial t} = \frac{1}{\rho}\nabla P + \frac{1}{\rho\mu}(\nabla \times B) \times B. \tag{A.26}$$

Then, the induction equation with no Ohmic diffusion can be used to relate fluid velocity and magnetic fields

$$\frac{\partial B}{\partial t} = \nabla \times (U \times B). \tag{A.27}$$

We assume a background state with no large-scale velocity field

$$U = u \tag{A.28}$$

and only a uniform, steady background magnetic field with a small perturbation,

$$B = B_0 + b. \tag{A.29}$$

with some substitution, and assuming that terms including only b and u are small, we obtain

$$\frac{\partial u}{\partial t} = \frac{1}{\rho}\nabla p + \frac{1}{\rho\mu}(B_0 \cdot \nabla)b \tag{A.30}$$

and

$$\frac{\partial b}{\partial t} = (B_0 \cdot \nabla)u. \tag{A.31}$$

We then can obtain the wave equation by taking the curl of each equation ($\nabla\times$) and defining the fluid vorticity as $\xi = \nabla \times u$. Then, take the time derivative of the fluid vorticity equation to obtain

$$\frac{\partial^2 \xi}{\partial t^2} = \frac{1}{\rho\mu}(B_0 \cdot \nabla)^2 \left(\nabla \times \frac{\partial b}{\partial t}\right) \tag{A.32}$$

$$\nabla \times \frac{\partial b}{\partial t} = (B_0 \cdot \nabla)\xi. \tag{A.33}$$

By substitution, we obtain

$$\frac{\partial^2 \xi}{\partial t^2} = \frac{1}{\rho\mu}(B_0 \cdot \nabla)^2 \xi \tag{A.34}$$

which is recognized as the classical plane wave equation, with solutions of

$$\omega = \pm v_A(k \cdot \hat{B_0}) \tag{A.35}$$

where $v_A = \frac{B_0}{(\rho\mu)^{1/2}}$ is the Alvén velocity (Alfvén, 1943).

A.6.3 Rotation and Magnetic Fields: MC Waves

Now, if we combine rotation, inertia, and a uniform magnetic field the governing equations become

$$\frac{\partial \mathbf{u}}{\partial t} + s(\mathbf{\Omega} \times \mathbf{u}) = -\frac{\mathbf{1}}{\rho}\nabla \mathbf{p} + \frac{\mathbf{1}}{\rho\mu}(\mathbf{B_0} \cdot \nabla)\mathbf{b} \tag{A.36}$$

and

$$\frac{\partial \mathbf{b}}{\partial t} = (\mathbf{B_0} \cdot \nabla)\mathbf{u}. \tag{A.37}$$

We then take the curl of each side and the time derivative of the momentum equation. Then, substitute the result from the Ohmic diffusion equation into the momentum equation we we obtain

$$\frac{\partial^2(\nabla \times \mathbf{u})}{\partial t^2} - 2(\mathbf{\Omega} \cdot \nabla)\frac{\partial \mathbf{u}}{\partial \mathbf{t}} = \frac{\mathbf{1}}{\rho\mu}(\mathbf{B_0} \cdot \nabla)^{\mathbf{2}}(\nabla \times \mathbf{u}) \tag{A.38}$$

By taking another curl and substituting, we obtain

$$\left(\frac{\partial^2}{\partial t^2} - \frac{1}{\rho\mu}(\mathbf{B_0} \cdot \nabla^{\mathbf{2}})\right)^2 \nabla^2\mathbf{u} = -\mathbf{4}(\mathbf{\Omega} \cdot \nabla)^{\mathbf{2}}\frac{\partial^{\mathbf{2}}\mathbf{u}}{\partial \mathbf{t^2}} \tag{A.39}$$

which is the wave equation for Alfvén-Inertial or Magnetic-Coriolis (MC) waves.

This equation admits solutions which have the dispersion relation

$$\omega = \pm\frac{(\mathbf{\Omega} \cdot \mathbf{k})}{k} \pm \left(\frac{(\mathbf{\Omega} \cdot \mathbf{k})^{\mathbf{2}}}{k^2} + \frac{(\mathbf{B_0} \cdot \mathbf{k})^{\mathbf{2}}}{\rho\mu}\right)^{1/2} \tag{A.40}$$

(Lehnert, 1954). When $\mathbf{\Omega} \to \mathbf{0}$ we recover the Alfvén wave dispersion relation, while when $\mathbf{B_0} \to \mathbf{0}$ we recover the inertial wave dispersion relation. Hide (1966) applied a similar analysis to derive magnetically-modified Rossby waves and MC Rossby waves in Earth's core.

A.6.4 Magnetic Archimedes Coriolis: MAC Waves

Then, we can now include a buoyancy gradient in our system

$$\nabla T_0 = \beta' \hat{z} \tag{A.41}$$

with a background magnetic field

$$\mathbf{B_0} = \mathbf{B_{0x}}\hat{\mathbf{x}} + \mathbf{B_{0y}}\hat{\mathbf{y}} + \mathbf{B_{0z}}\hat{\mathbf{z}}. \tag{A.42}$$

This results in the governing equations

$$2\mathbf{\Omega} \times \mathbf{u} = -\frac{\mathbf{1}}{\rho_\mathbf{0}}\nabla\mathbf{P} + \frac{\mathbf{1}}{\mu\rho_\mathbf{0}}(\mathbf{B_0} \cdot \nabla)\mathbf{b} + \gamma\alpha\mathbf{\Theta}\hat{\mathbf{z}} \tag{A.43}$$

and

$$\frac{\partial \mathbf{b}}{\partial t} = (\mathbf{B_0} \cdot \nabla)\mathbf{u} \tag{A.44}$$

where μ is magnetic permeability, ρ is density, γ is the Grüneisen parameter, and α is the expansivity, respectively. Then, we also have a non-dimensional buoyancy equation

$$\frac{\partial \Theta}{\partial t} = \beta'(\hat{z} \cdot \mathbf{u}) \tag{A.45}$$

where Θ is a non-dimensional measure of the vertical displacement through a background buoyancy gradient and β' is a measure of the buoyancy gradient.

After a significant amount of algebra, we obtain

$$\left(4(\mathbf{\Omega} \cdot \nabla)^{\mathbf{2}} \frac{\partial^{\mathbf{2}}}{\partial \mathbf{t}^{\mathbf{2}}} + \left[\frac{(\mathbf{B_0} \cdot \nabla)^{\mathbf{2}}}{\mu \rho_{\mathbf{0}}}\right]^{\mathbf{2}} \nabla^{\mathbf{2}} - \gamma \alpha \beta' \frac{\mathbf{B_0} \cdot \nabla)^{\mathbf{2}}}{\mu \rho_{\mathbf{0}}} \nabla^{\mathbf{2}}_{\mathbf{H}}\right) u_z = 0 \tag{A.46}$$

which, when using the definitions

$$\omega_M^2 = \frac{(\mathbf{B_0} \cdot \mathbf{k})^{\mathbf{2}}}{\mu \rho_0}$$

$$\omega_A^2 = \frac{\gamma \alpha \beta' (k_x^2 k_y^2)}{k^2}$$

$$\omega_C^2 = \frac{4(\mathbf{\Omega} \cdot \mathbf{k})^{\mathbf{2}}}{k^2}$$

can be written in the slightly simpler form

$$\omega_{MAC} = \pm \frac{\omega_M^2}{\omega_C} \left(1 + \frac{\omega_A^2}{\omega_M 62}\right)^{1/2} \tag{A.47}$$

(Braginsky, 1964). For further details on all of these wave modes and their derivations, see Finlay (2007).

Appendix B

FVF Operators

This chapter details the complete set of operators used for the FVF method of fluid simulation, including their derivation and final form.

B.1 Derivation of Method

The governing equations are discretized using a combination of finite volume and Fourier (FVF) methods. Each term in the governing equations is integrated over the cell volume, then the volume integral is converted into a surface integral using Gauss' theorem. We index cells by the letter k in the radial direction and l in the latitudinal direction, while the letter m denotes the longitudinal wave number of the Fourier mode. Radial positions r, r_+, and r_- respectively denote the location of the center, top, and bottom faces of the cell in question, and Δr denotes the radial thickness of the cell. Analogous notations is used for θ values. An example cell can be seen in Figure B.1.

B.1.1 Pressure Gradient

For the pressure gradient, we sketch out the derivation in the main text, but for illustration, we show the full derivation below. The pressure gradient is integrated over the cell volume and divided by the total cell volume to define the average force density for each cell

$$\nabla P = \frac{1}{\Delta V} \int_{\Delta V} (\vec{\nabla} P) dV \tag{B.1}$$

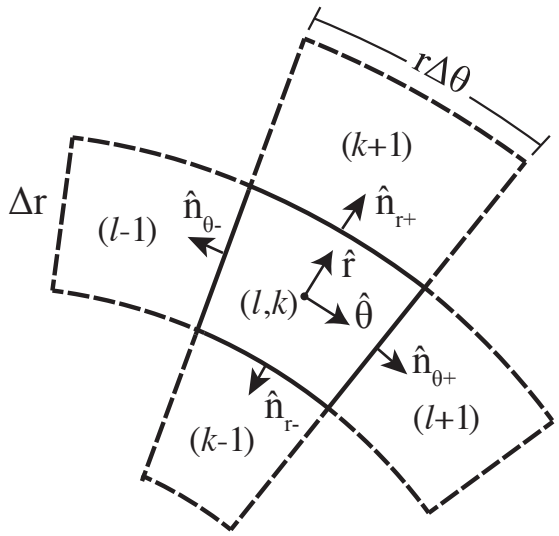

Figure B.1: Finite-volume cell geometry. Dimensions exaggerated for illustration purposes.

where $\Delta V = r^2 \sin\theta \Delta r \Delta\theta \Delta\phi$ represents the volume of the cell and integral is taken over the total cell volume ΔV. We convert the volume integral into a surface integral using Gauss's theorem:

$$\frac{1}{\Delta V}\int_{\Delta V}(\vec{\nabla}P)dV = \frac{1}{\Delta V}\int_S P d\vec{S} \tag{B.2}$$

where the integral is now taken over the total surface area of the cell S. The average pressure gradient in (B.2) is a vector quantity with three components. We define the vector components using the spherical basis vectors $\hat{r}, \hat{\theta}, \hat{\phi}$ at the center of the cell (Figure 1). For example, the radial component is

$$(\nabla P)_r = \left(\frac{1}{\Delta V}\int_S P d\vec{S}\right)\cdot \hat{r}. \tag{B.3}$$

The surface integral split over individual faces, where A_{r_+} and A_{r_-} denote the area of the top and bottom radial faces and $\hat{n}_{r_+}$ and $\hat{n}_{r_-}$ represent the vectors normal to those faces (Figure B.1). Using similar notation for other

faces gives

$$
\begin{aligned}
(\nabla P)_r = \frac{1}{\Delta V}\big\{ & P_{r_+} A_{r_+} (\hat{r}\cdot\hat{n}_{r_+}) + P_{r_-} A_{r_-} (\hat{r}\cdot\hat{n}_{r_-}) \\
& + P_{\theta_+} A_{\theta_+} (\hat{r}\cdot\hat{n}_{\theta_+}) + P_{\theta_-} A_{\theta_-} (\hat{r}\cdot\hat{n}_{\theta_-}) \\
& + P_{\phi_+} A_{\phi_+} (\hat{r}\cdot\hat{n}_{\phi_+}) + P_{\phi_-} A_{\phi_-} (\hat{r}\cdot\hat{n}_{\phi_-})\big\}\,.
\end{aligned}
\tag{B.4}
$$

The scalar product between the basis vectors and the surface normals account for the spherical geometry. For example, there is a contribution to the pressure force due to the influence of pressure on the A_{θ_+} and A_{θ_-} faces. The normal vectors n_{θ_+} and n_{θ_-} each have a small radial component at the center of the cell, which depends on the cell width $\Delta\theta$, so we quantify $\hat{r}\cdot\hat{n_{\theta_+}}$ to first order in $\Delta\theta$. Similarly, the surface areas and cell volume are calculated to first order in the cell dimensions. Expanding (B.4) gives

$$
\begin{aligned}
(\nabla P)_r = \frac{1}{\Delta V}\big\{ & P_{r_+} r_+^2 \sin\theta \Delta\theta\Delta\phi(1) + P_{r_-} r_-^2 \sin\theta\Delta\theta\Delta\phi(-1) \\
& + P_{\theta_+} r\Delta r\Delta\phi \sin\theta_+ (-\sin\tfrac{\Delta\theta}{2}) + P_{\theta_-} r\Delta r\Delta\phi\sin\theta_- (-\sin\tfrac{\Delta\theta}{2}) \\
& + P_{\phi+} r\Delta r\Delta\theta(-\sin\theta\sin\tfrac{\Delta\phi}{2}) + P_{\phi-} r\Delta r\Delta\theta(-\sin\theta\sin\tfrac{\Delta\phi}{2})\big\}\,.
\end{aligned}
\tag{B.5}
$$

Using the definition of the infinitesimal volume element $\Delta V = r^2\sin\theta\Delta r\Delta\theta\Delta\phi$ and taking the small-angle approximation $\sin\frac{\Delta\theta}{2}\approx\frac{\Delta\theta}{2}$ and $\sin\frac{\Delta\phi}{2}\approx\frac{\Delta\phi}{2}$, the resulting equation is

$$
\begin{aligned}
(\nabla P)_r = P_{r_+}\frac{r_+^2}{r^2\Delta r} - P_{r_-}\frac{r_-^2}{r^2\Delta r} - P_{\theta_+}\frac{\sin\theta_+}{2r\sin\theta} \\
- P_{\theta_-}\frac{\sin\theta_-}{2r\sin\theta} - P_{\phi_+}\frac{1}{2r} - P_{\phi_-}\frac{1}{2r}.
\end{aligned}
\tag{B.6}
$$

The final form of the radial component of the pressure gradient is obtained by approximating the pressure at each face as the average of the pressure in each adjoining cell e.g. $P_{r_+} = \frac{1}{2}(P^{(k+1,l)} + P^{(k,l)})$. Here, k, l are cell indices in the radial and latitudinal coordinate directions (see fig. B.1). Using the identity $r_+^2 - r_-^2 = 2r\Delta r$ and recognizing that $P^{(k,l)} = \frac{1}{2}(P_{\phi_+} + P_{\phi_-})$, we obtain

$$
\begin{aligned}
(\nabla P)_r^{(k,l)} = \frac{r_+^2}{2r^2\Delta r}P^{(k+1,l)} - \frac{r_-^2}{2r^2\Delta r}P^{(k-1,l)} - \frac{\sin\theta_+}{4r\sin\theta}P^{(k,l+1)} \\
- \frac{\sin\theta_-}{4r\sin\theta}P^{(k,l-1)} - \frac{\sin\theta_+ + \sin\theta_-}{4r\sin\theta}P^{(k,l)}.
\end{aligned}
\tag{B.7}
$$

The $\hat{\theta}$ component of the pressure gradient is derived in a similar manner, so we simply state the result:

$$(\nabla P)_{\theta}^{(k,l)} = \left(\frac{sin\theta_{+}}{2r\sin\theta\Delta\theta}\right) P^{(k,l+1)} - \left(\frac{sin\theta_{-}}{2r\sin\theta\Delta\theta}\right) P^{(k,l-1)} + \left(\frac{(sin\theta_{+} - \sin\theta_{-})}{2r\sin\theta\Delta\theta} - \frac{cos\theta}{rsin\theta}\right) P^{(k,l)} \tag{B.8}$$

The $\hat{\phi}$ component of the pressure gradient, all faces but those in the $\hat{\phi}$ direction are perpendicular to the $\hat{\phi}$ basis vector and therefore do not influence $(\nabla P)_{\phi}$. Then, adopting the small angle approximation $\sin\frac{\Delta\phi}{2} \approx \frac{\Delta\phi}{2}$ and following a similar procedure as used in $\hat{r}$ and $\hat{\theta}$ components, the expression for $(\nabla P)_{\phi}$ simplifies into

$$(\nabla P)_{\phi}^{(k,l)} = \left(\frac{im}{rsin\theta}\right) P^{(k,l)} \tag{B.9}$$

where m represents the Fourier mode.

B.1.2 Vector-Valued Variables

A similar procedure is used for other terms in the governing equations. One small difference arises with vector-valued variables because the basis vectors change across the cell. To illustrate, we derive the numerical expression for divergence. Integrating over the cell volume gives

$$\nabla \cdot \vec{v} = \frac{1}{\Delta V}\int_{\Delta V} (\nabla \cdot \vec{v})\, dV = \frac{1}{\Delta V}\int_{S} \vec{v} \cdot d\vec{S}. \tag{B.10}$$

The surface integral involves the dot product of the normal vector of each face and the local vector variable, $\hat{v}$, giving

$$\nabla \cdot \vec{v} = \frac{1}{\Delta V}\left\{\vec{v}\cdot\hat{n}_{r_+}A_{r_+} + \vec{v}\cdot\hat{n}_{r_-}A_{r_-} + \vec{v}\cdot\hat{n}_{\theta_+}A_{\theta_+} + \vec{v}\cdot\hat{n}_{\theta_-}A_{\theta_-} + \vec{v}\cdot\hat{n}_{\phi_+}A_{\phi_+} + \vec{v}\cdot\hat{n}_{\phi_-}A_{\phi_-}\right\}. \tag{B.11}$$

As the coordinate vectors are locally orthogonal, only one component of the vector variable contributes on each face. Hence, the divergence simplifies to

$$\nabla \cdot \vec{v} = \frac{1}{\Delta V}\left\{v_{r_+}A_{r_+} + v_{r_-}A_{r_-} + v_{\theta_+}A_{\theta_+} + v_{\theta_-}A_{\theta_-} + v_{\phi_+}A_{\phi_+} + v_{\phi_-}A_{\phi_-}\right\}. \tag{B.12}$$

For notational simplicity, we introduce notation for numerical derivative operators

$$\nabla_r v_i^{(k,l)} = \left(\frac{r_+^2}{2r^2\Delta r}\right) v_i^{(k+1,l)} - \left(\frac{r_-^2}{2r^2\Delta r}\right) v_i^{(k-1,l)} + \left(\frac{1}{r}\right) v_i^{(k,l)} \tag{B.13}$$

$$\nabla_\theta v_i^{(k,l)} = \left(\frac{sin\theta_+}{2r\sin\theta\Delta\theta}\right) v_i^{(k,l+1)} + \left(\frac{-sin\theta_-}{2r\sin\theta\Delta\theta}\right) v_i^{(k,l-1)} + \left(\frac{sin\theta_+ - \sin\theta_-}{2r\sin\theta\Delta\theta}\right) v_i^{(k,l)} \tag{B.14}$$

$$\nabla_\phi v_i^{(k,l)} = \left(\frac{im}{rsin\theta}\right) v_i^{(k,l)}. \tag{B.15}$$

where $i \in \{r, \theta, \phi\}$ as the operators are valid for any component of the velocity and magnetic fields. Using this notation, the mass continuity equation simplifies to

$$\nabla \cdot \vec{v} = \nabla_r v_r + \nabla_\theta v_\theta + \nabla_\phi v_\phi \tag{B.16}$$

The scalar Laplace operator is derived by the same method and is simply

$$\begin{aligned}\nabla^2 v_i^{(k,l)} = &\left(\frac{r_+^2}{r^2\Delta r^2}\right) v_i^{(k+1,l)} + \left(\frac{r_-^2}{r^2\Delta r^2}\right) v_i^{(k-1,l)} + \left(\frac{sin\theta_+}{r^2\sin\theta\Delta\theta^2}\right) v_i^{(k,l+1)} \\ &+ \left(\frac{sin\theta_-}{r^2\sin\theta\Delta\theta^2}\right) v_i^{(k,l-1)} - \left(\frac{r_+^2 + r_-^2}{r^2\Delta r^2} + \frac{sin\theta_+ + sin\theta_-}{r^2 sin\theta\Delta\theta^2} + \frac{m^2}{r^2 sin^2\theta}\right) v_i^{(k,l)}.\end{aligned} \tag{B.17}$$

B.1.3 Composite Terms

All other terms in the governing equations can be expressed in terms of the gradient operators (B.13 - B.15) and scalar Laplacian operator (B.17). The derivations follow the same method as detailed above but include much more algebra, so we simply state the results. The components of the vector Laplacian are

$$(\nabla^2\vec{v})_r = \nabla^2 v_r - \frac{1}{r}\nabla_\theta v_\theta - \frac{1}{r}\nabla_\phi v_\phi \tag{B.18}$$

$$(\nabla^2\vec{v})_\theta = \nabla^2 v_\theta + \frac{1}{r}\nabla_\theta v_r - \frac{\cot\theta}{r}\nabla_\phi v_\phi \tag{B.19}$$

$$(\nabla^2\vec{v})_\phi = \nabla^2 v_\phi + \frac{1}{r}\nabla_\phi v_r + \frac{\cot\theta}{r}\nabla_\phi v_\theta. \tag{B.20}$$

The components of divergence of magnetic stress are

$$(\nabla \cdot T_l)_r = \nabla_r(B_{0r}b_r - B_{0\theta}b_\theta - B_{0\phi}b_\phi) + \nabla_\theta(B_{0\theta}b_r + B_{0r}b_\theta) + \nabla_\phi(B_{0r}b_\phi + B_{0\phi}b_r) \tag{B.21}$$

$$(\nabla \cdot T_l)_\theta = \nabla_r(B_{0r}b_\theta - B_{0\theta}b_r) + \nabla_\theta(B_{0\theta}b_\theta - B_{0r}b_r - B_{0\phi}b_\phi) + \nabla_\phi(B_{0\theta}b_\phi + B_{0\phi}b_\theta) \tag{B.22}$$

$$(\nabla \cdot T_l)_\phi = \nabla_r(B_{0r}b_\phi - B_{0\phi}b_r) + \nabla_\theta(B_{0\theta}b_\phi + B_{0\phi}b_\theta) + \nabla_\phi(B_{0\phi}b_\phi - B_{0r}b_r - B_{0\theta}b_\theta). \tag{B.23}$$

And the magnetic advection terms in the Induction equation are

$$(\nabla \times \vec{v} \times \vec{B})_r = \nabla_\theta(B_{0\theta}v_r - B_{0r}v_\theta) + \nabla_\phi(B_{0\phi}v_r - B_{0r}v_\phi) \tag{B.24}$$

$$(\nabla \times \vec{v} \times \vec{B})_\theta = \nabla_r(B_{0r}v_\theta - B_{0\theta}v_r) + \nabla_\phi(B_{0\phi}v_\theta - B_{0\theta}v_\phi) \tag{B.25}$$

$$(\nabla \times \vec{v} \times \vec{B})_\phi = \nabla_r(B_{0r}v_\phi - B_{0\phi}v_r) + \nabla_\theta(B_{0\theta}v_\phi - B_{0\phi}v_\theta).. \tag{B.26}$$

B.2 Boundary Conditions

Boundary conditions are implemented directly into the cells at the top boundaries. The top core-mantle boundary is taken at the edge of the uppermost cell in the domain, with boundary conditions modifying the form of the operators used for the governing equations in the boundary cell, while the bottom boundary is more complex due to magnetic coupling.

B.2.1 Core-Mantle Boundary

At the core-mantle boundary, we apply free-slip conditions at the CMB, so that $v_r = 0$. This modifies the derivation of the operators in a simple way, so that in (B.12) the term involving v_{r_+} is zero. Then, following the same derivation as used previously, we obtain

$$\nabla_r v_r^{(N_k-1,l)} = -\left(\frac{r_-^2}{2r^2\Delta r}\right) v_r^{(N_k-2,l)} - \left(\frac{r_-^2}{2r^2\Delta r}\right) v_r^{(N_k-1,l)} \tag{B.27}$$

to replace (B.13) for cells at the top of the domain ($k = N_k - 1$).

For horizontal velocities governed by the free-slip conditions at the CMB, $\partial v_{\theta,\phi}/\partial r = 0$. This causes the stress to disappear on the top face and modifies the derivation of the radial operator (B.13) in a similar manner, resulting in

$$\nabla_r v_{\theta,\phi}^{(N_k-1,l)} = -\left(\frac{r_-^2}{2r^2\Delta r}\right) v_{\theta,\phi}^{(N_k-2,l)} + \left(\frac{2r_+^2 - r_-^2}{2r^2\Delta r}\right) v_{\theta,\phi}^{(N_k-1,l)} \tag{B.28}$$

for the top cells of the domain.

Pressure, as a scalar variable, requires a bit more consideration. At the top of the domain $\partial P/\partial r = 0$. Using a first-order interpolation, this implies that $p^{N_k,l} = p^{N_k-1,l}$. Applying this constraint to (B.7), we find

$$(\nabla P)_r^{(N_k-1,l)} = -\left(\frac{r_-^2}{2r^2\Delta r}\right) P^{(N_k-2,l)} - \left(\frac{\sin\theta_+}{4r\sin\theta}\right) P^{(N_k-1,l+1)}\,. \tag{B.29}$$

Pseudo-vacuum boundary conditions are used for the horizontal magnetic field at the CMB

$$b_{\phi,\theta}|_{CMB} = 0\,. \tag{B.30}$$

This is mathematically identical to the conditions for v_r, and results in the same expression for the operator at the boundary, given in (B.27).

B.2.2 Layer Bottom Boundary

At the base of the layer, wave motion within the layer couples to fluid motion in the bulk of the core through Lorentz forces and this coupling must be taken into account in the boundary conditions for the magnetic field. In the main text, we work through a derivation of the magnetic boundary conditions and end up with the relation shown in equation (31, main text) and reproduced here

$$b_{\theta,\phi}^+ = \frac{\delta B_{0r} P_m}{2(1+i)E}\, v_{\theta,\phi}^+ \tag{B.31}$$

where

$$\delta = \sqrt{\frac{2E}{\omega P_m}} \tag{B.32}$$

is the non-dimensional magnetic skin depth. This relation relates (dimensionless) magnetic perturbations directly to (dimensionless) velocity perturbations on the bottom layer boundary.

In order to implement this in our numerical model, we choose to place the bottom boundary of the layer in the center of the lowermost cell in the domain. With this choice, the variables in the bottom cell are taken to be identically at the boundary, and are therefore governed purely by their respective boundary conditions. For horizontal magnetic perturbations $b_{\theta,\phi}$, this means we now use (B.31) instead of the Lorentz equation in the bottom cell

$$b_{\theta,\phi}^{(0,l)} - \frac{\delta B_{0r} P_m}{2(1+i)E}\, v_{\theta,\phi}^{(0,l)} = 0\,. \tag{B.33}$$

For velocity, we use free-slip conditions and we impose zero radial gradients in pressure. For a detailed discussion justifying these choices, see section 2.1.6 in the main text. Again, these variables are completely governed by their respective boundary conditions in the bottom cell, so that radial velocity and displacement are identically zero

$$v_r^{(0,l)} = u_r^{(0,l)} = 0\,. \tag{B.34}$$

Then, the boundary condition for horizontal velocities v_θ and v_ϕ, are implemented using a first-order numerical approximation

$$\frac{\partial v_{\theta,\phi}}{\partial r}\Big|_{bottom} = 0 \implies v_{\theta,\phi}^{(0,l)} - v_{\theta,\phi}^{(1,l)} = 0\,. \tag{B.35}$$

For pressure, $\partial_r P|_{\text{bottom}} = 0$ and we again use a first-order numerical approximation

$$\partial_r P|_{\text{bottom}} = 0 \implies P^{(1,l)} - P^{(0,l)} = 0\,. \tag{B.36}$$

Appendix C

eMAC Wave Structures

This chapter details the spatial wave structure of all magnetic field and fluid variables for a selection of representative eMAC wave modes.

C.1 Fundamental Radial Mode

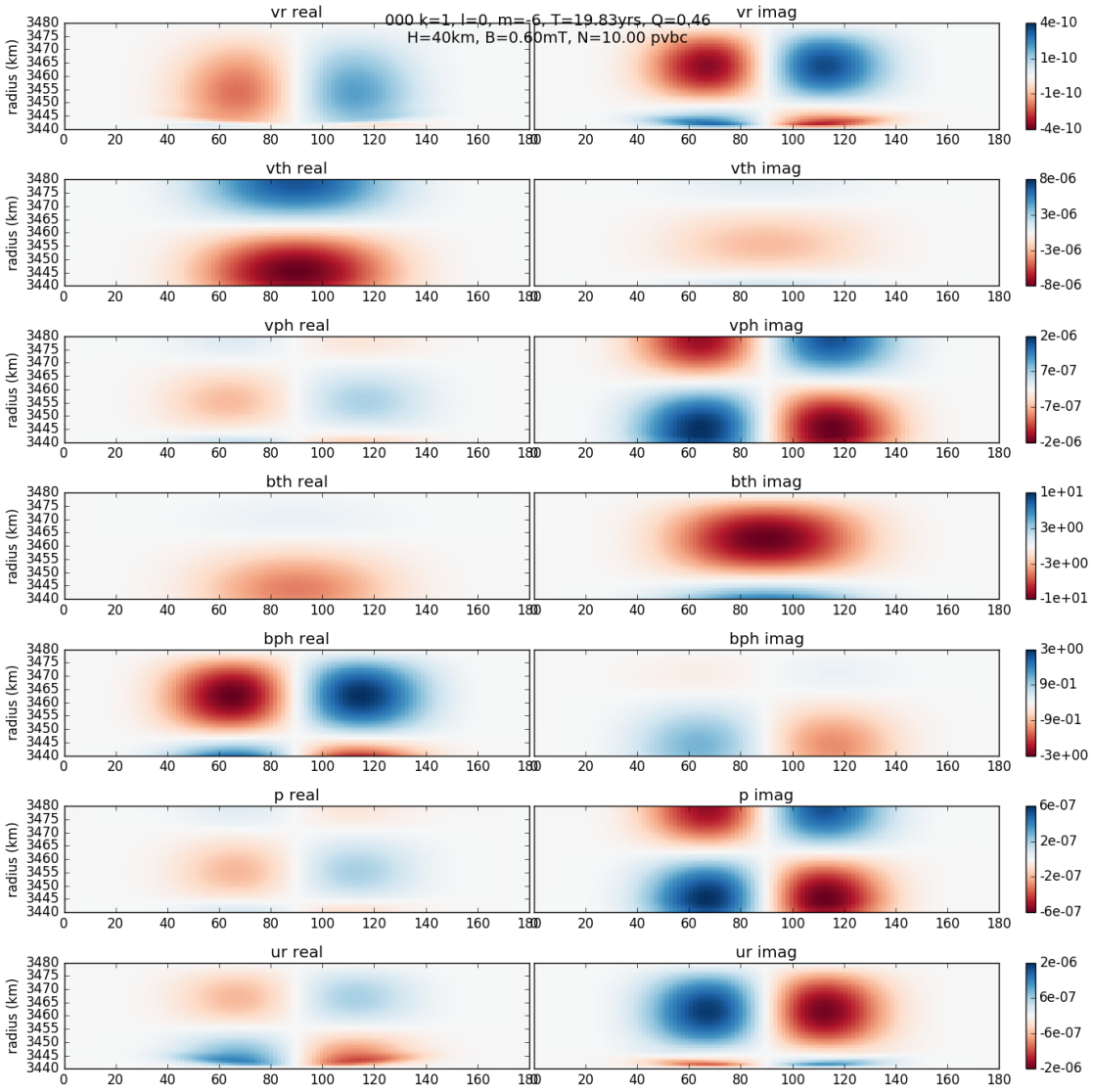

Figure C.1: eMAC wave structure, k=1, l=0, m=6, period=19.8 yrs, Q=0.46. SOC properties of H=40 km , N=10, B=0.6 mT.

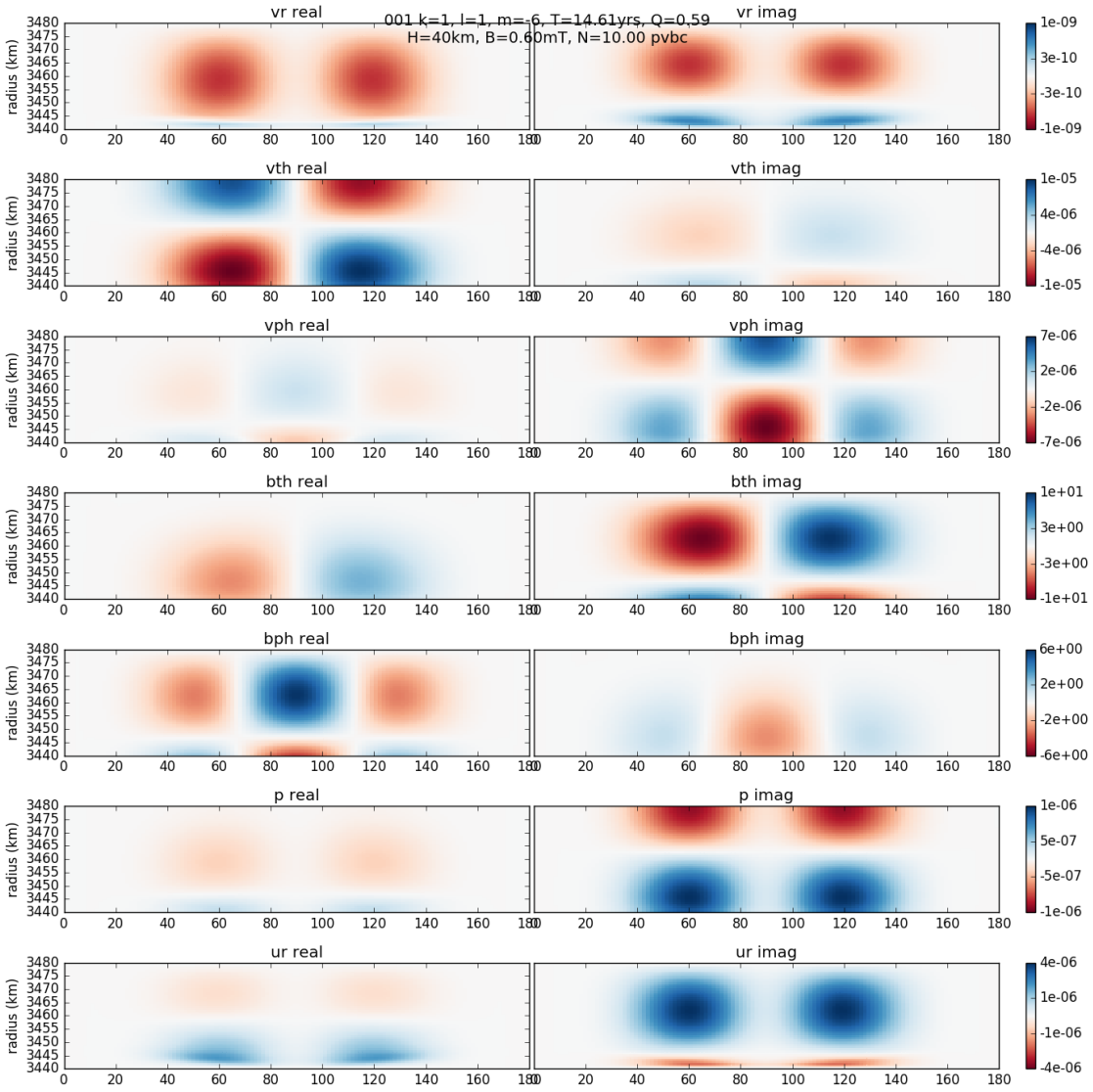

Figure C.2: eMAC wave structure, k=1, l=1, m=6, period=14.61 yrs, Q=0.59. SOC properties of H=40 km , N=10, B=0.6 mT.

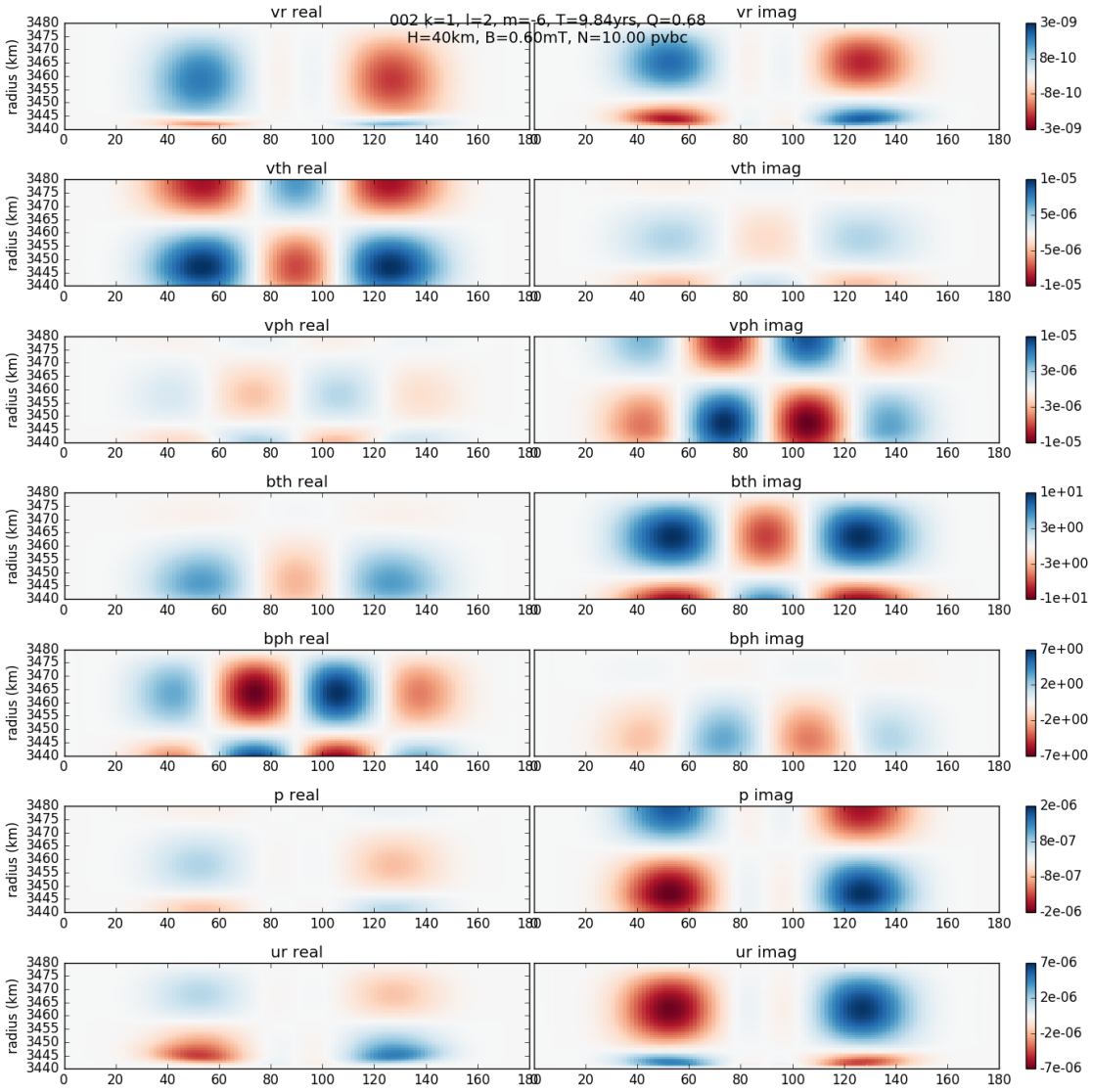

Figure C.3: eMAC wave structure, k=1, l=2, m=6, period=9.84 yrs, Q=0.68. SOC properties of H=40 km , N=10, B=0.6 mT.

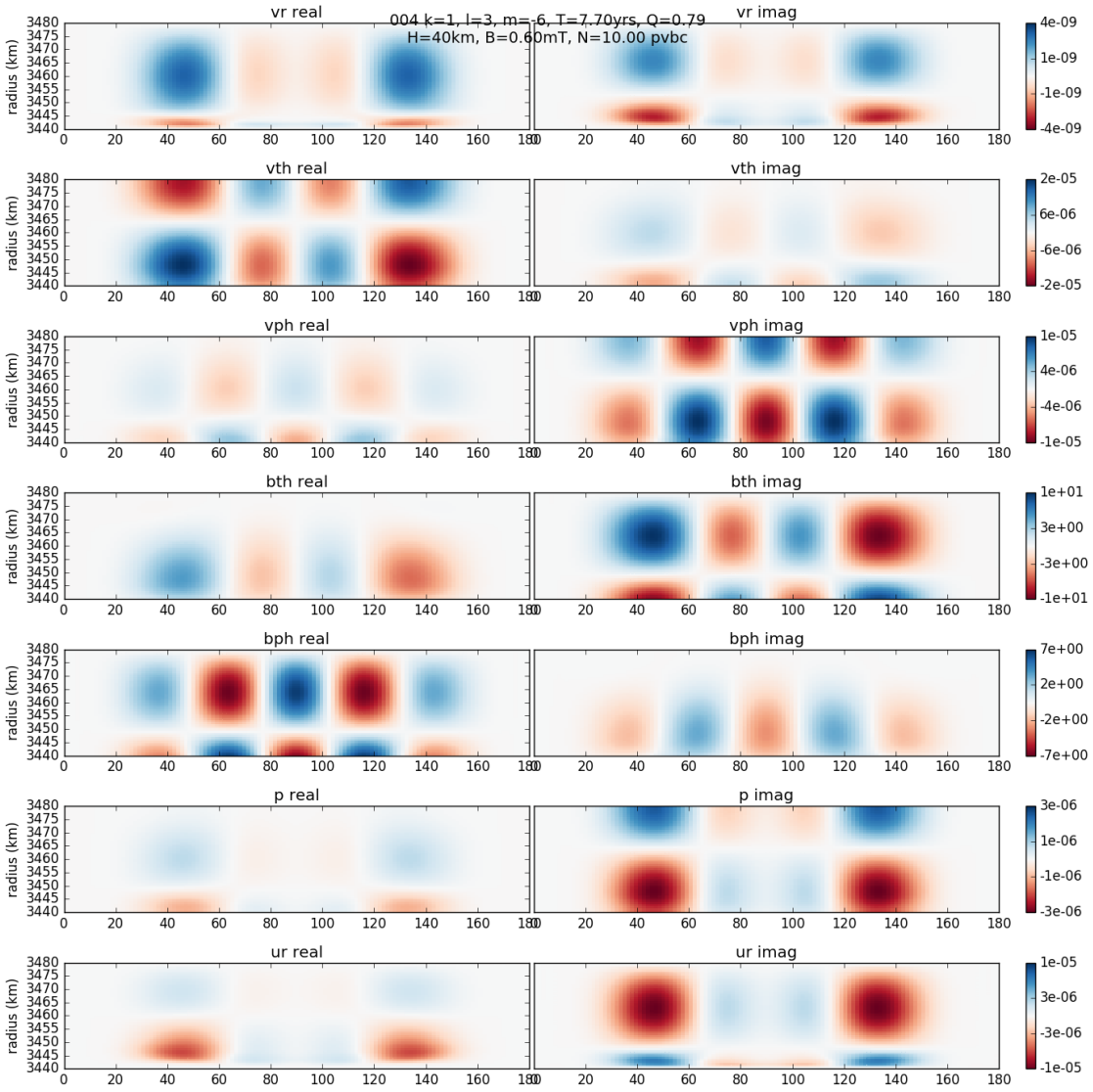

Figure C.4: eMAC wave structure, k=1, l=3, m=6, period=7.70 yrs, Q=0.79. SOC properties of H=40 km , N=10, B=0.6 mT.

C.2 First Radial Overtone

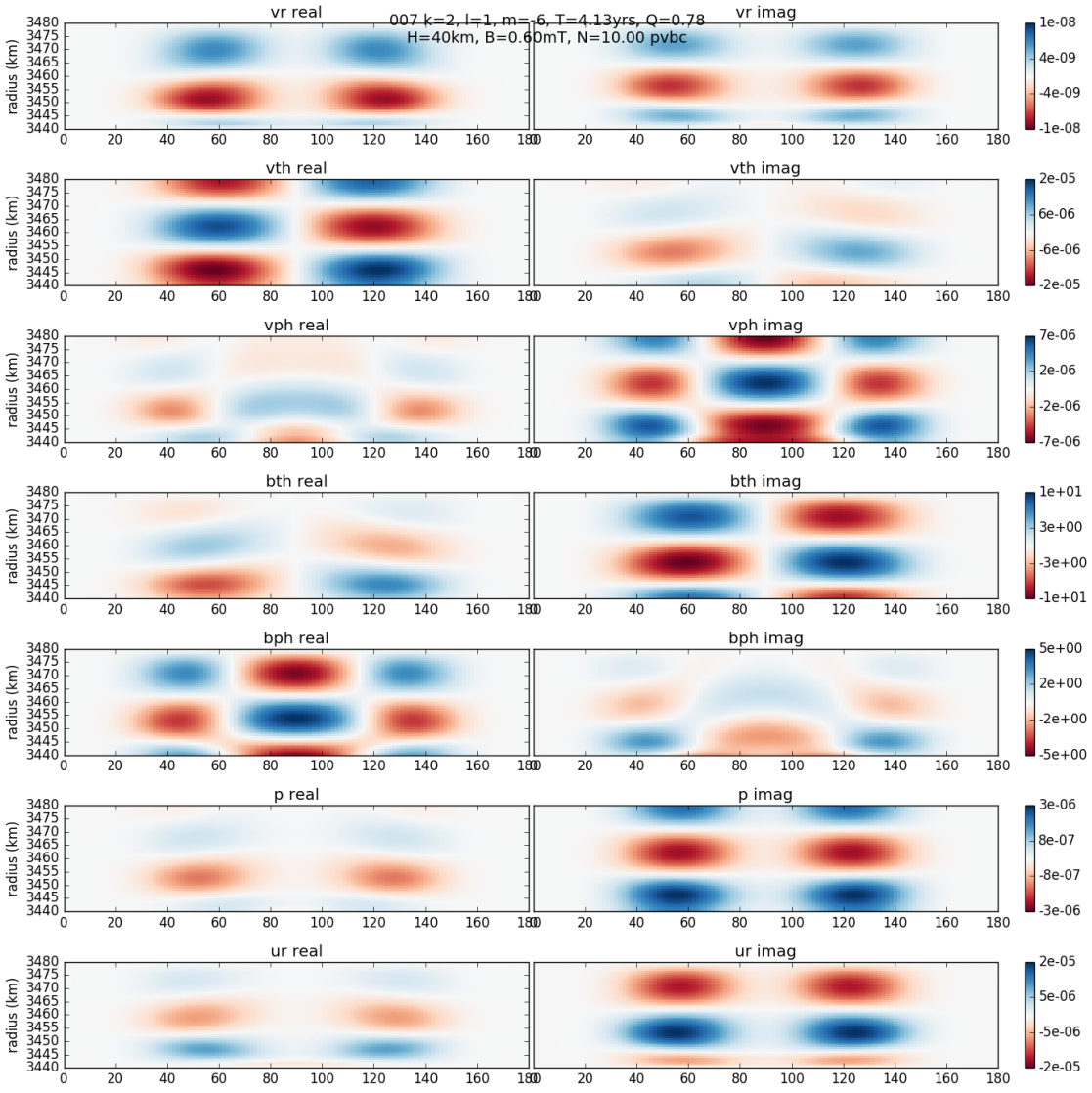

Figure C.5: eMAC wave structure, k=2, l=1, m=6, period=4.13 yrs, Q=0.78. SOC properties of H=40 km , N=10, B=0.6 mT.

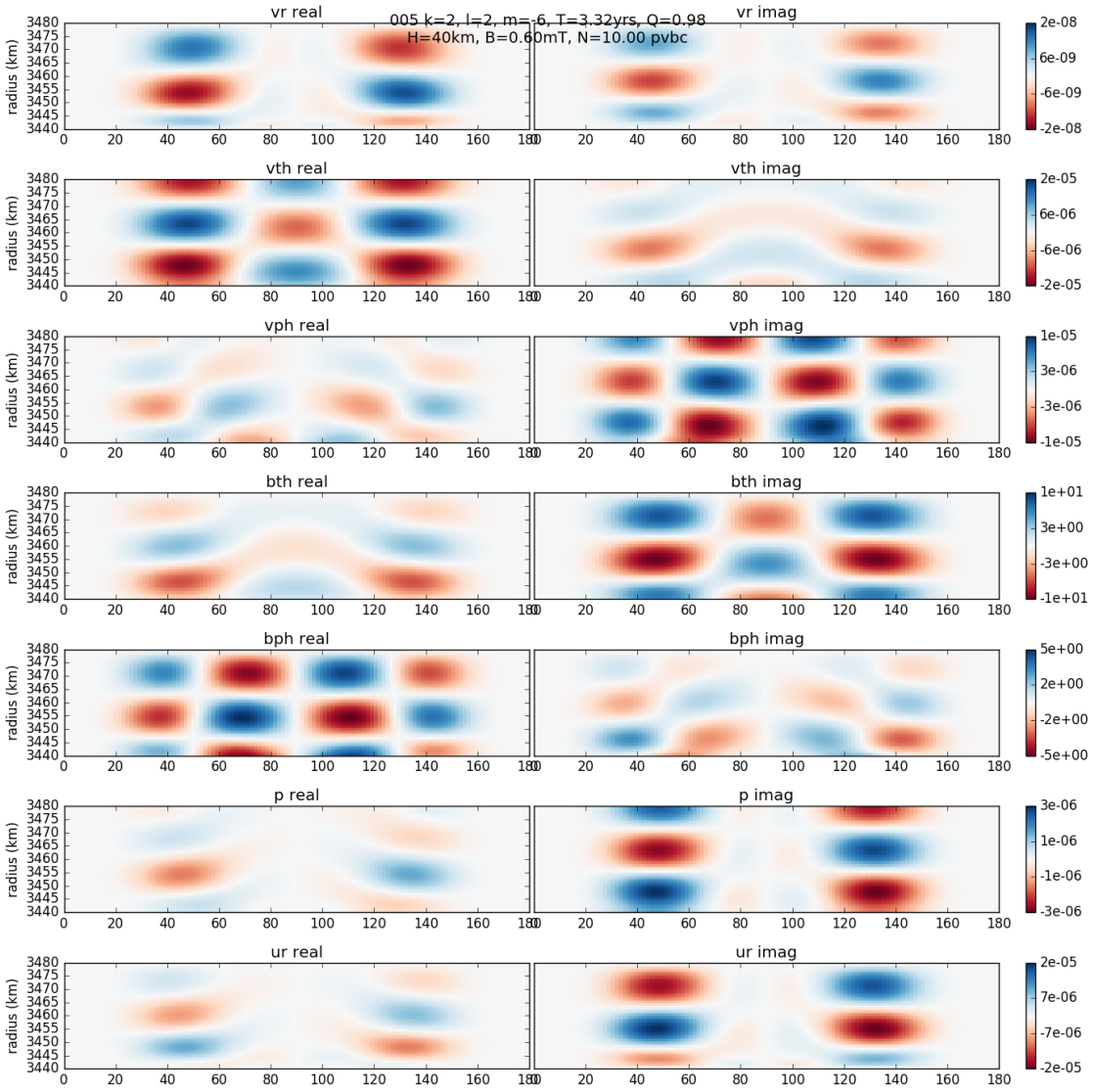

Figure C.6: eMAC wave structure, k=2, l=2, m=6, period=3.32 yrs, Q=0.98. SOC properties of H=40 km , N=10, B=0.6 mT.

Appendix D

SOC Wave Variations

This chapter details the wave periods, quality factors, and latitudinal extent of SOC waves found across many model runs.

D.1 Westward Modes

D.1.1 Mid-Latitudes

D.1.1.1 Variation with Magnetic Field Strength

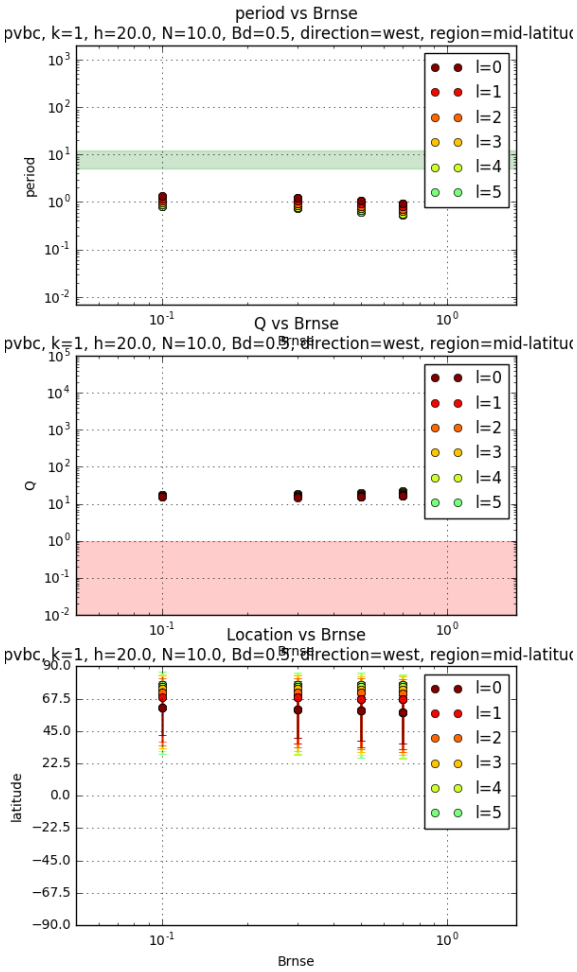

Figure D.1: Wave Dependence on magnetic field strength (B), westward modes, mid-latitudes, H=20 km, N=10 Ω

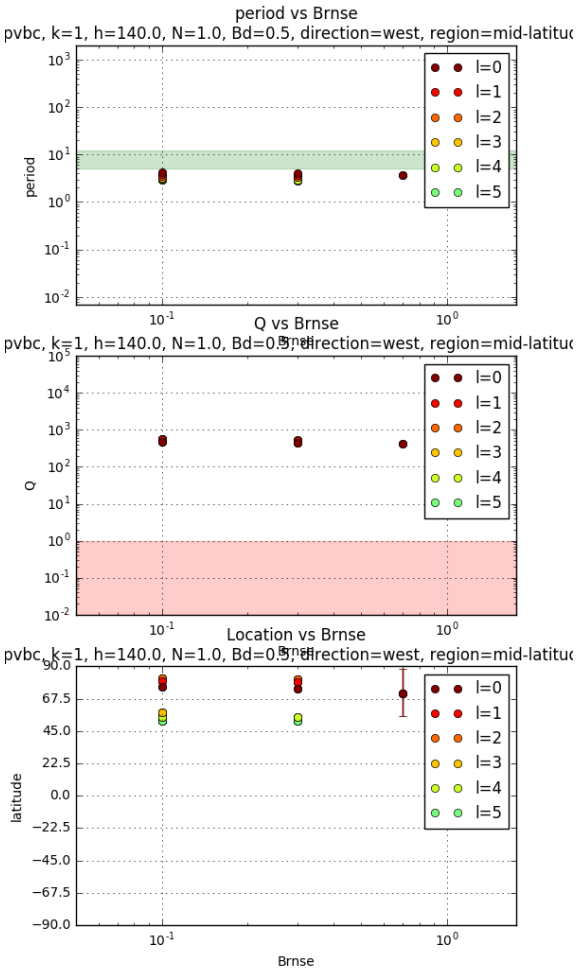

Figure D.2: Wave Dependence on magnetic field strength (B), westward modes, mid-latitudes, H=140 km, N=1 Ω

D.1.1.2 Variation with SOC Thickness

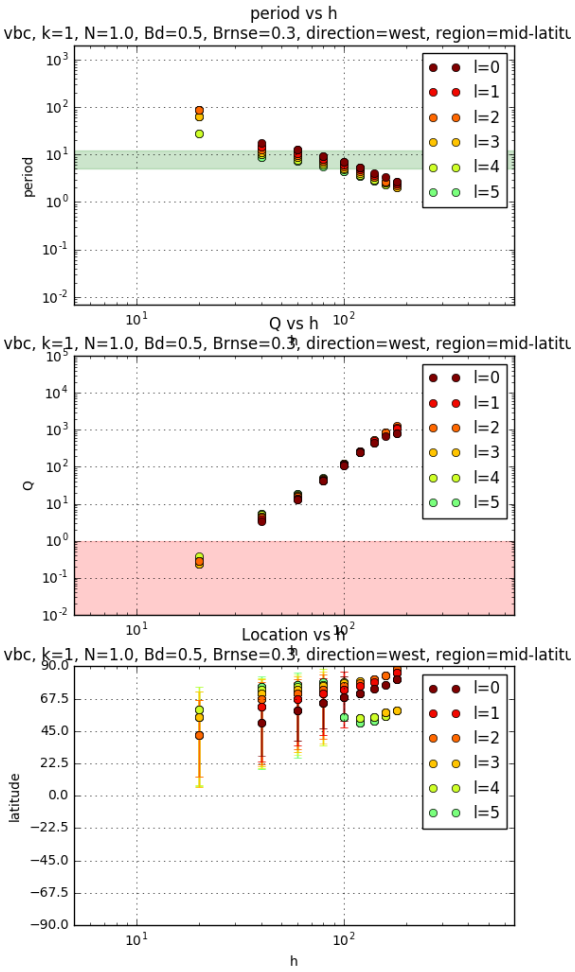

Figure D.3: Wave Dependence on SOC thickness (H), westward modes, mid-latitudes, N=1 Ω

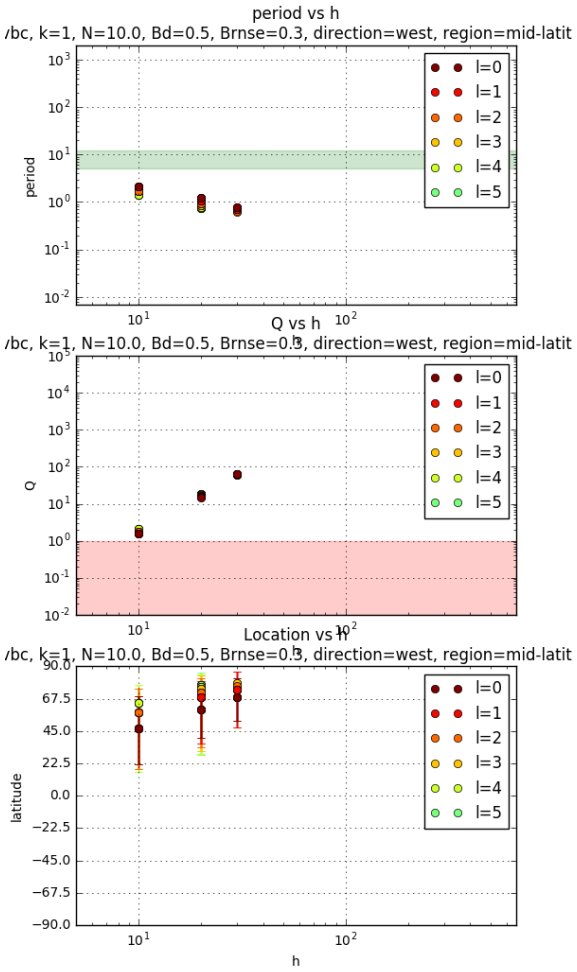

Figure D.4: Wave Dependence on SOC thickness (H), westward modes, mid-latitudes, N=10 Ω

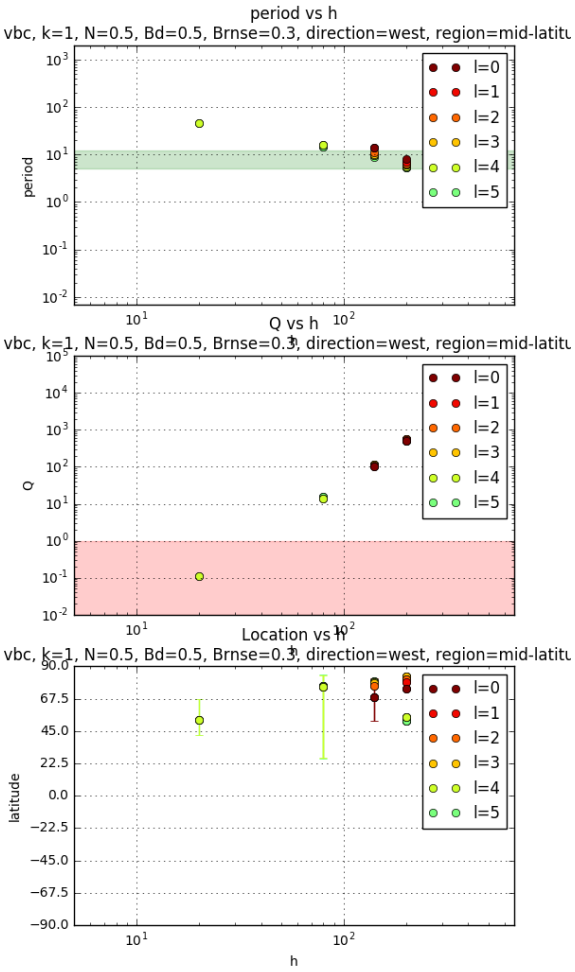

Figure D.5: Wave Dependence on SOC thickness (H), westward modes, mid-latitudes, N=0.5 Ω

D.1.1.3 Variation with SOC Buoyancy

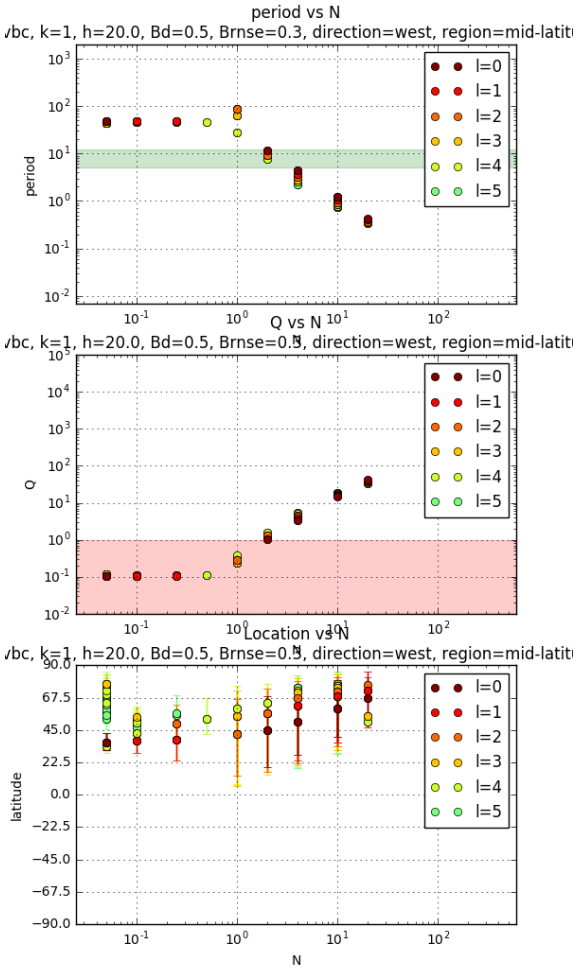

Figure D.6: Wave Dependence on SOC buoyancy (N), westward modes, mid-latitudes, H=20 km

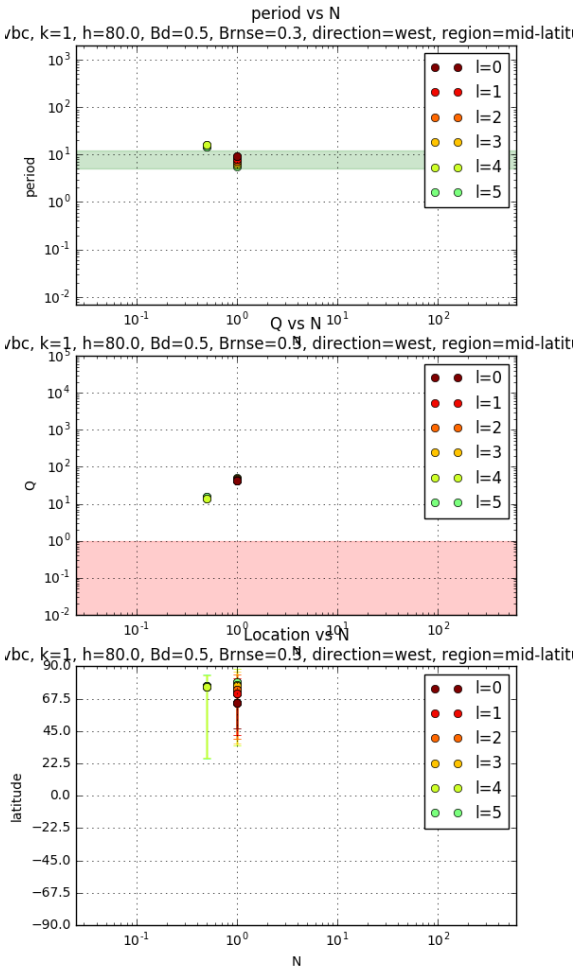

Figure D.7: Wave Dependence on SOC buoyancy (N), westward modes, mid-latitudes, H=80 km

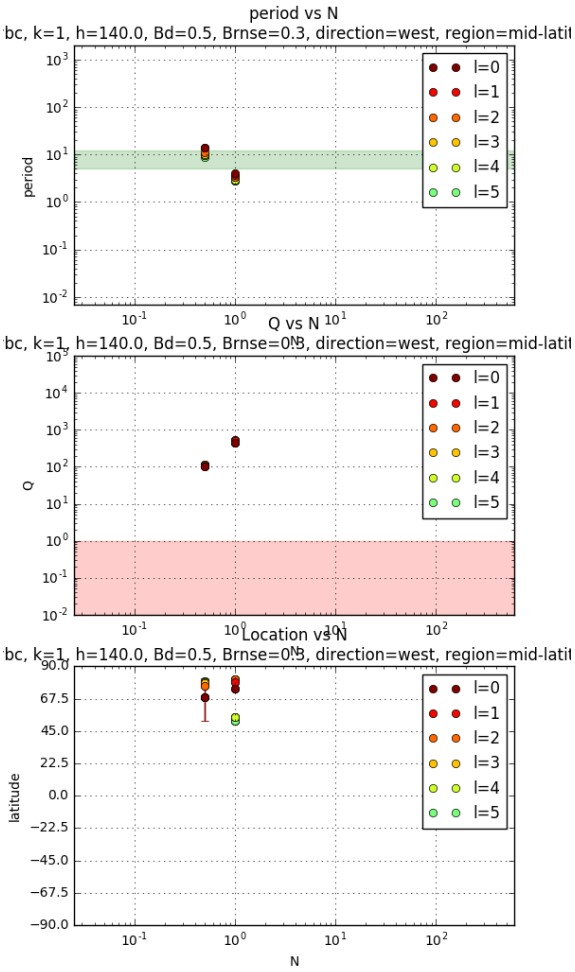

Figure D.8: Wave Dependence on SOC buoyancy (N), westward modes, mid-latitudes, H=140 km

D.1.2 Equatorial Region

D.1.2.1 Variation with Magnetic Field Strength

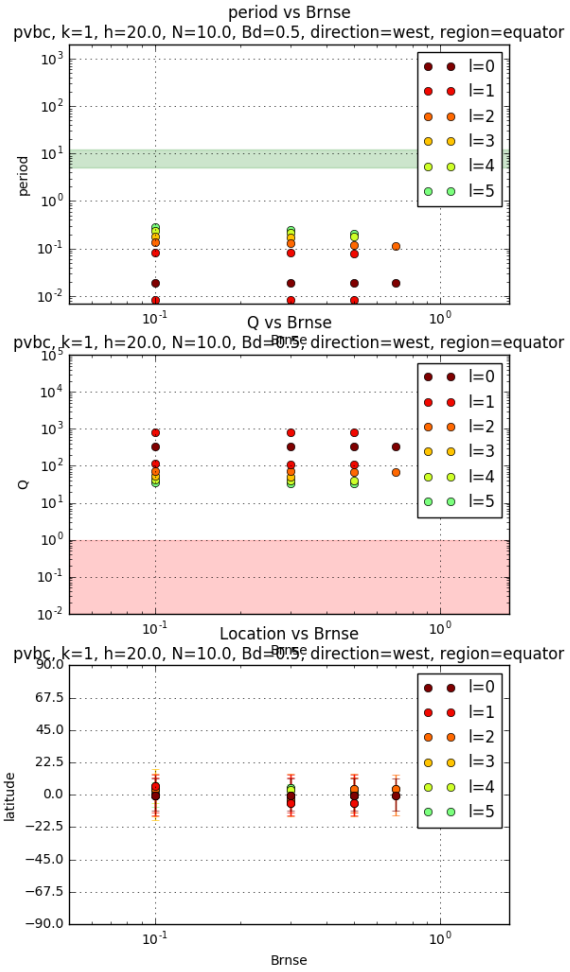

Figure D.9: Wave Dependence on magnetic field strength (B), westward modes, equatorial region, H=20 km, N=10 Ω

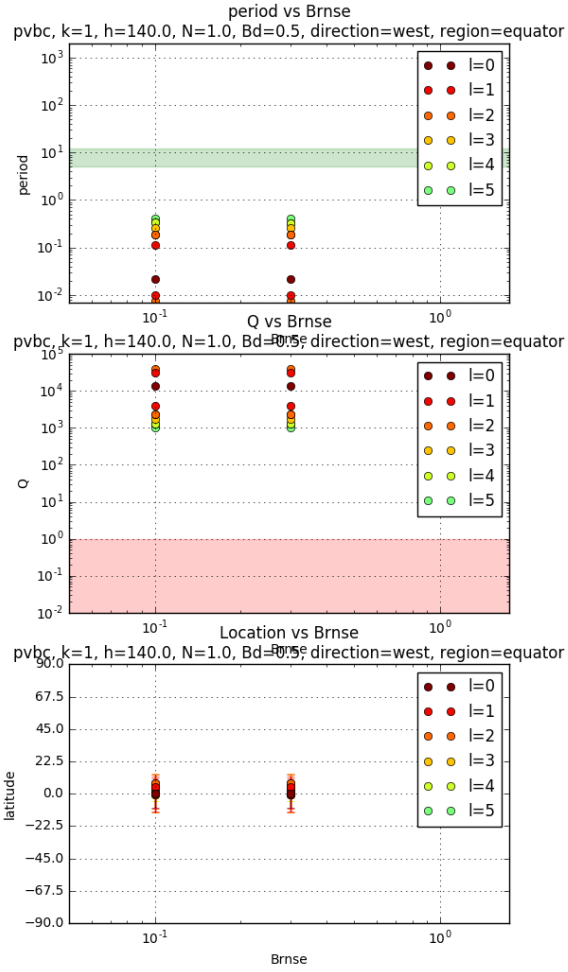

Figure D.10: Wave Dependence on magnetic field strength (B), westward modes, equatorial region, H=140 km, N=1 Ω

D.1.2.2 Variation with SOC Thickness

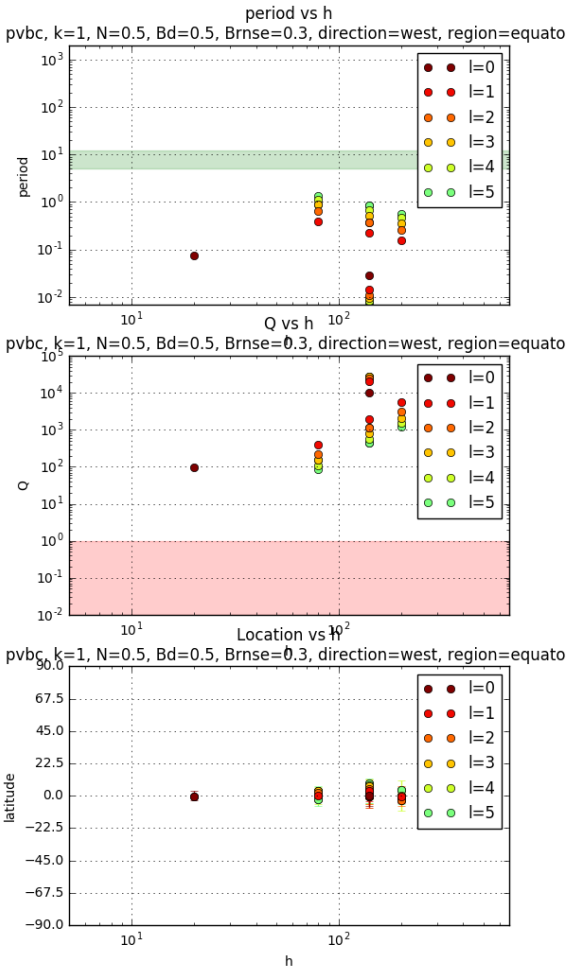

Figure D.11: Wave Dependence on SOC thickness (H), westward modes, equatorial region, N=0.5 Ω

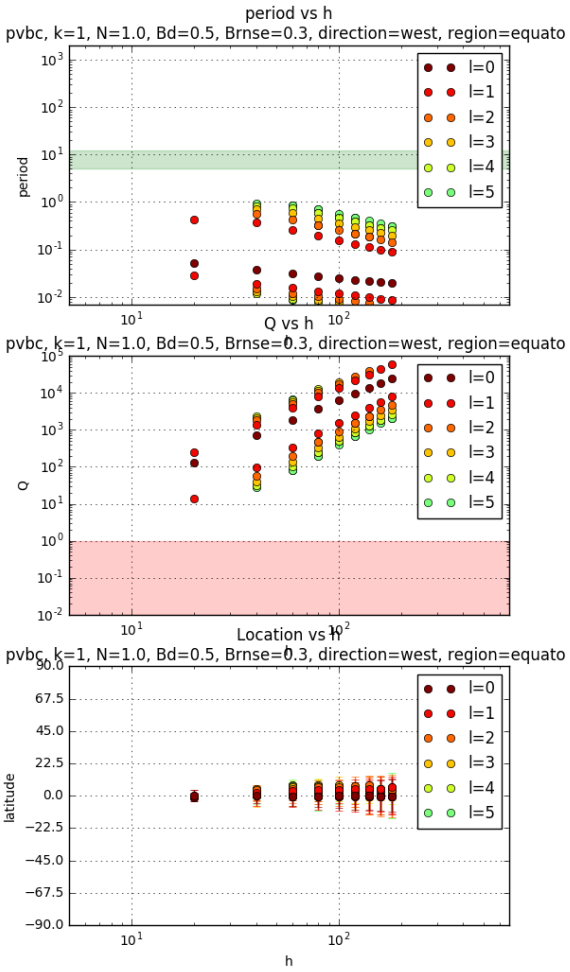

Figure D.12: Wave Dependence on SOC thickness (H), westward modes, equatorial region, N=1 Ω

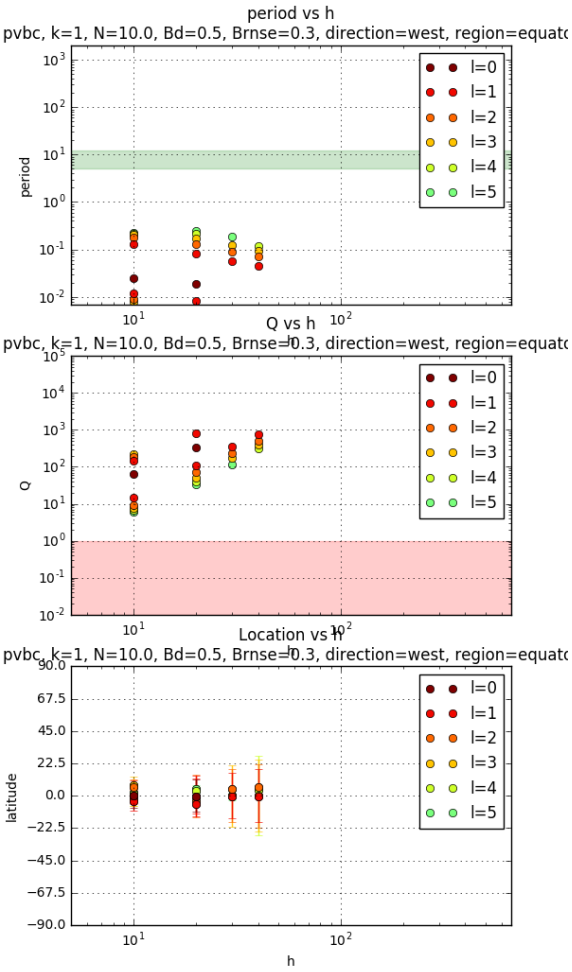

Figure D.13: Wave Dependence on SOC thickness (H), westward modes, equatorial region, N=10 Ω

D.1.2.3 Variation with SOC Buoyancy

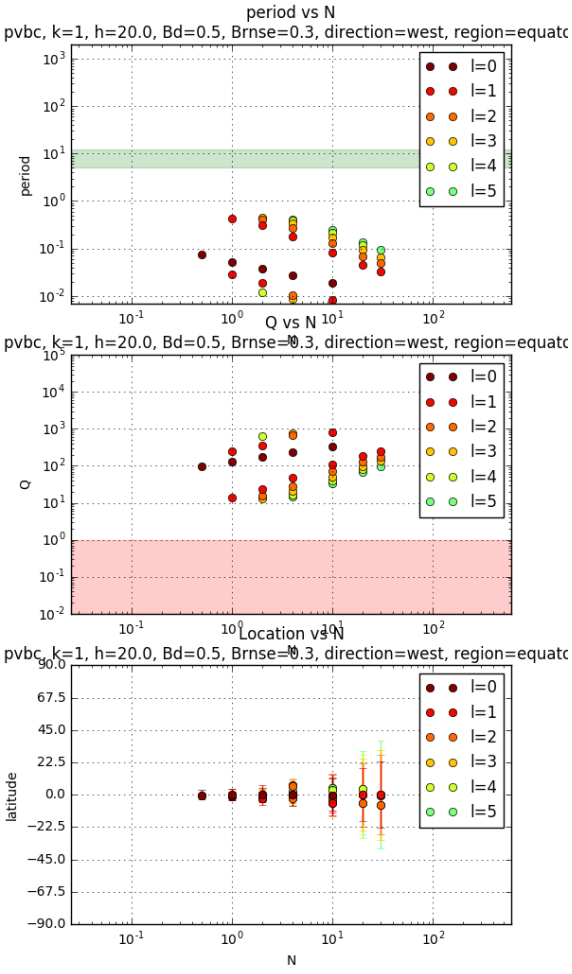

Figure D.14: Wave Dependence on SOC buoyancy (N), westward modes, equatorial region, H=20 km

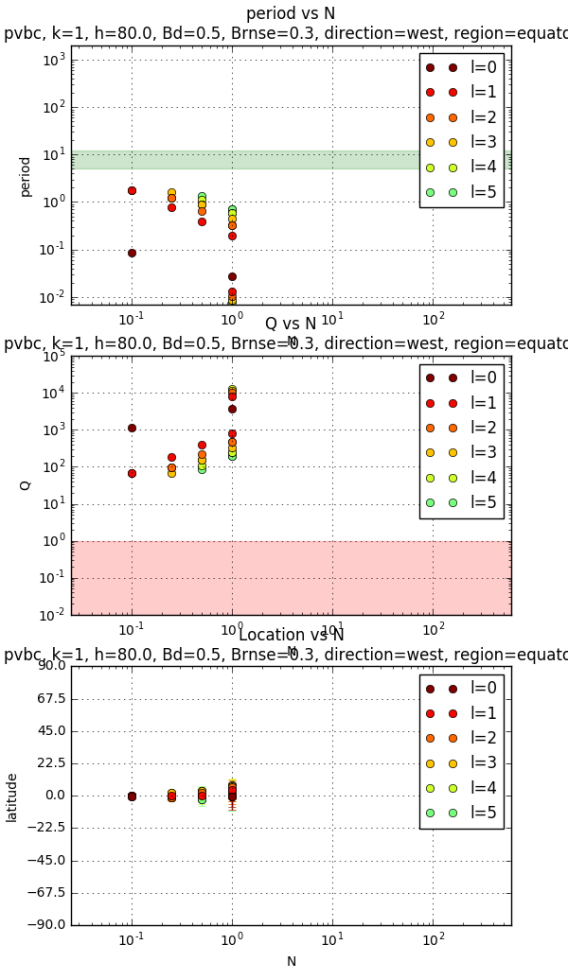

Figure D.15: Wave Dependence on SOC buoyancy (N), westward modes, equatorial region, H=80 km

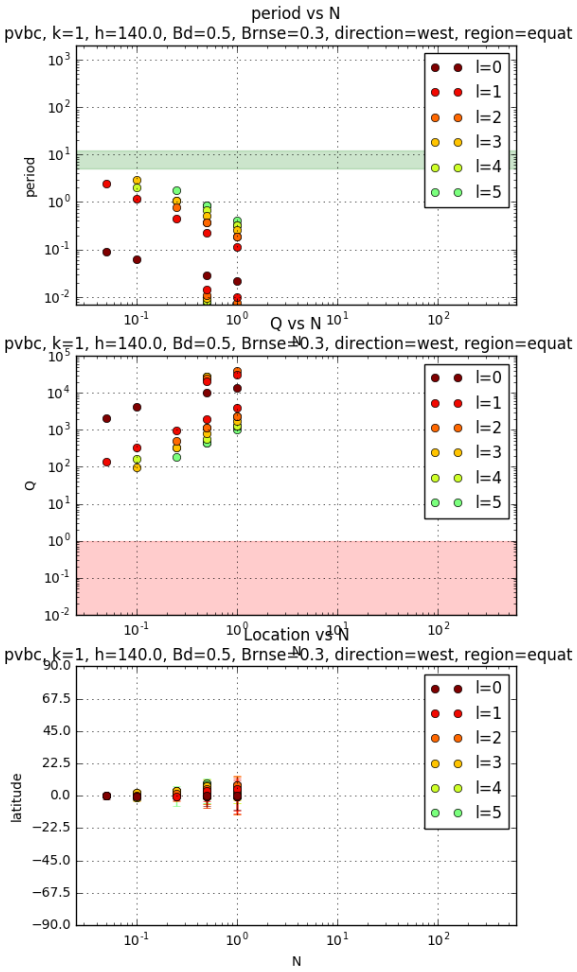

Figure D.16: Wave Dependence on SOC buoyancy (N), westward modes, equatorial region, H=140 km

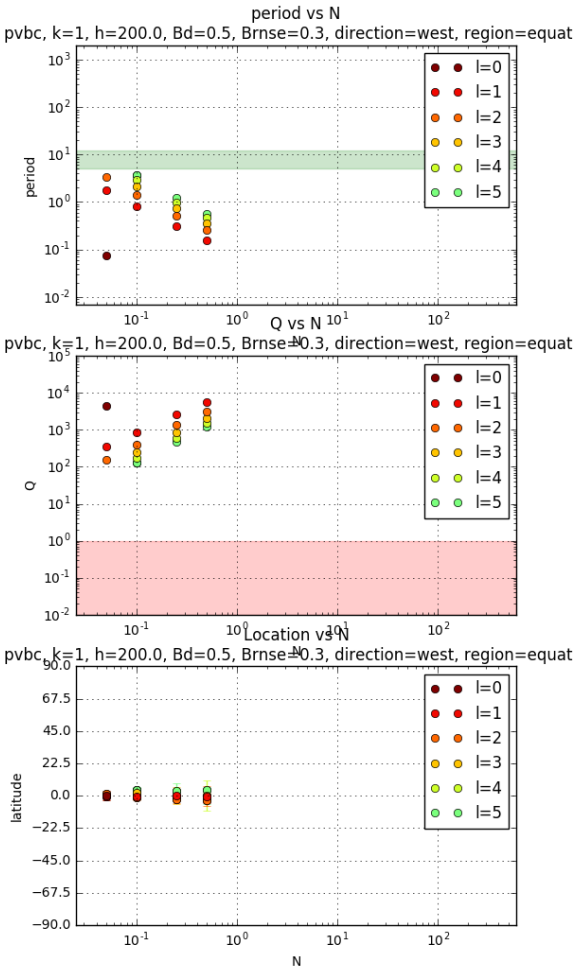

Figure D.17: Wave Dependence on SOC buoyancy (N), westward modes, equatorial region, H=200 km

D.2 Eastward Modes

D.2.1 Equatorial Region

D.2.1.1 Variation with Magnetic Field Strength

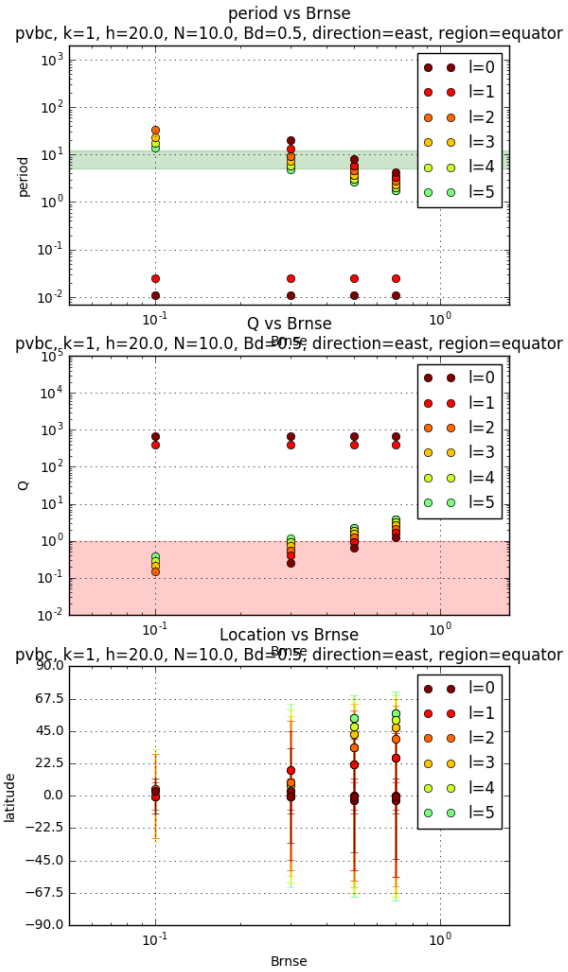

Figure D.18: Wave Dependence on magnetic field strength (B), eastward traveling modes, equatorial region, H=20 km, N=10 Ω

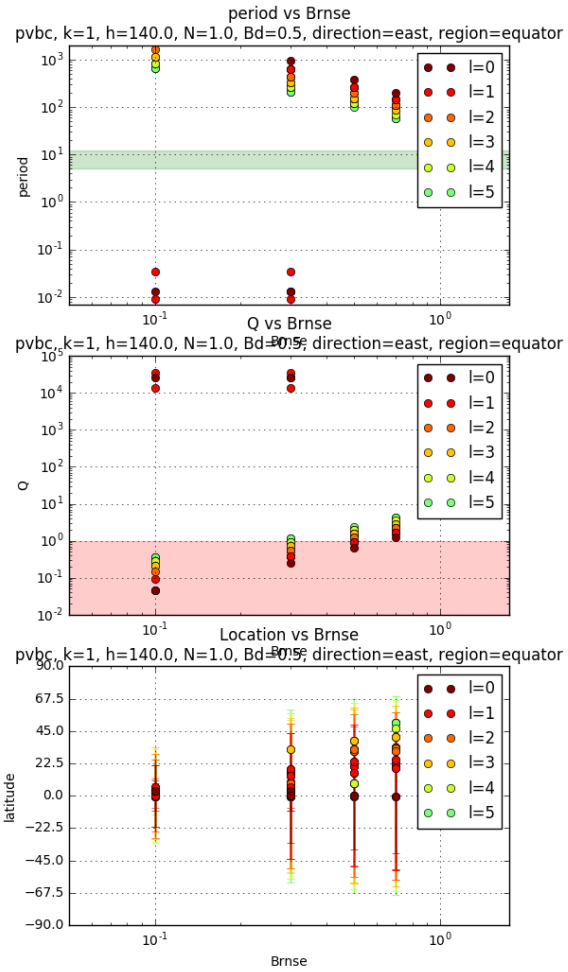

Figure D.19: Wave Dependence on magnetic field strength (B), eastward traveling modes, equatorial region, H=140 km, N=1 Ω

D.2.1.2 Variation with SOC Thickness

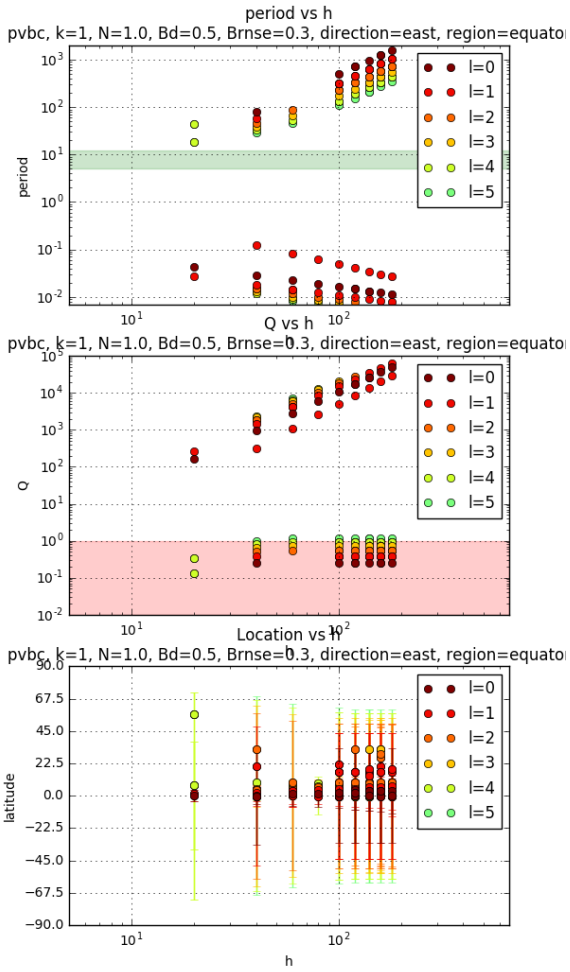

Figure D.20: Wave Dependence on SOC thickness (H), eastward traveling modes, equatorial region, N=1 Ω

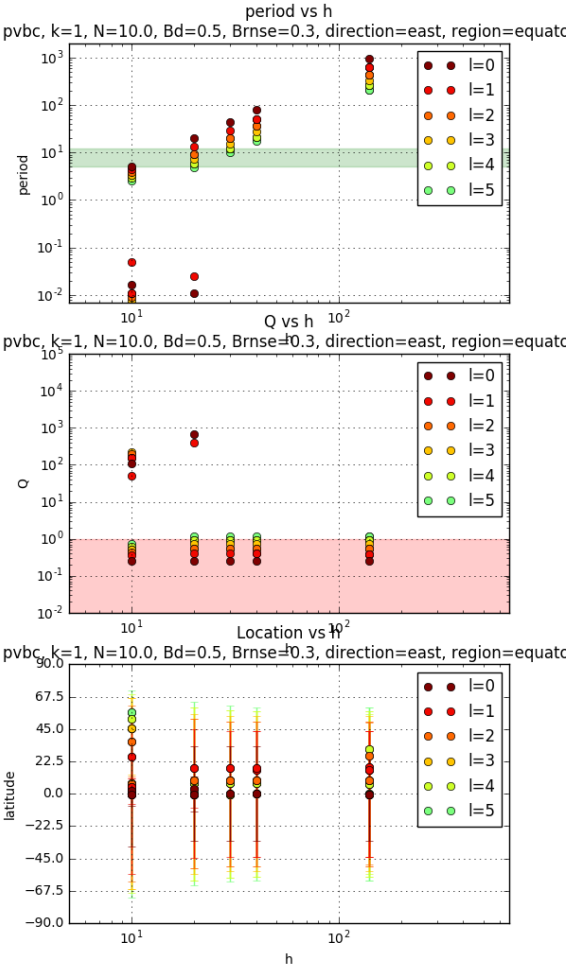

Figure D.21: Wave Dependence on SOC thickness (H), eastward traveling modes, equatorial region, N=10 Ω

D.2.1.3 Variation with SOC Buoyancy

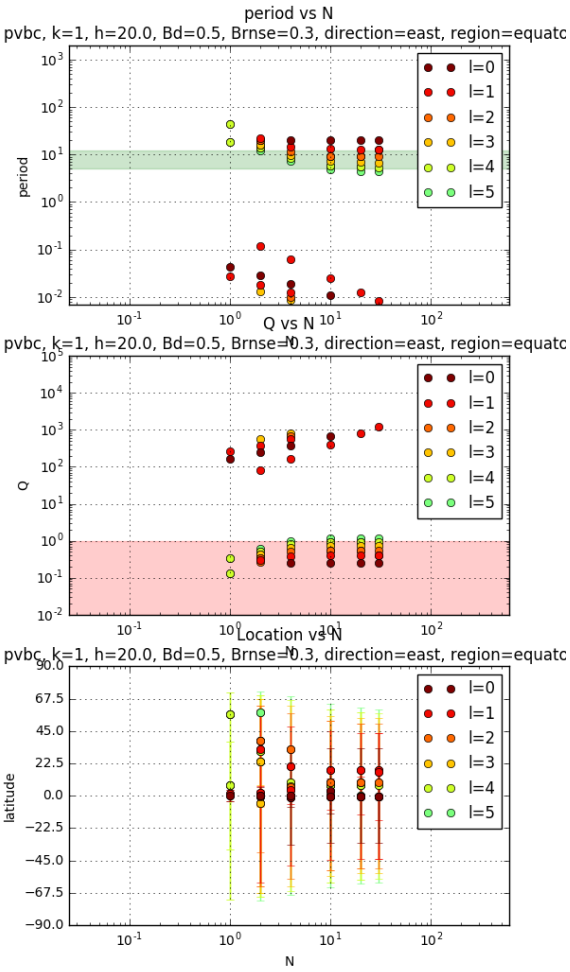

Figure D.22: Wave Dependence on SOC buoyancy (N), eastward traveling modes, equatorial region, H=20 km

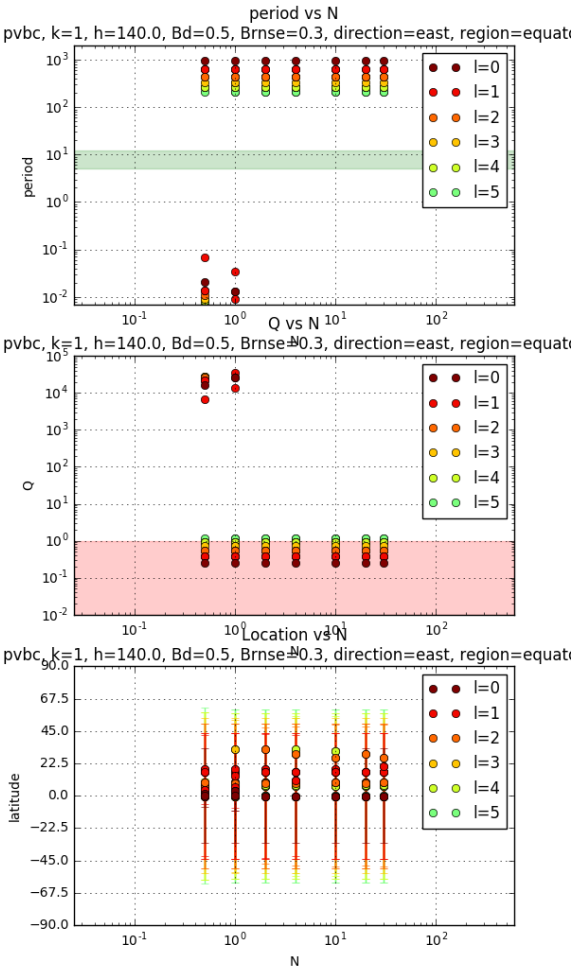

Figure D.23: Wave Dependence on SOC buoyancy (N), eastward traveling modes, equatorial region, H=140 km